100th anniversary of E.K. Zavoiskii

Russian Ministry of Education and Science
Russian Academy of Science
Government of Tatarstan Republic
Kazan State University
Zavoiskii Physical-Technical Institute
Bruker Ltd (Moscow)

ACTUAL PROBLEMS OF MAGNETIC RESONANCE AND ITS APPLICATION

XI International Youth Scientific School

“NEW ASPECTS OF MAGNETIC RESONANCE APPLICATION”

Program
Lecture Notes
Proceedings

Kazan
23 - 28 September 2007

NEW ASPECTS OF MAGNETIC RESONANCE APPLICATION. Proceedings of the XI International Youth Scientific School “Actual problems of magnetic resonance and its application”, 23 – 28 September 2007, Kazan. Edited by professor M.S. Tagirov (Kazan State University) and professor V.A. Zhikharev (Kazan State Technological University).

The reports of young scientists submitted on XI International Youth Scientific School “Actual problems of magnetic resonance and its application” are included in the present collection.

Lecture notes are approved by the methodical commission of Physical Faculty of Kazan State University (chairman: professor D.A. Tayurskii)

ISBN 5-94605-015-X

The administration of School

professor M.S. Tagirov (KSU, Kazan) — rector
professor V.A. Zhikharev (KSTU, Kazan) — vice-rector
V.K. Voronkova (KFTI RAS, Kazan) — scientific secretary
I.P. Volodina (KSU, Kazan) — secretary

The program committee

The chairman
professor V.A. Atsarkin (IREE, Moscow)

Committee members

professor A.V. Aganov (KSU, Kazan)
professor B.I. Kochelaev (KSU, Kazan)
professor I.V. Ovchinnikov (KFTI RAS, Kazan)
professor K.M. Salikhov (KFTI RAS, Kazan)

The organizing committee of School’2007

M.S. Tagirov, V.A. Zhikharev,
I.P. Volodina, I.G. Motygullin,
A.V. Klochkov, K.R. Safiullin
A.N. Yudin, Ya.V. Dmitriev,
O.N. Chibisova, I.V. Romanova,

Program

Sunday, September 23

10:00 – 10:15 **Opening Ceremony** (Hall B, CSC UNICS)

Lectures (Hall B, CSC UNICS)

10:15 – 11:00 **E.B. Fel'dman,** "Methods of Spin Dynamics for Solving Problems of Quantum Information Theory"

11:00 – 11:30 **Coffee break**

11:30 – 12:15 **I.R. Mukhamedshin,** "NMR/NQR Study of Sodium Cobaltates"
12:15 – 13:00 **S.B. Orlinskii,** "Quantum Confinement: from Model to Reality"

13:00 – 14:00 **Lunch**

Oral session (Hall B, CSC UNICS)

14:00 – 14:15 **V.S. Iyudin,** "The Application of Time Resolved EPR to the Study of Energy Transfer Processes in Photodynamic Therapy"
14:15 – 14:30 **T.A. Zinkevich,** "Subunit Mobility Researching at Alpha-Crystalline by ^{1}H NMR"
14:30 – 14:45 **L.V. Mingalieva,** "EPR Study of Exchange Interaction in Compound $\{[Nd_2(\alpha\text{-Fur})_6(H_2O)_2]\}_n$"
14:45 – 15:00 **A.A. Sukhanov,** "Time Resolved EPR of the Excited Triplet States Using ELEXSYS E580"
15:00 – 15:15 **S.V. Abramova,** "The Axonal Transport and Water Molecules Mobility in Nerve. Investigation by PFG NMR method"
15:15 – 15:30 **V.V. Kuzmin,** "Nuclear Spin-kinetics of ^{3}He in Magnetic Aerogel"
15:30 – 15:45 **L.G. Eidinov,** "Spin-echo NMR Study of the Translational Water Diffusion in Various Zones of Maize Root and its Sensitivity to the Water Channel Blocker"

16:45 – 16:15 **Coffee break**

16:15 – 16:30 **T.P. Gavrilova.** "Anisotropic Exchange Interaction in $CuTe_2O_5$"
16:30 – 16:45 **A.A. Ershova,** "Study of EPR Spectra in $LiLuF_4:U^{3+}$ and $LiYF_4Yb^{3+}$ Single Crystals"
16:45 – 17:00 **N.Yu. Panarina,** "Study of Low-Dose Irradiation Effects on Properties of Thin HTSC Films by Means of EPR and Hall Probes"
17:00 – 17:15 **R.R. Gainov,** "Copper NQR Studies of Ag-doped Ternary Sulfide $Cu_{12}As_4S_{13}$ (Tennantite)"
17:15 – 17:30 **A.A. Rodionov,** "ESR Studies of Solid Substrates for the Dynamic Polarization of the Noble Gases"
17:30 – 17:45 **M.I. Valitov,** "Paramagnetic Monitoring of Electrochemical Reactions"

18:00 **Welcome party**

PROGRAM

Monday, September 24

10:00 – 14:00	Opening of the International Scientific Conference “Modern Development of Magnetic Resonance (Zavoisky100)” and Bruker User’s Meeting. (Hall A, CSC UNICS)
15:30	Excursion to Raifa Monastery

Tuesday, September 25

9:30 – 12:00	Plenary lectures of Forum “Zavoiski week 2007”

Oral session (Hall B, CSC UNICS)

12:15 – 12:30	**A.A. Levantovsky,** “Application of Non-Linear Approximation for Electron Paramagnetic Resonance Signal Processing: *EPRMultiPeak* Software”
12:30 – 12:45	**T.V. Popov**, “New Approach to the Design of Real Time Controlling Software for the Automation of Mobile EPR Spectrometer”
12:45 – 13:00	**N.A. Mavrinskaya,** “Experimental study of ESR absorption temperature dependence of chemically dehydrohalogenated poly(vinylidene fluoride)”
13:00 – 13:15	**E.L. Golovkina,** “pH Spin Labeling Technique for Determining Acid-Base and Electrochemical Characteristics of Nanoporous and Nanostructural Oxides”
13:15 –13:30	**A.V. Soukhorukov,** “Spin Relaxation of Conduction Electrons in Ion Implanted Layers of Si with Modified Isotopic Composition”
13:30 – 14:30	**Lunch**

Lectures (Bruker User’s Meeting , aud. 305, Physical Department)

14:30 – 15:10	**A. Kamlowski,** “Новые аппаратные возможности в X, W, Q и L диапазонах: решения разной степени сложности”
15:10 – 15:50	**I. Gromov,** “ЭПР спектроскопия в ETH Цюрих. (Методика передовых экспериментов, от рутинного к сложному и недосягаемому)”

Oral session (Hall B, CSC UNICS)

16:00 – 16:30	**Coffee break**
16:30 – 16:45	**I.E. Rapoport,** “Usage of Low-Field Extremity MRI for Wrist Bone Erosions Detection and Evaluation in Comparison with Plane Radiography Data in the Diagnostics of Patients with Early Rheumatoid Arthritis”
16:45 – 17:00	**O.V. Masina,** “Radiological Diagnostics of Pancreatic Pseudocysts”
17:00 – 17:15	**V.V. Zuev,** “MRI Cystourethrography”
17:15 – 17:30	**A.S. Shavyrin,** “Novel Cyclic Derivatives of Substituted Iminoquinones or Aminophenols: NMR Study”
17:30 – 17:45	**A.V. Fokin,** “Models of Paramagnetic Centres Gd^{3+} in Tetrahedral Yttrium Clusters in Cadmium Fluoride”
17:45 – 18:00	**A.I. Poddel’sky,** “The Application of EPR and NMR Spectroscopy for the Reversible $^3O_2$ Binding by Complexes With Redox Active Ligands”
18:00 – 18:15	**E.V. Morozov,** “Phosphorus-31 Spin-lattice Relaxation in Aqueous Solutions Digidrophosphate Sodium”

PROGRAM

Wednesday, September 26

9:00 – 12:15 Musters classes or (and) plenary lectures of Forum “Zavoiski week 2007”

Oral session (Hall B, CSC UNICS)

12:15 – 12:30 **S.S. Zalesskiy,** “Ni-Catalyzed Phenylthiol Addition to Alkynes: Identification of Products Structure by Means of NMR Spectroscopy”

12:30 – 12:45 **K.A. Chernyshev,** “Configurational Assignment and Conformational Analysis of Azomethines Based on their ^{13}C–^{13}C, ^{13}C–^{1}H and ^{15}N–^{1}H Spin-Spin Coupling Constants”

12:45 – 13:00 **A.B. Mantsyzov,** ”NMR Assignments of the C-Terminal Domain of Human Polypeptide Release Factor eRF1”

13:00 – 13:15 **M. Gafurov,** “Dynamic Nuclear Polarization: From Solids towards to Liquids, Biomolecules, and High Frequencies”

13:15 – 14:15 **Lunch**

Lectures (Hall B, CSC UNICS)

14:15 – 15:00 **F.S. Dzheparov,** “Spin Dynamics in Disordered Solids”

15:00 – 15:45 **L.R. Tagirov,** “Ferromagnetic Resonance Studies of Magnetic Nanostructures”

15:45 – 16:15 **Coffee break**

Oral session (Hall B, CSC UNICS)

16:15 – 16:30 **Ya.V. Baclanova,** “NMR ^{1}H and ^{7}Li in $Li_{2-x}H_xMO_3$ (M=Ti, Zr)”

16:30 – 16:45 **A.V. Donets,** “Relaxation of ^{2}H, ^{23}Na, and ^{35}Cl Nuclei in Binary and Ternary Aqueous Solutions”

16:45 – 17:00 **I.V. Drebushchak,** “Reorientation mobility of NH_3-group and thermodynamic parameters of glycine polymorphs”

17:00 – 17:15 **A.A. Sitnikov,** “Analysis of the Radical Formation in Electron Irradiated Synthetic Carbonate-Containing Hydroxylapatite by IR, EPR and ESE Spectroscopy”

17:15 – 17:30 **D.V. Savchenko,** “EPR, ESE and Pulsed ENDOR Investigations of Nitrogen Aggregated Center in 4H-SiC Wafers Grown by Different Technologies”

17:30 – 17:45 **A.K. Shukla,** “EMR and Optical Absorption Studies of Vanadyl Doped L-Asparagine Monohydrate”

17:45 – 18:00 **A.C. Başaran**, “Magnetic Properties of Chemically Deposited Ferromagnetic Semi-Conducting $CuCr_2S_4$ Thin Films on Si(100) and YSZ(100) Substrates”

Thursday, September 27

9:00 – 12:00 Musters classes or (and) plenary lectures of Forum “Zavoiski week 2007”

Oral session (Hall B, CSC UNICS)

12:00 – 12:15 **I.G. Mammadov,** “Research of Molecular Dynamics of 4-methyl-2-allylphenol Derivatives in Solution by NMR Spectroscopy Method”

12:15 – 12:30 **M.S. Gruzdev,** “Synthesis and EPR-investigation of Iron (III) Containing Dendrimeric Complex of Second Generation, Derivative of 3,4-*n*-Decyloxybenzoyl Poly(Propylene Imine)”

12:30 – 12:45 **B.V. Munavirov,** “The Influence of Lysozyme on Self Diffusion of Monoolein in Cubic Phase”

12:45 – 13:00 **N.V. Shkalikov,** “Part P_s of Solid Component in the ^{1}H NMR Signal as a New Oil Characteristic”

13:00 – 14:00 **Lunch**

Lecture (Bruker User’s Meeting, aud. 305, Physical Department)

14:00 – 14:45 **D. Mueller,** “Твердотельный ЯМР сегодня: мифы и реальность (Исследование новых материалов, био - ЯМР, классика)”

Lectures (Hall B, CSC UNICS)

15:00 – 15:45 **U. Eichhoff,** “Trends in NMR Hardware Development: Magnet Design and Automation”

15:45 – 16:30 **A.V. Egorov,** “Continuous Wave (CW) Method in NMR”

16:30 – 17:00 **Coffee break**

Oral session (Hall B, CSC UNICS)

17:00 – 17:15 **A.A. Mozhegorov,** “Antiferromagnetic Resonance in $LaTiO_3$ and $YTiO_3$”

17:15 – 17:30 **V.L. Parshina,** “Using RF Pulses Sequences for Slice Selection in NMR Imaging”

17:30 – 17:45 **S.L. Veber,** “High-Field EPR Study of the Exchange Interactions in Strongly-Coupled Spin Triads Undergoing Thermally-Induced Structural Rearrangements”

17:45 – 18:00 **A.C. Başaran,** “Magnetic Properties of Chemically Deposited Thin Films of Ferromagnetic-Semi-Conducting $CdCr_2S_4$ Compounds”

Friday, September 28

Oral session (Hall B, CSC UNICS)

9:30 – 9:45 **A.D. Siraev,** “EPR of Ni^{2+} Impurity Centers in BaF_2 Crystal”

9:45 – 10:00 **S.B. Zikirin,** “EPR Spin Probe Study of Surface Properties of Magnetic-Heterogeneous Oxide Systems”

10:00 – 10:15 **O.V. Smirnova,** “Alignment of 1,2– and 1,3–Dichloronaphtalene and 1,2,3–Trichloronaphtalene Induced by Strong Magnetic Field”

10:15 – 10:30 **O.N. Sorokina,** “Magnetic Nanoparticles Influence on the Radical ESR Spectra”

10:30 – 10:45 **K.V. Kholin** “Paramagnetic Monitoring of Electrochemical Conversion of Some Free Radicals and Nickel Complexes”

10:45 – 11:00 **M.A. Fayzullin,** “Image-potential States in Small Metal Particles”

11:00 – 11:30 **Coffee break**

11:30 – 11:45 **K.R. Safiullin,** “Observation of the Magnetic Coupling Between Nuclei of Liquid ^{3}He and ^{141}Pr in PrF_3 Crystal Powder”

11:45 – 12:00 **M.M. Stepanov,** “`1-D Magnetic Photonic Crystals: Dispersion and Optical Properties”

12:00 – 12:15 **A.V. Chertkov,** “Conformation of Saturated Five-Membered Heterocecles as Studied by NMR and *ab’initio* Calculations”

12:15 – 12:30 **A.R. Gabidinova,** “Engineering and Production of “Fast” Impulse Sequences for Low-Field Magnetic-Resonance Tomographs”

12:30 – 12:45 **V.V. Novikov,** “Describing Spin Label Motion: Ordering Potential or Partial Averaging?”

12:45 – 13:00 **A.A. Uchevatkin,** “Morphometric Analysis MR Imaging of Experimental Ischemic and Hemorrhagic Stroke in Rats”

13:00 – 14:00 **Lunch**

Lectures (Hall B, CSC UNICS)

14:00 – 14:45 **N.M. Sergeev,** “Identification of Ortho and Para Isomers of Water by Means of NMR Spectroscopy”

14:45 – 15:30 **U. Eichhoff,** “Technical Advances in Spin Labelling EPR”

15:30 – 16:15 **L.E. Svistov,** “Quasi-Two-Dimensional Triangular Lattice Antiferromagnet $RbFe(MoO_4)_2$”

16:15 – 17:00 **I.N. Tarasov,** “ЯМР в нанотехнологиях. Перспективы. «Брукер» представляет журнал «Российские нанотехнологии»”

17:00 **Closing ceremony**

Methods of Spin Dynamics for Solving Problems of Quantum Information

E.B. Fel'dman

Institute of Problems of Chemical Physics of Russian Academy of Sciences, Chernogolovka, 142432, Moscow Region, Russia

e-mail: efeldman@icp.ac.ru

The problems of quantum computations are one of the central directions of current investigations. The creation of quantum computers [1] allow to solve the problems that cannot be solved by classical computers. These investigations posed some new problems in quantum information theory. A quantum-mechanical system possesses additional correlations that do not have a classical counterpart. Entanglement [1] is determined by such correlations and the entangled states are a main resource of quantum computers. It is well known [1] that nuclear spins are the simplest realization of quantum bits (qubits) and the theoretical methods of spin dynamics, which describe a system of interacting nuclear spins, are adequate in order to solve the corresponding problems of quantum information theory. One-dimensional spin systems (chains, rings) are the most suitable for these goals. The point is that the Hamiltonian of the one-dimensional system of spins coupled by spin–spin interactions (SSI) can be exactly diagonalized in the approximation of the nearest neighbor interactions [2] and the quantitative measure of the entanglement [3] can be determined. However the classical methods of diagonalization [2,4] are restricted by homogeneous systems when coupling constants of all nearest neighbors are equal one another and the external magnetic field is homogeneous. It is insufficient for solving some problems of quantum computations. For example, these methods cannot solve the qubit addressing problem. Recently the XY-Hamiltonian of the alternating open chain of spins was diagonalized [5,6]. Then, on the basis of the generalization of the method presented in [5] the Hamiltonian of an open chain with periodically varying SSI constants and Larmor frequencies was diagonalized [7]. Thus, the possibility of treating such a chain as a model quantum register with qubit addressing appears. A lot of interesting phenomena were recently found in quantum registers on the basis of inhomogeneous open spin chains.

In the present lecture new methods of diagonalization of the XY- Hamiltonian are briefly discussed. The problems of reliable transmission of a quantum state (qubit) from one end of a chain to the other end are considered for an alternating open spin chain. I demonstrate that the ideal transfer of qubits is possible in alternating chains with a larger number of spins than that in homogeneous chains [6]. The entanglement in alternating open spin chains of nuclear spins ($s=1/2$) with the XY Hamiltonian is discussed in detail. In particular the numerical results [8,9], which describe the dependence of the spin pair entanglement on the temperature, the chain length, the distance of a pair of spins from the chain ends, and the ratio of SSI constants, are presented.

It is naturally that the entanglement disappears in the high external magnetic field. However this is not the case in a staggered magnetic field [10] when the Larmor frequencies are alternating ones. This case is also considered.

A new phenomenon, long-distance entanglement, was recently predicted [11] on the basis of the theory [6] when the entanglement of spins (qubits) in the two end points of the open alternating chain appears. It means that such spin chains can be used as channels for long-distance, high-fidelity quantum teleportation. The long distance entanglement and quantum teleportation in XX spin chains are also discussed.

In conclusion some new one-dimensional models are considered and their application to the problems of quantum information theory are discussed.

This work is supported by the Russian Foundation for Basic Research (project no. 07-07-00048)

References

[1] M.A. Nielsen and I.L.Chuang. Quantum Computation and Quantum Information. Cambridge Univ. Press, Cambridge. 2000.

[2] E.Lieb, T.Shultz, and D.Mattis, Ann.Phys. (N.Y.) **16**, 497 (1961).

[3] W.K.Wootters, Phys.Rev.Lett. **80**, 2245 (1998).

[4] H.B.Cruz, L.L.Gonsalves, J.Phys.C **14**, 2785 (1981).

[5] E.B.Fel’dman, M.G.Rudavets, JETP Letters **81**, 47 (2005).

[6] E.I.Kuznetsova, E.B.Fel’dman, JETP **102**, 882 (2006).

[7] K.E. Feldman, J.Phys.A: Math. Gen. **39**, 1039 (2006).

[8] S.I.Doronin, A.N.Pyrkov, E.B.Fel’dman, JETP Letters **85**, 519 (2007).

[9] S.I.Doronin, A.N.Pyrkov, E.B.Fel’dman, JETP**132**, (2007).

[10] J.Hide, W.Son, I. Lawrie, V.Vedral, Phys.Rev.A **76**, 022319 (2007).

[11] L.Campos Venuti, S.M.Giampaolo, F.Illuminati, P.Zanardi, arXiv: 0708.0587 [quant-phys] (2007).

NMR/NQR Study of Sodium Cobaltates

I.R. Mukhamedshin

Kazan State University, 420008, Kremlyovskaya str. 18, Kazan, Russia

e-mail: Irek.Mukhamedshin@ksu.ru

Sodium cobaltates Na_xCoO_2 is a new family of lamellar transition metal oxides. Cobaltates have attracted attention of condensed matter physics and materials science communities recently due to the fact that the cobalt average charge state can be tuned over a great range by varying the Na concentration, leading to unusual properties from unconventional superconductivity when hydrated [1] at $x \approx 0.35$ to a novel "Curie-Weiss metal" [2] for $x \approx 0.7$ and enhanced thermopower [3] for $x \approx 0.85$.

In the lecture I summarize the results of our investigations of sodium cobaltates with different sodium contents by NMR/NQR [4-6]. After a short introduction to the basics of NMR and NQR, I shall present SQUID and NMR/NQR data taken on different cobaltates powder samples synthesized and characterized by X-ray diffractometry.

^{59}Co NMR data in the x=0.35 phase reveal a single electronic Co state with weakly T dependent NMR shift tensor components. The susceptibility of this phase is Pauli like and there is no evidence of any charge ordering. Comparison of this phase with the ^{59}Co NMR data in the superconducting compound clearly allow us to show that the charge state of cobalt is the same in both phases [5].

In the relatively narrow sodium content range $0.65 < x \leq 0.75$ we have synthesized and characterized four different stable phases of Na ordered Na_xCoO_2 [4,6]. Above 100 K they display similar Curie-Weiss spin susceptibilities as well as ferromagnetic $q = 0$ spin fluctuations in the CoO_2 planes revealed by ^{23}Na NMR data. In all phases the cobalts display different charged states, and the Na and Co charges form an ordered pattern. Above 300 K Co disproportionate already into non magnetic Co^{3+} and magnetic Co sites on which holes delocalize with an average valence $\approx Co^{3.5+}$. This allows us to understand that metallic magnetism is favoured. Below 100 K the phases differentiate, and a magnetic order sets in only for x=0.75. So the Na charge order governs then the low T energy scales and transverse couplings in lamellar cobaltates with high sodium content.

We show that ferromagnetic 2D fluctuations are indeed characteristic of all studied phases with high sodium content at high T, and the x=0.67 phase appears as an ideal 2D nearly ferromagnetic metal without 3D ordering settling in at low T [6].

The work was partially supported by Russian Foundation for Basic Research (Grant No. 06-02-17197) and by INTAS (Ref. Nr. 04-83-3891).

Reference

[1] K. Takada *et al.*, Nature (London) **422**, 53 (2003).

[2] M.L. Foo *et al.*, Phys. Rev. Lett. **92**, 247001 (2004).

[3] M. Lee *et al.*, Nature Mater. **5**, 537–540 (2006).

[4] I.R. Mukhamedshin *et al.*, Phys. Rev. Lett. **93**, 167601 (2004).

[5] I.R. Mukhamedshin *et al.*, Phys. Rev. Lett. **94**, 247602 (2005).

[6] I.R. Mukhamedshin, H. Alloul, G. Collin, and N. Blanchard, cond-mat/0703561.

Quantum confinement from model to reality

S.B. Orlinskii

Kazan State University, 420008, Kremlyovskaya str. 18, Kazan, Russia
e-mail: Sergei.Orlinskii@ksu.ru

Possibility of quantum dots doping [1] opens a wide field for investigation of fundamental properties of electron *s*-type wave function on quantum confinement regime.

We have recently shown that ZnO nanocrystals can be doped with shallow donors by the introduction of interstitial Li and Na atoms [1] and substitutional Al atoms. It demonstrated that high-frequency EPR and ENDOR spectroscopy at 95 GHz is the method of choice to identify the atomic structure of these donors and to probe for the first time the effect of confinement on their electronic wave function.

For the shallow Li donor in ZnO nanoparticles, an increase of the hyperfine interaction with the ^{7}Li nucleus and the ^{1}H nuclei of the $Zn(OH)_2$ capping layer is observed proportionally to R^{-3} (R is the radius of the ZnO core) when reducing the radius of the nanoparticles from 2.2 to 1.6 nm. These experiments are carried out at liquid-helium temperatures to ensure that the electron is bound to the positively charged Li^{+} core. When reducing the radius of the particle further to 1.1 nm there is a clear deviation from the R^{-3} dependence. This change in behaviour is attributed to the transition from semiconductor to molecular-cluster-type properties [2].

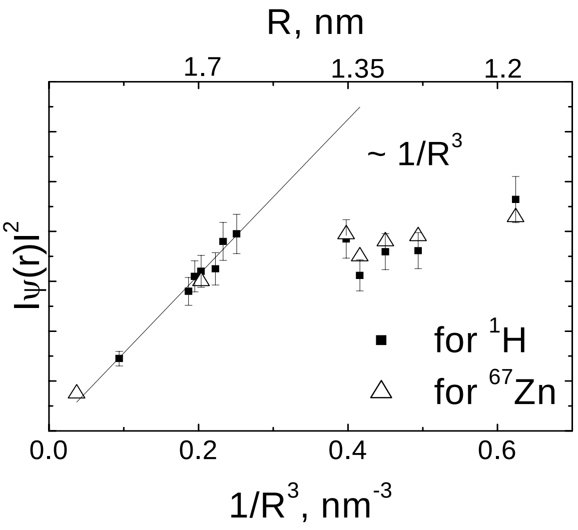

In addition to the hyperfine interactions with the ^{7}Li and ^{1}H nuclei, information is also supplied by the hyperfine interactions with the ^{67}Zn nuclei. It is concluded that even for the smallest particles the Zn nuclei carry non-zero spin density at the $ZnO/Zn(OH)_2$ interface. Moreover this density increases with decreasing size of the particles. We conclude that effective mass theory, that works so well in bulk semiconductors, does not apply for semiconductor nanocrystals with dimensions equal to or smaller that the Bohr radius of the shallow donor wave function in bulk material. Quantum confinement effect has limit as well.

Reference

[1] S.B. Orlinskii, J. Schmidt, P.G. Baranov et al, Phys. Rev. Lett. **92**, 047603 (2004).

[2] S.B. Orlinskii, J. Schmidt, E.J.J. Groenen, P.G. et al, Phys. Rev. Lett. **94**, 097602 (2005).

Spin Dynamics in Disordered Solids

F.S. Dzheparov

Institute for theoretical and experimental physics, 117218 B.Cheremushkinskaya 25, Moscow, Russia

email: dzheparov@itep.ru

Modern studies of spin dynamics in statically disordered media are presented. Main attention is attracted to new results, which were produced after writing time of preceding review lecture [1]:

1) experimental and theoretical studies on spin diffusion in disordered nuclear subsystems [2,3], and
2) investigations of influence of pulse sequences on disordered nuclear systems [4-6], which indicate particularly, that experimental technique gives now the possibility of measuring of free induction decay and dynamical nuclear polarization in disordered nuclear spin systems consisting of ^{29}Si or ^{13}C.

References

[1] F. S. Dzheparov, J. Superconductivity and Novel Magnetism **20**, 161 (2007).

[2] F. S. Dzheparov, JETP Lett. **82**, 521 (2005).

[3] A. D. Gul’ko, O. N. Ermakov, S. V. Stepanov and S. S. Trostin, J. Superconductivity and Novel Magnetism, **20**, 169 (2007).

[4] A. E. Dementyev, D. Li, K. MacLean, and S. E. Barrett, Phys. Rev. **B 68**, 153302 (2003).

[5] D. Li, A. E. Dementyev, Y. Dong, R. Ramos, and S. E. Barrett, Phys. Rev. Lett. **98**, 190401 (2007).

[6] D. Li, Y. Dong, R. G. Ramos, J. D. Murray, K. MacLean, A. E. Dementyev, and S. E. Barrett, arXiv:0704.3620.

Ferromagnetic Resonance Studies of Magnetic Nanostructures

B. Aktaş[1)], L.R. Tagirov[2,3)], B. Heinrich[4)]

[1)]Gebze Institute of Technology, 41400 Gebze-Kocaeli, Turkey
[2)]Zavoiski Physical-Technical Institute of RAS, 420029 Kazan, Russia
[3)]Kazan State University, 420008 Kazan, Russia
[4)]Simon Fraser University, Burnaby, BC, V5A 1S6, Canada

e-mail: Lenar.Tagirov@ksu.ru

In the lecture we give an example of application of magnetic resonance for studies of spin-valve like ferromagnetic nanostructures. Crucial property of these functional nanostructures is the in-plane magnetic anisotropy which determines equilibrium directions of magnetizations in ferromagnetic layers as well as switching field of a structure. Extremely small thickness of the ferromagnetic films (10-30 monolayers) makes hard even the SQUID magnetometry of the structures because of obscuring signal from a substrate.

The ferromagnetic resonance (FMR) is a highly sensitive and straightforward tool to measure basic magnetic properties as well as fine details of magnetic anisotropies of ultra-thin-film ferromagnetic nanostructures. It offers a possibility to characterize several magnetic layers simultaneously and selectively [1]. To demonstrate these advantages of the FMR technique we studied the magnetic anisotropies and magneto-elastic effects in single ferromagnetic layer samples GaAs/15Fe/20Au(1001), GaAs/15Fe/20Cr(001), GaAs/16Fe/9Pd/20Au(001), and double GaAs/15Fe/20Au/40Fe/20Au(001) magnetic layer structures grown on the surface-reconstructed GaAs(001) single crystalline substrate wafers [2,3]. The magnetic parameters of the films were determined by FMR in the temperature range of 4-300 K. We observed unconventional triple-mode FMR spectra allowing us to discriminate between various contributions to the in-plane magnetic anisotropies. Extraordinary angular dependence of the FMR spectra was explained by the presence of the four fold and two fold in-plane anisotropies induced by the substrate. Beside dominant interface effects the non-magnetic cap layers are observed to deeply affect the magnetic anisotropies of individual magnetic layers [2]. The magnetic anisotropies are discussed in terms of the interface and bulk anisotropy energies. They were found to be linearly-temperature dependent. This temperature dependence is attributed to magneto-elastic energy arising due to the lattice mismatch and differential thermal expansion of the metallic materials employed in these multilayer structures.

The valuable contribution of G. Woltersdorf[2], R. Urban (SFU), A.R. Köymen (UTA, USA), K. Özdoğan, M. Özdemir, B.Z. Rameev, O. Yalçın, F. Yıldız (GIT), and C. Birlikseven, H.Z. Durusoy, C. Topaçli (HUA, Turkey), to the original works is gratefully acknowledged.

References

[1] C.Birlikseven, C.Topaçli, H.Z.Durusoy, L.R.Tagirov, A.R.Köymen, B.Aktaş, Journal of Magnetism and Magnetic Materials **202**, 342-348 (1999).

[2] B. Aktaş, B. Heinrich, G. Woltersdorf, R. Urban, L.R. Tagirov, F. Yıldız, K. Özdoğan, M. Özdemir, O. Yalçın, and B.Z. Rameev, Journal of Applied Physics **102**, 013912(8) (2007).

[3] B. Aktaş, B. Heinrich, G. Woltersdorf, R. Urban, L.R. Tagirov, F. Yıldız, K. Özdoğan, M. Özdemir, O. Yalçın, and B.Z. Rameev, *Magnetic Anisotropies in Ultra-Thin Iron Films Grown on the Surface-Reconstructed GaAs Substrate*, in “Magnetic Nanostructures”, Springer Series in Materials Science, v. 94 edited by B. Aktaş, L.R. Tagirov and F. Mikailov, 2007), p. 167-184.

Trends in NMR hardware development: magnet design and automation

T. Gianotti[1)], D. Baumann[2)], U. Eichhoff[1)]

[1)]Bruker BioSpin GmbH, Silberstreifen, D-76287 Rheinstetten/Germany
[2)]Bruker BioSpin AG, CH-8117 Fällanden/Switzerland

email: tonio.gianotti@bruker.de, daniel.baumann@bruker.ch, uwe.eichhoff@bruker.de

In the last decades NMR had to meet many new requirements and was extended to completely new fields of application. This fact presented a real challenge to the hardware and software development to make all new ideas accessible and easy to use on commercial equipment. We will mainly concentrate in this lecture on two aspects: magnet design and automation features.

The needs of Biomolecular NMR extended the NMR frequencies up to the limits of the possibilities of modern supecrconductors. The 800 and 900 MHz frequency marks, corresponding to 18.79 and 21.14T, could only be reached by cooling the solenoid coil down to 2^{o}K. This “superstabilized” magnet technology proved to be very reliable. But a general drawback of superconducting magnets was their stray field. Already for the 600MHz-magnets the 5G-line extended to 6m and siting of those magnets became a problem. 800MHz- and 900MHz spectrometers with conventional magnets could not be placed in existing buildings. The solution to this problem was the active shielding, which was first used in NMR imaging for whole body clinical magnets. Bruker introduced this technology into the field of analytical NMR spectroscopy. From 1996 until 2004 more than 2000 UltraShield-magnets have been delivered.

Now UltraShield-Plus magnets are available, which keep the 5G line inside the magnet dewar. These magnets allow a new compact design of NMR spectrometers. Especially in industrial areas the easy handling is of great importance. The INCA (Integrated Chemical Analyzer) together with the appropriate software can be operated by non-NMR-people in almost a black-box approach. The UltraShield-Plus-magnet is mounted on ball bearings and can be moved inside the laboratory like any other analytical instrument.

The active shielding reduces not only the stray field but it also shields the solenoid from external perturbations. You can run a crane just above the magnet without seeing a perturbation on the lock signal.

Another aspect of cryotechnology in NMR is the development of cryoprobes. Cryoprobes increase sensitivity by a factor of almost three and decrease measurement time by almost one magnitude. They are cooled to liquid He temperature and with the according cryoplatform they are as easy to use and as reliable as normal probeheads.

The introduction of NMR into many branches of industry with large series of routine measurements and the lack of highly qualified and expensive NMR scientists led to increasing automation of all steps of NMR measurements beginning with sample preparation and ending with spectra evaluation.

Automatic sample handling is possible by preparation of samples in tubes and transfer to the magnet by sample changers or by sample preparation in vials and liquid injection into flow through-probeheads. This approach was initially used for LC-NMR, but proved so effective, that it was adopted as another method of sample changing, which we call BEST-NMR (**B**ruker **E**fficient **S**ample **T**ransfer).

Stabilization of measuring conditions continued over 3 decades. The introduction of microprocessors in the early 70’s opened completely new possibilities for automation of many features of the NMR spectrometer. Calibration curves and main instrument parameters such as shim values etc. could be stored and recalled. The whole spectrometer operation became much easier and more accurate and reliable. Control functions could be decentralized. Local intelligence could be placed on boards and separate units. This led to a much higher flexibility of the spectrometer functions. Both Frequency and Field settings can now be used for Lock Automation. Drift can be compensated by frequency adjustment. Direct digital synthesis (DDS) allowed frequency jumps and lock at various field positions.

The high accuracy and stability of the spectrometer electronics must be extended to the main accessories. For example the regulation accuracy for MAS rotation must be in the range of 0.01-0.1% during a test time of 5 hours in order not to deteriorate the overall spectral performance. Only in 2003 high precision piezo-regulators became available allowing to meet these requirements.

The development for automatic matching and tuning of probeheads continued over two decades. The torque of classical electric motors becomes very weak in strong magnetic fields. A ferromagnetic shielding could improve this situation, but would lead to unacceptable distortions of the magnetic field and degrade the resolution.

All tuning and matching trimmers had to be carefully selected regarding their performance in high magnetic field and care had to be taken to protect these devices against mechanical overload. Rotation had to be stopped before reaching the limit. For all these features sensors had to be implemented and all of them had to perform reliably in high magnetic field.

We tried to show on some selected examples that designing NMR spectrometers means working at the edge of today technology. Often little details require a lot of attention, time and money. There is no part in the spectrometer, which can be neglected, if you try for the best performance.

Continuous Wave (CW) Method in NMR

A.V.Egorov

Kazan State University, 420008, Kremlevskaya 18, Kazan, Russia

e-mail: Alexander.Egorov@ksu.ru

Nuclear Magnetic Resonance (NMR) — the phenomenon of resonance energy adsorption by nuclear spins – was discovered nearly simultaneously by two groups of american scientists in 1946. Both groups used CW technique. In a few years pulse method was developed as alternative technique of NMR studies. After that there was rather long time of improvement for both methods. The general point of view of experimentalists at that time was that the choice of method depends on problem and both approaches add each other. Nowadays NMR associates mainly with high resolution Fourier transform spectrometer. What are the reasons of that? Is CW NMR really dead? Present report pretends to answer these questions.

There are many reasons for the wipe out of CW NMR. The first, objective — higher sensitivity of pulse NMR compared to CW. Another one — commercial. There is general tendency to use commercial spectrometers instead of home-built of 70-th. Chemists and biologists who really need high resolution NMR occupy the market. CW setups are not produced. As a result continuous wave NMR survived where commercial setups cannot be used — for example, ultra low temperature physics. All these factors lead to the situation that newcomers in NMR are not familiar with CW and believe that if something cannot be done with a help of Bruker spectrometer, it can’t be done at all.

There is a brunch of NMR spectroscopy called “broad lines”. Here CW NMR is definitely advantageous. Taking into account of the receiver dead time one can show that CW sensitivity can be even higher than pulse. The fact that inhomogeneous NMR line broadening can overrun pulse spectrometer bandwidth makes it necessary to sweep frequency in the pulse experiment. The variation of transverse relaxation rate over the line results in lineform distortions. In general, CW has advantages in NMR spectroscopy of broadlines over the pulse method.

There are also a number of experimental problems, which can be solved, with a help of simple CW NMR setups even for narrow lines. The dominance of sensitivity considerations is not a usual case. The examples will be overviewed in the report.

Continuous Wave (CW) Method in NMR

A.V.Egorov

Kazan State University, 420008, Kremlevskaya 18, Kazan, Russia

e-mail: Alexander.Egorov@ksu.ru

Nuclear Magnetic Resonance (NMR) — the phenomenon of resonance energy adsorption by nuclear spins – was discovered nearly simultaneously by two groups of american scientists in 1946. Both groups used CW technique. In a few years pulse method was developed as alternative technique of NMR studies. After that there was rather long time of improvement for both methods. The general point of view of experimentalists at that time was that the choice of method depends on problem and both approaches add each other. Nowadays NMR associates mainly with high resolution Fourier transform spectrometer. What are the reasons of that? Is CW NMR really dead? Present report pretends to answer these questions.

There are many reasons for the wipe out of CW NMR. The first, objective — higher sensitivity of pulse NMR compared to CW. Another one — commercial. There is general tendency to use commercial spectrometers instead of home-built of 70-th. Chemists and biologists who really need high resolution NMR occupy the market. CW setups are not produced. As a result continuous wave NMR survived where commercial setups cannot be used — for example, ultra low temperature physics. All these factors lead to the situation that newcomers in NMR are not familiar with CW and believe that if something cannot be done with a help of Bruker spectrometer, it can’t be done at all.

There is a brunch of NMR spectroscopy called “broad lines”. Here CW NMR is definitely advantageous. Taking into account of the receiver dead time one can show that CW sensitivity can be even higher than pulse. The fact that inhomogeneous NMR line broadening can overrun pulse spectrometer bandwidth makes it necessary to sweep frequency in the pulse experiment. The variation of transverse relaxation rate over the line results in lineform distortions. In general, CW has advantages in NMR spectroscopy of broadlines over the pulse method.

There are also a number of experimental problems, which can be solved, with a help of simple CW NMR setups even for narrow lines. The dominance of sensitivity considerations is not a usual case. The examples will be overviewed in the report.

Identification of ortho and para isomers of water by means of NMR spectroscopy

N.M. Sergeyev, V.N. Torocheshnikov, N.D. Sergeyeva

Department of Chemistry, M. V. Lomonosov Moscow State University, Leninskie Gory, 119899 Moscow, Russia.

e-mail: sergeyev@nmr.chem.msu.su

Spin isomer phenomenon is well known since 1930s. First of all it concerns the ortho and para isomers of molecular hydrogen H_2 [1]. Last years the interest to spin isomer phenomenon was supported in the works by Chapovsky (Novosibirsk, Russia) (see e.g. [2]) especially for CH_3F molecule, where existence of two spin isomers is also possible.

Substantial increase of interest to this problem was caused by recent publication of Tikhonov and Volkov, devoted to spin isomers of water [3]. They managed to separate water by using chromatography into two isomers, to save up macro amounts of both isomers (milliliters), and even to estimate lifetimes for both isomers. For spin isomers in liquid state lifetimes were estimated as several minutes. This result seriously contradicts to the previous estimates of lifetimes of individual water molecules [3].

In the present report the methods of identification of spin isomers by means of NMR spectroscopy will be analyzed. First of all the fundamental property of symmetry of spin systems will be used. Para isomer with total spin equal to 0 will not give any ^1H NMR signal. Thus one can use ^1H NMR spectra for determination of the ortho-para ratio. In the precalibrated graph 100 % of para form will give intensity equal to 0, while 100 % of ortho form will give intensity of NMR signal equal to 133% . According to quantum chemical calculations the averaged chemical shifts of protons and ^{17}O nuclei will noticeably differ only at very low temperatures (< 50K). Finally the identification by using ^{17}O NMR is possible for isotopic water $H_2{}^{17}O$. Para isomer will give no proton multiplicity, while pure ortho isomer should give 1:1:1 triplet (due to interaction with spin 1).

The authors are grateful to the European Community, Sixth Framework Programme EC, New and Emergency Science and Technology, Proposal/Contract no. 5032, 2005 and to Russian Foundation for Basic Research (grant 06-03-32995) for financial support.

References

[1] A. Farcas, *Orthohydrogen, Parahydrogen and Heavy Hydrogen* (Cambridge Univ. Press, Cambridge, 1935).

[2] P.L. Chapovsky, *RIKEN Review* No. 44 pp 30-32, (February, 2002): 2002

[3] V. Tikhonov and A. A. Volkov, *Science* , v 296. 28 June, 2002, pp 2363

[4] N.M. Sergeyev, N.D. Sergeyeva, *Phys. Chem.Chem. Phys.*,2994-2999 (2002)

Technical Advances in Spin Labelling EPR

U. Eichhoff, P. Höfer

Bruker BioSpin GmbH, Silberstreifen, D 76287 Rheinstetten, Germany

e-mail: Uwe.Eichhoff@bruker.de

EPR-Techniques have experienced some kind of revival and increased interest, especially in connection with biological and biomedical applications of EPR. The main aim is to get information on the localization of the spin label and its interaction with the substrate molecule.

CW-saturation experiments as well as pulse techniques like Saturation-recovery-ELDOR and Dead-Time-free Double Electron-Electron Resonance can be used for this purpose. All these techniques require some special hardware development in addition to our routine and research EPR spectrometers. The necessary power for saturation must be available and the conversion factor of the resonator must allow the effective utilization of the microwave power to saturate the sample. The power leading to saturation of the signal to half of its maximum value must be evaluated for various resonator types. In general smaller resonators have a higher conversion factor and therefore show better saturation behaviour. Often the sample quantities are very small and must be measured in aqueous solution. In these cases high sensitivity must be combined with high B1 for saturation and good B1 homogeneity. For exact saturation results all paramagnetic impurities, especially O_2 must be removed from the cavity. O_2 leads to increased relaxation and obscures the saturation and relaxation behaviour of the spin label. Autotune capability is important for automatic saturation experiments.

The resonators must be matched to the corresponding application. For general cw-EPR a standard resonator with a Q-factor of 2.500 and sample volume of 30µl H_20 may be used. The dielectric resonator has a high Q of 4.000 and a very good conversion factor. The high conversion factor leads to saturation at lower microwave power and therefore this resonator is ideal for cw-saturation experiments. It also allows to measure small sample volumes of 3µl in aqueous solution. Split ring resonators have a good conversion factor, small sample volume and low Q-factor. The high conversion factor allows convenient saturation measurements and the small Q-factor resulting in short dead times makes them ideal for transient EPR. In the High-Q dielectric resonator with is much better conversion factor the DPPH-sample is saturated at 25 times less microwave power than in the standard resonator. At the right we show, that the same applies for a spin label Tempol in aqueous solution. A microwave power of 10mW is sufficient to saturate the sample. Power saturation is a simple cw-experiment, but gives only qualitative results. The measured quantity is related to $\sqrt{T_1 T_2}$. So no real physical quantity can be determined from this experiment, which could be compared to a calculated value.

Pulsed EPR measurements enable direct determination of relaxation times T_1 and T_2 and many more parameters, which are not accessible by cw-methods. But Pulse methods require special high sophisticated hardware. We have developed a stand-alone Pulsed EPR and Pulse accessory to our X-band EPR spectrometer. Both instruments can be upgraded to Q-band and W-band operation. All digital pulse generation and signal detection from X-band is preserved in Q- and W-band.

The important items for a Pulse Spectrometer are: Pulse generator (Pattern jet) time resolution 4 or 2 nsec; Fast digitizer and signal avarager (Specjet). Pulse signals are often too small to be seen directly and therefore tuning may be difficult. The Specjet has a sampling rate of 250MHz (2nsec). Fast signals can be digitized and 1 million shots can be avaraged in one second. Signal is accumulated and displayed real time in second time interval. Furthermore we need a resonator with short dead time and high bandwidth and quadrature receiver with high gain and bandwidth. All pulse sequences can be easily edited and visualized on the control monitor. The parameters can be set and the effect on the sequency will be immediately visible. The actual quadrature signal is shown on the SpecJet monitor.

Furthermore the spectrometer can be extended to Pulsed ELDOR and ENDOR operation. Electron-Nuclear-Electron-Triple Resonance involves 3 frequencies, two microwave frequencies and one rf frequency. The allowed transition 1 is observed and the allowed transition 2 is pumped and both transitions are connected by an rf pulse. The microwave pump frequency and the rf-frequency are swept. The rf sweep gives the ENDOR spectrum and the sweep of the microwave pump frequency gives the hyperfine couplings for the ENDOR lines.

ELDOR is a quite old method, but its implementation in cw spectrometers was very difficult and technically imperfect. This is the reason, why its use was quite limited. Pulse techniques are much easier and avoid the previous limitations, which were mainly due to the limited bandwidth of the cavity. A large variety of ELDOR-based methods have evolved immediately like Saturation Recovery ELDOR, Double Electron-Electron-Resonance (DEER), ELDOR detected NMR and Electron-Nuclear-Electron Triple Resonance.

Saturation-Revovery Electron-Electron Double Resonance is a method to determine T_1 in cases where T_2 is too short to obtain an FID or Spin-Echo. The EPR-signal is inverted or saturated by a strong microwave pulse and detected directly without modulation in a low microwave field with the Quad-receiver. The preparation and detection frequencies can be identical or different. In the first case we measure T_1 and in the second case we have additional information on electron-electron double resonance. The pulse sequence looks very simple but this experiment is very difficult to perform. We need high pulse power and the low Q-resonator has to be critically coupled. Since signal is detected without modulation, stability of the experimental conditions is very important. Because of the direct detection any instability will immediately disturb the measurements. The experiment can be set up on a special pulse panel screen.

The standard methods for distance determinations in molecules are X-ray-diffraction and NMR. NMR does not need single crystals, which in many cases cannot be obtained from biological macromolecules like proteins. Another limitation for NMR is the molecular weight. Up to now structures could be determined for up to 50KDalton. The NOE allows to see distances up to 5 Angstroms. EPR also does not need single crystals, but has no limitation for molecular weight and can see much larger distances in the range from 5 up to 80 Angstroms.

Various EPR methods can probe various distances. CW-EPR can probe distances up to about 10 Angstroms, ENDOR and ESEEM probe nuclear-electron interactions and ELDOR electron-electron interactions. Since the dipolar interactions are proportional to the magnetic moment of the involved particles ELDOR is the most sensitive method and can detect dipolar interactions at larger distances. This is especially important for site directed Spin labelling, where labels can be placed at various residues of a protein and dipolar interaction can probe the distance between the labelling sites.

In DEER (3-pulse-ELDOR) the signal is detected by an echo. The sequence consists of a 2-pulse SE-subsequence with fixed interpulse delay τ between the two mw-pulses at the observer frequency. The pump pulse at MW2 inverts the upper transition changing the local field at the other spin species due to electron-electron-coupling ω_{ee}. At the time of echo formation the magnetization is out of phase by a ω_{ee}. By shifting the MW2-pulse electron-electron-coupling can be determined by observing the echo amplitude as a function of t. This experiment needs also a large bandwidth resonator, high B1-values (high conversion factor), large bandwidth of the ELDOR source, large bandwidth of the power amplifier.

In EPR tomography the relationships between FOV, resolution, pixel bandwidth and gradient strength for EPRI are the same as for NMR. In practice, however, there is a large difference regarding the pixel bandwidth. In proton imaging at low to medium field the gradient strength is often large enough to ensure that no chemical shift distortion appears in the image. In EPRI, to suppress the appearance of hyperfine interaction in any image would require enormous gradients. Instead, the spectral distortion is tackled in the data processing. For tomographic investigations in material science a gradient accessory has to be added to a standard EPR spectrometer. Biological objects due to their greater size and high water content are better investigated in the L-band with a special large bore magnet and gradient assembly. For an EPR line width of 100mG a resolution of 25μG can be achieved.

One of the most promising applications of EPR imaging is oximetry. The width of the EPR line depends on the partial oxygen pressure as. The line width can be calibrated against the partial oxygen pressure and then the partial oxygen pressure, calculated from the EPR line width is displayed in a colour code. The image therefore reflects the oxygen concentration in the sample.

Quasi-two-dimensional triangular lattice antiferromagnet $RbFe(MoO_4)_2$

L.E. Svistov

P.L. Kapitza Institute for Physical Problems RAS, 117334 Moscow, Russia

e-mail: svistov@kapitza.ras.ru

Thesis

I. Why it is interesting?

The problem of finding the ground state of a two-dimensional triangular lattice antiferromagnet is of particular interest due to the possibility of solutions with unconventional magnetic order, which are influenced significantly by both frustration and zero-point fluctuations. As the magnetic exchange interactions between the ions located on a regular two-dimensional triangular lattice are frustrated, a usual Neel-type ground state with an antiparallel alignment of the nearest neighbour moments is hindered by the geometry. In the molecular field approximation, the minimum energy is reached for a planar spin configuration, with the magnetization of the three sublattices arranged at an angle 120^o to each other. Such a spin configuration has been found in numerous compounds with a stacked triangular lattice [1], regardless of the dimensionality of the magnetic interactions, which can have a pronounced one-dimensional or two-dimensional character.

In an applied magnetic field, the mean-field ground state of the two-dimensional triangular antiferromagnet remains highly degenerate, as the overall energy is defined only by the total spin of the three sublattices, while there is an infinitely large number of different states with the same total spin [2,3]. Indeed, any possible value of the total spin can be represented either as an umbrella-type structure of equally tilted magnetic moments with identical transverse components, or, alternatively, as a variety of planar structures with variable angles between the magnetic moments and the direction of the field.

This degeneracy is removed by thermal and quantum fluctuations, which select a symmetric planar structure for a purely isotropic (Heisenberg) case and also for an easy-plane type of anisotropy, if the field is applied in the basal plane [4,5,6,7]. If the field is applied perpendicular to the easy-plane, the mean-field approach yields an umbrella-type structure, which is non-degenerate with respect to the mutual orientation of magnetic moments. For the planar structures, fluctuation analysis reveals a characteristic feature of the magnetization curve M(H) in the vicinity of the field $H_s/3$, where H_s is the saturation field. Namely, the stabilization of the collinear structure by the fluctuations in the vicinity of the field $H_s/3$ is seen as a plateau on the M(H) curve, while in the molecular field approximation the magnetization curve has a continuous derivative. This collinear structure is referred to as “two spins up, one down”.

Apart from this, two-dimensional triangular lattice antiferromagnets are distinguished significantly from conventional collinear ferro- and antiferromagnets by the fact that for some phases, called *chiral* phases, even when the direction of the spin on a particular apex of the triangle is fixed, there are still two ways to arrange the rest of the structure. Chiral degeneracy considerably influences the nature of the phase transition to an ordered state [2,8]. Within a magnetic **H-T** phase diagram for a single two-dimensional triangular lattice antiferromagnet both chiral and nonchiral structures are possible, therefore the second order phase transitions with the different critical indices should be expected for the different values of an applied magnetic field.

II. Ultimate aim

To find a stacked layered triangular lattice antiferromagnet with a pronounced magnetic quasi-two-dimensionality (*inter*layer exchange interaction must be as small as possible in comparison with *intra*layer exchange interaction).

To study the magnetic phase H-T diagram and compare with the theories.

III. The choice of the experimental object

The majority of triangular lattice antiferromagnets have quasi one-dimensional character. These systems have been known and studied for a long time [1]. Two-dimensional triangular lattice antiferromagnets demonstrating the properties described above are less common and have only recently become a subject of the intense investigations. $RbFe(MoO_4)_2$ offers a rare opportunity to study a model system, which resembles closely an ideal two-dimensional triangular lattice antiferromagnet. The crystal structure of $RbFe(MoO_4)_2$ described by the space group D_{3d}^3 consists of layers of magnetic Fe^{3+} ions separated by MoO_4^{2-} groups and Rb^+ ions. The C_3 axis is perpendicular to the layers. The magnetic Fe^{3+} ions form an equilateral triangular lattice within the layers, whereas along the C_3 axis they are interspaced by the Rb^+ ions. Such a layered structure ensures the magnetic quasi-two-dimensionality of $RbFe(MoO_4)_2$. Relatively weak exchange interactions in $RbFe(MoO_4)_2$ allow one to reach the saturation field experimentally, while the large spin (S=5/2) of the magnetic Fe^{3+} ions justifies a quasi classical description of the magnetic system.

IV. Experiments

Magnetization and specific heat [9,10,11,12,13]

Experiments on powder and single crystal samples of $RbFe(MoO_4)_2$ revealed the presence of a long range magnetic order below T_N=3.8 K and also demonstrated the stabilization of the collinear structure around $M_s/3$. By measuring the field and temperature dependencies of the magnetization and the specific heat, the magnetic H-T phase diagram was mapped out. Specific heat measurements gave estimates of the magnetic entropy change during the ordering process. The two-dimensional – three-dimensional crossover in the temperature dependence of specific heat confirms the domination of two-dimensional features in the thermodynamic behaviour of $RbFe(MoO_4)_2$.

ESR measurements [10]

The dynamics of low-frequency excitations probed by the ESR measurements estimated the *intra*plane to the *inter*plane exchange interaction ratio to be 100:1. The results of ESR measurements were also used to evaluate the magnetic anisotropy.

Neutron diffraction experiments [14]

Neutron diffraction measurements performed in zero field revealed an ordered structure with a wave vector **k**=(1/3,1/3,0.453), which corresponds to a 120°-configuration within the layers and to an incommensurate ordering along the C_3 axis.

The wave vector of the magnetic structure changes with field, so that in the middle field range it becomes commensurate **k**=(1/3,1/3,1/3).

NMR on nuclei of nonmagnetic ions [12,15]

NMR spectra of the $RbFe(MoO_4)_2$ ions located between the magnetic Fe^{3+} ions from neighbouring planes have allowed identification of various low-temperature phases: a structure with incommensurate modulation along the C_3 axis in low fields, a tilted commensurate structure and a ``two spins up, one down" structure in higher fields.

VI. Discussion

The discussion of the magnetic phase diagram obtained by different experimental methods and the critical behaviour in different phases of $RbFe(MoO_4)_2$ obtained by thermodynamic measurements and by the ^{87}Rb NMR spectroscopy. The magnetic properties, phase diagram and critical indices demonstrate good quantitative agreement with the theoretical predictions for a classical two-dimensional XY-model on the triangular lattice.

VII. Conclusions

References

[1] M.F. Collins and O.A. Petrenko, Can. J. Phys. **75**, 605 (1997).

[2] H. Kawamura, J.Phys.Soc.Jpn. **54**, 3220 (1985).

[3] D.H. Lee, J.D. Joanopoulos, J.W. Negele and D.P. Landau, Phys.Rev.B **33**, 450 (1985).

[4] S.E. Korshunov, J.Phys.: Solid State Phys., **19**, 5927 (1986).

[5] A.V. Chubukov and D.I. Golosov, J.Phys.:Cond.Matt. **3**, 69 (1991).

[6] E. Rastelli and Tassi, J.Phys.:Cond.Matt. **8,** 1811 (1996).

[7] R.S. Gekht and I.N. Bondarenko, Zh. Eksp. Teor. Fiz. **111**, 627 (1997).

[8] H. Kawamura and S. Miyashita, J.Phys.Soc.Jpn. **53**, 4138 (1984).

[9] T. Inami, Y. Ajito and T.Goto, J.Phys.Soc.Jpn. **65**, 2374 (1996).

[10] L.E. Svistov, A.I. Smirnov, L.A. Prozorova, O.A. Petrenko, L.N. Demianets and A.Ya. Shapiro, Phys.Rev.B **67**, 094434 (2003).

[11] G.A. Jorge, C. Capan, F. Ronning, M. Jame, M. Kenzelmann, G. Gasparovich, C. Broholm, A.Ya. Shapiro and L.N. Demianets, Physica B **354**, 297 (2004).

[12] L.E. Svistov, A.I. Smirnov, L.A. Prozorova, O.A. Petrenko, A. Micheler, N. Buettgen, A.Ya. Shapiro and L.N. Demianets, Phys.Rev.B **74,** 024412 (2006)

[13] A.I. Smirnov, H. Yashiro, S. Kimura, M. Hagiwara, Y. Narumi, K. Kindo, A. Kikkawa, K. Katsumata, A.Ya. Shapiro and L.N. Demianets, Phys.Rev.B **75**, 134412 (2007).

[14] M. Kenzelmann, G. Lawes, A.B. Harris, G. Gasparovic, C. Broholm, A.P. Ramirez, G.A. Jorge, M. Jaime, S. Park, Q. Huang, A.Ya. Shapiro, and L.N. Demianets, Phys. Rev. Lett. **98**, 267205 (2007)

[15] 15. L.E. Svistov, L.A. Prozorova, N. Buettgen, A.Ya. Shapiro and L.N. Demianets, JETP Letters **81**, 102 (2005).

The Application of Time Resolved EPR to the Study of Energy Transfer Processes in Photodynamic Therapy

V.S. Iyudin, A.A. Obynochny, K.M. Salikhov

Zavoisky Physical-Technical Institute of the Russian Academy of Sciences, Kazan, Russia

email: vasilius@yandex.ru

Introduction

Study of energy transfer processes in photochemical reactions always was paid with the special attention. It is caused by development of selective excitation technique (for example, laser technique), together with a problem of isotopes separation.

This work is devoted to investigation the influence of energy transfer from a molecule having more high energy levels of electron excitation, on forming of electron spins polarization in a triplet molecule. A physical base of effect is the difference in energies of electron excitation of the chosen triplet molecules. Selectivity here is achieved due to transfer of energy to those molecules which excited levels are lower in comparison with molecules of other composition.

The influence of energy transfer process of between molecules on photoinduced forming of electron spins polarization in porphyrin molecules is shown at the example of the photodynamic reactions (FDR) proceeding at photodynamic therapy.

Reactions of photosensitized oxidation of organic compounds by oxygen are known from the beginning of XX century. However, till now their molecular mechanisms remain a subject of an acute discussion [1]. In the modern representations two types of FDR are supposed. The first type of FDR reactions is photoreduction of a triplet molecule of a photosensitizer by oxidable bond, then the photorestored stain transfer an electron to the molecular oxygen [2].

$$P + h\nu \rightarrow {}^1P^* \rightarrow {}^3P^* + D \rightarrow {}^\bullet P^- + {}^\bullet D^+$$
$${}^\bullet P^- + O_2 \rightarrow P + {}^\bullet O_2^-$$

At the second type of FDR there is an energy transfer from a triplet molecule of a photosensitizer to the molecule of oxygen with populating singlet 1Δg states (${}^1O_2$), then singlet oxygen realizes oxidation of the conforming substrates [2]:

$$P + h\nu \rightarrow {}^1P^* \rightarrow {}^3P^* + O_2 \rightarrow {}^1O_2 + P$$
$${}^1O_2 + D \rightarrow D_{ox}\,,$$

where P, ${}^1P$ *, and 3P* — photosensitizer molecules in basic both excited singlet and triplet states, D - substrate of oxidation.

Both types of reactions are prevailing. These reactions determine photodynamic therapy of the cancer tumors. Thus, singlet oxygen plays special role. On the one hand it is the participant of many FDR, and another - the degree of its participation is the indicator of their mechanism. In this case, the study of formation ${}^1O_2$ both in chemical and biological systems and study of its interaction with components of these systems has essential value.

TR EPR and steady-state EPR (CW EPR) investigations have been carried out on the modified spectrometer EPR ER 200-E-SRC at the X-band. As a system of registration we used modified EPR spectrometer, the system of excitation was solid-state YAG laser " Brilliant " by Quantel (France). This facility has two basic advantages in comparison with stationary EPR

(CW EPR): it allows to record reactions in microsecond and nanosecond range and sensitivity of the device is higher with orders than sensitivity of stationary EPR. [3] The sample was irradiated using the second harmonic of Nd-YAG laser(λ=532 nm) . Also, the following

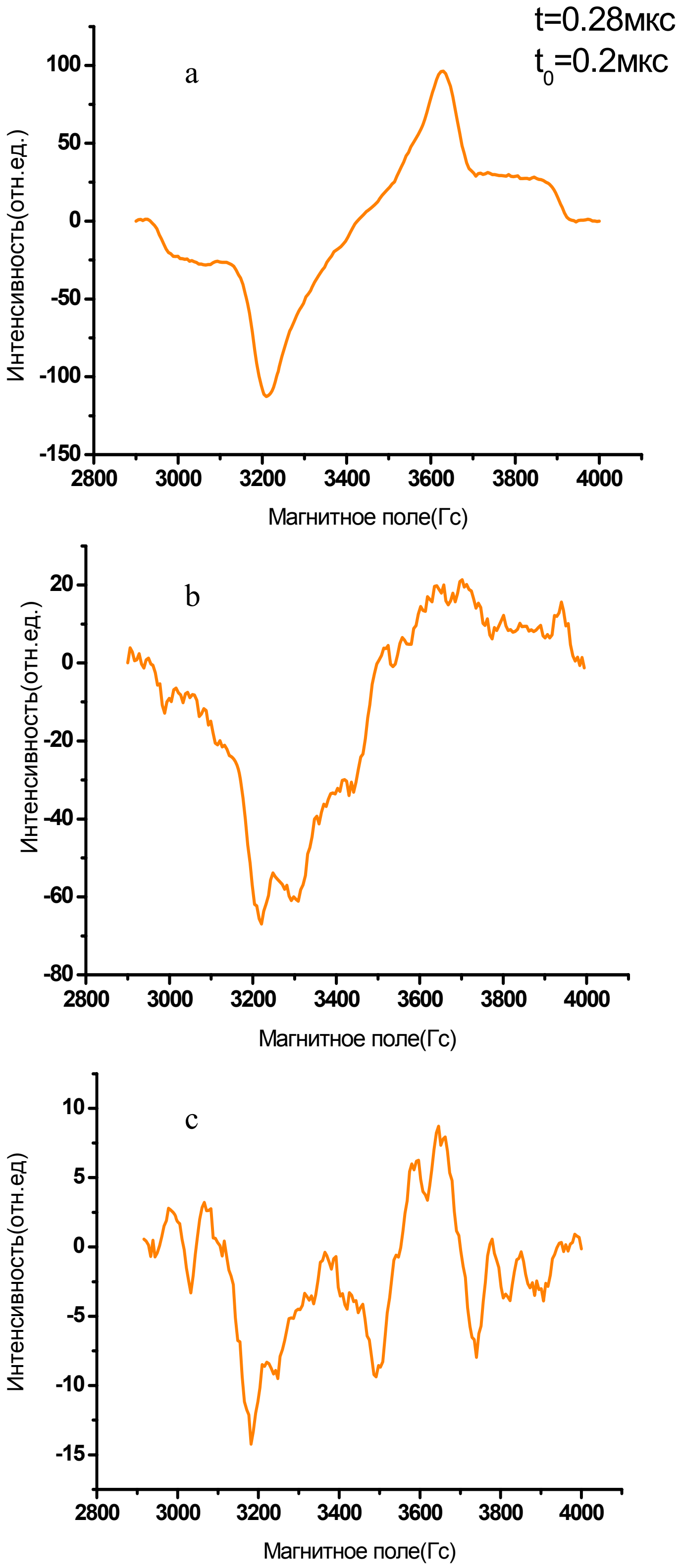

Fig.1. TR EPR spectra of hematoporphyrine IX molecule at different concentration of oxygen. a) 0 мM, b) 0.0062 мM, c) 0.015 мM

systems have been explored: tetraphenyl-porphine zinc (ZnTPP) + tetraphenyl-porphine (H2TPP), tetraphenyl-porphine (H2TPP) +fulleren (C60), tetraphenyl-porphine zinc (H2TPP) +fulleren (C60).

Results of experiment

The oxygen influence on the electron spins polarization line form of the triplet molecule - hematoporphyrin IX.

The fig. 1 shows the spectra changing at different concentration of oxygen.

In this case the oxygen influences both on a form line, and on intensity of TR EPR spectra (fig.1.) When the concentration of dissolved oxygen increasing in the sample, the form and the intensity of TR EPR spectrum is changing. Excited oxygen reacts with hematoporphyrin IX at the great concentrations of dissolved one (Fig. 1c). A variation of integrated intensity of TR EPR spectra of hematoporphyrin IX in dependence of dissolved oxygen concentration is submitted on fig. 2.

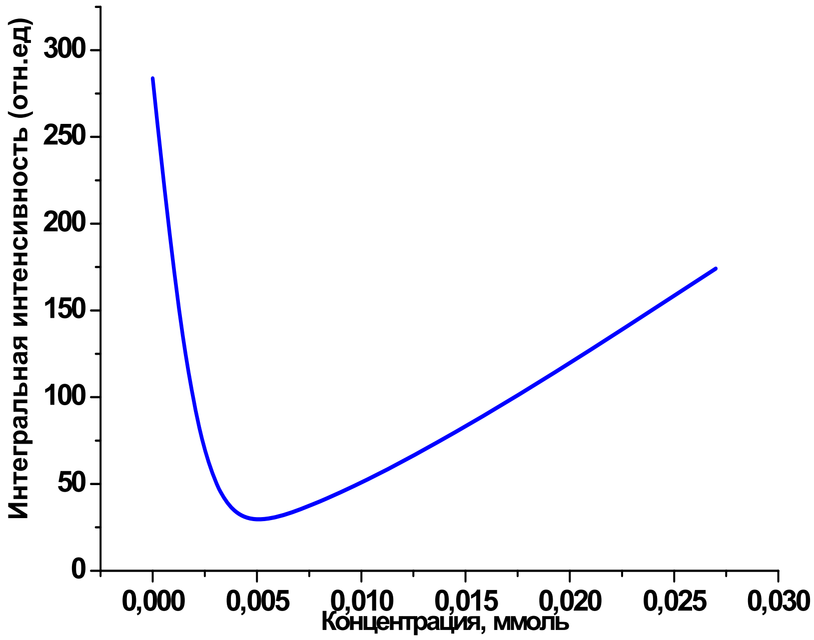

Fig.2 Dependence of intensity of TR EPR spectra in relation of concentration of oxygen.

We associated an explanation of such oxygen influence by the following reactions. The increase of integrated intensity at 0.0050 mM oxygen concentration, in comparison with the degassing sample (a maximum of the emission on fig. 2), is linked with the intercombination conversion:

$$^1(HP)^* + {}^3O_2 \rightarrow {}^3(HP)^* + {}^3O_2 \qquad (1)$$

In spite of the fact that intercombination conversion is forbidden on a spin, bimolecular process (1) is resolved by a Vigner rule of spin conservation [4].

It is supposed, that process (1) proceeds through the intermediate state:

$$^1(HP)^* + {}^3O_2 \rightarrow {}^3(HP\ O_2)^* \rightarrow {}^3(HP)^* + {}^3O_2 \qquad (2)$$

The increasing of the integrated intensity of electron spins polarization explains by this process (2).

The decrease of polarization integrate intensity is observed with the increasing of the oxygen concentration from 0.015 mM (see fig. 2). On our opinion it is associated with energy transfer from an excited molecule of a porphyrin to triplet oxygen by the mechanism:

$$^3(HP)^* + {}^3O_2 \rightarrow HP + {}^1O_2 \qquad (3)$$

This process is similar to a triplet - triplet annihilation.

Direct registration method of singlet oxygen is luminescent spectrum $^1O_2$ at λ = 1272 nanometers by laser excitation of our system (fig 3.).

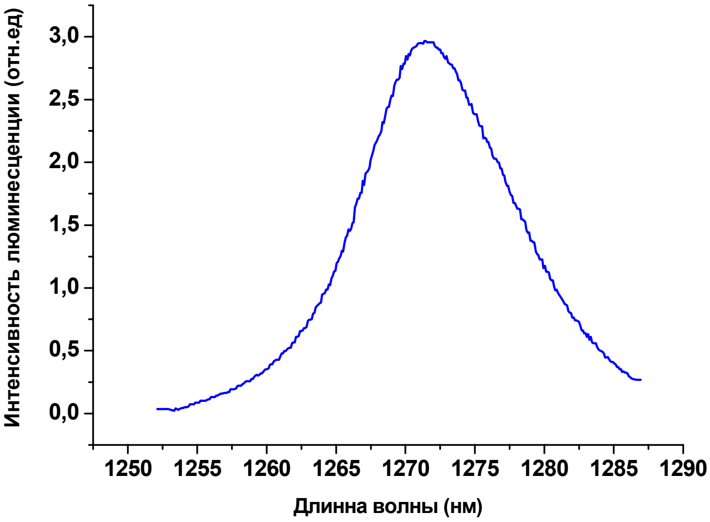

Fig.3 Luminescence spectrum of singlet oxygen (λ макс = 1272 нм).

The important role in FDR is the processes of energy transfer because these processes have a direct influence on efficient generating of excited sensitizer molecules and, as a result, on formations of highreactive singlet oxygen. The physical idea of energy transfer effect is the energy differences of electron excitation of the chosen triplet molecules. The selectivity in these reactions achieved due to energy transfer to those molecules which excited levels are lower, than other molecules. It is necessary to note, that the solubility of a photosensitizer into different fields of a tissue in the affected organ also played important role. To bypass this problem (evenly to excite all fields of the affected organ) we have suggested to apply the mixtures of porphyrins with a different solubility in different fields of the affected organ. This aspect calls us to investigate the energy transfer process.

Fig. 4 represents a scheme of an energy transfer between levels at a laser photolysis of a binary mixture tetraphenyl-porphine zinc (ZnTPP) + tetraphenyl-porphine zinc (H2TPP) in toluene at temperature 140K.

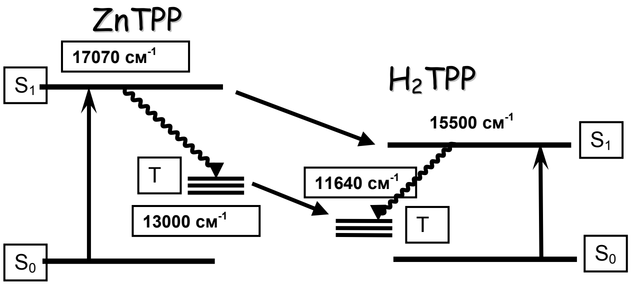

Fig.4 Scheme of energy transfer between energy levels for binary mixture tetraphenyl-porphine zink (ZnTPP) + tetraphenyl-porphine zink (H2TPP) in toluene at temperature 140K.

As it shown from this figure, the maximal energy will accumulate the molecules tetraphenyl-porphine, due to energy transfer under irradiation of such system. This will increase the number tetraphenyl-porphine excited molecules and finally will reduce in smoothing a content of excited molecules in a system.

Also energy transfer between tetraphenyl-porphine (H2TPP) +fulleren (C60), hematoporphyrin (HP) + tetraphenyl-porphine zinc (ZnTPP) had been explored.

TR EPR spectra of electron spin polarization of molecules fulleren C_{60} (2c)+ tetraphenyl-porphine (2b) and tetraphenyl-porphine zinc+ tetraphenyl-porphine triplet states are given at fig. 5,. The condition of TR EPR spectra registration is identical.

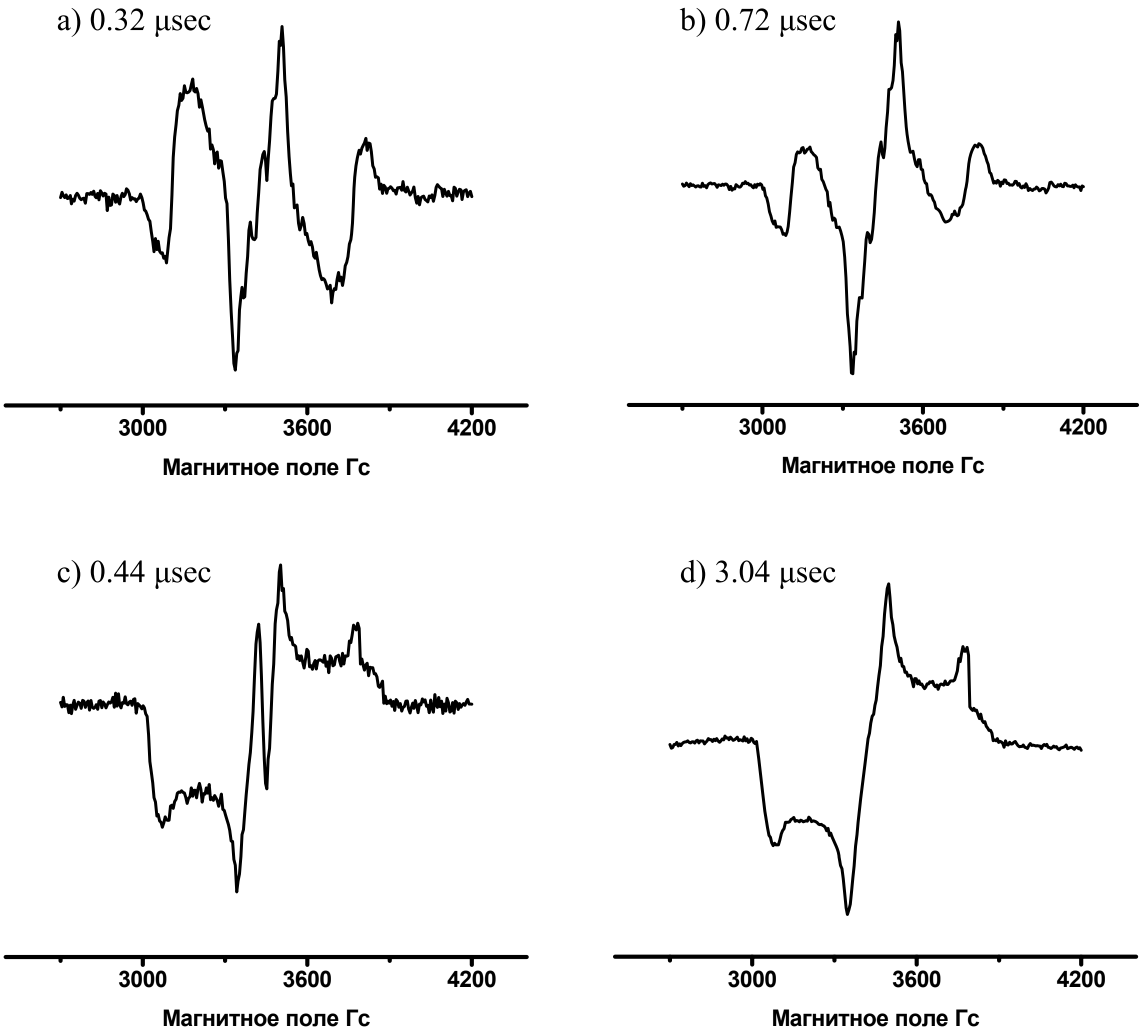

Fig.5 TR EPR spectra of ZnTPP + H_2TPP (a), b)) and fulleren C_{60} + H_2TPP (c), d)) with the initial concentrations 1:1 mM and T=140 K

As you see from the fig.5 in these systems have very efficiently energy transfer between molecules.

Conclusion

In this work we studied the oxygen influence on hematoporphyrin IX triplet molecule. It had been established the formation of singlet oxygen by the luminescent spectroscopy, showed electron excitation transfer on such triplet molecules such as tetraphenyl-porphine zinc (ZnTPP) and tetraphenyl-porphine (H2TPP) in a binary mixture (ZnTPP + H2TPP) in toluene and energy transfer between fulleren and tetraphenyl-porphine in the system fulleren+ tetraphenyl-porphine+toluene. The detection of such phenomenon in our systems is most interesting from the point of view in increasing the efficacy of the photodynamic reactions proceeding at photodynamic therapy. In this case there is additional freedom degree of influence on efficacy FDR- energy transfer between sensitizers.

References

[1] Rabinovich E.I. Photosyntehesis and related processes, v.1. N.Y.: Interscience Publ., Inc., 1945.

[2] Krasnovsky A.A., Neverov K.V.//Chem.Phys.Lett. 1990, v. 167,№6, p. 591.

[3] Gnezdilov O. I., Mambetov A.E., Obynochny A.A., and K.M. Salikhov K.M. // Appl. Magn. Reson., 2003, 25, 157

[4] Schuhardt H., Nultch W.//J.Photochem, 1984, v.25, №2, p. 317

Subunit Mobility Researching at Alpha-Crystalline by ^{1}H NMR

T.A. Zinkevich[1)], O.I. Gnezdilov[1)], A.G. Krushelnitsky[2)]

[1)]Zavoisky Physical-Technical Institute, Russian Academy of Sciences, 420029, Sibirsky trakt 10/7, Kazan, Russia
[2)]KIBB, 420111, Lobachevsky street, Kazan, Russia

e-mail: tatyana-vilkova@yandex.ru

Proteins are large organic compounds made of amino acids arranged in a linear chain and joined together by peptide bonds between the carboxyl and amino groups of adjacent amino acid residues. Like other biological macromolecules such as polysaccharides and nucleic acids, proteins are essential parts of organisms and participate in every process within cells. Many proteins are enzymes that catalyze biochemical reactions, and are vital to metabolism. Proteins also have structural or mechanical functions, such as actin and myosin in muscle, and the proteins in the cytoskeleton, which forms a system of scaffolding that maintains cell shape. Other proteins are important in cell signaling, immune responses, cell adhesion, and the cell cycle. The chief characteristic of proteins that enables them to carry out their diverse cellular functions is their ability to bind other molecules specifically and tightly. The region of the protein responsible for binding another molecule is known as the binding site and is often a depression or "pocket" on the molecular surface. This binding ability is mediated by the tertiary structure of the protein, which defines the binding site pocket, and by the chemical properties of the surrounding amino acids' side chains.

Chaperones are proteins that assist the non-covalent folding/unfolding and the assembly/disassembly of other macromolecular structures, but do not occur in these structures when the latter are performing their normal biological functions. Chaperons are one of the less investigated, but one of the most interesting for study classes of proteins.

The goal of investigation of proteins is an understanding of its biological functioning mechanism; it’s of great importance in medicine and biotechnology. It’s necessary to define the characteristics of different types of molecular motions for studying protein interaction mechanism. Frequency range of oscillations of these motions is very broad. Typical time of the most rapid motions – is femtoseconds, the slowest is seconds and even minutes. The femtosecond range corresponds to oscillation of valence bonds and valence angles. The picoseconds range, and slower, is determined by conformational degree of protein structure freedom – dihedral (torsion) angles, that provide the flexibility of protein backbone, as well as dihedral angles, which determine conformation of side bones of aminoacid residues. Correlation time of large-scale conformational transitions is in the micro- and millisecond range.

It’s important to note that time scale of slow dynamics clashes with time scale of different molecular-biological processes, such as binding to substrate, catalysis, folding. Thus, it’s quite natural to assume studying of slow dynamics is more important for understanding of protein biological function.

The object of investigation in this work is alpha-crystalline – the protein that possesses high chaperon activity. Alpha-crystallines (αA and αB) are major lens structural proteins of the vertebrate eye that are related to the small heat shock protein family. In addition, crystallines are found in many cells and organs outside the lens, and αB is overexpressed in several neurological disorders and in cell lines under stress conditions. Alpha-crystalline is very sufficient in suppressing the thermally induced aggregation of β- and γ-crystallines, the two other major mammalian structural lens proteins. Alpha-crystalline was also effective in preventing aggregation in the transparent eye lens and that in nonlens cells alpha-crystalline may have other functions in addition to its capacity to suppress aggregation of proteins.

Recently alpha-crystalline has been intensively investigated by different methods, but the issue of the role of molecular dynamics in its chaperon activity hasn't been discussed. So, its important and interesting to define characteristics of different types of alpha-crystalline molecular motions as whole globule as well as its individual segments at free and linked states; to reveal these characteristics with variations of protein chaperon activity.

There are two genes in the alpha-crystalline family, one for αA-crystalline one for αB-crystalline. αA- and αB- crystalline always occur as heterogeneous high molecular weight aggregates. The range of molecular weights observed can vary from 1200 to 300 kD.

Solutions have been prepared by mixing with following centrifugation. In order to weaken water signal we have used deuterated water (98%). The concentration of solutions was determined by weighing and controlled through spectrophotometry.

The main method of investigation in our work was 13C NMR spectrometry in solid state and solution. For studying the influence of temperature and some chemical agents on protein molecules we have applied NMR method with magnetic field pulse gradient. The principle advantage of NMR method for our goal in the protein molecular dynamics is selectivity of structural and dynamical information. We used the stimulated echo method for measuring translation diffusion coefficients.

There is the scheme of pulse sequence in fig. 1. The action of this pulse sequence is as follows: first radiofrequency pulse turns the magnetization vector to the xy-plane. Then first magnetic field gradient pulse is applied to skew spin isochromates. Second rf-pulse turns these isochromates to the xz-plane and during the t_1 time spin-lattice relaxation occurs. Third rf-pulse returns the magnetization to the xy-plane, inverting isochromates phases. Simultaneously, second phased gradient pulse is applied. On condition that two gradient pulses are identical to each other one-to-one correspondence of phases will appear only if their precession frequencies during the sequence haven't changed, which is possible if nuclei haven't changed their location. Neglecting the nuclei displacement during the gradient δ and magnitude of constant magnetic field gradient g_0, so the root-mean-square phase value $<\Phi^2>$ acquired as a result of nuclei displacement during Δ – the time between two gradient pulses can be written as $<\Phi^2>=\gamma^2\delta^2g^2<r^2>$. The root-mean-square displacement of spins related to SDC of molecule according to statement $<r^2>=2D\cdot\Delta$, and echo attenuation can be shown as

$$A(g,\tau,\tau_1)=\frac{A_0(0)}{2}\exp\left(-\frac{2\tau}{T_2}-\frac{2\tau_1}{T_1}\right)\exp\left(-\gamma^2\delta^2g^2D(\Delta-\delta/3)\right)$$

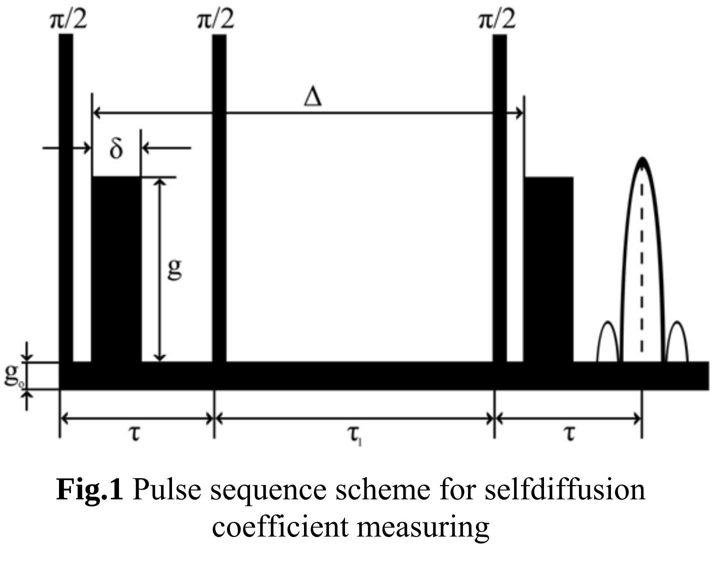

Fig.1 Pulse sequence scheme for selfdiffusion coefficient measuring

where A_0 – signal amplitude, measured right after 90^o-pulse of echo at the initial moment of time, D-selfdiffusion coefficient, g-the magnitude of magnetic field gradient, T_1 and T_2 – spin-lattice and spin-spin relaxation times respectively.

The value of selfdiffusion coefficient (SDC) can be determined as tangent of angle of echoes amplitude slope envelope. It is a straight line in terms of $lgA=f(g^2)$ where g and Δ are constant.

We used single pulse excitation of spin system (DP) as well as cross-polarisation method (CP) for 13C solid state NMR spectra registration. All measurements are made at multi-nuclear NMR spectrometer AVANCE 400. Which lets us obtain 1D and 2D liquid and solid state NMR spectra with dynamical decoupling; take relaxation and selfdiffusion coefficient measurements.

There is ^{1}H spectrum of 4%-solution of alpha-crystalline at D_2O in fig. 2. Spectrum has been carried out at room temperature. Long correlation times of molecular motions, linked with large size of alpha-crystalline aggregates, provide low resolution of ^{1}H spectra. But it's good enough for determination of SDC. We measured SDC for native and cross-linked oligomers of alpha-crystalline, both samples revealed that the SDC magnitude is about $(2.6\pm0.15)*10^{-11}$ m/s^2.The absolute magnitude is in close agreement with literary data. While the comparison of SDC for two samples discloses the formation of intra-oligomer links only, without essential part of inter-nuclear links.

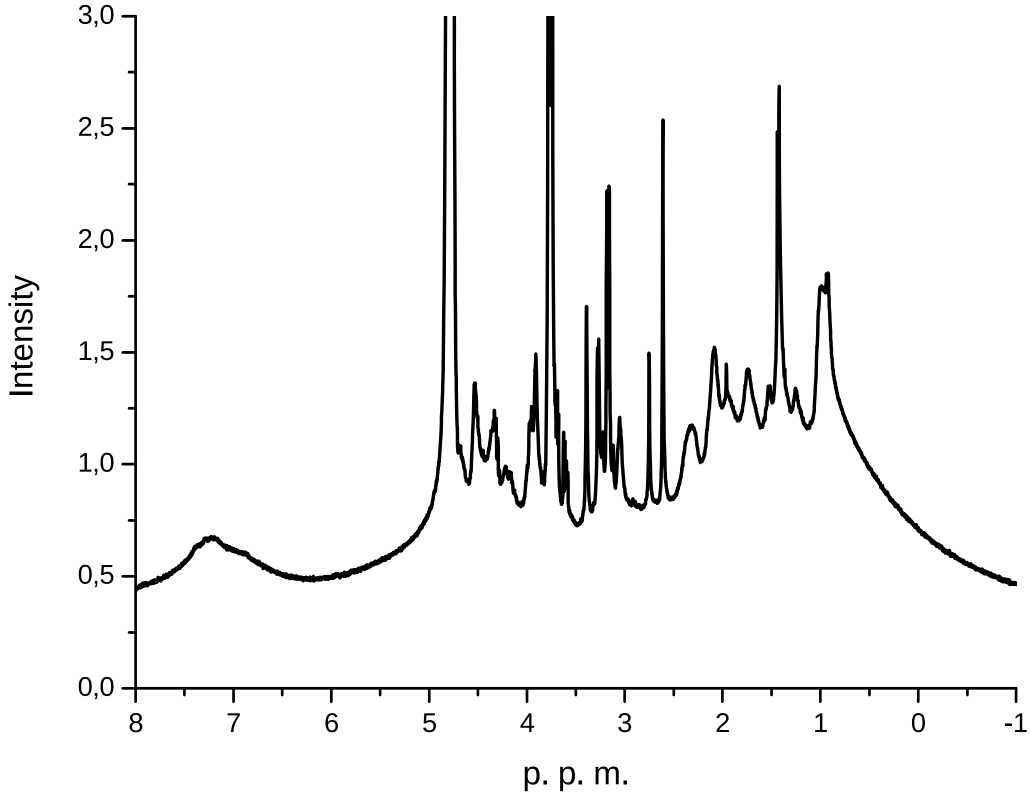

Fig.2 ^{1}H spectrum of 4%-solution of alpha crystalline.

In fig. 3 there is alpha-crystalline SDC on detergent concentration. Deoxycholat is used as detergent here. The goal of its addition is to achieve alpha-crystalline aggregates dissociation. This experiment shows that the process of dissociation begins at concentration about 4%.

Thus, our data unambiguously reveal that subunit mobility at alpha-crystalline olygomers is a very important part of molecular mechanism of its chaperone activity. The disagreement with the work results [6] may be put down by two reasons. At first we can't exclude, that there are different link mechanisms for different target proteins: in our case, target protein can build into alpha-crystalline olygomer, in the other case, as assumed in work [6], binding occurs on the surface of chaperone. We consider this explanation improbable, but in order to prove we have to do the research with different target proteins.

The disagreement between result [6] is more likely to be explained by the source of alpha-crystalline, which is different from the one used in work [6]. We used recombinant protein and our sample is purer, more homogeneous and isn't subjected to past-translational modifications. Accordingly, our data can be interpreted more soundly unambiguously.

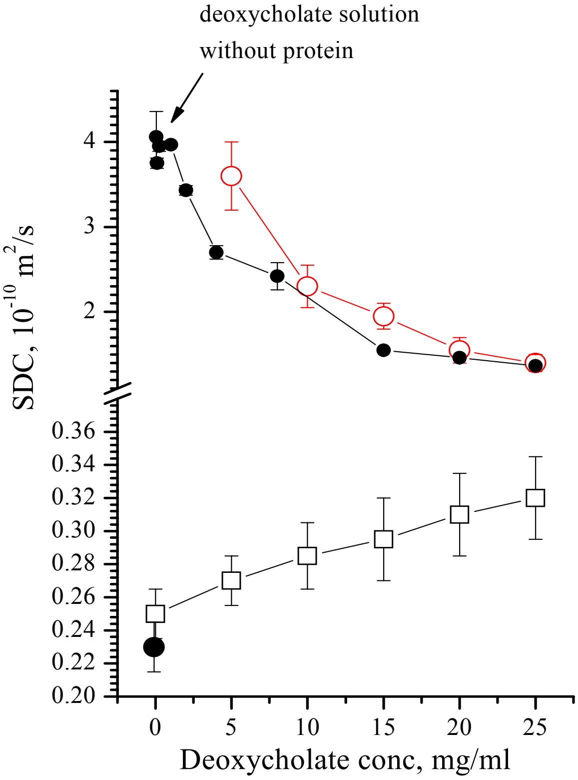

Fig.3 Alpha-crystalline SDC on detergent concentration

References

[1] Derham B.K., Harding J.J. Prog. Ret. Eye Res. 18, 463-509, 1999.

[2] Horwitz J. Exp. Eye Res. 76, 145-153, 2003

[3] Augusteyn R.C. Clin. Exp. Optom. 87, 356-366, 2004.

[4] Horwitz J. Proc. Natl. Acad. Sci. USA 89, 10449-10453, 1992.

[5] Groth-Vasselli B., Kumosinski T.F., Farnsworth P.N. Exp. Eye Res. 61, 249-253, 1995.

[6] Augusteyn R.C. Exp. Eye Res. 79, 781-784, 2004.

[7] Sun T-X.**,** Das B.K., Liang Jack J.-N. J. Biol. Chem. 272, 6220-6225, 197.

[8] Andries C., Backhovens H., Clauwaert J., de Block J., de Voeght F., Dhont C., Exp. Eye Res. 34, 239-255, 1982.

EPR Study of Exchange Interaction in Compound $\{[Nd_2(\alpha\text{-Fur})_6(H_2O)_2]\}_n$

L.V. Mingalieva[1], V.K. Voronkova[1], R.T. Galeev[1], S. Melnik[2], D. Prodius[2], C.I. Turta[2]

[1]Zavoisky Physical-Technical Institute, Russian Academy of Sciences, 420029, Sibirsky trakt 10/7, Kazan, Russia
[2]Institute of Chemistry, Academy of Sciences of Moldova, MD-2028, Academiei str. 3, Chisinau, Moldova

e-mail: klyuda@yandex.ru

Study of materials built on the base of rare-earth ion dimers is of fundamental interest connected with the possibility of their application in quantum informatics and quantum computers. Interactions between rare-earth ions which play the role of qubits are important to perform controlled logic. Precise knowledge of the coupling mechanism in dimers can help to better understand and to optimize properties necessary for their application.

Molecular systems with rare-earth ions are also very promising for creating new magnetic nanomaterials due to the non-frozen orbital moment, short relaxation time and anisotropy of properties of rare- earth ions. The aim of the present work is to study of the anisotropy of the exchange interaction between neodymium ions in case of low symmetry of their local environment. The investigation is carried out by the example of a new compound $\{[Nd_2(\alpha\text{-Fur})_6(H_2O)_2]\}_n$ (where α-Fur = $C_4H_3OCOO^-$) build up from dimer fragments of neodymium ions. The ligands of the nearest environment of Nd^{3+} ions form a distorted antiprism, completed by the ninth ligand. The distance between two nearest Nd^{3+} ions in the compound $\{[Nd_2(\alpha\text{-Fur})_6(H_2O)_2]\}_n$ is $r_{12} = 4.4508$ A.

The ground term of the Nd^{3+} ion ($4f^{3,}$ $^4I_{9/2}$) in the ligand field of low symmetry is split onto five Kramers doublets. At liquid helium temperature the EPR spectrum is observed only due to the transitions on the lower doublet and described by the effective spin S' =1/2.

EPR spectra (Figs.1 and 2) of dimers were measured in X- and Q – bands at 4.2 K. The analysis of the frequency dependence of EPR spectrum was carried out by numerical calculations in the framework of the Hamiltonian taking into account Zeeman, dipole-dipole and anisotropic exchange interactions:

$$H = \{g\}\mu B(S_1^{'} + S_2^{'}) + \beta^2 r^{-3}\{(g \bullet S_1^{'})(g \bullet S_2^{'}) - 3r^{-2}(gS_1^{'}r)(gS_2^{'}r)\} + S_1^{'}\{J_{12}\}S_2^{'},$$

where S_1', S_2' = 1/2 are the effective spins of single Nd^{3+} ions in dimer, $\{J_{12}\}$ is the tensor of the exchange interaction.

The principal values of {g} - and $\{J_{12}\}$ - tensors were obtained by fitting theoretical and experimental EPR spectra of a polycrystalline sample (Figs.1 and 2). Parameters of the fine structure {D}-tensor shown in the spectra are the sum of anisotropic exchange and dipole-dipole contributions. The contribution of the dipole-dipole interaction was calculated from structural data r_{12} = 4.45 A, θ = 90° , where θ - is the angle between principal axes of the g-tensor and the vector connecting neodymium ions in a dimer. The principal values of {g} - and $\{J_{12}\}$ - tensors: g_x= 1.35, g_y= 2.5, g_z= 3.2 and j_{x12}= 1900 Oe, j_{y12}= 1400 Oe, j_{z12}= -3300 Oe reflect the strong orthorhombic anisotropy of local properties and exchange interaction.

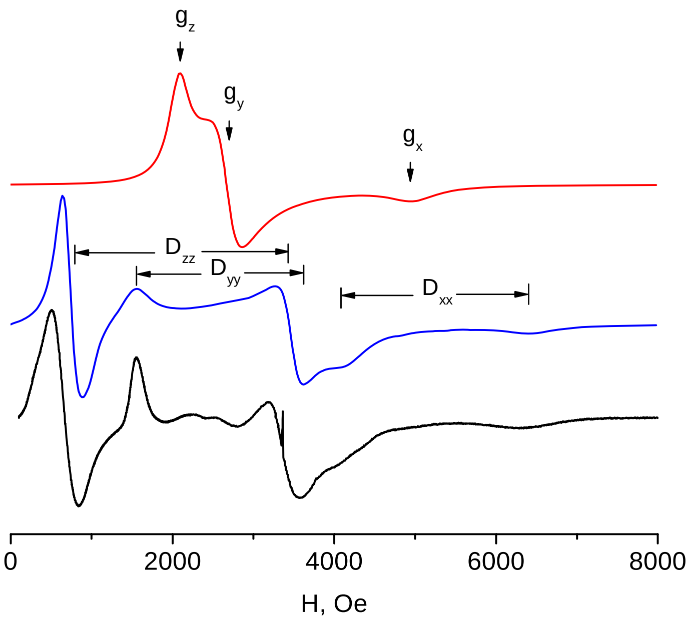

Fig.1 EPR spectrum of the $\{[Nd_2(\alpha\text{-}Fur)_6(H_2O)_2]\}_n$ compound in X- band at 4.2 K(black line).Theoretical EPR spectrum for two interacting spins $S_1 = S_2 = 1/2$ with g_x=1.35, g_y=2.5, g_z=3.2 and j_{x12}= 1900 Oe, j_{y12}= 1400 Oe, j_{z12}= -3300 Oe at 4.2 K (blue line), dipole-dipole interaction was calculated from structural data r_{12}= 4.45 A, θ= 90°. Theoretical EPR spectrum for two non-interacting spins $S_1 = S_2 = 1/2$ with g_x=1.35, g_y=2.5, g_z=3.2 at temperature 4.2 K in X- band (red line).

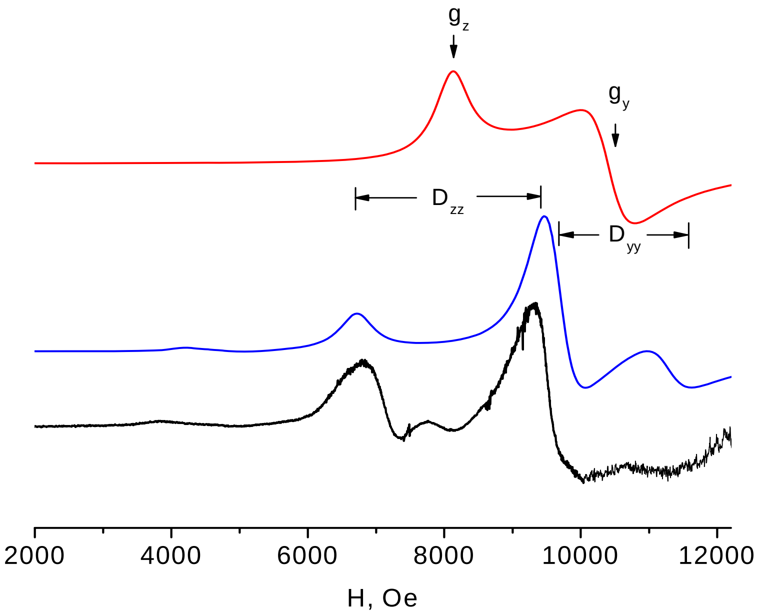

Fig.2 EPR spectrum of the $\{[Nd_2(\alpha\text{-}Fur)_6(H_2O)_2]\}_n$ compound in Q- band at 4.2 K(black line). Theoretical EPR spectrum for two interacting spins $S_1 = S_2 = 1/2$ with g_x=1.35, g_y=2.5, g_z=3.2 and j_{x12}= 1900 Oe, j_{y12}= 1400 Oe, j_{z12}= -3300 Oe at 4.2 K in Q- band (blue line), dipole-dipole interaction was calculated from structural data r_{12}= 4.45 A, θ= 90°. Theoretical EPR spectrum for two non-interacting spins $S_1 = S_2 = 1/2$ with g_x=1.35, g_y=2.5, g_z=3.2 at temperature 4.2 K in Q- band (red line)

This work is carried out at partial financial support by Scientific School-6213.2006.2.

Time Resolved EPR of the Excited Triplet States Using ELEXSYS E580

A.A. Sukhanov[1)], R.B. Zaripov[1)], V.K Voronkova[1)], K.M. Salikhov[1)], C. Corvaja[2)]

[1)]Zavoisky Physical-Technical Institute of the Russian Academy of Sciences, Kazan, Russian Federation
[2)]Department of Chemical Sciences, University of Padova, Padova, Italy

e-mail: ansukhanov@mail.ru

For investigation short lived states has used so-called time resolved EPR (TR EPR) method. This method concludes direct detection of signals at that one has not used modulation of static magnetic field. Time resolved experiment represents 2D time-domain picture of absorption energy. Basic principle concludes in detection of time evolution of absorption signal in every point of magnetic field after light excitation of sample by pulse laser. We realized the time resolved EPR method on pulse spectrometer *ELEXSYS E580. Laser YAG Brio* was used as a source of optical excitation. This method is used for studying short-lived paramagnetic particles in nanosecond and microsecond ranges.

The time resolved EPR method has been applied for studying electron spin polarization of excited triplet states caused by mutual annihilation of triplets in *Ph/TCNQ* single crystal. The triplet-triplet annihilation in molecular crystal causes a delayed fluorescence which was intensively researched [1,2]. It is shown in [3] that mutual annihilation of triplet excited states results in electron spin polarization. The electron spin polarization of excited triplet states caused by the triplet-triplet annihilation of triplet states was observed in *A/TCNB* and *Ph/TCNQ* crystals [4].

In this paper we present the angular dependences of TR EPR spectra of excited triplet excitons and located triplet states in *Ph/TCNQ* single crystals.

Crystals of *Ph/TCNQ* are built up from phenazine *(Ph)* and tetracianhinodimetan *(TCNQ)* molecules (fig.1.) and represent as dark – vinous prisms with the size of 1*2*4 mm. Parameters of a crystal lattice: triclinic lattice, $a=0,8437$ nm, $b=0,7253$ nm, $c=0,8571$ nm, $\alpha=105,610$, $\beta=71,410$, $\gamma=101,600$. Molecules of pair are parallel each to other and complexes are collected along an axis *c*. Average distance between planes is 0.338 nm. The perpendicular to plane makes with a direction *c* a corner of 38°[5].

EPR spectrum of triplet state consists of two signals in an opposite phases (fig.2). Width of TR EPR spectrum for mobile triplet exciton ~1Gs, whereas for the located triplets ~14 Gs. From experiment it is established, that the time evolution of signals caused by triplet excitons and located triplet states essentially differs: signal intensity of the delayed polarization in the first case considerably exceeds the intensity in the second case. This fact in addition confirms that the delayed polarization on triplet excitons in crystal *Ph/TCNQ* is associated with their triplet – triplet annihilation.

The observed effect of the delayed polarization strongly depends on orientation of the crystal in magnetic field for two types of single crystals. For samples with the basic type excitation storage - exciton the effect is detected most distinctly for orientation of magnetic field along an X axis of the fine structure tensor and absent for orientation along a Z axis. For intermediate orientations the effect was observed with different intensity and different sign of polarization relatively to initial polarization. The weak polarization for the samples with the located triplets doesn't depend from orientations of the single crystal. But angular dependences of TR EPR spectra for excitons and located triplets are indentical (fig.3).

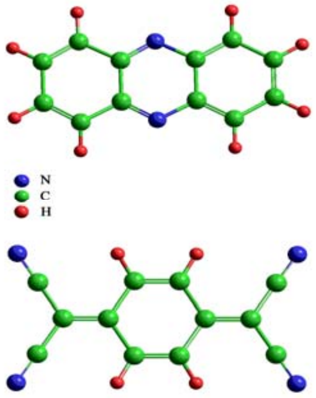

Fig.1. Structure of *Ph/TCNQ*

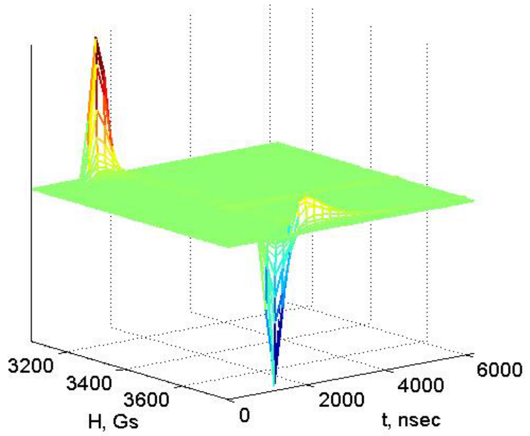

Fig.2 TR EPR spectrum of *Ph/TCNQ* for random orientation

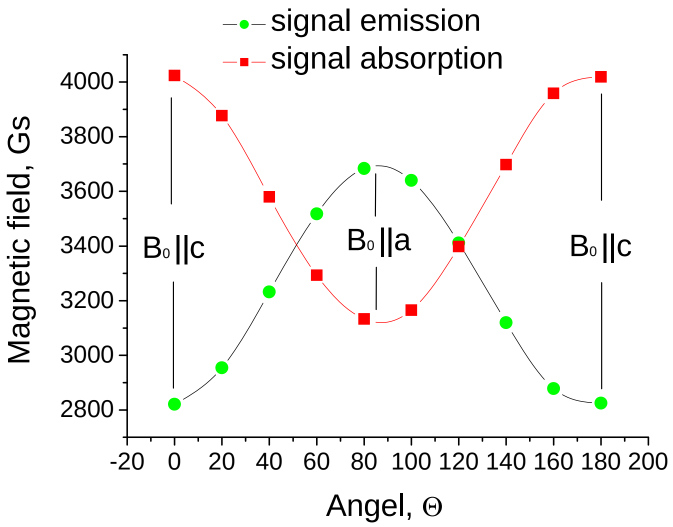

Fig.3. Angular dependence of resonance fields of the located triplets in a plane close to plane ZX of the main axes of fine structure tensor. The Z axis of fine structure tensor corresponds to orientation θ=0, the X axis is close to orientation θ=90.

References

[1] Johnson R.C., Merrifield R.E.: Phys.Rev. B 1, 896-902, (1970)

[2] Tsuchiya H., Marumo F., Saito Y.: Acta Crystallogr. B 28, 1935-1941, (1972)

[3] Salikhov K. M.: Appl. Magn. Reson. 26, 135-144, (2004)

[4] C. Corvaja, L. Franco, K.M. Salikhov,V.K. Voronkova, Appl. Magn. Reson. 28, 181-293, (2005)

[5] D. Gundel, J.Frick and all, Chem. Phys. 132, 363-372, (1989)

The Axonal Transport and Water Molecules Mobility in Nerve. Investigation by PFG NMR method

S.V. Abramova[1)], E.A. Mishagina[2)], T.A. Sibgatullin[2)]

[1)]Kazan State University, 420008, Kremlyovskaya str. 18, Kazan, Russia
[2)]Kazan Institute of Biochemistry and Biophysics, Russian Academy of Science, 420111, Lobachevsky str. 2/31, Kazan, Russia

e-mail: Sibgatullin@mail.knc.ru

Introduction

There are two ways of the information transmission through nerves known in physiology: 1) electric impulses; 2) transport of the different substances and organelles along a nerve - axonal transport. The mechanism of transmission of electric impulses is studied well, and the axonal transport is studied insufficiently. At the same time it is known, that a number of diseases of nervous and muscular system is interrelated with the disturbances of the axonal transport of substances.

For many years it's been known that there are at least two kinds of motility systems in eukaryotes. One kind is based on actin, and uses myosin molecules plus ATP to provide the driving force for movement (muscle contraction, e.g.). Myosin is called the motor protein that propels itself and anything attached to it along the actin microfilaments. The other kind of system is microtubule based and the motor protein here is dynein, which also uses ATP as an energy source. Flagella are examples of dynein/microtubule motility systems [1].

The axonal transport characterized by the wide distribution of velocities. Fast components of axonal transport provide anterograde and retrograde movement of the certain type membrane's organelles along microtubules with average velocity 50 - 400 mm/day (~0.5 - 5 μm/s). Slow components of axonal transport related to the transfer of cytoskeletal proteins; the nature of their carriers is unknown. Proteins which associated with neurofilaments and macromolecules move with average velocity approximately 0.3 - 3 mm/day (~0.004 - 0.04 μm/s), and proteins, which associated with microfilaments, are transported with average velocity 2 - 8 mm/day (~0.02 - 0.09 μm/s) [2,3].

Methods and materials

It is of great interest to study the axonal transport by non-invasive technique. It is proposed that the water molecules can be involved in the process of the axonal transport of substances in nerve. The NMR seems to be the most advanced non-invasive method to study the molecule motility. At present work the stimulated echo sequence with pulsed field gradient (PFG) used to investigate the mobility of water molecules involved in the axonal transport. The experiments were carried out on a custom-made ^{1}H NMR spectrometer operating at 16 MHz.

The experiments were performed on the isolated frog sciatic nerve. The objectives were as follows: to assess the contribution of the axonal transport to the apparent diffusion coefficients of water in nerve; to examine the temperature dependence of translation motion of water molecules in nerve; to determine the effect of temperature on activation of the axonal transport.

Results and discussion

The temperature dependence of the apparent diffusion coefficient was examined in the temperature range 8-29ºC for different orientations of the nerve fibers. Signal attenuation plots at different temperatures are shown for longitudinal (Fig. 1) and transverse (Fig. 2) orientations of the nerve fibers.

The slowly diffusing component is particularly absent at longitudinal orientation, therefore non-exponential shape of the signal attenuation plot at transverse orientation can be explained by the restricted diffusion caused by membranes.

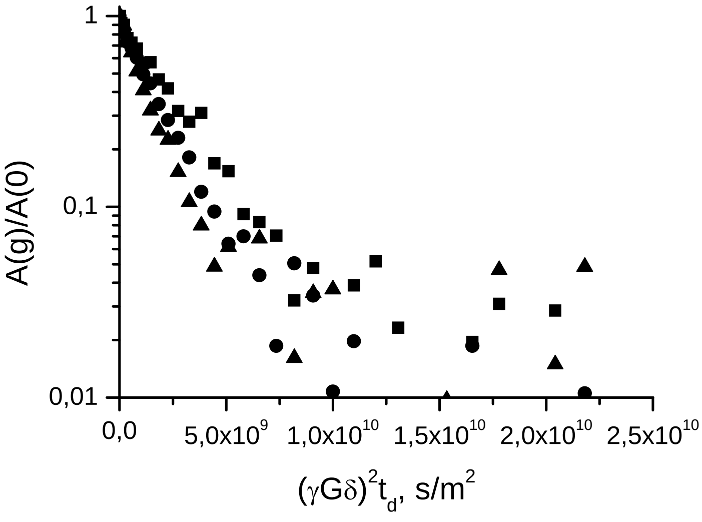

Fig.1 Signal attenuation plots for longitudinal orientation of the nerve fibers at observation time t_d = 30 ms and various temperatures: 8ºC (squares); 18ºC (circles); 29ºC (triangles).

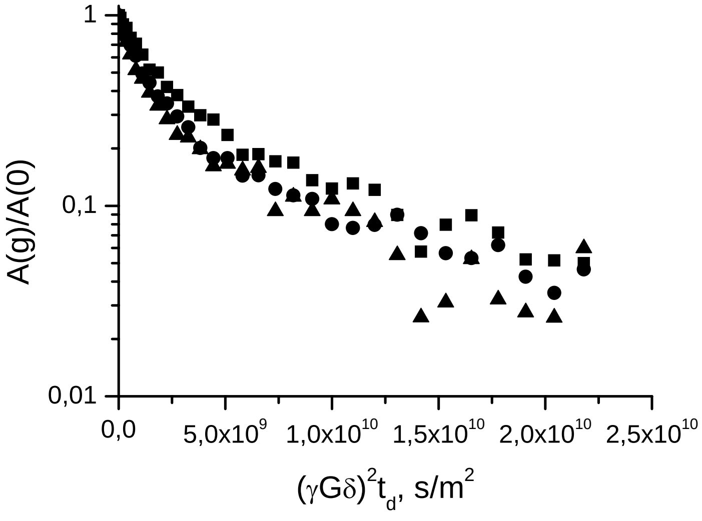

Fig.2 Signal attenuation plots for transverse orientation of the nerve fibers at observation time t_d = 30 ms and various temperatures: 8ºC (squares); 18ºC (circles); 29ºC (triangles).

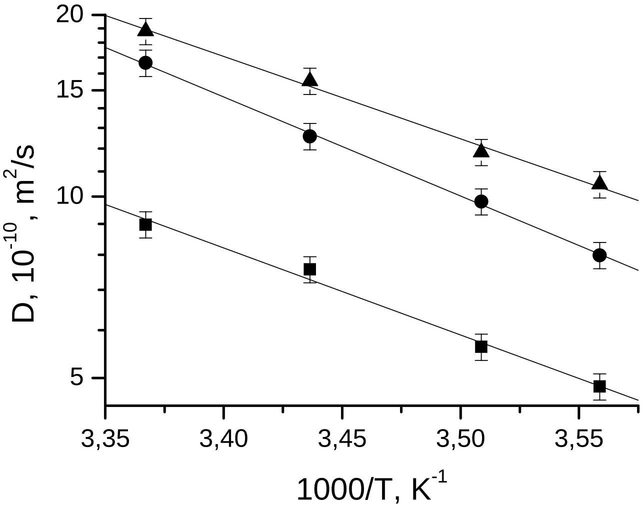

Fig.3 The temperature dependence of the apparent diffusion coefficients in Arrhenius's coordinates at various orientations of nerve fibers and observation times: transverse, $t_d = 30$ ms (squares); longitudinal, $t_d = 30$ ms (circles); longitudinal, $t_d = 300$ ms (triangles). The lines correspond to the approximation of present dependences by Arrhenius's law (1).

The apparent diffusion coefficient was determined by initial slope of the signal attenuation plot. As so it is corresponds to the mean diffusion coefficient of water in the sample. The temperature dependence of the apparent diffusion coefficient follows Arrhenius's law (1) in the range of 8-29ºC. This is shown on Fig. 3.

$$D(T) = D(0)\exp(Ea/RT) \tag{1}$$

The obtained values of activation energy (Table. 1) happened to be characterized by the higher value than that of free water molecules. We consider that this is due to retard of the water molecules mobility near the membrane surface by the components of membrane.

The contribution of flow of the water molecules involved in the axonal transport to the overall translation displacement increases as a function of the observation time

$$\Delta\overline{X}^2(t_d) = 2D_0 t_d + (Vt_d)^2, \tag{2}$$

where D_0 – diffusion coefficient of the bulk water, V – average velocity of axonal transport. Hence, the apparent diffusion coefficient can be derived as follows

$$D_{app}(t_d) = D_0 + \frac{V^2}{2} t_d\,. \tag{3}$$

Table 1 Values of the activation energy of apparent diffusion coefficient at various orientations of the nerve fibers (relative to the field gradient) and observation times

Orientation of the nerve fibers	Observation time (t_d), ms	Activation energy (E_a), kJ/mol
transverse	30	27,6 ± 1,9
longitudinal	30	29,0 ± 3,0
longitudinal	300	26,2 ± 1,3

Table 2. The theoretically calculated values of axonal transport velocities at different temperatures (based on the increase of apparent diffusion coefficient measured along nerve fibers ($D_{||}$) with observation time according the Eq. 3)

T, ºC	$D_{\|\|}$, 10^{-9} m^2/s (t_d = 30 ms)	$D_{\|\|}$, 10^{-9} m^2/s (t_d = 300 ms)	V, µm/s
8	7,56 ± 0,04	9,80 ± 0,05	40 ± 8
12	9,28 ± 0,05	11,20 ± 0,05	37 ± 9
18	12,35 ± 0,06	14,52 ± 0,07	40 ± 12
24	15,75 ± 0,08	17,50 ± 0,09	35 ± 11
29	17,50 ± 0,08	19,60 ± 0,09	38 ± 8

For the evaluation of the contribution of flow to the total displacement of water molecules in longitudinal direction of the nerve fibers we compared the apparent diffusion coefficients at different observation times: 30 ms and 300 ms. The values of velocities were theoretically calculated according to the Eq. 3 from the increase of the apparent diffusion coefficient with the increase of observation time (Table 2). They were found to be significantly larger than rates of the axonal transport in nerve known from the literature [2, 3]. This could be partly explained by the redistribution of population of water components due to relaxation of magnetization during observation time.

Conclusions

- The axonal transport in nerve doesn’t significantly influence the increase of apparent diffusion coefficient with the increasing observation time. It is proposed that the main contribution to the increase of apparent diffusion coefficient is caused by the redistribution of population of water components due to the relaxation.
- The activation energy of the apparent diffusion coefficient in nerve was found to be higher than that for the pure water. This fact is related to the retard of mobility of the water molecules by the components of membrane.

References

[1] Reiness G. Axonal transport. Neurobiology, 2005, pp. 1-5.

[2] Terrada S., Kinjo M., Hirokawa N. Oligomeric tudulin in large transporting complex is transported via kinesin in squid giant axons. Cell, 2000, vol. 103, pp. 141-155.

[3] Hirokawa N. The mechanism of fast and slow transport in neurons: identification and characterization of the new kinesin superfamily motors. Curr. Opin. Neurobiol., 1997, pp. 605-614.

Nuclear Spin-kinetics of ^{3}He in Magnetic Aerogel

V.V. Kuzmin$^{1)}$, K.R. Safiullin$^{1)}$, A.V. Klochkov$^{1)}$, R.R. Gazizulin$^{1)}$, A.A. Rodionov$^{1)}$,
G.V. Mamin$^{1)}$, M.S. Tagirov$^{1)}$, D.A. Tayurskii$^{1)}$, N. Mulders$^{2)}$

$^{1)}$ Kazan State University, Kremlevskaya, 18, Kazan 420008, Russia
$^{2)}$ University of Delaware, Newark, DE 19716, USA

e-mail: Slava625@yandex.ru

Aerogels are very dilute networks of randomly interconnected thin strands of silica. The typical strand diameter is thought to be on the order of 50 Å. The open geometry together with the small diameter of strands make aerogel very attractive and unique system for study of impurities effects in liquid ^{3}He. Spin kinetics of liquid ^{3}He inside aerogel depends on geometry (porosity, dimensionality of aerogel inner space etc.) as well as on magnetic fields created by some magnetic moments inside aerogel. For example, some paramagnetic centers can appear in aerogel after X-rays irradiation at room temperatures.

In this work the influence of the paramagnetic centers uncurtain in aerogel after irradiation on relaxation of longitudinal magnetization (T_1) of liquid ^{3}He under T=1.5 K and at the frequencies 10–20 MHz was investigated.

Aerogels with porosity 95% was used as the sample. Three lines in EPR spectra of annealed samples of aerogel have appeared after the irradiation (fig.1).

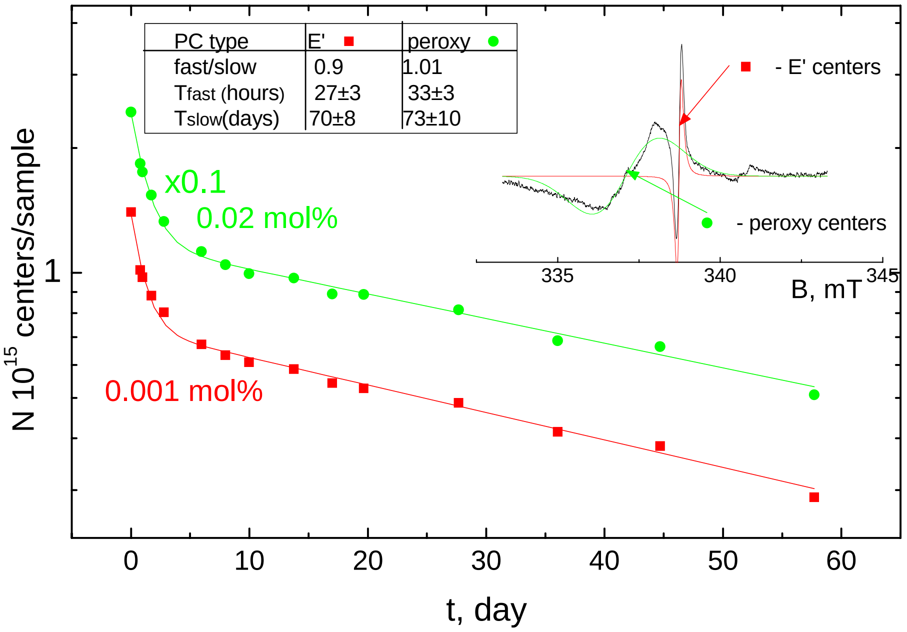

Fig.1 The decay paramagnetic centers in annealed and irradiated aerogel.

The narrow line with g-factor equal 2.0035 is ascribed to the E’-centers and two lines with inhomogeneous broadening are ascribed to the hyperfine structure. Also the broad line (g=2.01) was observed in the unannealed samples of aerogel, these paramagnetic centers were named “peroxy”-centers. These centers occurred due to the O_2 and H_2O surface film in unannealed aerogel and have concentration about 10^{15}centres/cm^3. The decay of paramagnetic centers in aerogel was studied during the two month at the room temperature . There are the fast process and the slow process of decay. In the beginning the concentration of the paramagnetic centers decreased in a half in three days, after that decay process became slow. The characteristic times of the exponential decay of all types of paramagnetic centers are 30 hours for the fast process and 70 days for the slow process.

The relaxation time T_1 of liquid ^{3}He at 1.5 K in the annealed and then irradiated aerogel was investigated. The hand made pulse NMR spectrometer has been used (^{3}He Larmour frequency range 10 – 25 MHz).

It was found that T_1 of liquid ^{3}He linearly depend on frequency, but doesn't depend on the time of aerogel ageing, i.e. on concentration of paramagnetic centers in irradiated aerogel.

After that the T_1 of liquid ^{3}He in annealed and unannealed, but unirradiated aerogel was investigated (fig.2).

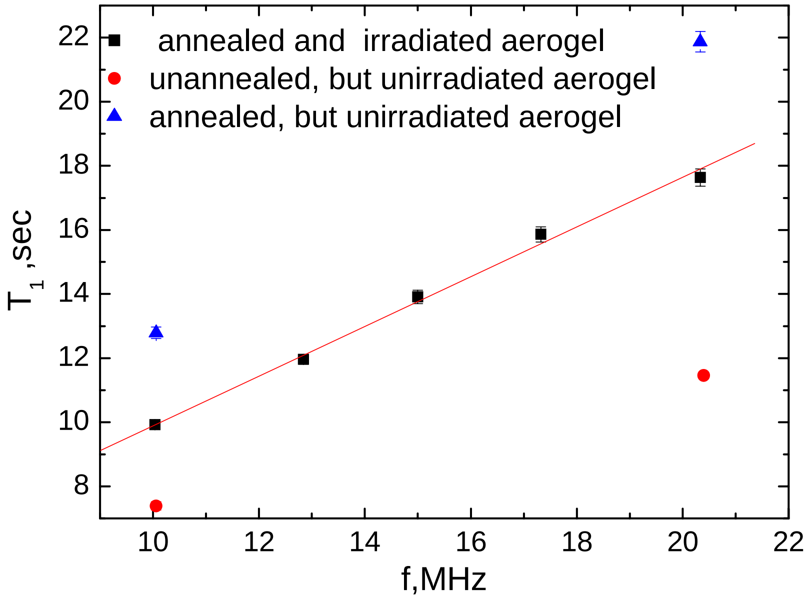

Fig.2 The field dependence of T_1 of ^{3}He in aerogel

It was supposed that the field dependence of T_1 appears due to existence of paramagnetic centres on walls of experimental cell, but experiments with ^{3}He in empty experimental cell shows that T_1 in this case is much more longer than in case of cell with aerogel (≈300sec), therefore cell doesn't make essential influence on experimental data.

There is no influence of paramagnetic centres on T_1 of liquid ^{3}He in irradiated aerogel. These result probably could be explained by:

1. Short interaction time between ^{3}He and paramagnetic centres, because of fast spin diffusion of ^{3}He in aerogel.
2. The concentration of paramagnetic centres is rather small, which means that magnetic reservoir of ^{3}He spin system is much bigger than magnetic reservoir of paramagnetic centres.

T_1 of liquid ^{3}He in aerogel is much less than in case of bulk ^{3}He.

This work is supported by BRHE (REC-007)

Spin-echo NMR Study of the Translational Water Diffusion in Various Zones of Maize Root and its Sensitivity to the Water Channel Blocker

L.G. Eidinov(1), I.F. Ionenko(2)

(1)Kazan State University, 420008, Kremlevskaya 18, Kazan, Russia
(2)Kazan Institute of Biochemistry and Biophysics, Russian Academy of Sciences, 420111, Lobachevskogo 2/31, Kazan, Russia

e-mail: ionenko@mail.knc.ru

Important advances in studying water movement at the cell and tissue level include the use of traditional physiological method — the pressure probe — for roots and for individual cells [1,2]. Because the movement of water through plant tissues involves several barriers, including apoplastic, symplastic and transmembrane ones, a single set of measures of overall hydraulic conductivity is not sufficient for determining how particular water channels (aquaporins) function in plant membranes. The results of pressure-probe experiments require careful interpretation, and independent nondestructive ways of measuring water fluxes are desirable [3].

In the present paper we propose to use the spin-echo NMR method for study of water transport through cell membranes in maize seedling roots. This method is the most adequate one for water transport studies at all levels and is widely used in the investigation of plant water relations [4-6]. Our previous NMR-spin echo studies with the pulsed magnetic field gradient revealed that the diffusional water flow in maize roots is sensitive to mercury chloride, an inhibitor of water channels [7]. Considering that changes in water transport parameters are based on structural differences related to cell and tissue differentiation along the root axis and taking into account functional features and differential contribution of various water-conducting pathways, we intended to study diffusional water transport in various zones of growing maize root and to assess the sensitivity of this transport to mercury chloride. Mercury chloride was used as an inhibitor of water channels; it was found effective for the majority of aquaporins.

Experiments were performed on roots of 9-day-old maize seedlings (Zea mays L., cv. Donskaya 1) grown at the laboratory conditions on wet filter paper at 22°C. The root segments were cut from various root zones. Zone I is the apical root segment measuring 1.5-2.0 mm that included the meristem and the transition zone; zone II is the root region with a length of 7 mm excised from the extension zone; zone III is the root segment measuring 8 mm and located at a distance of 60-70 mm from the root apex (zone of differentiated cells). In order to measure diffusion coefficients, samples from the respective zones were placed into a measuring ampoule (30-40 segments per ampoule). The diffusion was measured in the radial direction of root. All measurements were performed at 22°C.

The experiments were carried out on the NMR spin-echo relaxationmeter-diffusionmeter at a frequency of 16 MHz with a pulsed magnetic field gradient and with pulse current stabilization in the stimulated echo pulse sequence [8]. When the pulsed gradient is applied the diffusional echo decay is described by the expression:

$$R = \exp\left[-\gamma^2 \cdot \delta^2 \cdot g^2 \cdot \left(t_d - 1/3 \cdot \delta\right) \cdot D\right] \tag{1}$$

where γ is the gyromagnetic ratio, D is the diffusion coefficient, g and δ are, respectively, the amplitude and duration of the pulses of the magnetic field gradient, the interval between pulses, t_d , is the diffusion time, and R is the relative amplitude: $R = A(g)/A(0)$.

During experiment, we recorded the diffusional decays of spin echo signals as a function of parameters characterizing the pulse sequence (Fig.1). The echo signal amplitude was registered within the range of three orders of magnitude using a computer controlled attenuator. Average values of effective diffusion coefficient (D_{ef}) were calculated from the tangent to the echo envelope $\ln R(g^2)$ as $g \to 0$ for various t_d with the use of the equation (1). The diffusometer data were processed with a computer. Each diffusional decay curve represents the mean of seven accumulated signals of echo amplitude. All experiments were performed in triplicate.

The decay curves of the relative echo amplitude were nonexponential irrespective of t_d for all root zones (Fig. 1). Such nonexponential patterns are characteristic of live heterogeneous systems where water diffusion is restricted by the presence of compartments of

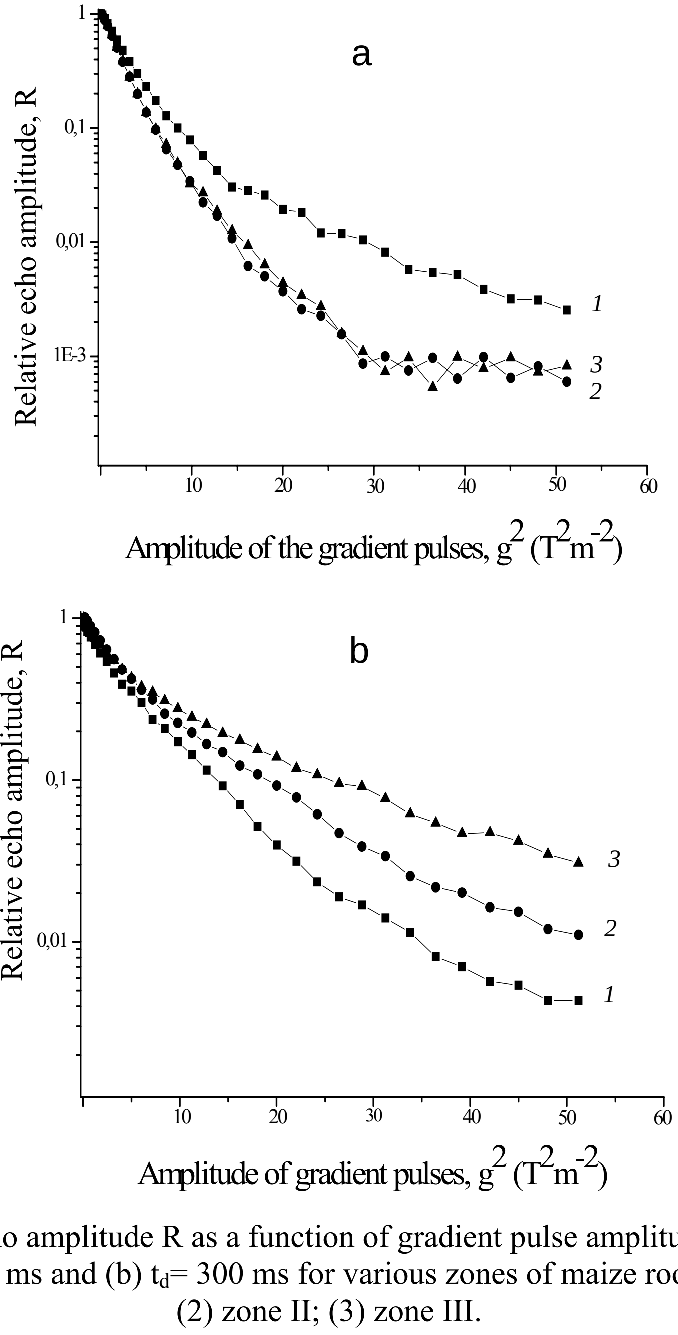

Fig.1. Relative echo amplitude R as a function of gradient pulse amplitude g^2 at diffusion times (a) t_d= 15 ms and (b) t_d= 300 ms for various zones of maize roots: (1) zone I; (2) zone II; (3) zone III.

various dimensions. The curves of diffusional echo decay differed for various root zones; namely, the slopes of these curves were different indicating variations in the water diffusion coefficients D_{ef}.

The shapes of dependences of D_{ef} on t_d (Fig. 2) for various root zones were obviously different. The differences of these curves are conditioned first of all by the morphological features of cells of the various root zones including the cell size. At short diffusion times the D_{ef} values in zones II and III were considerably higher than D_{ef} values in zone I. The diffusional path length of water molecules in this case did not exceed the average dimension of one cell (about 10 μm), and the differences of D_{ef} were likely caused by the presence of large vacuoles and cytoplasm fluidization in cells of the distant regions above the root apex. At higher t_d values, a different pattern of changes in water diffusion coefficients was observed (Fig. 2). Namely, the D_{ef} values were lower in zones II and III than in zone I. In this case, the diffusional path length of water molecule (at t_d = 500 ms) was equal to 70-80 μm, which is more than two times higher than the average dimension of root cells in the radial direction (especially for zone I cells). In this case, the differences in D_{ef} for various root zones could be due to disparate tissue morphologies and membrane permeabilities. Namely, the water permeability of cell membranes seems lower in zone II and especially in zone III compared to zone I. The higher water permeability of meristematic cells in zone I may promote faster transmembrane exchange of extra- and intracellular water, thus ensuring adequate conditions for cell transition to the elongation stage. A considerable decrease in D_{ef} for zone III at higher t_d values could be due to the formation in this zone of additional barriers for water movements, such as the endoderm with developed Casparian strips and suberized cell walls.

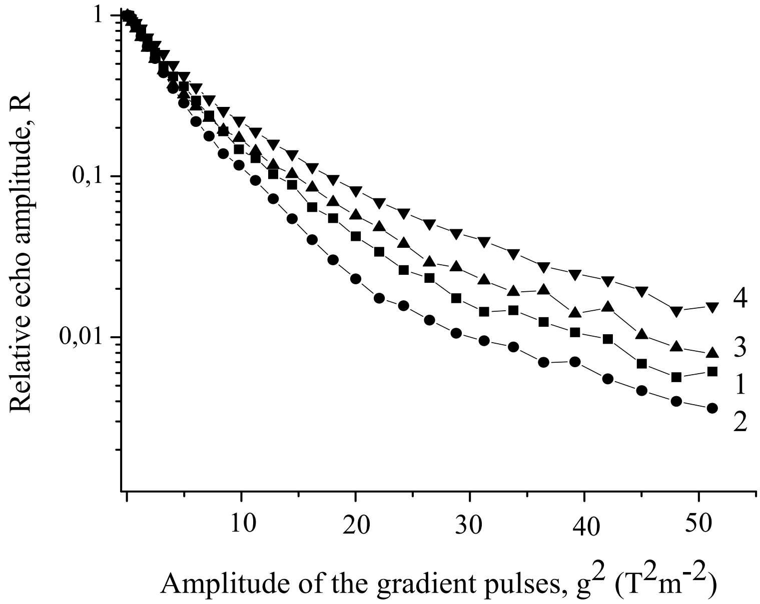

Fig. 2 Dependence of water diffusion coefficients D_{ef} on the diffusion time t_d in maize roots: (1) zone I; (2) zone II; (3) zone III.

Effects of aquaporin blocker $HgCl_2$ on water diffusion were different in various root zones and depended on the diffusion time (Fig.3, table).

The 15-min treatment of roots with $HgCl_2$ slowed down the diffusional decay in zone II (curves 3 and 4) and, on the contrary, accelerated water diffusion in zone I (curves 1 and 2).

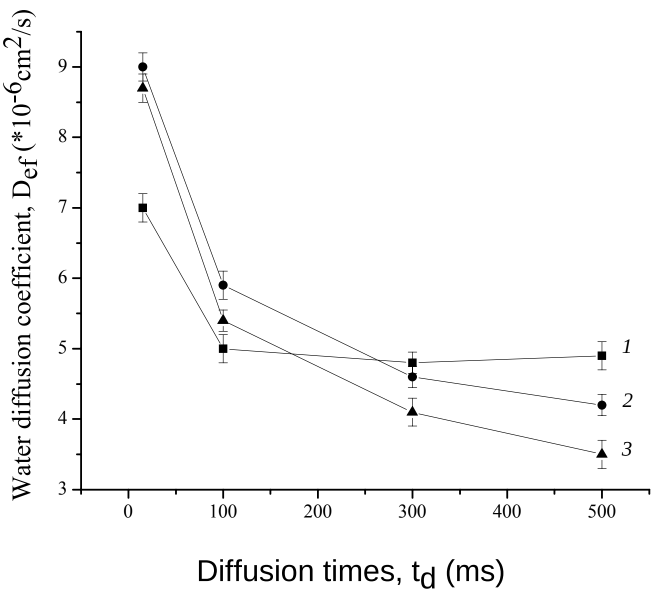

Fig.3 Relative echo amplitude R as a function of gradient pulse amplitude g^2 at diffusion times t_d = 300 ms for various zones of maize roots: (1, 2) zone I; (3, 4) zone II; (1, 3) – control; (2, 4) 0.1 mM $HgCl_2$.

Table. Effect of mercury chloride on diffusional water transport in various zones of maize roots at different diffusion times

Variant	Water diffusion coefficient ($D_{ef} \times 10^{-6}$ cm^2/s)			
	15 ms	100 ms	300 ms	700 ms
Zone *I*, control	7.0 ±0.2	4.9 ±0.2	4.8 ±0.15	-
Zone *I*, $HgCl_2$	7.5 ±0.15	5.9 ±0.3	5.4 ±0.2	-
Zone *II*, control	9.2 ±0.2	6.2 ±0.2	4.6 ±0.15	4.2 ±0.15
Zone *II*, $HgCl_2$	9.4 ±0.2	5.4 ±0.2	3.3 ±0.2	2.9 ±0.1
Zone *III*, control	8.8 ±0.2	5.7 ±0.15	4.2 ±0.2	3.3 ±0.2
Zone *III*, $HgCl_2$	9.0 ±0.1	5.2 ±0.1	2.8 ±0.2	1.9 ±0.1

At large t_d the inhibitory effect of mercury chloride was revealed in zones II and III, which was manifested as a large decrease in D_{ef} values. The inhibitory effect of $HgCl_2$ on D_{ef} is presumably attributed to the blocking of water-permeable membrane pores [9, 10]. According to these authors, Hg^{2+} ions interact with free sulfhydryl groups of proteins engaged in the membrane pore structure and induce closing of water-conducting pores. A different profile of changes was observed in zone I cells. Instead of inhibiting the diffusion rate, $HgCl_2$ caused a slight increase in D_{ef}. Such an effect of $HgCl_2$ is probably related to specificity of cell responses in the transition zone [11] upon the action of adverse factors. Ishikawa and Evans [12] noted "specific" physiological properties of cells in this zone, which were often opposite to cell properties in the elongation zone (for example, water stress induced equivocal responses in these cells). The increase in water diffusion coefficients after the treatment of zone I with $HgCl_2$ might also originate from compensatory increase in water diffusion along the symplastic route.

Differential effects exerted by $HgCl_2$ in various root zones provide evidence that dominant pathways for radial water transport may differ in these root regions. In the meristem, the symplastic route seems predominant, while in the distant regions above the apex, the contribution of transmembrane aquaporin-mediated transport increases. The elevated sensitivity of water flow to $HgCl_2$ inhibition in the cell elongation zone correlates with the enhanced activity (gene expression) of aquaporins in this zone established in some studies [13]. The strongest inhibition of water flow was observed at long diffusion times in root regions remote from the apex, where the vacuolar water is the main contributor to the diffusional decay (the relaxation time of the vacuolar water T_1 = 700-800 ms). This finding suggests that the inhibiting effect of mercury is mainly attributed to its action on the vacuolar membrane, the tonoplast.

References

[1] Steudle E., Peterson A. How does water get through roots? /J. Exp. Bot. 1998, 49: 775-788.

[2] Tomos A.D., Leigh R.A. The pressure probe: a versatile tool in plant cell physiology./Annu Rev Plant Physiol Plant Mol Biol. 1999, 50: 447-472.

[3] Quigley F., Rosenberg J.M., Shachar-Hill Y., Bohnert H.J. From genome to function: the *Arabidopsis* aquaporins./Genome Biology 2001, 3: 1-17.

[4] Van As H., Van Vliet P.A., Schaafsma T.J. ^{1}H spin-echo nuclear magnetic resonance in plant tissue. The effect of Mn (II) and water content in wheat leaves. /Biophys. J. 1980, 32: 1043-1051.

[5] Van Dusschoten D., De Jager P.A., Van As H. Extracting diffusion constants from echo-time-dependent PFG NMR data using relaxation-time information. /J. Magn. Resonance 1995, 116: 22-28.

[6] 6. Van der Weerd L., Claessens M.M.A.E., Rutink T., Vergeldt F.J., Schaafsma T.J., Van As H. Quantitative NMR microscopy of osmotic stress responses in maize and pearl millet. /J. Exp. Bot. 2001, 52: 2333-2343.

[7] Ionenko I.F., Anisimov A.V., Karimova, F.G. Water transport in maize roots under the influence of mercuric chloride and water stress: a role of water channels./Biol. Plant. 2006, 50: 74-80.

[8] Tanner J.E. Use of the stimulated echo in NMR diffusion studies./J. Chem. Phys. 1970, 52: 2523-2526.

[9] Tazawa M., Ohkuma E., Shibasaka M., Nakashima S. Mercurial-sensitive water transport in barley roots./J. Plant Res. 1997, 110: 435-442.

[10] Maggio A., Joly R.J. Effects of mercuric chloride on the hydraulic conductivity of tomato root systems./Plant Physiol. 1995, 109: 331-335.

[11] Baluska F., Volkmann D., Barlow P.W. A polarity crossroad in the transition growth zone of maize root apices: cytoskeletal and developmental implications. /J. Plant Growth Regul. 2001, 20: 170-181.

[12] Ishikawa H., Evans M.L. Specialized zones of development in roots. /Plant Physiol. 1995, 109: 725-727.

[13] Hukin D., Doering-Saad C., Thomas C.R., Pritchard J. Sensitivity of cell hydraulic conductivity to mercury is coincident with symplasmic isolation and expression of plasmalemma aquaporin genes in growing maize roots. /Planta 2002, 215: 1047-1056.

Anisotropic Exchange Interaction in $CuTe_2O_5$

T.P. Gavrilova[1)], R.M. Eremina[1)], H.-A. Krug von Nidda[2)], J.Deisenhofer[3)], A.Loidl[2)]

[1)]Zavoisky Physical-Technikal Institute, 420029, Kazan, Russia
[2)]Institute for Physics, Augsburg University, D-86135 Augsburg, Germany
[3)]Departement de Physique de la Matiere Condensee, Universite de Geneve, CH-1211 Geneve 4, Switzerland

e-mail: tatyana.gavrilova@gmail.com

Introduction

The discovery of a spin-Peierls transition in the onedimensional (1D) Heisenberg antiferromagnet $CuGeO_3$ [1] in 1993 entailed an intensive search for other inorganic spin-Peierls systems. This renewed the investigations of transition-metal oxides with spin S=1/2 ions such as Cu^{2+}. Transition-metal compounds based on Cu^{2+} ions with a $3d^9$ configuration exhibit an enormously rich variety of magnetic structures depending on the effective magnetic dimensionality.

The compound investigated in this study is the related system $CuTe_2O_5$ which exhibits a monoclinic structure with space group $P2_{1/c}$ and lattice parameters $a = 6.871$ Å, $b = 9.322$ Å, $c = 7.602$ Å, and $\beta = 109.08°$ [2]. The lattice unit includes four Cu positions. The lattice consists of pairs of strongly distorted and edge-sharing CuO_6 octahedra with a Cu-Cu distance of 3.18 Å. These structural dimer units Cu(1)-Cu(2) or Cu(3)-Cu(4) are separated by Te-O bridging ligands and a Cu-Cu distance of 5.28 Å. The copper ions in position Cu(1)-Cu(2)-Cu'(1) form the alternatig chain along c axis. This chain lies practically in (ac) plane. The copper ions Cu(3)-Cu(4)-Cu'(3) form a second magnetically nonequivalent chain like structure running approximately along crystallographic *c* axis. The chains are arranged along the approximate crystallographic *b* axis.

The magnetic susceptibility of $CuTe_2O_5$ shows a maximum at T_{max}=56.6 K and a strong decrease for lower temperatures, which can be roughly modeled by isolated magnetic dimers. The high-temperature susceptibility corresponds to a Curie-Weiss law with a Curie-Weiss temperature of $\theta = -41\,K$. The spin susceptibility in $CuTe_2O_5$ was studied in [3]. They cannot unambiguously determine the magnetic structure by fitting the susceptibility. But the alternating spin-chain and the modified Bleaney-Bowers approach well described experimental dates. For this reason, authors [3] and [4] investigated in detail the possible exchange paths between adjacent Cu ions. In the spin dimer analysis based on EHTB calculations, the strength of an antiferromagnetic interaction between two spin sites is estimated by considering the antiferromagnetic spin exchange parameter $J = -(\Delta e)^2 / U_{eff}$ [5], where U_{eff} is the effective on site repulsion, Δe – energy split. The strongest interaction is J_6. The first-principles NMTO-downfolding study [4] reveals that the strongest Cu-Cu interaction is given by the Cu pairs (№4) belonging to different structural dimer units, and connected to two O-Te-O bridges. The results of examination by EHTB [3] and NMTO [4] methods are listed in Table 1.

The results [4] is contrary to resent study by [3], which represented the $CuTe_2O_5$ system as alternating spin chain system with strong intra and inter dimmer coupling. For solved this problem here we present a detailed investigation of the angular and temperature dependence of the ESR linewidth in $CuTe_2O_5$. We will show that the anisotropy of the linewidth can be well described by symmetric anisitropic exchange interaction between nearest neighbor spins in alternating chain.

Experimental details

Large single crystals of $CuTe_2O_5$ was in the form of platelets with a maximum size of 0.2×1×1 mm^3. ESR measurements were performed in a Bruker ELEXSYS E500 cw spectrometer at 9.4 GHz in the temperature range $5<T<300$ K. The ESR signal of $CuTe_2O_5$ consists of a single exchange narrowed resonance line with nearly temperature independent g tensors, except for the temperatures (T<25K), where a splitting of the ESR line occurs due to the formation of clusters. The linewidth shows a pronounced anisotropy with the largest values for the magnetic field applied along the *b* axis. Figure 1 presents the detailed angular dependence of the ESR linewidth at 60K and room temperature.

Table 1. The relative strengths of the spin exchange interactions compared to the strongest interaction J_i/J_6 [3] and Cu-Cu hopping parameters t_i^2/t_4^2 [4] in $CuTe_2O_5$.

№	R Cu-Cu (Å)	J_i/J_6 [3]	$(t_i/t_4)^2$ [4]
1	3.187	0.59	0.12
2	5.282	0.05	-
3	5.322	0.14	0.01
4	5.585	0.11	1
5	5.831	0.01	0.015
6	6.202	1	0.28
7	6.437	0.05	0.002
8	6.489	0.09	-
9	6.871	0.26	-

Theoretical background

The theory of the ESR linewidth is well developed for conventional exchange-coupled spin systems. It has been shown that in the case of sufficiently strong exchange interaction the ESR spectrum is narrowed into a single Lorentz line with a linewidth ΔH (half width at half maximum) determined by second M_2 and forth M_4 moments [6]:

$$\Delta H = \frac{\pi}{\sqrt{3}}\left(\frac{M_2^3}{M_4}\right)^{1/2} \tag{1}$$

We consider a system of exchange-coupled spins S_{1i} with an effective spin Hamiltonian given by:

$$\begin{aligned} H = {} & J_{1a}\left(S_1 S_a\right) + \sum_{\alpha,\beta=x,y,z} J_{1a}^{\alpha\beta} S_1^{\alpha} S_a^{\beta} + J_{1b}\left(S_1 S_b\right) + \\ & + \sum_{\alpha,\beta=x,y,z} J_{1b}^{\alpha\beta} S_1^{\alpha} S_b^{\beta} + J_{1c}\left(S_1 S_c\right) + \sum_{\substack{\alpha,\beta=x,y,z \\ \gamma=1,3}} g_{\gamma}^{\alpha\beta} \mu_B H_{\gamma}^{\alpha} H_{\gamma}^{\beta}, \end{aligned} \tag{2}$$

where the scalar J_{1a} denotes the strongest isotropic exchange between two spins 1 and a, J_{1b} denotes the second value isotropic exchange between two spins 1 and b, J_{1c} is the minimum isotropic exchange between two spins 1 and c. The last term described the Zeeman splitting of the spin states in an external magnetic field H_{γ}^{α} with gyromagnetic tensor $g_{\gamma}^{\alpha\beta}$ and Bohr magneton μ_B. If $J_{1c} << J_{1a}$ and $J_{1c} << J_{1b}$, in coordinates x, y, z, where the z axis is defined by the direction of the applied magnetic field H, the second and forth moments due to anisotropic exchange is given by:

$$M_2(J)=\frac{2S(S+1)}{3}\left(B(J_{1a})+B(J_{1b})\right) \tag{3}$$

$$M_4=\frac{a(6a-7)}{30}\left(J_{1a}^2B(J_{1a})+J_{1b}^2B(J_{1b})\right)+\frac{a^2}{9}\left(J_{1b}^2B(J_{1a})+J_{1a}^2B(J_{1b})\right)+ \\ +\frac{a^2J_{1a}J_{1b}}{9}\begin{pmatrix}\left(2J_{1a}^{zz}-J_{1a}^{xx}-J_{1a}^{yy}\right)\left(2J_{1b}^{zz}-J_{1b}^{xx}-J_{1b}^{yy}\right)+ \\ +\left(J_{1a}^{xx}-J_{1a}^{yy}\right)\left(J_{1b}^{xx}-J_{1b}^{yy}\right) \\ 10J_{1a}^{xz}J_{1b}^{xz}+10J_{1a}^{yz}J_{1b}^{yz}+4J_{1a}^{xy}J_{1b}^{xy}\end{pmatrix} \tag{4}$$

where $B(J_{1a})=\left(2J_{1a}^{zz}-J_{1a}^{xx}-J_{1a}^{yy}\right)^2+\left(J_{1a}^{xx}-J_{1a}^{yy}\right)^2+10\left(J_{1a}^{xz}\right)^2+10\left(J_{1a}^{xy}\right)^2+4\left(J_{1a}^{xy}\right)^2$ and $a=S(S+1)$. The value $J_{1\gamma}^{\alpha\beta}$, where $\alpha,\beta=x,y,z$, $\gamma=a,b$ are exchange-tensor components in the coordinates with z‖H. They can be expressed via the intrinsic exchange parameters [7].

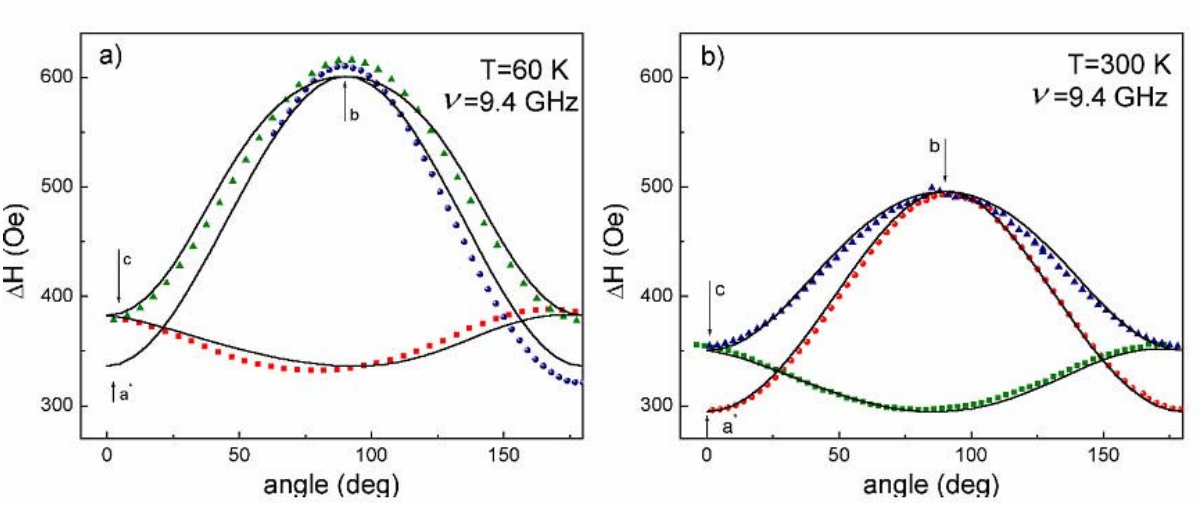

Fig.1 Angular dependence of the resonance linewidth for three planes (a*b), (bc), (a*c). The solid lines have been obtained from the fit as described in the text.

Determination of the exchange parameters

Now we focus our attention on the angular dependence of the ESR linewidth, which we investigated in detail for the three crystallographic planes at 60K, 200K and room temperature. Typical data are shown in Fig.1.

We will describe the angular dependence of the ESR linewidth using anisotropic exchange interaction between neighboring spins. The symmetric anisotropic exchange interaction between two neighboring spins S_i and S_j can be written in local coordinates as $H^{(i,j)}=J_{x'x'}S_i^{x'}S_j^{x'}+J_{y'y'}S_i^{y'}S_j^{y'}+J_{z'z'}S_i^{z'}S_j^{z'}$, where $J_{x'x'}+J_{y'y'}+J_{z'z'}=0$. The local coordinates for inequivalent pairs are different. It is necessary for the estimation of the anisotropic exchange constants to find $\sim[(g-2)/g]^2J$. In this case the largest anisotropic exchange interaction is for strongest isotropic exchange value. The strongest interaction has number 6 pair in. EHTB model [3] (see table 1). In this case the maximum of ESR linewidth must shift on 37 degrees from b axis in (bc) plane. But experimental curve hasn't such behavior. For this reason we believe that the strongest interaction in the fourth pair (see table 1) [4] is between two Cu^{2+} ions, which are situated at different structural dimer (Cu(2)-Cu'(1) or Cu(4)-Cu'(3)). The second strongest interaction is between two Cu^{2+} ions situated within the same structural dimer unit (first pair of table1). In Fig. 2 we show alternating chain model in the (bc) plane. The angular dependence of the ESR linewidth was approximated by Eqs (1), is illustrated in Fig. 1. For the all temperatures the results of the fit procedure are plotted in Table 2. According to the magnetic susceptibility fit [3] for alternating chain, the strongest interaction is J_{1a}=93.3K for 4 pair. The second strongest value is J_{1b}=40.7K for 1 pair. The g-tensor was founded before from angular dependencies resonance field and anisotropic effect Zeeman [8].

Table 2. The parameters of anisotropic exchange interaction at different temperatures.

T(K)	$J_{1a}^{x''x''}$ (K)	$J_{1a}^{z''z''}$ (K)	$J_{1b}^{x'x'}$ (K)	$J_{1b}^{z'z'}$ (K)
60	-1	2.19	0.55	-0.33
200	-0.82	1.98	0.65	-0.42
300	-0.82	1.92	0.64	-0.42

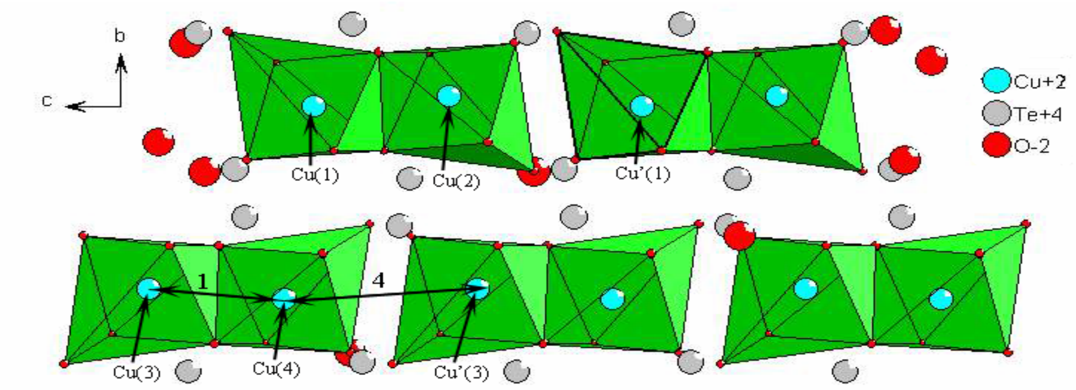

Fig.2 The model of alternating spin-chain Cu(1)-Cu(2)-Cu'(1) and Cu(3)-Cu(4)-Cu'(3) in (bc) plane.

Conclusions

To summarize, we presented detailed ESR linewidth investigations on $CuTe_2O_5$ single crystals. The anisotropic exchange interaction within the Cu alternating chain was successfully applied to describe its angular dependence. Hence from an ESR point of view, $CuTe_2O_5$ turns out to be alternating chain Cu(1)-Cu(2)-Cu'(1) and magnetic inequivalent Cu(3)-Cu(4)-Cu'(3) chain. Based on previous results on magnetic susceptibility in [3] and angular dependence ESR linewidth analyses, we believe that strongest isotropic exchange interaction is in 4 pair [Cu(2)-Cu'(1) or Cu(4)-Cu(3)] and equal J_{1a}=93.3K and the second strongest value of exchange interaction in structural dimer (1 pair) is J_{1b}=40.7K.

Acknowledgments

It is pleasure to thank prof. M.V. Eremin for fruitful discussion. We are grateful to P.Lemmens for sample preparation. This work was supported by project of Russian Foundation for Basic Research (RFBR) 06-02-17401.

References

[1] M. Hase, I. Terasaki and K. Uchinokura. Phys. Rev. Lett. **70**, 3651 (1993)

[2] K. Hanke, V. Kupcik, O.Lindqvist. Acta Cryst. B **29**, 963 (1973)

[3] J.Deisenhofer, R.M. Eremina, A. Pimenov, T. Gavrilova, H. Berger, M. Johnsson, P. Lemmens, H.-A. Krug von Nidda, A. Loidl, K.-S. Lee and M.-H. Whangbo. Phys. Rev. B. **74**, 174421 (2006)

[4] H. Das, T. Saha-Dasgupta. cond-mat 0703675 (2007)

[5] P.W. Anderson. Solid State Phys. **14**, 99 (1963)

[6] A. Abragam and B. Bleaney, Electron Paramagnetic Resonance of Transition Ions (Clarendon Press, Oxford, 1970).

[7] R.M. Eremina, M.V. Eremin, V.N. Glazkov, H.-A. Krug von Nidda, A. Loidl. Phys. Rev. B **68**, 014417 (2003)

[8] R.M. Eremina, T.P. Gavrilova, H.-A. Krug von Nidda, A. Pimenov, J.Deisenhofer, A.Loidl, Phys. of Solid State (to be published in 2008)

Study of EPR Spectra in LiLuF$_4$:U^{3+} and LiYF$_4$Yb^{3+} Single Crystals

L.K. Aminov, A.A. Ershova, D.G. Zverev, S.L. Korableva, I.N. Kurkin, B.Z. Malkin

Kazan State University, 420008, Kremlevskaya str., 18, Kazan, Russia.
e-mail: ershovaa@bk.ru

Double fluorides with the scheelite structure LiRF$_4$ (R=Y, Lu), activated by rare earth ions, are highly technological laser materials [1] extensively investigated by optical spectroscopy and EPR methods. Optical investigations of the LiLuF$_4$ and LiYF$_4$ single crystals activated by uranium [2-4] show them as promising materials for laser generation in the $2.5-2.8\,\mu\text{m}$ range. Meanwhile, there are no literature data on EPR of actinides in double fluorides. In this work we present the results of measurements of EPR spectra in the LiLuF$_4$:U single crystal, the observed EPR signals are unambiguously assigned to the U^{3+} ions. These results are compared with the appropriate data for double fluorides doped by rare earth ions.

Among the systems with the same scheelite structure, the CaMoO$_4$ single crystals activated by uranium were studied by EPR methods [5]. Authors of [5] attributed the observed spectrum to the U^{5+} ion in the Mo^{6+} position. The valence aspect is significant since it is known that actinides implanted into the crystals form centers with different valence states (see, e.g. [6,7]). So the valence states U^{2+}, U^{3+}, U^{4+}, U^{5+} were found for uranium; in particular the states U^{2+}, U^{3+}, U^{4+} were revealed among optical centers in the LiLuF$_4$:U [3].

One more aspect of the considered problem is of great interest, it is a question about coupling of *5f*-shell electrons of paramagnetic centers with ligands. Seemingly this coupling is stronger than that for 4*f*-shells of rare earth ions, which is testified by the existence of SHFS due to fluorine nuclei ($I=1/2$) in the EPR spectrum of $CaF_2:U^{3+}$ crystal (unfilled $5f^3$ shell) and the lack of such a structure for $CaF_2:Nd^{3+}$ ($4f^3$ shell) [6]. This question is discussed in detail in the present work on the basis of experimental results.

EPR spectra of LiLuF$_4$:U^{3+} and LiYF$_4$:Yb^{3+} single crystals were taken on IRES-1003 and Bruker ESP-300 spectrometers at the frequency of $\approx 9.35\,GHz$ (X-band) and temperatures in the range of $10-20$ K all samples were grown by Bridgman- Stockbarger method, in the argon atmosphere.

Two LiLuF$_4$+0.1%U samples grown with the time interval more than 10 years (samples 1 and 2) have been studied. The first sample has the pale yellow color, the second one is colored yet weaker. The EPR lines observed in the applied magnetic field $\boldsymbol{B}$ in the range of 5000 – 5800 G oriented along the crystal *c*-axis were attributed to different isotopes of three-valent uranium. The actual concentration of U^{3+} ions as compared to the standard specimen (CaF$_2$+0.8%Er^{3+}) appeared equal to 0.035% (sample 1) and 0.007% (sample 2). These values differing from sample to sample are significantly less than inserted into the crystals (0.1%). Possibly, some uranium ions enter into the crystal matrix in other valence states, U^{2+} and U^{4+} [3], inactive in EPR. The ionic radius of U^{3+} ion (1.18 A) is close to that of isovalent Lu^{3+} ion (1.11 A), so it is safe to suppose that U^{3+} ion substitutes Lu^{3+} in the crystal.

The center of the spectrum corresponds to the g-factor value $g_{||}=1.228$. The intensive line observed in the field of about 3300G has been attributed to Nd^{3+} ions by its g-value ($g_{||}=2.074$) and characteristic for neodymium hyperfine structure. Just the presence of Nd^{3+} ions complicated measurements of the U^{3+} signals for the perpendicular field orientation

($B \perp c$), since in this orientation the Nd^{3+} ($g_\perp = 2.548$) and U^{3+} ($g_\perp = 2.516$) spectra were superimposed. Besides Nd^{3+} and U^{3+} spectra, the lines attributed to Yb^{3+} ions and the lines characteristic for Yb^{3+}, Er^{3+} and Dy^{3+} ions were observed in the samples 1 and 2, respectively.

Fig. 1 shows the fragment of the EPR spectrum for the magnetic field along the *c*-axis. Very intensive central piece is accompanied by eight nearly equidistant replicas, that is characteristic for the hyperfine structure (HFS) due to a nuclear spin $I = 7/2$. Therefore it is safe to attribute the intensive central piece of the spectrum and the weak HFS with intensity by three orders less to the most prevailing even isotope ^{238}U (natural abundance 99.28%, the life time 4.8×10^9 years [7]), and to the odd isotope ^{235}U ($0.71\%, 7.1 \times 10^8$ years, $I = 7/2$), respectively. The average spacing between hyperfine components equals $\approx 80G$. The small deviations from this figure allowed to estimate the hyperfine interaction parameters as $A_{\|} = 81\,\mathrm{G}$ and $A_\perp = 83.8\,\mathrm{G}$.

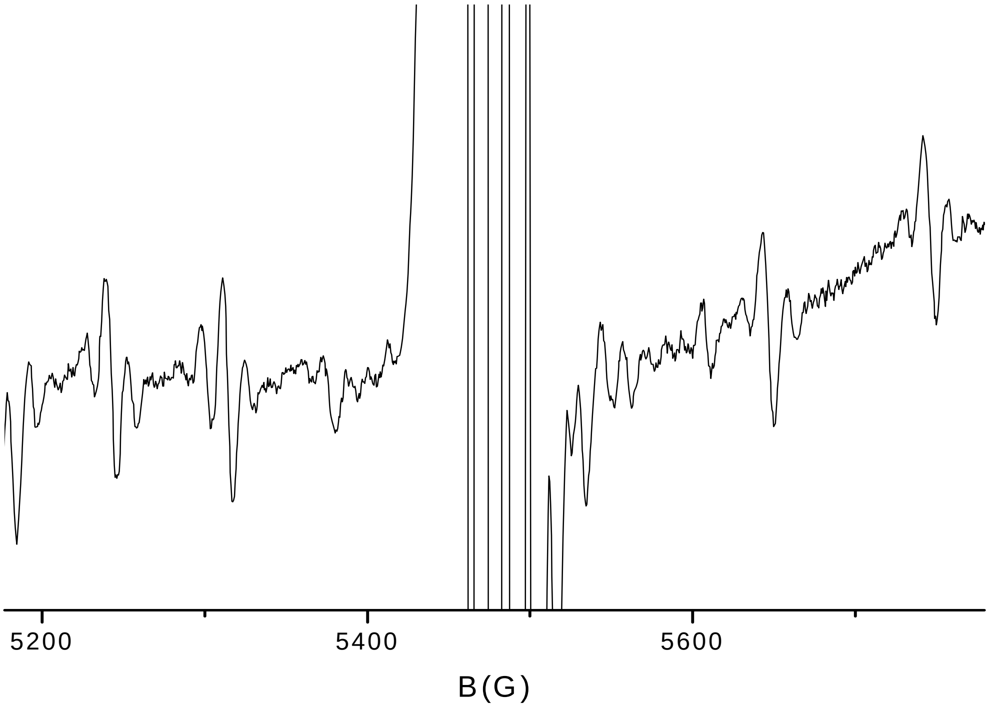

Fig.1 EPR spectrum of U^{3+} ion in LiLuF$_4$ single crystal; $\nu = 9.42\,\mathrm{GHz}$, $B \parallel c$, $T = 10\,\mathrm{K}$. Intensive lines in the central part of the spectrum are due to even isotopes of uranium. Satellites represent hyperfine structure due to isotopes ^{235}U.

The central piece of the spectrum and each HFS component display the pronounced additional structure with spacing between adjacent lines of 12.7G, which is evidently due to the super-hyperfine interaction (SHFI) of the unfilled *f*-shell electrons with nuclear magnetic moments of ligands (that is, F^- ions). The part of the spectrum containing the spectral lines of $^{238}U^{3+}$ is given in Fig. 2 with smaller magnification, so that these lines are seen completely. Of course, in this case the lines of ^{235}U isotope are not seen at all. Seven components of SHFS can be confidently singled out in Fig. 2, their intensities falling from center to the edge in the ratio of 360 : 90 : 11 : 1. Yet two lines with the intensity ≈ 0.1 are

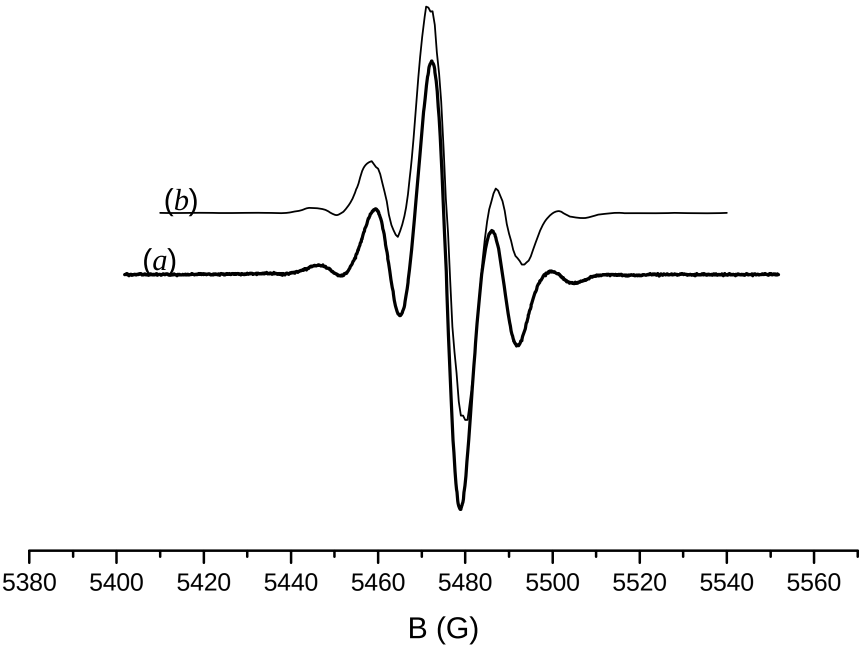

Fig.2 The measured (*a*) and simulated (*b*) SHFS of $^{238}U^{3+}$ EPR signal in LiLuF$_4$:U. The curve (b) is slightly shifted upwards.

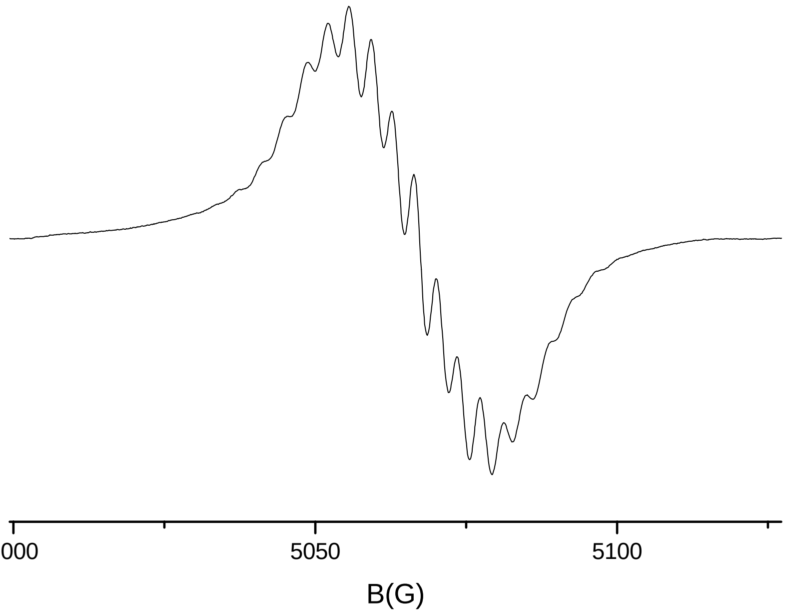

Fig.3 SHFS of $^{170}Yb^{3+}$ EPR line in LiYF$_4$:Yb, $\nu = 9.43\,\mathrm{GHz}$, $B \| c$, $T = 18\,\mathrm{K}$.

revealed at higher magnification. Further possible lines are superimposed with HFS lines of the odd isotope.

For comparative analysis of SHFS of EPR spectra of rare earth and actinide ions we present in Fig. 3 the spectrum of the LiYF$_4$: 0.1%Yb^{3+} single crystal ($g_{\|} = 1.33, g_{\perp} = 3.92$). In this case the SHFS lines are separated by intervals $\approx 3.7\,\mathrm{G}$. The spectrum practically coincides with that given in [8] without detailed interpretation. In the spectrum of Nd^{3+} in $LiYF_4$ (which is the direct analog of U^{3+}: three electrons on *f*-shell) no SHFS was observed [8].

Rare earth and actinide ions substitute for Y^{3+} (Lu^{3+}) ions in LiY(Lu)F_4 crystals in the sites with the S_4 point symmetry. The nearest surrounding of impurity ions is constituted by two groups of four fluorine ions (Fig. 4), which form two tetrahedrons, oblate and elongated along the crystallographic *c*-axis (*z*-axis), turned around the *c*-axis so that their second-order axes (*x,y*) do not coincide. Positions of F^- ions in each group of four are crystallographic equivalent, and for the parallel orientation of an applied field, ***B*** || *c*, they are also magnetically equivalent. Radius vectors coordinating the center (origin) with fluorine ions will be designated as r_{01} and r_{02}, respectively, for ions of the first and second groups pointed out in Fig. 4.

Let us consider the paramagnetic center (U^{3+} or Yb^{3+}) and its ligands (F^- ions) in the magnetic field ***B***, the interaction between ligands is neglected, as usual [6,9]. The Hamiltonian of the system includes the electron Zeeman term, the interaction of electrons with the fluorine nuclear spins, and for the J-multiplrt it may be written in the following form:

$$H = g_J\mu_B\mathbf{BJ} + A_J\mathbf{JI_0} - \gamma_{I_0}\hbar\mathbf{BI_0} + \gamma_I\hbar\sum_i\left(-\mathbf{B}+\mathbf{N}^{(i)}\right)\mathbf{I}^{(i)} \qquad (1)$$

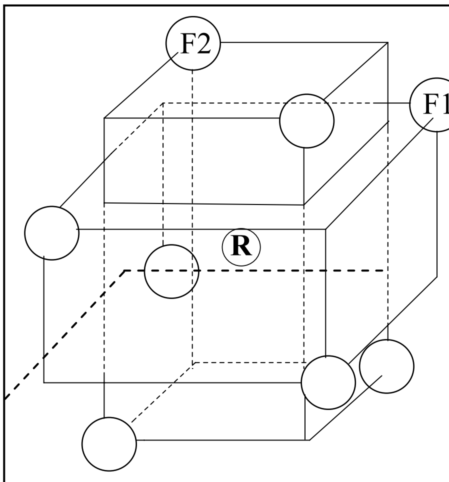

Fig.4 The nearest surroundings of R^{3+} ion in LiRF$_4$ crystals.

where g_J, μ_B, A_J are the Lande factor, the Bohr magneton, the hyperfine structure constant, respectively; γ_{I_0}, γ_I are nuclear gyromagnetic ratios for the central ion and ligands (F^-), respectively. The sum in eq. (1) is taken over ligands ($i = 1 \div 8$), and the vector $N^{(i)}$ is defined in the most general one-particle form as follows [6]:

$$\mathbf{N}(i) = 2\mu B\sum_a\left[\frac{\mathbf{l}_a-\mathbf{s}_a}{r_{ai}^3}+\frac{3\mathbf{r}_{ai}\left(\mathbf{s}_a\mathbf{r}_{ai}\right)}{r_{ai}^5}+\frac{8}{3}\pi\mathbf{s}_a\delta\left(\mathbf{r}_{ai}\right)\right], \qquad (2)$$

here the sum is taken over *f*-electrons, r_{ai} is the distance between an electron and the *i*-th nucleus, l_a, s_a are orbital and spin moments of an electron.

Then to aforesaid the Hamiltonian (1) may be presented as follows:

$$\widehat{H}_{eff} = \sum_{q\nu} g_{q\nu}\mu_B S_\nu B_q + \sum_{q\nu} A_{q\nu} S_\nu I_{0q} - \gamma_{I0}\hbar\mathbf{BI_0} + \gamma_I\hbar\sum_i\left(-\mathbf{BI}^{(i)} + \sum_{p\nu} T^{(i)}_{p\nu} I^{(i)}_p S_\nu\right), \qquad (3)$$

where

$$g_{pz} = 2g_J\langle\alpha|J_p|\alpha\rangle, g_{px} = 2g_J\operatorname{Re}\langle\alpha|J_p|\beta\rangle, g_{py} = -2g_J\operatorname{Im}\langle\alpha|J_p|\beta\rangle,$$

$$T^{(i)}_{pz} = 2\langle\alpha|N^{(i)}_p|\alpha\rangle, T^{(i)}_{px} = 2\operatorname{Re}\langle\alpha|N^{(i)}_p|\beta\rangle, T^{(i)}_{py} = -2\operatorname{Im}\langle\alpha|N^{(i)}_p|\beta\rangle.$$

Since the observed quantities are defined only by parameters T_{zz}, $T_t^2 = T_{xz}^2 + T_{yz}^2$ the experimental data give incomplete description of SHFI. Some more detailed description can be obtained by simulating the spectrum on the basis of the detailed microscopic model taking into account the spin transfer from the paramagnetic ion to the ligands. Such a model was used earlier to interpret SHFS of optical spectra in $LiYF_4 : Nd^{3+}$, two factors correlating overlap integrals of *f*-functions with *s*-, *p*-functions of ligands and corresponding covalence constants being chosen as model parameters [10]. The spectrum computation program developed in Ref. [10] can immediately be used for the $LiYF_4 : U^{3+}$ in view of the similar unfilled electron shells of Nd^{3+} ($4f^3$) and U^{3+} ion ($5f^3$).

The EPR spectrum in the $LiYF_4 : Yb^{3+}$ system, the only double fluoride doped with rare earth ions which shows SHFS, resembles the EPR spectrum in $CaF_2 : Yb^{3+}$, considered in detail by Ranon and Hyde [9]. The X-band spectra in both systems include 17 components, the adjacent components being separated by an interval of 3 – 3.7 G. the nearest surrounding of paramagnetic ion in both cases consists of eight fluorine ions, however the structures of surroundings are essentially different. Moreover g-factor of the Yb^{3+} cubic center in CaF_2 equals 3.443, consequently the nuclear Zeeman energy (7.5 MHz) is small compared to its value $\approx 20\,\text{MHz}$ (12 G) in $LiYF_4 : Yb^{3+}$. Therefore the similarity of the spectra in two systems should be admitted as somewhat occasional.

The distinction of the spectra in $LiLuF_4 : U^{3+}$ and $LiYF_4 : Yb^{3+}$ should probably be attributed to that the magnitude of the parameter T_{zz} in the second case approaches to parameters T_{xz} and T_{yz}. Then the groups of lines become wider, their structure is resolved, and the observed spectrum will contain more components separated by comparatively small intervals. Assuming the following numerical values for the combinations of parameters T_{pv} defining the spectral appearance: $|T_{zz}| = 6.3\,\text{MHz},\ T_t^2 = T_{xz}^2 + T_{yz}^2 = 40(\text{MHz})^2$, we obtain

$$B_{eff}(M_z = 1/2) = 24\text{MHz}, B_{eff}(-Mz) = 18\text{MHz}, q = 0.12, r = 0.88,$$

and the corresponding spectrum consists of 17 lines symmetrically disposed around the center. Adjacent components are separated by intervals of 6 MHz (3.6 G), the intensities fall non-monotonically with moving away of the center, approximately in the ratio of: 6.5:4.25:1.6:1.6:1.6:0.6:0.12:0.24:0.12. yet three extremely weak lines (with relative intensity ≤ 0.01) are disposed at somewhat greater distance from the marked lines.

The assumed value of the parameter $T_t^2 \approx 40(MHz)^2$ nearly coincides with its dipolar value for F2 ligands, while the value of $|T_{zz}|$ substantially exceeds it. The general appearance of the spectrum is practically preserved at accounting for two fours of fluorine ions if parameters of both fours are taken almost equal or for one set of four ligands the dipole values are retained.

Therefore, in the framework of the semi-phenomenological approach it is possible to explain almost all peculiarities of the observed ligand hyperfine structure (SHFS) in double fluorides activated by ions with unfilled *f*-shells, rare earth and actinides. However, it is necessary to turn to microscopic models for more detailed description of super-hyperfine interaction parameters.

Summing up, the present paper contains results of studying the EPR spectra of $LiLuF_4 : U^{3+}$ and $LiYF_4 : Yb^{3+}$, double fluorides activated by ions with unfilled 5*f*- and 4*f*-shells representing groups of actinides and rare earths. Both Yb^{3+} and U^{3+} ions in the ground state are described by the effective spin S=1/2. spectra in the parallel magnetic field, $\boldsymbol{B} \parallel c$, reveal pronounced super-hyperfine structures essentially different for two ions in spite of the closeness of their g-factors $g_{\|}$, which results in the coinciding of the magnetic dipole-dipole interactions of the paramagnetic ions with nuclei of surrounding fluorine ions. This distinction is described within the semi-phenomenological approach by different influence of covalent coupling of central ions with ligands on parameters of the super-hyperfine interaction. In average, the changes of these parameters as compared to their dipole values are approximately equal for 4*f*- and 5*f*-ions. The microscopic models of SHFI in general confirm this conclusion. EPR spectra present information only about some combinations of parameters defining SHFI. To obtain more complete data, it is necessary to study the double electron-nuclear resonance of such systems, as was noted earlier by Ranon and Hyde [9].

This work was supported by the Ministry of Education and Science of Russian Federation (project RNP 2.1.1.7348).

References

[1] Kaminskii A.A.: Laser crystals. Moscow: Nauka 1975.

[2] Abdulsabirov R.Yu., Dubinskii M.A., Kazakov B.N., Korableva S.L., Safiullin G.M., Semashko V.V.: IX-th All-Union Symposium on spectroscopy of crystals activated by rare earth and transition metal ions. Abstracts. Leningrad, 1990, p. 186.

[3] Jenssen H.P., Noginov M.A., Cassanho A.: OSA Proc. Adv. Solid-State Lasers, vol. **15**, 463 (1993).

[4] Hubert S., Simoni E., Louis M., Zhang V.P., Gesland J.Y. : J. Lumin. **60-61**, 245 (1994).

[5] Baikova R.A., Efimov V.N., Kurkin I.N., Shlenkin V.I.: Solid State Physics (St. Petersburg) **32**, 3537 (1990).

[6] Abragam A., Bleaney B.: Electron Paramagnetic Resonance of Transition Ions. Oxford: Clarendon 1970.

[7] Ursu I.: Magnetic resonance in uranium compounds.Energoatomizdat, Moscow, 1983.

[8] Sattler J.P., Nemarich J.: Phys. Rev. B **4**, 1 (1971).

[9] Ranon U., Hyde J.S. : Phys. Rev. **141**, 259 (1966).

[10] Macfarlane R.M., Meltzer R.S., Malkin B.Z.: Phys. Rev. B **58**, 5692 (1998).

Study of Low-Dose Irradiation Effects on Properties of Thin HTSC Films by Means of EPR and Hall Probes

N.Yu. Panarina, A.N. Bukharaev, Yu.I. Talanov, V.Yu. Petukhov, G.G. Gumarov,
A.A. Validov

Zavoisky Physical -Technical Institute, 420029, Sibirsky tract 10/7, Kazan, Russia.

e-mail: npanarina@kfti.knc.ru

In present work we studied the influence of the low-energy irradiation (40 keV) with iron and cobalt ions on superconducting properties of the $Bi_2Sr_2CaCu_2O_8$ thin films. The critical current density j_c was estimated from magnetic flux profiles and full-penetration field measured by EPR and Hall probes. These methods appeared to be effective in monitoring the j_c changes in high-temperature superconductors (HTSC) with variation of the irradiation dose.

Thin films were prepared by magnetron sputtering of initial compound $Bi_2Sr_2CaCu_2O_8$ in the oxygen atmosphere and further material deposition on a dielectric single-crystal substrate of $LaAlO_3$. The film thickness was 200 nm. Subsequently, the samples were irradiated at room temperature with monovalent ions of iron and cobalt with energies of 40 keV on accelerator ILU-3 at Kazan Physical-Technical Institute. The implantation dose varied from $5\cdot10^{11}$ ions/cm^2 to $3\cdot10^{13}$ ions/cm^2.

Since films were divided into parts, each irradiated with various doses, there was no possibility to prepare the contact system for the transport measurements on all parts of the films. Therefore, we used indirect methods to determine the critical current density j_c. The value of critical current density can be obtained from magnetic flux profile and the field of full penetration. Magnetic flux profile is the variation of magnetic field on the SC surface with coordinate. The local magnetic field can be measured directly by Hall probes and can be determined from the shift of EPR signal of a paramagnetic probe. The field of full penetration H^* is the value of magnetic field at which vortices penetrate to the center of a superconducting sample upon increasing the field from zero. The full-penetration field can be obtained from dependence of the resonance field of a paramagnetic probe on the sweep range and by monitoring the profile shape variation by Hall probes as well.

The measurements of magnetic flux profile by means of EPR and Hall probes have the similar principle. The probes are moved along the central line of the sample and the value of local magnetic field is determined either by direct measurements with Hall probes or from the EPR signal shift. For example, magnetic flux profiles of B3 sample (irradiated with the dose of $3\cdot10^{13}$ Co$^+$/cm^2) measured by means of EPR and Hall probes are given in Fig. 1. The presence of two characteristic minima in the profiles can be explained either by presence of inhomogenities on the sample surface (scratch, for example) or deviation of the probe movement from the central line of the sample. From Fig. 2 it is apparent that the profile amplitude registered by EPR and Hall probes is almost the same. To estimate the j_c value, a theoretical curve, described by Brandt for infinitely thin strip [1] and modified by T.S. Shaposhnikova for the case of a rectangular film:

$$H(x) = j_c \cdot d \cdot F(x, y, z, b, d, w) \qquad (1),$$

was fitted to the experimental profile. Here j_c is the critical current density, d is the thickness of a superconducting film and $F(x,y, z, b ,d, w)$ is the function of the film's geometry, including the sample width w and length b, variable coordinate x and fixed

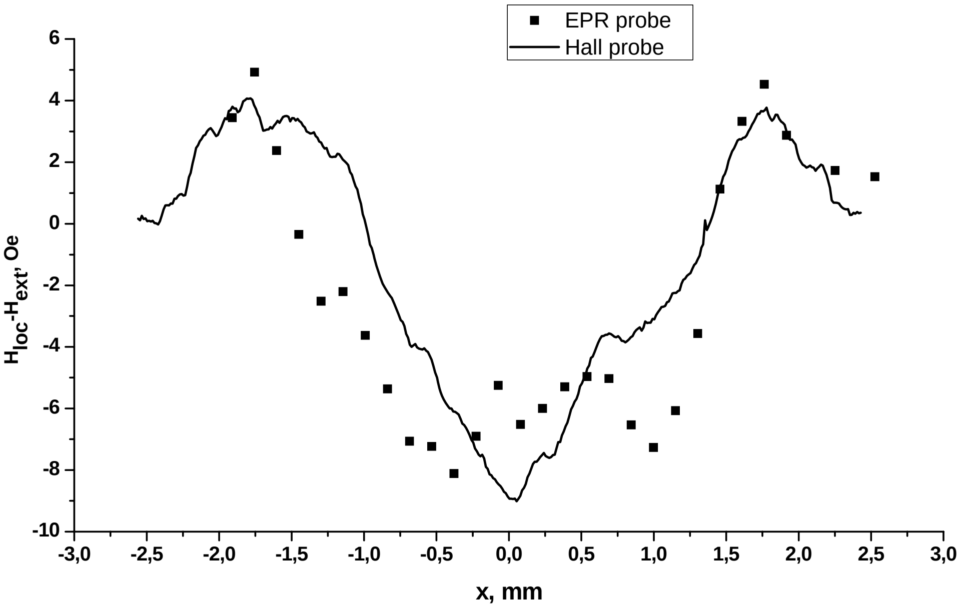

Fig.1. Magnetic flux profiles of B3 sample irradiated with the dose of $3 \cdot 10^{13}$ Co^+/cm^2 measured by means of EPR probe (dots) and Hall probe (solid line) at external field of 3000 Oe.

coordinate y of the probe position, as well as the distance from the probe to the sample surface z. The estimates of the critical current density were made using Eq. (1) and are given in Table 1.

Table 1. Critical current density estimated from the profile measurements, $T = 34$ K.

Sample	Irradiation dose, ion/cm^2	j_c, A/cm^2
B2	0	$1{,}7 \cdot 10^4$
B4	$5 \cdot 10^{11}$	$1{,}5 \cdot 10^4$
B3	$3 \cdot 10^{13}$	$3 \cdot 10^4$

In order to estimate the critical current density by the full-penetration field H^* the following procedures were applied. For EPR measurements a DPPH probe was placed at the center of the studied film. Then the sample was cooled from $T>T_c$ to the temperature of measurements in the field H_{cool}, close to the resonance field of free DPPH H_{R0}. ("Free" means "without a superconductor".) Then the EPR spectrum was recorded at this temperature upon sweeping the applied magnetic field from H_{cool} to $H>H_R$. H_R is the field where the resonance signal is observed. The EPR signal position depends on the magnetic field sweep value. So the shift of the DPPH resonance signal ($\Delta H_R = H_R - H_{R0}$) changes with HB_{cool}. The results of the shift measurements performed on the film B3 are depicted in Fig.2. The shift ΔH_R versus the cooling field demonstrates a nonmonotonous behavior. When the cooling field varies close to H_{R0} the shift of the DPPH signal depends strongly on the difference ($H_{R0} - H_{cool}$). Such behavior of ΔH_R is due to the modification of the magnetic field profile by a tangential component H_x near the surface of a superconductor [2]. As the difference ($H_{R0} - H_{cool}$)

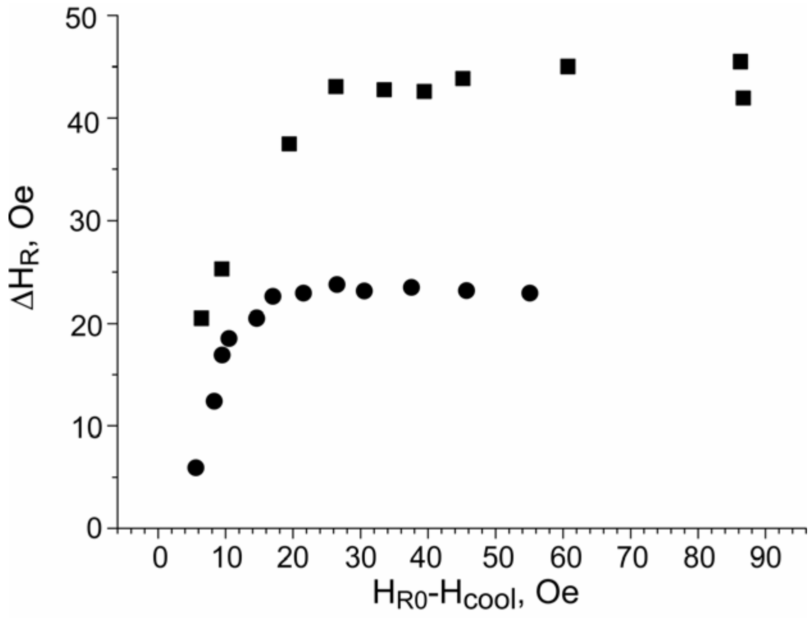

Fig.2. The dependence of DPPH resonance position on external cooling field for the film B3 irradiated with the dose of $3{\cdot}10^{12}$ Co^+/cm^2. The data are obtained at two temperatures: 25 K (■) and 34 K (●).

increases, the variation of the tangential field component decreases and becomes zero when the difference value reaches the full-penetration field H^*. Thereafter, the field profile is unchanged with the further variation of the field H_{cool}. This corresponds to the independence of the resonance signal shift on $(H_{R0} - H_{cool})$. In other words, the function $\Delta H_R(H_{R0} - H_{cool})$ comes to a plateau (Fig. 2). Thus, the value of the full-penetration field H^*, which is unambiguously connected with the critical current density [1], may be determined from the plot in Fig. 2.

According to the theoretical calculation [1] the relation between H^* and j_c is the following:

$$H^* \approx j_c \frac{2d}{\pi} \ln\left(\frac{2w}{d}\right). \tag{2}$$

Table 2. Critical current density determined from measurements by EPR and Hall probe at $T = 34$ K, $H = 3$ kOe.

Sample	Irradiation dose, ion/cm^2	EPR probe		Hall probe	
		H^*, Oe	j_c, A/cm^2	H^*, Oe	j_c, A/cm^2
B1	$3{\cdot}10^{12}$	21	$2.4{\cdot}10^5$	No data	No data
B2	As prepared	No data	No data	18	$2.1{\cdot}10^5$
B3	$3{\cdot}10^{13}$	26	$3.1{\cdot}10^5$	No data	No data
B4	$5{\cdot}10^{11}$	20	$2.3{\cdot}10^5$	19	$2.2{\cdot}10^5$
B5	As prepared	20	$2.3{\cdot}10^5$	17	$2.1{\cdot}10^5$

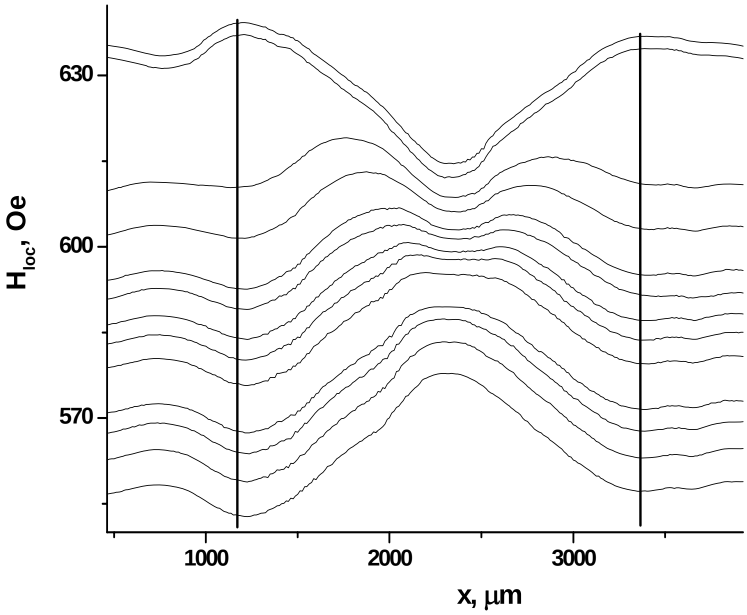

Fig.3. Variation of the magnetic flux profile of B2 sample as the full-penetration field changes. The sample's edges are indicated with solid lines.

Here d is the thickness of a superconducting film and w is its width. With the values of the full-penetration field and the film dimensions one can uniquely determine the critical current density using the above formula. It should be noted that the full-penetration field, as well as the critical current density, is temperature dependent. We have compared the critical current density of samples before and after irradiation at the fixed temperature of 34 K.

For determination of the full-penetration field by means of Hall probe measurements, the sample was again cooled in the zero external field from $T > T_c$ to the temperature of measurements. Then the starting magnetic field H_{start} was applied and the magnetic flux profile was recorded (Fig. 3). The magnetic field intensity was gradually reduced by steps of 5-10 Oe to the value of H_{final}, at which the shape of magnetic flux profile ceases to change. The full-penetration field was determined as $H^* = (H_{start} - H_{final})/2$.

The results of measurements of the full-penetration field by EPR and Hall probes and the estimates of the critical current density by Eq. (2) are summarized in Table 2. One can notice that H^* and j_c increases with higher implantation doses.

Thus, at the present stage of our studies it has been revealed that low-energy irradiation of superconducting thin films with medium-mass ions with a dose of about 10P^{13} ion/cm^{2} results in increase of the absolute value of the critical current density. This effect is due to the formation of radiation defects in the form of separated amorphous regions of about 10-15 nm in size. These radiation-induced defects appear to be effective pinning centers.

References

[1] Brandt E.H.: Phys. Rev. B **54**, 4246 (1996)

[2] Khasanov R., Talanov Yu., Vashakidze Y., Teitelbaum G.: Physica C **242**, 333 (1995)

Copper NQR Studies of Ag-doped Ternary Sulfide $Cu_{12}As_4S_{13}$ (Tennantite)

R.R. Gainov[1)], A.Yu. Orlova[1)], A.V. Dooglav[1)], I.N. Pen'kov[1)], N.N. Mozgova[2)]

[1)]Kazan State University, 420008, Kremlevskaya str., 18, Kazan, Russia.
[2)]Institute of Geology and Mineralogy, Russian Academy of Science, 119017, Moscow, Russia

e-mail: ramil.gainov@ksu.ru

Introduction

Tennantite is the representative of the *tetrahedrite*-group compounds, this family also called *fahlerz* or *fahlore*. Being one of the sources of economically important metals (Cu, Zn, Ag, Au and others), sensitive to physical-chemical conditions of ore-formation and having original crystal structure, these materials gave rise to numerous experimental and theoretical studies concerning their crystal chemistry (see [1], and references therein). However, in spite of intensive research during a long time (beginning from 18th century), many peculiarities of these compounds, their structure and properties haven't been clarified well enough. Thus, researchers are still concentrating their attention on the copper ions valence state and their distribution in the structure; lattice dynamics and its transport properties, isomorphous capacity of natural compounds.

In this report, we present the studies of ^{63,65}Cu NQR in natural crystal of Ag-doped tennantite in the temperature range 4,2 – 60 K. We found anomalies in the temperature dependences of nuclear spin-lattice relaxation (NSLR) rate T_1^{-1} and nuclear spin-echo decay (NSED) rate T_2^{-1}. The obtained data are interpreted from the viewpoint of internal motions in the structure of tennantite. Thereupon some peculiarities of tennantite crystal structure and its physical properties are considered.

Crystal-chemistry.

The composition of tetrahedrite-based compounds is usually expressed by a unified chemical formula $Cu(I)_{10}Cu(II)_2X_4S_{13}$, where Cu(I)/Cu(II) are monovalent/divalent copper, X – semimetal atoms. The main minerals of this family are tennantite (X = As) and tetrahedrite (X = Sb). Since natural compounds show a certain composition range owing to different impurities (Zn, Fe, Ag, Hg and others), the more commonly used chemical formula for natural tetrahedrite-group compounds is $(Cu,Ag)_{10}(Cu,Fe,Zn,Hg)_2(Sb,As)_4S_{13}$.

The elementary cell of tetrahedrite-group compounds has a cubic symmetry corresponding to a T_d^6-I43m; Z=2 [2-4]. The crystal structure can be presented as the framework formed by the $[Cu(I)S_4]$-tetrahedrons, which are turned to one direction and jointed by vertexes (Fig. 1) [1]. In such combination the framework possesses interstices ("lanterns") in the form of three-dimensional twelve-apical polyhedron, sometimes referred to as "laves polyhedron" (Fig. 1). Each laves polyhedron contains six $[CuS_3]$-triangles. These triangles form a three-dimensional propeller with only one common apex – central sulfur atom S_2 (Fig. 1). The rest two sulfur apexes of each $[CuS_3]$-"vane" concurrently represent the vertexes of laves polyhedron. It is proposed that active valence of copper atoms in laves polyhedron have different value within the ratio Cu(I):Cu(II)=4:2 [1, 5]. Semimetal atoms, Sb and As, are arranged over the edges of laves polyhedron. In natural samples the tetrahedral coppers are partially substituted for impurity metals (Zn, Fe, Ag, Hg). The average interatomic distances in tennantite are reported in [2].

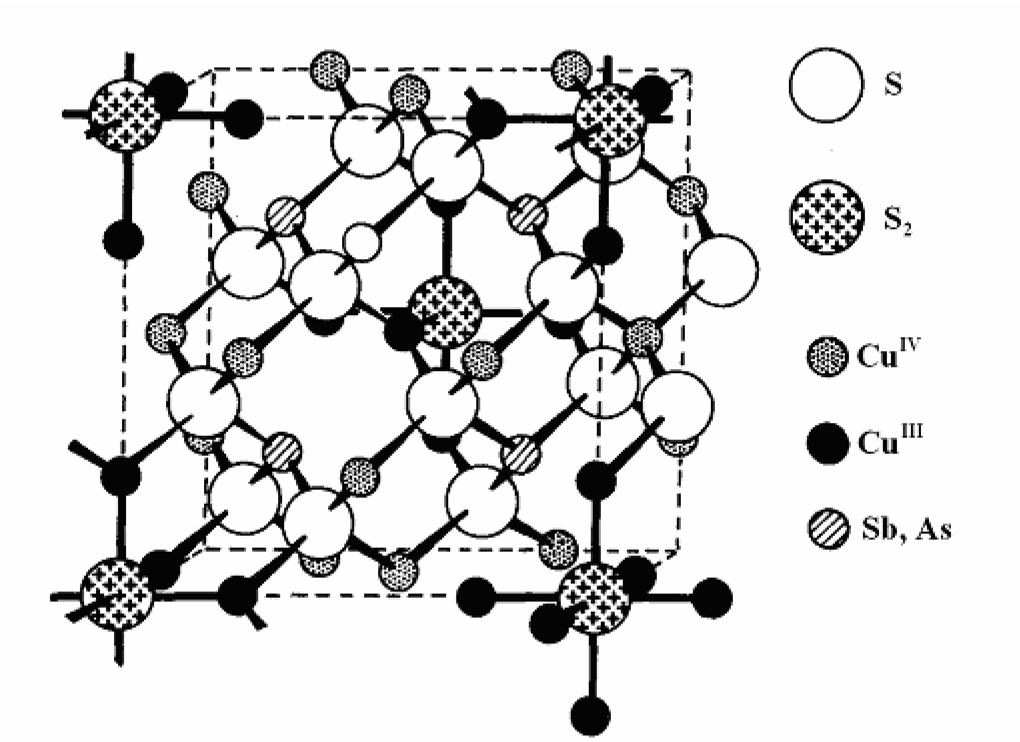

Fig. 1. The cell of tetrahedrite-group compounds. Triangular and tetrahedral coordinated copper atoms are signed as Cu^{III} and Cu^{IV}, respectively. The central sulfur atom in Cu_6S_{13} cluster is signed as S_2.

Experimental part

The natural sample of tennantite, originating from Berezovskii gold-ore deposit (Middle Ural, Russia), was used in this study. The sample was in the form of polycrystalline aggregate and had iron–black color. Its phase homogeneity and tennantite structure were confirmed by X-ray diffractometry. The chemical composition of tennantite sample under study is presented by the formulae: $(Cu_{10,04}Ag_{0,08})(Zn_{1,17}Fe_{0,94}Hg_{0,03})[As_{3,29}Sb_{0,98}]S_{12,44}$ (we denote this sample as ***B***). For comparison, we show *T*-dependences of nuclear relaxation rates in another tennantite $Cu_{10,57}(Zn_{1,10},Fe_{0,69})[As_{3,50},Sb_{0,44}]S_{12,70}$ (sample ***A***), which was studied earlier [6]. The NQR spectra of $^{63,65}Cu$ and nuclear relaxation were measured at T=4.2-65 K by a standard pulsed NQR method. For better penetration of the high-frequency magnetic field the sample was crushed in a mortar to a particle size of about 30 μm and packed in epoxy resin.

Results and discussions

The NQR resonance lines for both ^{63}Cu and ^{65}Cu isotopes were observed, with the NQR frequency ratio $F_Q(^{63}Cu)/F_Q(^{65}Cu) = 1,081$ consistent with the ratio of nuclear quadrupole moments $Q(^{63}Cu)/Q(^{65}Cu)$. The presence of only one spectral line for both copper isotopes permits to attribute NQR spectra to the crystallographically single site of copper nuclei. As a rule, the $^{63,65}Cu$ NQR signals pertain to monovalent (diamagnetic) copper nuclei Cu(I) [7]. The monovalent copper atoms in tennantite are located at both the tetrahedral-based framework and Cu_6S_{13} clusters. There is no electric field gradient (EFG) at the sites with cubic local symmetry [8, 9]. This case is realized for the tetrahedral Cu(I) sites in diamagnetic framework, so only trigonal planar copper nuclei in clusters can serve as resonance centers exhibiting NQR.

The temperature dependence of NSLR rate $1/T_1$ is shown in Fig.2a. This parameter shows pronounced peak near 24 K. Although the NSED rate $1/T_2$ is almost independent of temperature above 75 K, there are strong peaks near 14 K (Fig.2b).

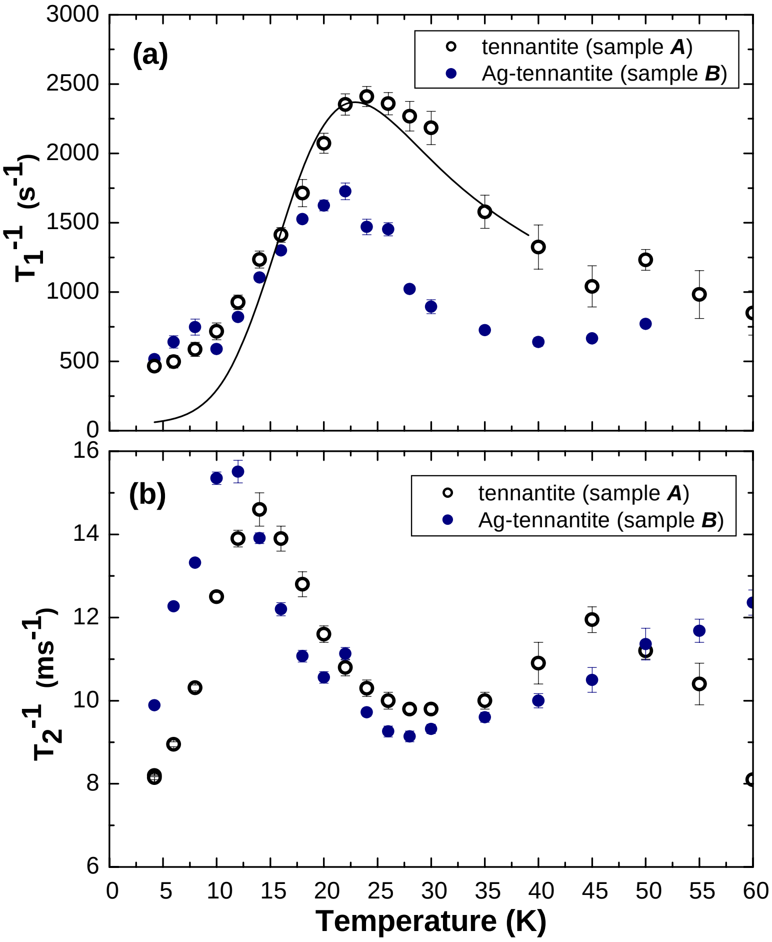

Fig.2. (a) The temperature dependence of the nuclear spin-lattice relaxation rates $1/T_1$ for ^{63}Cu, the curve shows a fit by (1) and (3), which predicts the activation energy of 65 K; (b) the temperature dependence of the nuclear spin-echo decay rates $1/T_2$ for ^{63}Cu

The peak in NSLR rate at 24 K points to the presence of field fluctuations [10-12] acting in our case on copper nuclear sites. As it is known, the NSLR rate in case of relaxation due to fluctuating fields is determined by the correlation time τ_C of fluctuations:

$$\left(\frac{1}{T_1}\right)_{fluc} = \frac{\Delta^2 \tau_C}{1+\omega_n^2 \tau_C^2}, \tag{1}$$

where Δ is a mean amplitude of fluctuations and ω_n is the NQR frequency. If Δ is constant but τ_C depends on temperature, $1/T_1$ attains the maximum value when $\omega_n \tau_C = 1$. Thus the peak of $1/T_1$ is naturally understood due to an increase of τ_C with decreasing temperature, i.e., slowing of the fluctuations at low temperatures. Usually, the correlation time is determined by a potential barrier according to Arrhenius law,

$$\tau_C = \tau_0 \exp\left(\frac{E_{ACT}}{T}\right), \tag{2}$$

where E_{ACT} is an activation energy. In general, there might exist two contributions to the NSLR of the ^{63,65}Cu nuclei:

$$\frac{1}{T_1}=\left(\frac{1}{T_1}\right)_{fluc}+\left(\frac{1}{T_1}\right)_{\mathrm{bg}}, \tag{3}$$

the first term reflecting contributions due to fluctuations, and the second one representing contribution typical for relaxation via the charge carriers. In case of a semiconductor [10],

$$\left(\frac{1}{T_1}\right)_{\mathrm{bg}}=A\cdot\sqrt{T}, \tag{4}$$

where A is constant. We applied equation (3) to fit the experimental data (sample ***A***) taking into account (1) together with (2) and (4). The best fits were obtained with the following parameters: $\Delta/2\pi = (128 \pm 4)$ kHz, $E_{ACT} = (65 \pm 3)$ K, $\tau_0 = 4\cdot10^{-10}$ sec, $A = 20$ $\mathrm{K}^{-1/2}\cdot\mathrm{sec}^{-1}$ (Fig.2a). The NSED rate takes the maximum value when $\Delta\cdot\tau_C \sim 1$ [11]. Since Δ is 2 orders of magnitude smaller than ω_n, gradual slowing of the fluctuations accounts for the fact that the peak in $1/T_2$ occurs at lower temperature than the peak in $1/T_1$ (Fig.2b). Thus, the observed peaks in nuclear relaxation rates $1/T_1$ at 24 K and $1/T_2$ at 14 K are correlated and show the existence of internal motions in the crystal lattice.

The possible nature of field fluctuations in the structure of tennantite is presented in earlier studies [6]. We supposed that Laves polyhedron Cu_6S_{13} represents the mixed-valence cluster, similar to some extent to systems, described by Eremin and co-workers [13]. Experimental data were analyzed from the viewpoint of inhomogeneous electron distribution of Cu(II) in the Cu_6S_{13} cluster. The basic aspect in this consideration is that the electronic spins of Cu(II) at high-T are delocalized, whereas at low-T (namely, T<65 K) spins are frozen near Cu sites in the form of spin-glass like constitution.

However, since the sample ***A*** contains also impurities Fe, Zn (besides paramagnetic Cu(II)), it would be expedient to confirm experimentally that the revealed data are caused exactly by Cu(II). The main goal of this study is reexamination of T-dependences of nuclear relaxation rates in another sample of tennantite (***B***) with amount of impurities, which differs from those in sample ***A***. As can see in Fig.2, the partial substitutions in sample ***B*** of magnetic Fe on non-magnetic Ag and Hg does not lead to appreciable change of T-dependences of nuclear relaxation rates $1/T_1$ and $1/T_2$. These facts, taking into account the high sensitivity of quadrupole interactions to any changes in the nearest crystal environment of quadrupole nucleus, indicate that the observed low-T peculiarities are not connected to different impurities or imperfections, but reflect the intrinsic properties of tetrahedrite-group compounds and are mainly determined by divalent ions Cu(II).

This work was partly supported by Russian Foundation for Basic Research under Grant 06-02-171-97-a.

References

[1] N.N. Mozgova, A.I. Tsepin, Fahlore, Nauka, Moscow (1983).

[2] B.J. Wuench, Y. Takeuchi, W. Novacky, Z. Kristallogr. 123 (1966) 1.

[3] J. Lima-de-Faria, Croat. Chem. Acta 72 (1999) 705.

[4] E. Makovicky, B.J. Skinner, Can. Mineral. 17 (1979) 619.

[5] R.A.D. Pattrick, G. van der Laan, V.J. Vaughan, C.M.B. Henderson, Phys. Chem. Mineral. 20 (1993) 395.

[6] R.R. Gainov, A.V. Dooglav, I.N. Pen'kov, Solid State Commun. 140 (2006) 544

[7] T.J. Bastow, I.D. Campbell, H.J. Whitfield, Solid State Commun. 33 (1980) 399.

[8] V.S. Grechishkin, Nuclear quadrupole interactions in solids, Nauka, Moscow (1973).

[9] C.P. Slichter, Principles of magnetic resonance, Springer-Verlag (1980).

[10] A.A. Abragam, Principles of Nuclear Magnetism, Clarendon Press, Oxford (1961).

[11] S. Fujiyama, M. Takigawa, S. Horii, Phys. Rev. Lett. 90 (2003) 147004.

[12] N. Bloembergen, E.M. Purcell, and R.V. Pound, Phys. Rev. 73 (1948) 679.

[13] M.V. Eremin, S.I. Nikitin, S.Yu. Prosvirnin, Appl. Magn. Reson. 23 (2002) 97.

ESR Studies of Solid Substrates for the Dynamic Polarization of the Noble Gases

A.A. Rodionov[1)], G.V. Mamin[1)], N. Mulders[2)], M.S. Tagirov[1)]

[1)]Department of Physics, Kazan State University, Kazan, Russia
[2)]Department of Physics and Astronomy, University of Delaware, Newark, DE, USA

e-mail: rodionovshurik@yandex.ru

One of the perspective methods of noble gas production can be the dynamic polarization of the noble gas. Solid substance with developed surface and big quantity of absorbed noble gas atoms need for the realization of the method. In this case the polarization can transfer from the electron subsystem of the solid substance to the nuclear subsystem of the gas. The main problem now is finding of solid substance with best properties to the method of dynamic polarization of the gas.

The carbonizate "astronium" was studied by us as the perspective solid substrate for the dynamic polarization of the noble gas [1]. The obtained results showed the possibility of the realization of dynamic polarization method.

Aerogel of silicon dioxide is the one more solid substrate, which seems to be perspective for the dynamic polarization method. It is also the perspective porous disordered media for ^{3}He investigation. Besides its pores and chains of SiO_2 the external magnetic fields can influence on behavior of liquid ^{3}He. Paramagnetic center creates the magnetic field around itself, the behaviors of liquid ^{3}He near the surface of aerogel may change, and this may entail the changes of ^{3}He in volume.

X-ray radiation has been used to create paramagnetic centers in aerogel [2]. The ESR spectra of these paramagnetic centers has been measured on the standard X-band ESR spectrometer ESP-300 (Bruker). The aerogels with porosity 95% (aerogel-95) and 98% (aerogel-98) were studied. The aerogel-95 had the protective film on the surface, which gave it the hydrophilic properties.

There are three lines in ESR spectra of the samples of aerogel-98 and annealed samples of aerogel-95 after the irradiation (Fig. 1). The narrow line with g-factor equal 2.0035 is ascribed to the E'-centers [3] and the two lines with inhomogeneous broadening are ascribed to the superhyperfine structure (SHF) ($T_{\perp}=5.1$ mT, $T_{\|}=3.7$ mT) of paramagnetic centers in the

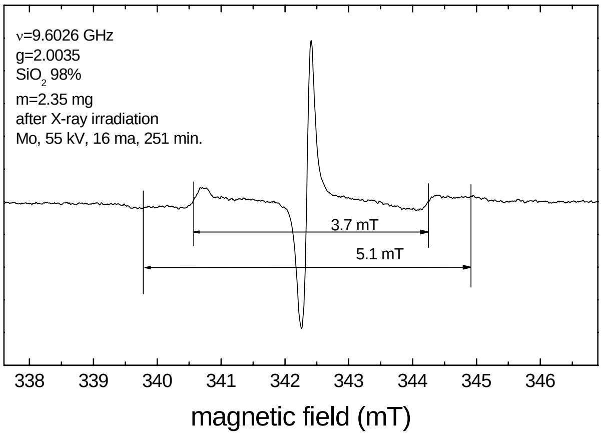

Fig.1 The ESR spectrum of aerogel-98

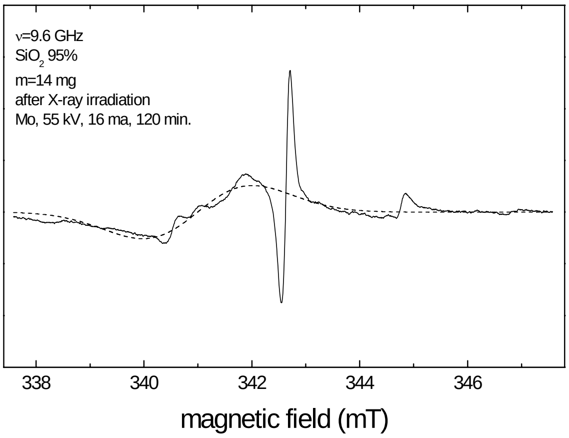

Fig.2 The ESR spectrum of unannealed aerogel-95

CH_2^- or OH^- radicals. Also the broad line (g=2.01) was observed in the unannealed samples of aerogel (Fig. 2), these paramagnetic centers were named “peroxy”- centers [3].

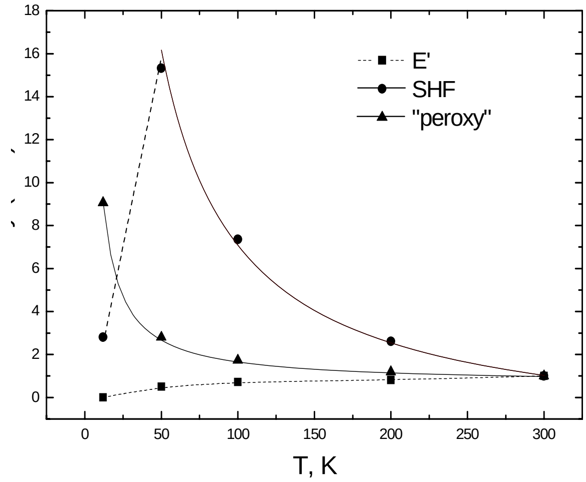

Fig.3 The temperature dependence of ESR signal’s intensities

The temperature dependence of ESR signal’s intensities has been measured (Fig. 3). The difference between the temperature behaviors of the intensities of E’-signals and signal with SHF proves the assumption, that this signals correspond to different types of paramagnetic centers.

To determine the nature of the “peroxy”- centers the annealing of the samples of aerogel-95 has been made (Fig. 4). The samples were annealed 10 minutes at the temperatures 100-500°C with fore-vacuum pump. When the temperature of annealing increased, the intensity of the signal of “peroxy”- centers decreased faster, than the intensities of other centers. Also there was not signal of “peroxy”- centers in the samples, which were annealed before the irradiation. This facts allowed to suppose, that “peroxy”- centers occurred due to the O_2 and H_2O surface film in unannealed aerogel-95.

The decay of paramagnetic centers in aerogel was studied during the two month at the room temperature (Fig. 5). There are the fast process and the slow process of decay. In the beginning the concentration of the paramagnetic centers decreased in a half in three days,

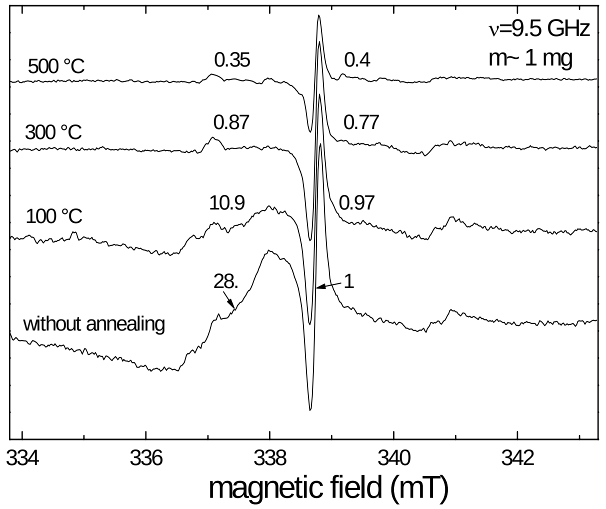

Fig.4 The ESR spectra of aerogel-95 after the annealing

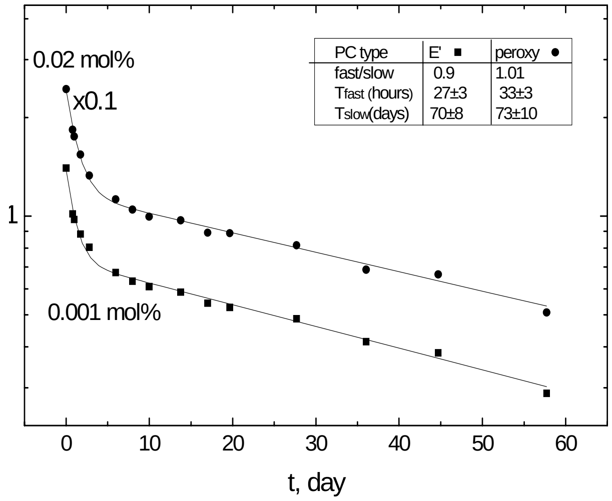

Fig. 5 The decay of paramagnetic centers in aerogel

after that decay process became slow. The characteristic times of the exponential decay of all types of paramagnetic centers are 30 hours for the fast process and 70 days for the slow process.

The activation energies were estimated for all types of paramagnetic centers. For the “peroxy”-centers this value amount 900±100 °C, for the E’-centers and the centers with hyperfine structure this value amount 2450±50 C.

The obtained data allow studying the behaviors of superfluid as well as normal ^{3}He according to concentration of paramagnetic centers in aerogel.

References

[1] Mamin, G.V. The surface effects influence on magnetic resonance in carbonizate / G.V. Mamin, A.A. Rodionov, M.S. Tagirov, D.A. Tayursky, B. Odintsov // X international Youth Scientific School “New aspects of magnetic resonance application”. – Kazan, 2006. – C. 47.

[2] Kazansky, By. V. Radiation-induced processes on the silica-gel surface / By. V. Kazansky, G.B. Pariisky, V.V. Voevodsky // Discuss. Faraday Soc. – 1961. - Vol. 31. – P. 203.

[3] Ikea, M. New Aplications of Electon Spin Resonance. Dating, Dosimetry and Microscopy / M. Ikea - Singapore: World Scientific Publishing Co, 1993. – 417 P.

Paramagnetic Monitoring of Electrochemical Reactions

M.I. Valitov[1)], K.V. Kholin[1)], M.K. Kadirov[2)], Yu.G. Budnikova[2)]

[1)]Kazan State University, 420008, 18 Kremlyovskaya St., Kazan, Russia
[2)]Institute of organic and physical chemistry KSC RAS, 420088, 8 Arbuzov str., Russia

e-mail: vmurad_5@mail.ru

Electrochemical methods in not mixible solution in which diffusion appears a prevailing kind of mass transfer, are the most useful and accessible methods of research of electrode processes with participation of organic compounds. Voltamperometry (VA) is especially noticeable because of its possibility of registration of depolarization or oxidation potentials and an estimation of reversibility of these processes. However dependence of a current on the applied potential is the generalized characteristic including a charging double-layer current, impurity currents and Faraday currents of the subsystems making the investigated substratum. Quite often it is difficult to determine what kind of process the half-waves belong to.

Products or intermediates, formed during reaction of organic substances on an electrode, quite often are paramagnetic; therefore the combination of the electrochemical equipment with the ESR spectrometer allows receiving the unique information about the processes on an electrode and in the bulk solution. ESR spectrum is extremely specific and almost unequivocally it characterises a paramagnetic substratum to which belongs.

The Hardware-software complex for research electrolysis ESR unites two classical methods - electrochemistry and ESR, and the uniting links are an original three-electrode cell of electrolysis ESR (El-ESR) for research of paramagnetic particles and the computer with the interface connected to the electrochemical installation, consisting of a programmer with a potentiostat and ESR spectrometer (Fig. 1). It allows to register automatically in a digital form usual VA curves and curves when along with dependence of ESR signal strength on potential s (E), its first-order derivative s’(E) is fixed also. s(E) is proportional to a transferred charge, and s’(E) - to a current through a cell, therefore distinctive feature of registration s’ (E) in comparison with a record only of s (E) is comparability of the first one to a curve i (E), received during VA. If initial change s (E) is connected with heterogeneous transfer of the first electron with formation of a paramagnetic product s’ (E) will repeat i (E) only with the difference it is the characteristic describing Faraday processes more precisely, since s’ (E), unlike i(E), it is not subject to influence of charging currents of a double-layer and impurity currents.

In measurement mode of a spectrum the computer gives out on digital-to-analogue converters of the module data for linear sweep of a current of a magnet of a spectrometer with the set rate of change and registers the signals measured ADC of the module on set channels. DAC signals are summarized in an interface card, are exposed to controlled analogue filtration and are transferred to the scheme of comparison which compares them to voltage on the basic resistor of a current of a magnet and operates output stages of control of a current. According to the set spectrum width is selected a range of scan of eight possible, differing in a step of change of a field. As a result of it the spectral region of the set width with the set position of the centre is registered. The results of measurement are brought into Excel table and displayed on the graphic. It is possible to work with affixment of a reference point of a spectrum. Thus on the chosen channel of registration up to two consecutive events are fixed, for example ESR signal exceeds the preset threshold, and then becomes less than other set level. The reference point can be within a registered spectrum as well as outside of it, but in a scan range.

In a measurement mode of volt-ampere graphics field scan is not used: the field is set on a maximum of ESR signal of the necessary spectrum line. Potential scan is set by the programmer. This signal after transformation by the potentiostat moves on a cell with investigated depolarizer, and ESR method simultaneously registers the response to changing of potential. Potential and current signals of potentiostat in the interface are transformed to the digital form and registered in Excel table and on the graphic together with ESR signal. During the subsequent processing the first-order derivative of ESR signal s'(E) can be received.

Cell characteristics of electrolysis- ESR give a chance to use for one experiment only 0,5 ml of a solution of depolarizer, to do air exhaust by the method of repeated freezing in liquid nitrogen - pumping out - defrosting and to fill a cell with inert atmosphere.

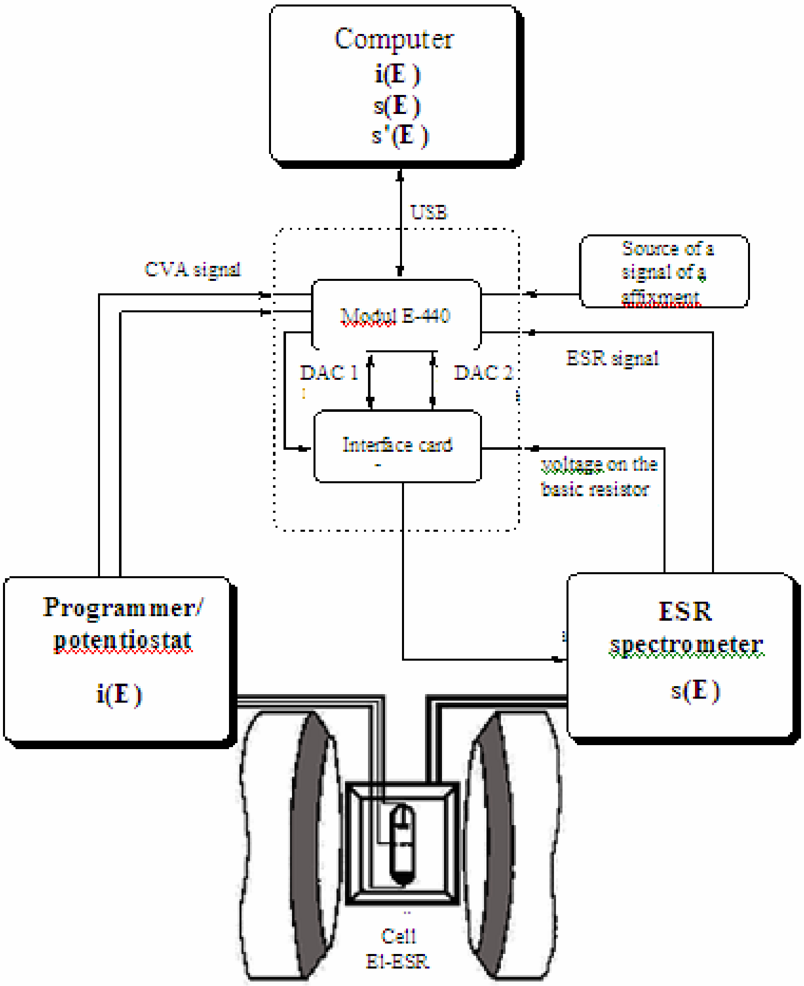

Fig. 1. The block diagram of a hardware-software complex

One more advantage of PMER method is its sensitivity to magnetic properties of polyspin systems and to exchange interactions between their substrates during electrochemical transformations. All this allows hoping, that, we can get the powerful tool for research of the complex molecular systems possessing magnetic properties.

Excellent identification possibilities of PMER is illustrated on an example of linear voltamperometry (LVA) of bivalent complex of copper Cu(II) with 4 (2 '-oksopropiliden)-2,2,5,5-tetramethylene-3- imidazoliden -1-oxyl (L**)** at overlaying of linearly changing potential. ESR spectrum nitroxyl radical LH in acetonitril (the first-order derivative of signal strength we will designate as s'_L) at 293 K has the following magnetic-resonant parametres: g

= 2.0061, and (N) = 1,44 мT. LCuL - three-spin system with considerable exchange interaction between the paramagnetic centres that leads to abridgement of time of an electronic relaxation of the radical centres of ligands till an electronic relaxation of an ion of copper. As a result, we can observe the generalised line (the first-order derivative of intensity - s'_{LCuL}) about 70 Gs by width with the weighted average g-factor equal to 2,037.

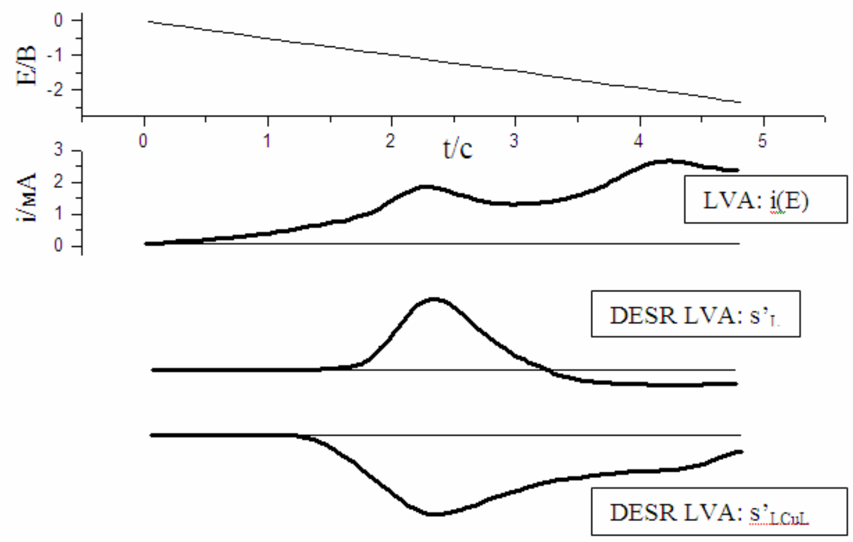

Fig.2. LVA i(E), DESR LVA s'_{LCuL} and DESR LVA s'_L complex of copper Cu(II) with 4 (2 '-oksopropiliden)-2,2,5,5-tetramethylene-3- imidazoliden -1-oxyl (L) against the background of $5 \cdot 10^{-2}$ Et_4NClO_4; sweep rate of potential E(t) 0,5 V/s; 293 K.

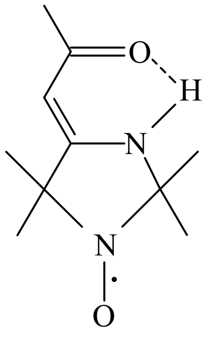

L

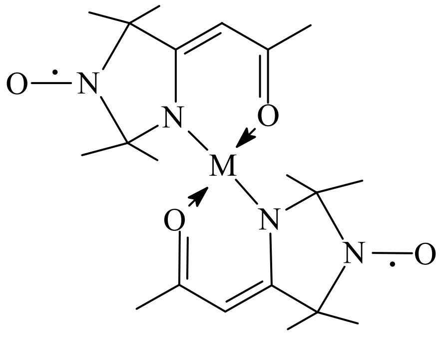

LCuL

At potentials of the first peak (Fig. 2) s'_{LCuL} decreases and synchronously s'_L increases, that is the copper ion passes to diamagnetic univalent condition without complex destruction. Increase of s'_L is caused by disappearance of exchange interaction with a copper ion, and, accordingly, reappearance of ESR signals of ligand. Changes at potentials of next peak are coordinated with the mechanism of stagewise reduction of ligands. Speed of disappearance of s'_L because of reduction of ligands exceeds growth rate of a signal because of reduction of Cu (II), and the curve detected by an electronic paramagnetic resonance (DESR) LVA of ligands goes below a zero line. Thus essential change in character of DESR LVA s'_{LCuL} is not observed. In this way, it is possible to ascertain, that first wave of LVA of complex CuL_2 corresponds to reduction of a bivalent ion of copper to univalent, and on following waves the reduction of ligands takes place.

Application of Non-Linear Approximation for Electron Paramagnetic Resonance Signal Processing: *EPRMultiPeak* Software

A.A. Levantovsky, A.V. Komolkin

Saint Petersburg State University, 198504, Ulianovskaya st., 1, Petrodvorets, Saint Petersburg, Russia.

e-mail: levantovsky@mail.ru

Introduction

Electron paramagnetic resonance (EPR) is nondestructive analysis method of biological, medical objects, minerals and other. The spectrum of EPR is a sum of a number of single lines and groups of lines which have different shapes; the lines can overlap and/or collide. The aim of researcher is to single out separate lines and to find its parameters (position, amplitude, shape, width). In this paper the new spectrum analysis method and its implementation as graphical user interface (GUI) based application is suggested.

EPR spectrum analysis

For signal-to-noise ratio increase differential passing technique with double modulation is used in most spectrometers [1]. Therefore, the registered signal is the first derivative of EPR spectrum.

There are two basic line shape models (which are good for liquids): Gauss function and Lorentz function. Those functions differently agree with experimental spectrum lines of different samples. Spectrum lines of solids are asymmetric and have more complicated shape because of g-factor anisotropy.

For spectrum analysis special software is used. Those software ordinary come with spectrometers, are very expensive and can be used only with spectra, recorded on one type of spectrometers. Freeware software has lesser functionality. Some separate operations of spectrum analysis can be made with general-purpose mathematical software, e.g. MatLab, gnuplot, Origin, but it takes much time and may cause errors because of much handwork.

The aim of the effort is to develop techniques for separate lines determination and overlapping lines decomposition, and to implement it in user software with GUI.

Separate lines determination technique

Determination of separate line is finding its shape, position, amplitude and width. This can be made by non-linear approximation of experimental spectrum by corresponding function (Gauss function, Lorentz function, etc.) In this work Levenberg-Marquardt algorithm is used as universal. This algorithm is stable on most approximation functions and has reasonably convergence speed [2].

Overlapped lines decomposition technique

ESR spectrum can enclose partly overlapped lines. In this case the following technique can be used. On the first step the widest spectrum line is approximated. On the second step the obtained approximation function of first line is subtracted from the experimental spectrum and the difference is used for approximation of the second line. For increasing accuracy, the first spectrum line is to be approximated while as the approximation function of second line is subtracted from the experimental spectrum. With this iteration algorithm more than two overlapping lines can be separated.

For increasing accuracy of the approximation it is essential to approximate one line of the spectrum only on the part of the experimental spectrum, where contribution of other spectrum lines is negligible. This requires setting of the approximation interval for each spectrum line.

Implementation: *EPRMultiPeak* software

The outlined algorithm was implemented in Java language as the application *EPRMultiPeak* with GUI. Java is multiplatform interpreted programming language; therefore the application can be run on multiple operating systems [3]. It is very useful because different spectrometer's software is running on different operating systems.

Each line of the spectrum is presented as a curve component in application. After creation of the new curve component the user have to set initial conditions of the approximation function. This can be done by moving the approximation function near to the experimental line using mouse (fig. 1). On the next step user sets the one or more approximation interval for the line and run the approximation. When the approximation is done, the approximation function of new line can be subtracted from experimental spectrum and the other lines can be approximated.

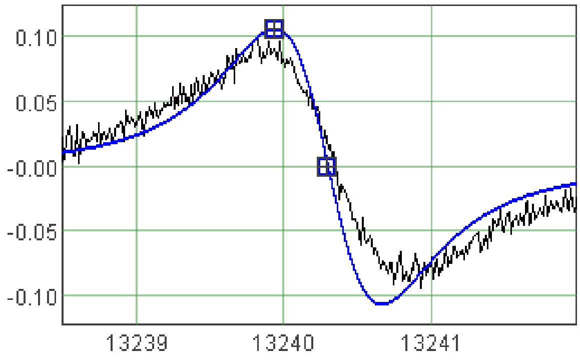

Fig.1 Initial conditions setting

The feature of the application is to evaluate the sum of all approximating functions which is approximates all spectrum. This sum can be compared with the experimental spectrum on one plot and the difference between experimental spectrum and the approximation sum (only noise in ideal) sum can be seen.

In current version of the application the following types of lines are implemented: derivative of Gauss and Lorentz function, Gauss multiplet, line function, and parabolic function. The two latter are used for trend removing on the first stage of analysis.

The application is able to import spectra, which was recorded on different spectrometers. It can be used not only for process EPR spectrum, but also for NMR spectrum and other.

Spectrum processing example

The functioning of application was tested on standard EPR spectrum of DPPH (di-phenyl-picrylhydrazyl), which spectrum line is good approximated by Lorentz function. The test showed agreement of the obtained line parameters with other sources and the right working of the application in simple case.

One of the processed spectra is the spectrum of archeological bone, which is shown on fig. 2. This spectrum consists of many lines. All components of approximation function are

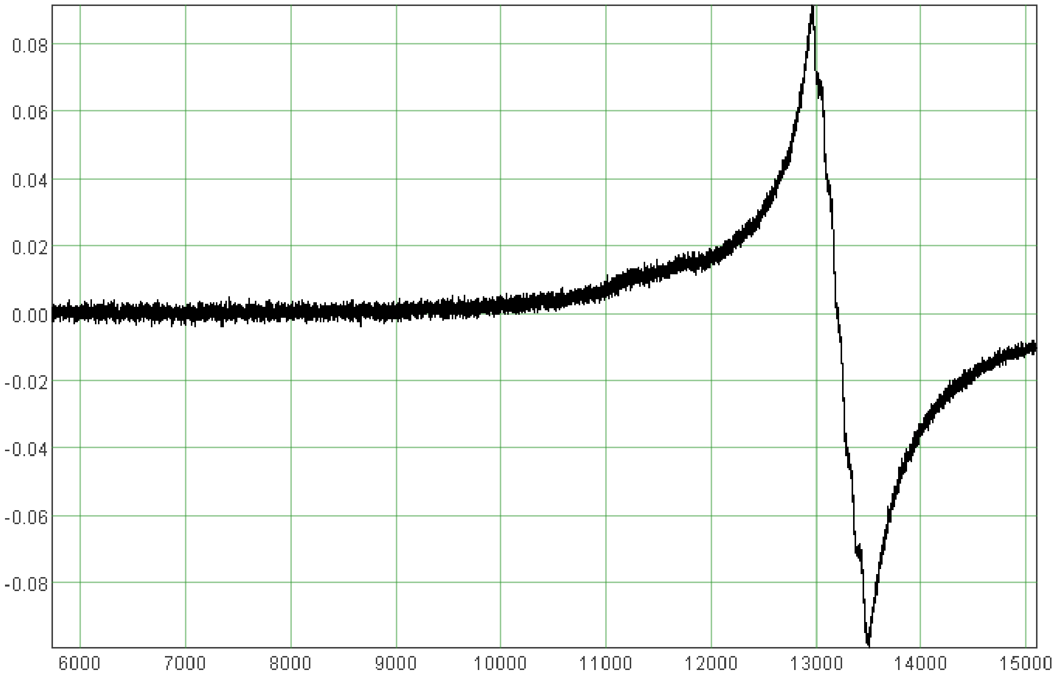

Fig.2. Bone spectrum

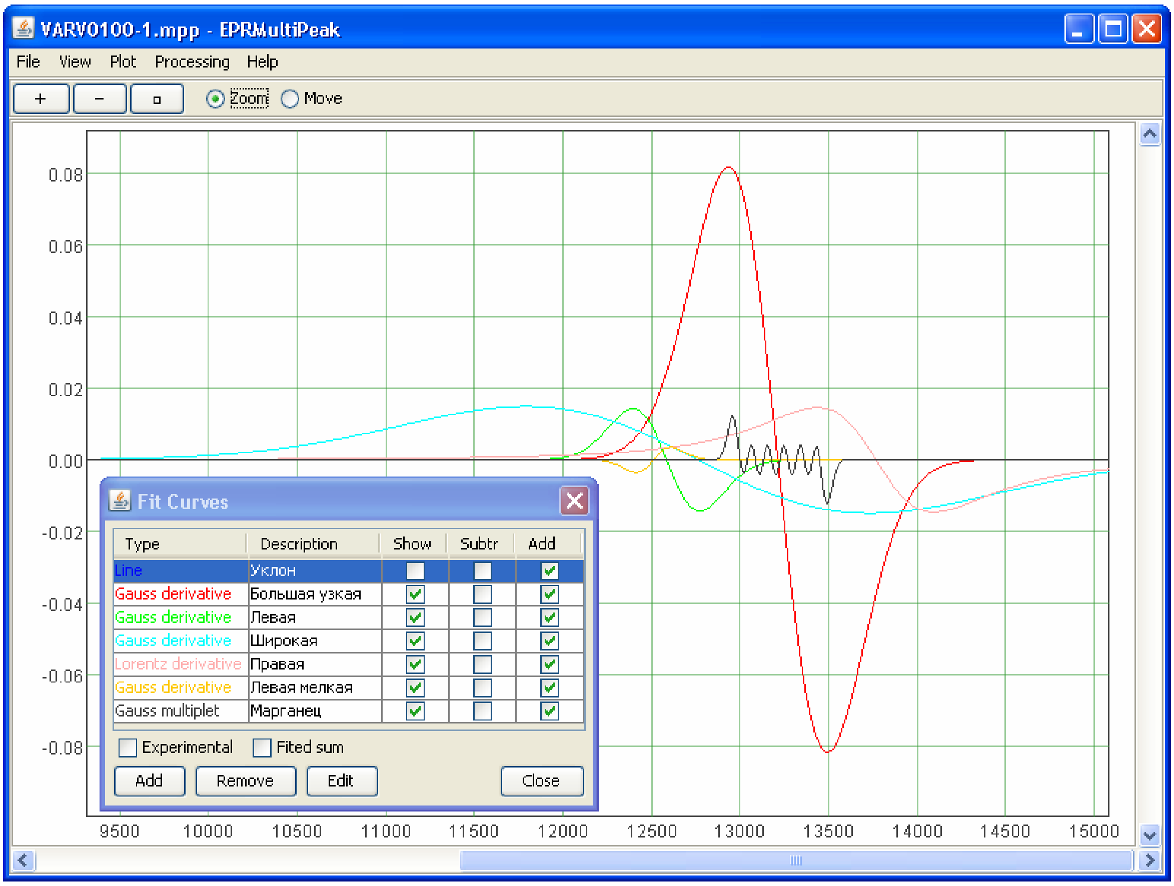

Type	Description	Show	Subtr	Add
Line	Уклон	☐	☐	☑
Gauss derivative	Большая узкая	☑	☐	☑
Gauss derivative	Левая	☑	☐	☑
Gauss derivative	Широкая	☑	☐	☑
Lorentz derivative	Правая	☑	☐	☑
Gauss derivative	Левая мелкая	☑	☐	☑
Gauss multiplet	Марганец	☑	☐	☑

☐ Experimental ☐ Fited sum

Fig.3 Approximation curves of bone spectrum and main window of the application

shown on fig. 3. Fig. 4 shows the sum of all approximation functions; this analytic function is approximation of full experimental spectrum.

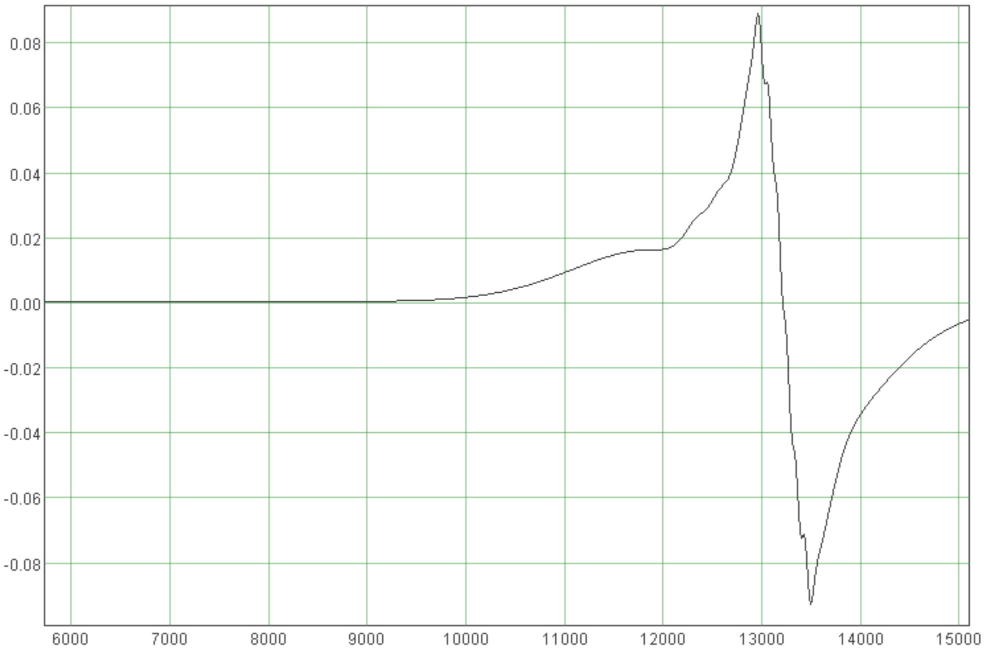

Fig.4. Approximation of bone spectrum

Conclusion

The new technique of EPR spectrum processing and its realization is proposed. The algorithm and the Java-application allow to process spectrum visually and very easy. The application was tested on several experimental spectrums.

In the current version of the application only Gauss and Lorents functions are implemented. It is planned to implement the Foight function and asymmetric lines for solid's spectrums.

References

[1] Charles P. Poole. Electron Spin Resonance. Comprehensive Treatise on Experimental Techniques. — Interscience Publishers a division of John Wiley & Sons, 1967.

[2] V.V. Nosatch. Solving approximation problems on personal computers. — Moscow, “MIKAP” Publisher, 1994 (in Russian).

[3] http://java.sun.com

New Approach to the Design of Real Time Controlling Software for the Automation of Mobile EPR Spectrometer

T.V. Popov, A.V. Komolkin

Saint-Petersburg State University, Physical Faculty, Department of Quantum Magnetic Phenomena. 198504, Ulianovskaya str., 3, Saint-Petersburg, Petrodvorets, Russia.

e-mail: timophey@rambler.ru, komolkin@esr.phys.spbu.ru

Introduction

Software for the controlling of electron paramagnetic resonance (EPR) spectrometer should fulfill several obligatory requirements. Most important requirements are linear scanning of magnetic field and spectral data recording in real time (RT). The most important wish to such software is friendly graphical user interface (GUI) for the controlling of spectrometer and data analysis and processing.

We developed new software for the automation of compact mobile EPR spectrometer “СЭПР-2”. The software works under operating system (OS) Linux in RT mode and provides GUI via X Window System (X11).

The key point of this work was to design two programs (“parallel processes” in terms of OS Linux) which interacts to each other via non-blocking message passing way and worked with different priority: one with RT priority for the hardware control and another with ordinary user priority for the handling of resource-intensive GUI.

Original software design

Initially the software was developed as one RT process which receives user commands through a GUI and controls spectrometer hardware via analog-to-digital and digital-to-analog converter (ADC and DAC) [1]. RT mode on the Linux platform is achieved with increase of a statically scheduling priority [2]. The graphical user interface is based on object-oriented C++ program language. As a graphical interface developing framework was chosen the latest version of cross-platform object-oriented C++ classes library *Qt 4.2* by Trolltech [3].

During an exploitation of software it was found out that there are delays in data acquisition and visible breaks during spectra drawing (simultaneously with data acquisition) on graphical screen. The reason of such delays is work of resource-intensive graphical library *Qt* which updates huge visual information content of the graphical window and sends commands to graphical server X11. While *Qt* library works in RT mode, the graphical server X11, which serves display and renovates contents on its screen, works with user priority. In this case X11 has no enough time to update screen.

We decided to divide entire automation program into two independent processes with a different scheduling priority: one for hardware control with RT priority and another for GUI handling with user priority. In addition to these two processes, graphical server X11 takes part in this work with user priority.

New approach: two processes

In OS Linux, process launched by superuser can change its scheduling priority to the highest static “real time” priority. In addition, such a process can capture their memory pages with command *mlockall()* to avoid swapping of memory. This way guarantees the shortest application response time to interruptions and events in contrast to standard "shared time" Linux scheduling mechanism [2].

Mechanism of a shared memory which is a part of inter process communication (Sun's IPC) is the most suitable tool to connect RT controlling process to user priority GUI. Thus the common structure in computer memory became the medium for interchange of controlling commands and spectral data between two processes. Reading and writing data are independent and asynchronous operations, so the processes can communicate to each other without blocking by counterparts. Access to shared memory is as fast as access to private memory of the process.

The diagram in Fig. 1 shows structure and connections (commands and data flow) of the different parts of the EPR hardware and controlling software. Two main parts, RT mode controlling process *RTserver* and user priority GUI process *SEPR*, use shared memory to interchange data and commands. Controlling process interacts with the ADC-DAC device driver through the high-level object-oriented interface *daqdevice*. The interface *daqdevice* uses system calls to communicate the device driver. The interface has suitable functions for the changing of electric current in spectrometer's electromagnet, measuring the voltage of EPR signal, and testing some critical voltages in the spectrometer. Shared memory structure is readable and writeable for either controlling process or user interface. This structure has an

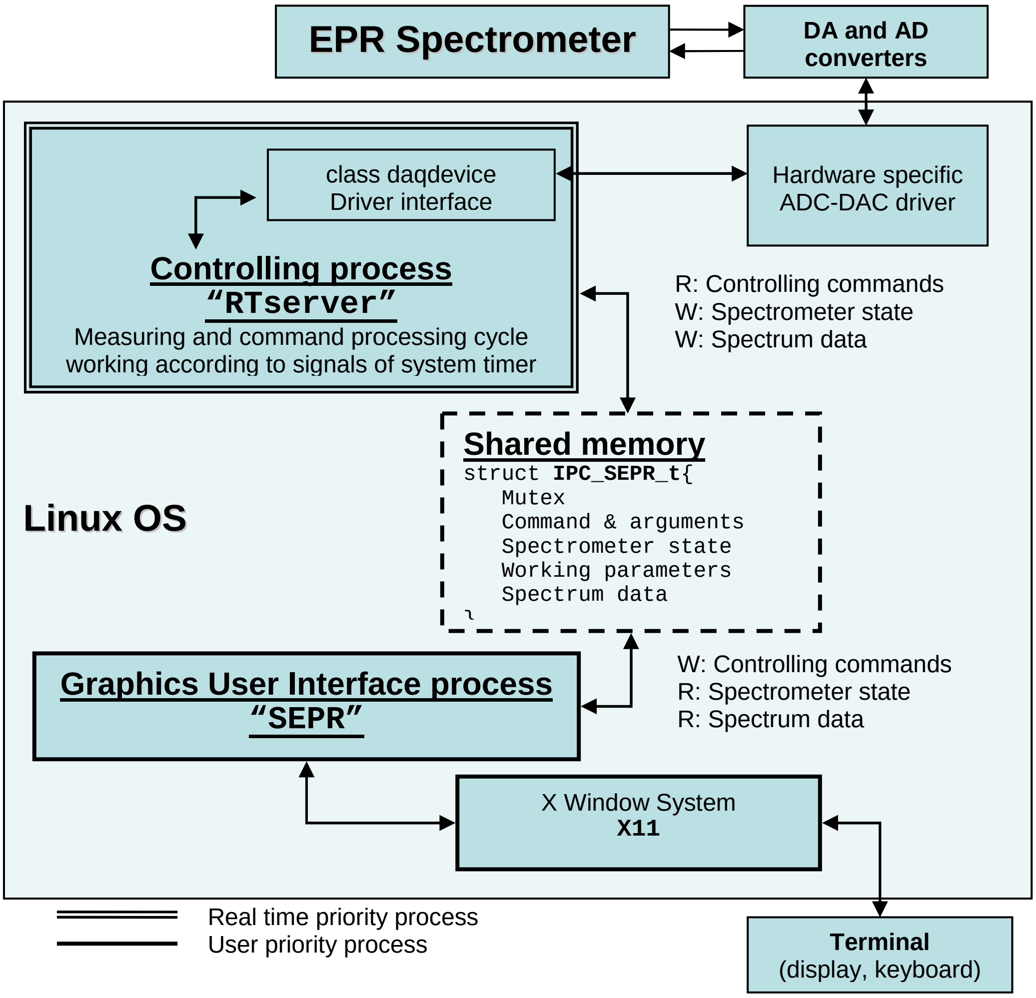

Fig.1. Block diagram of the spectrometer's software. Operations are: R – reading, W – writing.

internal flag (mutex) which helps to synchronize data exchange. The *SEPR* process organize window on the screen with all necessary control and status fields to show the most important operational characteristics of the spectrometer. Graphical library interact directly with X11 which shows all visual content on a display.

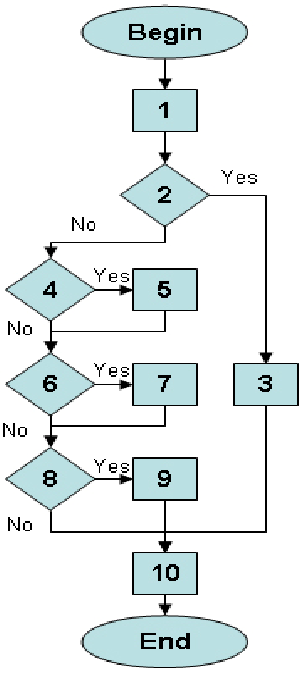

Fig.2 See explanation in text

Design of *RTserver*

The spectrometer works in several modes: 1) survey mode for the rapid recording of spectrum in oscilloscope (continuous) way; 2) production mode for the precise signal recording for the further analysis; 3) waiting mode (no operation on spectrum recording is being performed in this mode); and 4) “reset” mode to rapidly switch spectrometer to safe state after software detects serious errors in its current state.

The main part of the *RTserver* is the subroutine *handler()*. It performs cyclic execution of algorithm shown in Fig. 2 (explanation is below). The subroutine is called by the system timer with frequency of 1000 Hz. Timer is activated after initialization of RT mode and memory locking. Taking into account DAC resolution (12 bits, 4096 levels) this timer frequency corresponds to minimum scan time of 4.1 sec per spectrum. Faster scan may be achieved by decreasing of number of points in spectrum. In the survey mode minimum scan time is 0.5 sec (512 points per spectrum is recorded).

The algorithm of *handler()* subroutine is presented in Fig. 2. On each clock of the system timer the subroutine performs the following operations:

1. Increase the counter of subroutine calls.
2. Check condition: whether the user command is received from the graphical interface *SEPR*?
3. Execute user command, set new operating mode.
4. Check condition: whether the current point of spectrum should be registered?
5. Register of a spectrum point.
6. Check condition: whether magnetic field should be changed on this step for the next step?
7. Change of the magnetic field.
8. Check condition: whether the end point of scan is reached?
9. Change of the scan direction or switch to the new operating mode.
10. Make test of current state of spectrometer (e. g. measure voltage in some control points), check critical values of the voltage, and switch to “reset” mode if necessary.

The usual execution flow for spectrum record is 1–2–4–5–6–7–8–10. The time analysis of algorithm shows that steps 1, 2, 4, 6, 8 take short time (several processor instructions) with respect to the period of the system timer. Steps 5 and 7 take fixed time determined by ADC and DAC equipment. This execution flow ensures low jitter between the setting of new value of magnetic field in step 7 in the current call of *handler()* and the measuring of corresponding value in spectrum in step 5 during one of the next call of *handler()*.

Design of *SEPR*

GUI in program *SEPR* is realized as a hierarchical set of windows which correspond to parts of the task of investigation of samples by EPR. Data structures for the storing of sets of spectra also correspond to these parts of the task. The *Project* class is on the top of the data hierarchy (Fig. 3.) while individual spectrum is in the bottom. Project consists of several series of spectra (for example, spectra of different samples), while each series may contain some different spectra (for instance, showing orientation or time dependence of spectra). The use of different windows for each series and each spectrum allows user to analyze and process spectra simultaneously even in parallel to the recording of new spectrum. Building the multi-window graphical application became possible only with the centralized hierarchical structure of data storing.

SEPR software uses data base (DB) to store recorded spectra on disks in tree-like hierarchical structures. The *MySQL* package serves DB as relatively fast and open-source server. All the information in *Project*, *Series*, *Spectrum*, *SpecSettings*, and *Curves* classes are stored in DB.

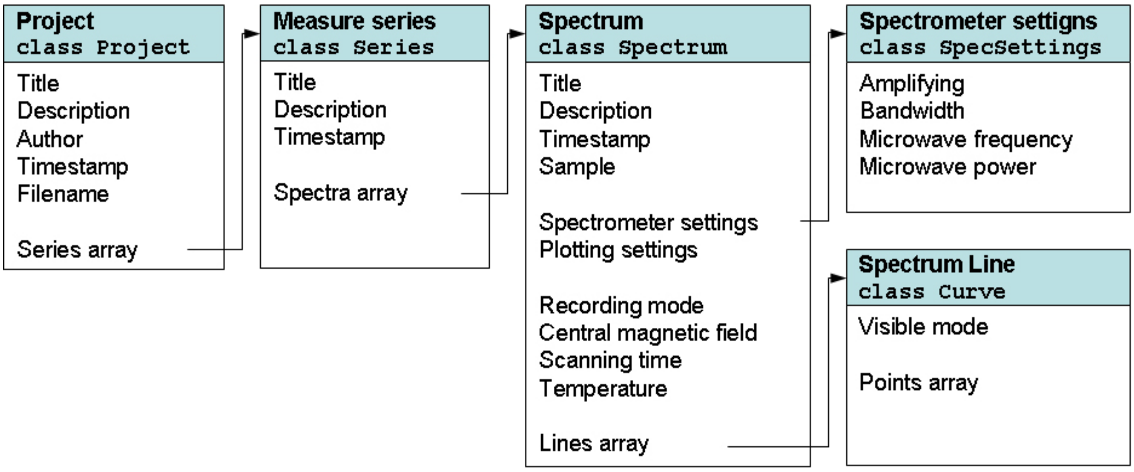

Fig.3. Hierarchy of GUI windows and data classes in *SEPR* software.

SEPR application has a possibility to set optimal (or nearly optimal) experimental conditions for investigations of different types of samples. Based on the kind of a sample, aggregate state, its mass and guessed concentration of paramagnetic impurities, the program sets main parameters of the spectrometer (scanning range of magnetic field, forward and backward duration of scan, ADC sensitivity) and recommends parameters which should be set manually. Nevertheless, experienced operator can carry out all settings in manual mode achieving maximum reliability of recorded spectrum.

Conclusion

Crucial innovation in this work was the dividing of controlling software into two processes with different scheduling priority. This allowed us to resolve a race condition for the processor resource between the hardware controlling program (*RTserver*) and the time-consuming GUI program (*SEPR*). Internal data structures allow us to build intuitive graphical interface. Reflecting these structures data base is capable to store all the needed information, search spectra by different criteria, and extract spectra for the analysis and processing. Data may be processed simultaneously with the recording of new spectrum.

References

[1] Popov T. V. Real time operating systems in EPR and NMR experiments. / In book: Magnetic resonance and its applications. — “Solo” Publisher, Saint Petersburg, 2004. P. 28–30. (In Russian)

[2] Markus Kuhn. POSIX.1b compatibility and support of real time functions: review. Translated to Russian by V. Tchernenkov. http://www.sao.ru/hq/vch/Publications/Russ/html/ linux-posix/linux-posix.html (In Russian)

[3] http://trolltech.com

[4] Popov T. V. Design of software for compact mobile EPR spectrometer “СЭПР-2” – Master's thesis. Saint Petersburg State University, Physical Faculty, Department of Quantum Magnetic Phenomena. 2007. (In Russian)

Experimental study of ESR absorption temperature dependence of chemically dehydrohalogenated poly(vinylidene fluoride)

N.A. Mavrinskaya1), L.A. Pesin1), M. Baumgarten2), A.V. Mavrinskiy1),
S.E. Evsyukov3), E.M. Baitinger4)

1)Chelyabinsk State Pedagogical University, 454080, pr. Lenina, 69, Chelyabinsk, Russia
2)Max-Planck-Institut für Polymerforschung, D-55128, Ackermannweg 10, Mainz, Germany
3)Technochemie GmbH, 69221, Gutenbergstr. 2, Dossenheim, Germany
4)Preußisches Privatinstitut für Technologie zu Berlin, 13187, Am Schlosspark 30, Berlin, Germany

e-mail: mav.natalia@gmail.com

Introduction

Poly(vinylidene fluoride) (PVDF) [1] is a polymer a unique set of physical and chemical properties of which allow its numerous technical [2] and biomedical [3] applications. Modified PVDF also possesses specific properties due to peculiarities of its chemistry, structure of the chain and crystal configuration. Chemical dehydrohalogenation leads to creation of paramagnetic centres of different nature [4]. Temperature dependence (TD) of paramagnetic susceptibility can give important information about atomic and electron structure of these carbonized samples.

Experimental technique

Partially crystalline PVDF films (Kynar 720) produced by blow extrusion, having the thickness ca. 50 μm and kindly submitted by "Atofina" (France) was used as a precursor. The films were treated with a dehydrohalogenating mixture consisting of a saturated (20%) KOH solution in ethanol and acetone (in a 1:9 volume ratio) at room temperature for different periods of time (3 and 12 hours). Immediately upon synthesis the samples were washed with ethanol, distilled water, acetone, and dried under reduced pressure.

Two sample series were studied. List of the samples, their chemical dehydrohalogenation (DHH) duration, storage conditions and reference designations are given in Table 1. After preparation all samples were stored at room temperature in the darkness. Samples 1A, 1C, 2A and 2C were stored in air; the others have been put in pumped tubes at pressure ca. 1 Pa just after synthesis. Samples 1C, 2C and 2D have been thermally treated at 393 K for 1 hour after a month and more since their preparation.

Table 1. Studied samples

Series number	Chemical DHH duration	Storage conditions	Sample designations	Notes
1	3 hours	air	1A	
		vacuum	1B	
		air	1C	heating
2	12 hours	air	2A	
		vacuum	2B	
		air	2C	heating
		vacuum	2D	heating

ESR measurements were performed employing the Bruker ESR spectrometer ESP 300 operating at X-band microwave frequencies (9,4 GHz) with 100 kHz magnetic modulation using a TE_{102} cavity under the same experimental conditions. ESR spectra have been recorded at different temperatures (maximum temperature range was 120-375 K) repeatedly at the increase and decrease of temperature. All TDs have been recorded not earlier that in 25 days after sample synthesis.

Results and discussion

Dehydrohalogenated films produce an ESR signal with the g-factor close to that inherent in a free electron. Untreated samples give no signal [5]. The sample spectra have both similar features and the differences presumably due to various content of carbon chains, fluorine, hydrogen and oxygen atoms. Spectra differ in width, intensity and g-factor value. Spectra have Lorenz-like shape. ESR intensity increases with DHH duration. According to [5] ESR intensity at samples during their storage in air decreases, the most essential drop of it occurs within a week after synthesis. The following variations become small; it may be evidence of structure stabilization.

In Fig. 1 TDs of the ESR integral intensity are represented. This parameter was calculated using a double integration routine.

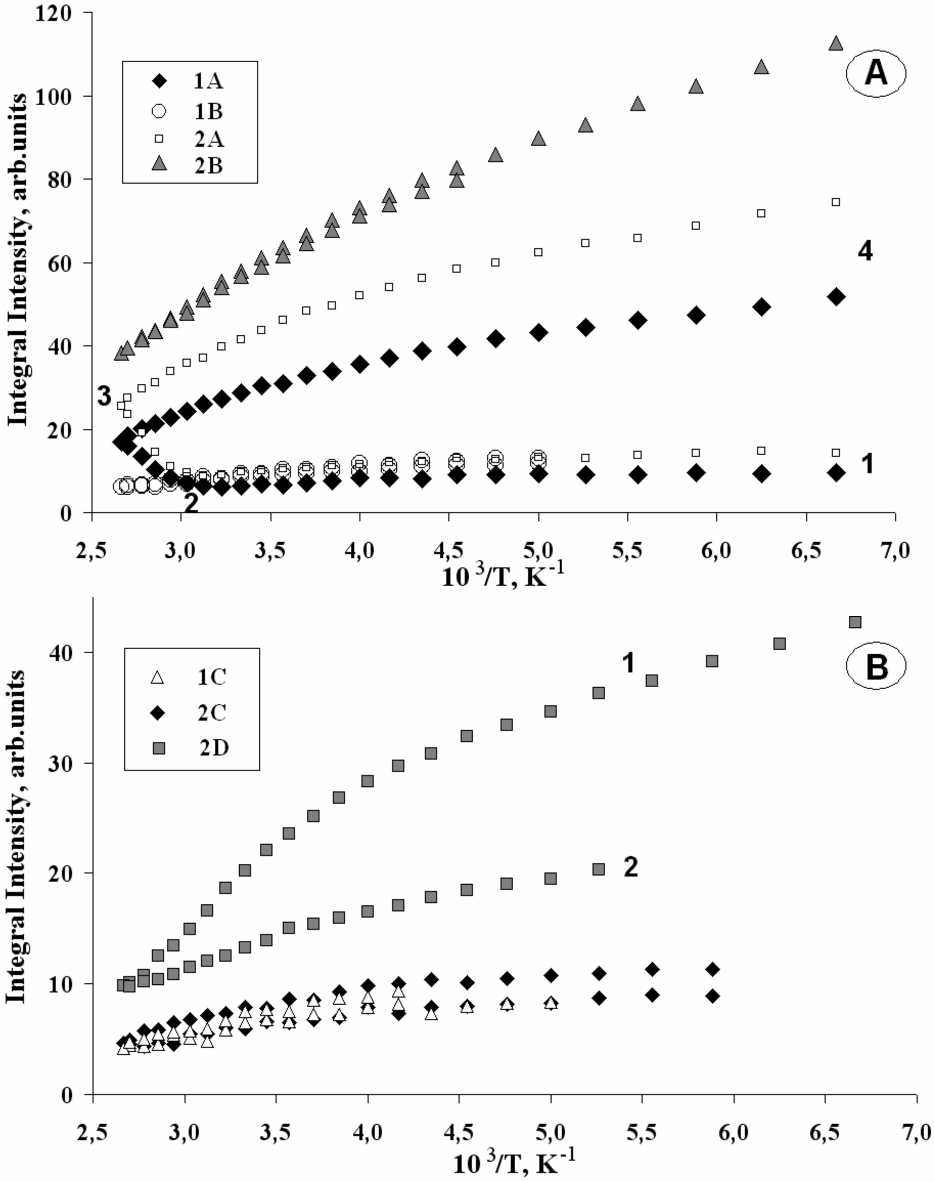

Fig. 1. Temperature dependences of the ESR intensity for the samples studied.

For the samples kept in air paramagnetism decreases at heating from 150 K to 320 K (range 1-2); at heating above 320 K (2-3) paramagnetism increases; at further cooling (3-4) the ESR intensity elevates again and the rate of this variation becomes higher than in 1-2 range (Fig. 1A). For series 2 these effects are more intensive. ESR parameters before TD recording and just after it modify greatly. For example, intensity and width of sample 1A spectrum at room temperature (RT) increase by 73% and 20% (from 12,8 to 16 G) accordingly.

After completing the above temperature study ESR spectrum parameters of sample 1A kept as previously in darkness and at RT continue to modify. Spectrum intensity and width decrease by 54% and 28% during the first 20 hours, and by 5% and 3% (to 11 G) at the following 30 hours accordingly. Thus at sample storage ESR spectra parameters tend to the original ones. Nevertheless after each heating circle the material modifies irreversibly. As one can see from Fig. 2 the difference between ESR intensity before and after heating at the same temperatures becomes less. Preliminary heating at 393 K for 1 hour removes hysteresis effects. For samples 1C and 2C TDs at heating and cooling nearly repeat; ESR intensity is close to that for samples 1A and 2A in 1-2 range. Conceivably observed effects may be caused by oxygen, hydroxyl groups, water molecule and moisture removal from a sample at heating.

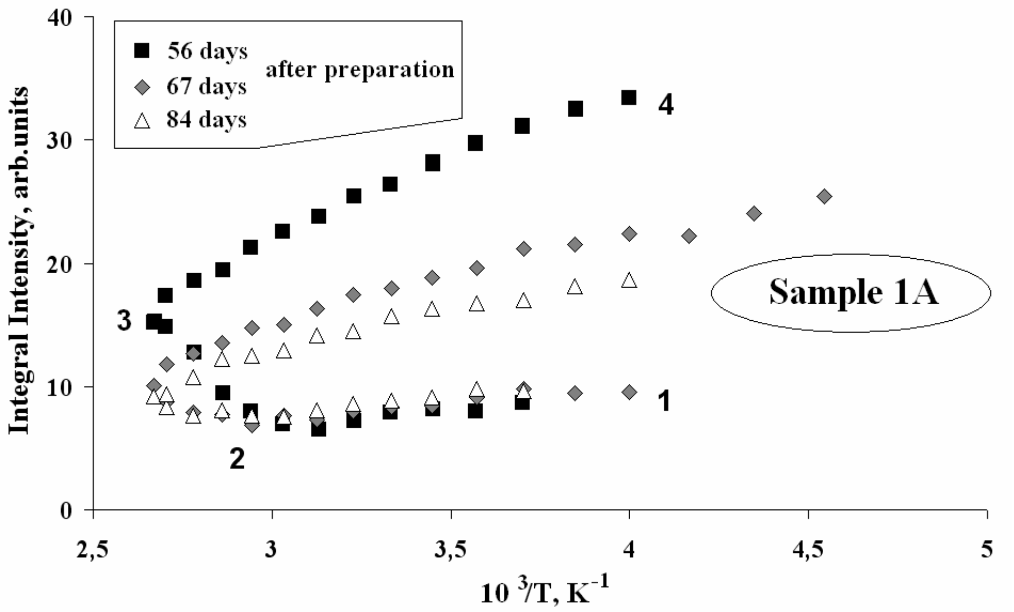

Fig. 2. Temperature dependences of the ESR intensity for sample 1A in 56, 67 and 84 days after its preparation.

For samples 1B and 2B kept in vacuum paramagnetism is lower at higher temperatures in the whole temperature interval. Temperature dependence of the ESR intensity for sample 2D additionally heated in vacuum is distinct: heating curve is located higher than cooling one (accordingly curves 1 and 2, Fig. 1B).

Deviation from the Curie law is observed for TDs of ESR signal of all the investigated samples.

Qualitative interpretation of experimental results is based on ideas evolved in studies on chemical dehydrofluorination of PVDF [6]. The interaction of the polymer with the alcoholic alkali solution results in successive elimination of hydrogen and fluorine atoms from the polymer chain to yield a fluorine-substituted polyene structure. Further elimination brings about the formation of nanofragments of linear carbon chains in various configurations. Side reactions such as nucleophilic substitution of fluorine atoms by ethoxy-groups may also occur. The presence of the ESR signal suggests the formation of free radicals during DHH. Conceivably, the paramagnetic centers observed are carbon-centered radicals bearing a hydrocarbon group and/or containing fluorine atoms. Some of the radicals become oxygenated in the air and, for example, peroxy radicals ($-CH_2-CF(OO)^{\bullet}-CH_2-$) may observed. The ESR spectra are described as composed of one or more types of radicals indicated above as well as long life polyenyl ($-CH_2-(CF{=}CH)_n-C^{\bullet}F-CH_2-$) radicals with free electrons delocalized over several C=C bonds [7-9]. Presumably observed ESR absorption can also be associated with a system of unpaired electrons delocalized over conjugated chain in the investigated samples [10].

Conclusions

1. ESR parameters of chemically dehydrohalogenated samples derived from PVDF depend on temperature and DHH duration.
2. A deviation from the Curie law is revealed for all the investigated samples.
3. Heating above 375 K modifies paramagnetic properties of the samples kept in air irreversibly.
4. For samples kept in vacuum TDs of ESR intensity at heating and cooling are very close to each other.

Acknowledges

We would like to thank the colleagues at Max Planck Institute for Polymer Research (Mainz, Germany) for their assistance in performing experiments and helpful discussions. The financial support by German Academic Exchange Service (DAAD) and the Ministry of Education and Science of Russia is gratefully acknowledged.

References

[1] B.-J. Jungnickel, in: Polymeric Materials Encyclopedia. Ed. by J.C. Salamone, CRC Press, Boca Raton, 1996, 9, 7115–7123.

[2] H.S. Nalwa (Ed.), Ferroelectric polymers: chemistry, physics and applications. Marcel Dekker, New York, 1995.

[3] G. Laroche, Y. Marois, R. Guidoin, M.W. King, L. Martin, T. How, Y. Douville, J. Biomed. Mater. Res., 1995, 29 (12), 1525-1536.

[4] Carbyne and Carbynoid Structures. Eds. Heimann R.B., Evsyukov S.E., Kavan L. Kluwer Academic Publishers, Dordrecht, the Netherlands, 1999.

[5] L.A. Pesin, N.A. Khayrullina, S.E. Evsukov, J.N. Shvachko, A.A. Fedij, New aspects of magnetic resonance application. Proceedings of the IX International Youth Scientific School "Actual problems of magnetic resonance and its application", 13-18 June 2005, Kazan. Edited by Professor M.S. Tagirov (Kazan State University), 104-107. (in Russian).

[6] S.E. Evsyukov, in: Polyynes: Synthesis, Properties, and Applications. Ed. by F. Cataldo, CRC Press, Boca Raton, 2006, 253–269.

[7] J. Goslar, B. Hilczer and H. Smogór, Acta Polonica A, 2005, 108, 89-94.

[8] A. Le Moël, J.P. Duraud, I. Lemaire, E. Balanzat, J.M. Ramillon, C. Darnez, Nuclear Instruments and methods in Physics Research B, 1987, 19/20, 891-894.

[9] E. Adem, G. Burillo, E. Munoz, J. Rickards, L. Cota, M. Avalos-Borja, Polymer Degradation and Stability, 2003, 81, 75–79.

[10] A.A. Berlin, Journal of Polymer Science, 1961, 55, 621-641.

pH Spin Labeling Technique for Determining Acid-Base and Electrochemical Characteristics of Nanoporous and Nanostructural Oxides

E.L. Golovkina, E.G. Kovaleva, L.S. Molochnikov

Ural State Forest Engineering University Sibirsky Trakt, 37, 620100, Yekaterinburg, Russia

e-mail: mag@planet-a.ru, Golovkina_E.L@mail.ru

Spin-labeling technique is widely used more 40 years. The success of this technique can be explained by achievements in the chemistry and physics of free stable radicals. Free radicals are the atoms or chemical compounds with unpaired electrons, resulting in their paramagnetism. This suggests the study of their containing systems using electron spin resonance (ESR) spectroscopy [1]. Nitroxide radicals (NR) are only a few of free radicals, which can be modified not using free valency. This possibility depends upon the fact that unpaired electron in NR is almost totally located on NO-group of radical, and not on radical residues whereby similar reaction is performed.

In the early 80's the NR with pH-sensitive EPR spectra were first synthesized in the Institute of Organic Chemistry of the Siberian Branch of the Russian Academy of Sciences. pH sensitivity of these NR occurs at the expense of lone electron pair near nitrogen atom located in the third position regarding radical fragment. pH-sensitive NR have been successfully used as pH-sensitive spin probes for the determination of local pH values (pH^{loc}) and for the investigation of proton-related transport processes in different biological objects including proteins, chloroplasts, wheat embryos and even living organisms [2]. Also a principal possibility of measurements of electrical potential of surface of the mixed bilayers composed of dimyristoylphosphatidylglycerol and dimyristoyl-phosphatidilcholine has been demonstrated by Prof. Valery Khramtsov and others [3]

Determination of the local pH^{loc} values and surface electrical potential (SEP) is very important also for characterizing the acid-base and electrochemical properties of different materials including nanoporous and nanostructure oxides. At present these materials are of important practical interest in different fields of science and technologies including heterogeneous catalysis and separation by adsorption in connection with novel and unusual properties as compared to the known before solid materials.

Recently a new technique for determining a medium acidity inside of solid-state pores (pH^{loc}) using pH-sensitive nitroxide radicals (NR) and ESR technique has been elaborated by us [4]. This method allowed to determine not only pH^{loc} in micropores of a large set of organic cross-linking polyelectrolyte [4] and ionization constants of their functional groups, but also to study sorption processes and hydrolysis in an ion-exchangers and catalytic properties of Cu^{2+}-containing carboxylic cation-exchange resins and critically examine the previous formed concept of regularities of adsorbents behavior in aqueous media [4]. Also the first attempts for measuring of solid-state surface electrical potential (SEP), in particular, for nanostructured particles TiO_2, using pH-sensitive NR as pH spin probes and ESR spectroscopy, have been made [5].

The purpose of this work is to characterize the features of the elaborated technique in application to mesoporous molecular sieves (MMS silicious materials), porous membranes based on anodic Al_2O_3 (AAO) and nanostructured SiO_2 and to study acid-base and electrochemical properties of the above-mentioned nanoporous and nanostructured oxide, respectively. The objects of the research were MMS silicious materials such as C12MMS-41, C16MMS-41 and SBA-15 with pore diameters 2.3, 3.2 and 8.1 nm, respectively, AAO membranes T155, RSA-3 and Prom with pore diameters 26, 38 and 200 nm, respectively and nanostructured SiO_2 with average particles diameter ($d_{av.}$) and specific surface area ($S_{sp.}$) 7 nm and 290 m^2/g, respectively. Stable pH-sensitive nitroxide radicals (NR) of such as 4- dimethylamine-2-ethyl-5,5-dimethyl-2-pyridine-4-yl-2,5-dihydro-1*H*-imidazol-1-oxyl (R1), 4-amino-2,2,5,5-tetramethyl-2,5-dihydro-1*H*-imidazol-1-oxyl (R2), and 4.4-bromhydromethyl-2,2,3,5,5-pentamethyl -1*H*-imidazolidine 1-oxyl (RBr), being pH-sensitive in the range from 2.5 to 7.5 pH units were used . They were synthesized in the Vorozhtsov Institute of Organic Chemistry, Siberian Branch of the Russian Academy of Sciences (Novosibirsk).

The spectra were recorded by X-band Bruker ElexSys 580 pulsed FT-ESR and an automatic X-band ESR PS 100.X spectrometer (Advanced Analytical Instruments Inc., Belarus) at room and liquid nitrogen temperatures. The ESR spectra of the NR in aqueous solution consist of three components reflecting an interaction between the unpaired electron and the unit nuclear spin of the nitrogen belonging to the ($=N-O^\bullet$) group of the radical. The nitrogen included in the heterocycle of NR used in this study is able to associate a proton [1].

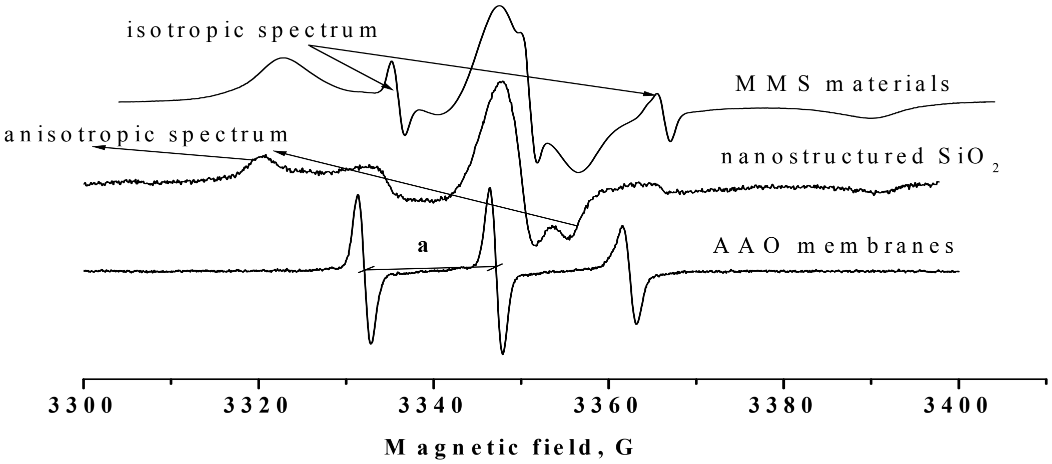

Fig.1. ESR spectra of NR inside of the studied nanoporous and nanostructured oxides

The ESR spectra of the NR in a phase of the studied objects are presented in Fig.1

The spectra in a phase of MMS and nanostructured oxides were simulated using Freed's program (version 1999) by three theoretical spectra (isotropic average and anisotropic protonated and nonprotonated signals) [6]. In the case of AAO membranes the simulation is carried out by isotropic protonated and nonprotonated signals.

It has been found that there are two species of molecular mobility of the used NR inside of MMS and nanostructured oxides, namely, fast motion and slow motion which differ from one another by correlation time (τ_c). When passing from the MMS with a lesser pore diameter (C12-, C16-MCM41) to those with a greater diameter (SBA-15), and also from the samples in the protonated form (RH^+) to those in nonprotonated form (R)both τ_c –values of fast-motioned and slow-motioned NR decrease and a fraction of fast-motioned NR increases. On the other hand, there is only fast motion of NR in a phase AAO membranes (Fig.1).

The elaborated technique consists in determining pH-sensitive parameters of ESR spectra of NR in a site of their location in a solid and pH inside of their pores using graduation dependences of pH-sensitive parameters on pH value aqueous solution (Fig.2,3.4).

Two pH-sensitive parameters of NR ESR spectra have been used for pH measurements

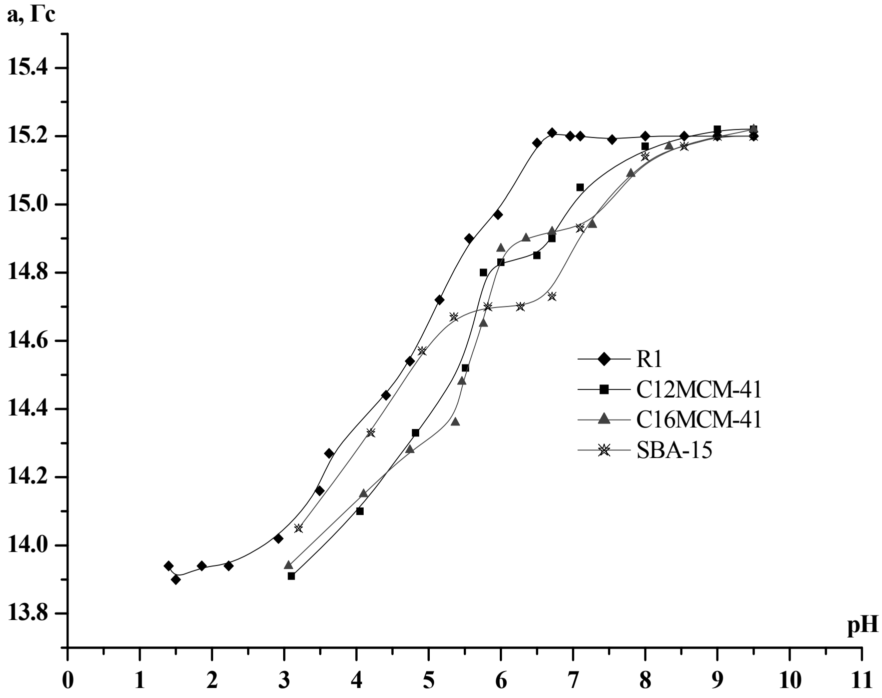

Fig.2 Titration curves of NR R1 in aqueous solution and in the studied MMS

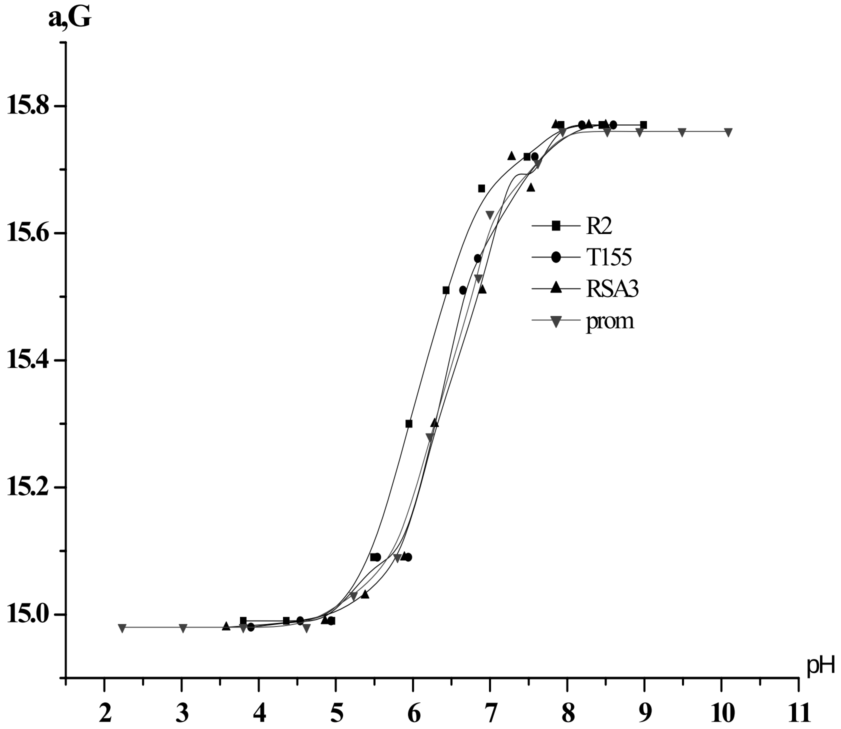

Fig.3 Titration curves of NR R2 in aqueous solution and in the studied AAO membranes

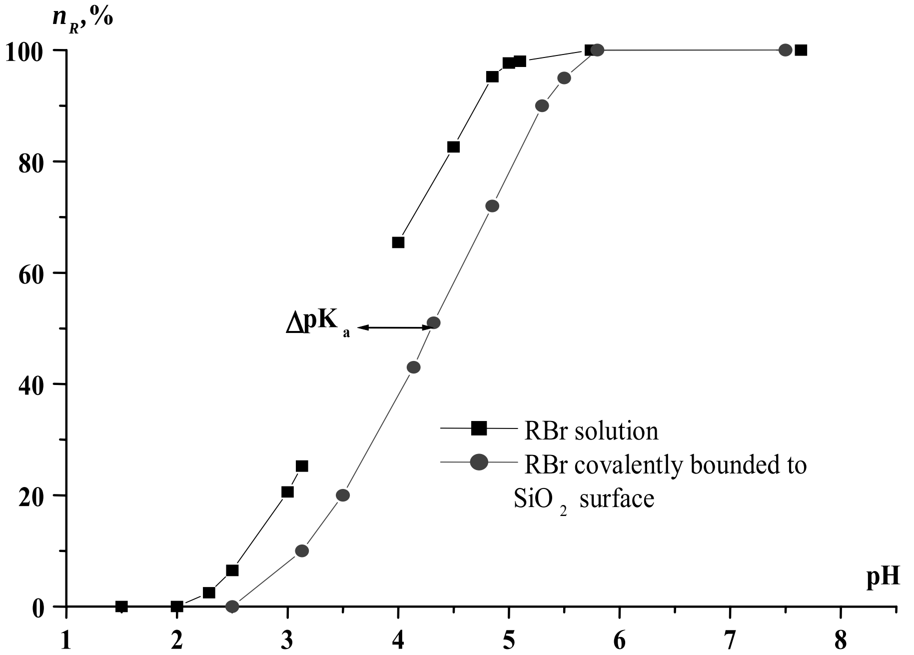

Fig.4 Titration curves of NR RBr in aqueous solution and nearby nanostructured SiO_2 surface

inside of porous solids. The first of them is: the parameter "a" characterizing hyperfine coupling constant of isotropic ESR signals of NR (a_N) ($\tau_c = 2 \div 9 \times 10^{-11}$s). This parameter can be estimated from ESR spectrum of NR directly as a distance between the first and the second components of isotropic triplet of NR. More precise determination of the parameter "a" can be conducted by the formula

$$a = \frac{a_{xx} + a_{yy} + a_{zz}}{3}, \tag{1}$$

where a_{xx}, a_{yy}, a_{zz}- components of tensor of a_N calculated using the Freed's program. Another parameter "f" is defined by the formula

$$f = \frac{n_R}{\left(n_R + n_{RH^+}\right)} \tag{2}$$

from an immobilized ESR spectrum of NR as a fraction of nonprotonated (n_R) or protonated forms of NR ($n_{RH}{}^{+}$). These fractions are found from the Freed's program. A signal from an immobilized NR ($\tau_c = 8\times10^{-9}$ s$\div 7\times10^{-10}$s) is given by the molecules of the NR adsorbed by a surface of MMS and can be used for determining a local concentration of protons near surface of MMS. For the nanosructured SiO_2 oxide only immobilized spectra from two forms NR ($\tau_c = 5\times^{-}10^{-6} \div 9\times^{-}10^{-6}$s) were detected. They are given by the molecules of NR covalently bounded to oxide surface.

From Fig. 2 we notice that the ESR spectra of NR in a phase of the studied MMS are shifted to right about the graduation curve of th NR in aqueous solution. This fact indicates the lesser pH^{loc} values in a phase of MMS as compared to pH values in external aqueous solution. The titration curves of NR in the studied MMS are differ from one another that indicate different pH^{loc} values in these phase. Also from titration experiments the pK_a-values were determined as pH^{loc}-values over a range of constancy of pH-values of an external solution. The titration curves of NR in pores of the AAO membranes almost coincide. This points to the fact that pH^{loc} values are equal. For all the studied AAO membranes over a range of sensitivity of NR, but are differ from pH external aqueous solution. In this connection we can conclude the AAO membranes with d$_{pore}$ more than 26 nm show identical acidic properties inside of pores.

The information on surface electrical potential (SEP) for nanoparticles (φ) can be obtained from the shift of ionization constants of NR located nearby nanomaterials surface regarding ones of the NR in aqueous solution (ΔpK_a^{el}). pK_a^{el} values are defined from the corresponding titration curves, and ΔpK_a^{el} calculated by the formula [2,3] :

$$\Delta pK_a^{el} = -\frac{e \times \varphi}{2.3k \times T}, \qquad (3)$$

where φ — surface electrical potential (SEP), *e*- electron charge, *k* — Bolzmann's constant, *T* — absolute temperature.

The titration curves of NR RBr in aqueous solution and nearby surface of nanooxide SiO_2 (Fig.4) present the dependences of the parameter "f" of anisotropic spectrum on pH of external solution (f=F(pH)) The shift of titration curve of the covalently bounded NR to right about the graduation curve in solution (to field of alkaline solutions) indicates negative surface charge [8]. The calculated by the formula (3) φ value at the site of NR locating was equal to -41.9 mV.

As is evident from the foregoing, pH spin –labeling technique is very informative. The novel data, namely pH^{loc} and pK_a values were obtained for inorganic nonporous objects. The principal possibility of using NR for SEP determination was demonstrated. The definition of specific values of surface electrical potential open up new properties of different nanostructured materials and possibility to predict novel fields of their application.

The results of the present research are taken to use in future in different pH-dependent processes with participation of nanoporous and nanostructured materials.

The work was supported the Ministry of Education of RF (Research Program, 2007-2011).

References

[1] 1.A.N. Kuznetsov, Spin –Labeling Technique .M.: Nauka, 1976.-210 p

[2] V.V. Khramtsov, Volodarsky L.B., Biological Magnetic Resonance, V.14: Spin Labeling: The Next Millennium, ed. Berliner. Plenum Press, N.Y., 1998, P. 109.

[3] V.V. Khramtsov, D. Marsh, L.M.Weiner et al, The application of pH-sensitive spin labels to studies of surface potential and polarity of phospholipid membranes and proteins // Biochim. Biophys. Acta. -1992. -V. 1104. -P. 317.

[4] L.S. Molochnikov, E.G. Kovalyova, I.A. Grigor'ev , A.A. Zagorodni // J.Phys.Chem. B. 2004. V.108. P.1302.

[5] Kovalyova E.G., Petkevich T.V., Medyantseva E.L. et. al. Study of Surface Electrical Potential of Nanostructured oxides //Russian Journal of "Sorption and Chromatographic Processes", V6(6), №2, p.2006 991.

[6] Budil D E., Sanghyuk L., Saxena S., Freed J. H.// J. Magn. Res. A. 1996. V.120. P.155.

[7] Fernandez, M.S., Fromherz P. Lipoid pH indicators as probes of electrical potential and polarity in micells // J. Phys.Chem.1977.-V. 81.- No. 18. - P. 1755.

Spin Relaxation of Conduction Electrons in Ion Implanted Layers of Si with Modified Isotopic Composition

A.A. Ezhevskii, D.V. Guseinov, A.V. Soukhorukov

N.I. Lobachevsky State University of Nizhni Novgorod, 603950, 23 Prospekt Gagarina, Nizhni Novgorod, Russia

e-mail: hatagus@mail.ru

In a present work the spin relaxation processes of conduction electrons in silicon with different isotopic composition were studied. The films of silicon single crystal doped under ion implantation by phosphorous with concentration averaged over irradiated layer from $1.5*10^{18}$ cm^{-3} to $1.1*10^{19}$ cm^{-3} were used for investigations. The concentration of impurity was calculated from intensity of EPR line. The contribution of several mechanisms to spin relaxation processes connected with electron-impurity, electron-electron and electron-phonon interactions is considered. The electron-phonon interaction is less observable in comparison with the electron-impurity and electron-electron interactions in the used range of impurity concentrations.

Experimental Procedures and Results

The investigations were carried out on monocrystalline epitaxial layers of natural and monoisotopic (^{28}Si - 99.99 at. %) silicon grown from silane on natural silicon wafers. The thickness of layer were ~11 μm. The layer was doped with phosphorous by mean of ion implantation (E=40 KeV) at doses $1.8\text{x}10^{14}$ and $1.8\text{x}10^{15}$. For the purposes of electrical activation and annealing of defects the samples were hold at 1000 °C for an hour. Thus, the samples of natural and monoisotopic silicon with different concentration of phosphorous in the maximum of impurity distribution were obtained.

All measurements of conduction electron spin resonance spectrums were done on Bruker EMX spectrometer at the temperature range 95-300K.

From the intensity of EPR line of conduction electrons the bulk concentrations of impurity in irradiated by phosphorous layer were calculated. In Table 1 the irradiation doses and corresponding mean values of concentration of impurity for studied samples are shown. For sample 3 we suggest that since the inhomogeneous distribution of impurity the concentration in the maximum can reach the value close to 10^{20} cm^{-3}.

Table 1

№	Si type	D, ions/cm^2	N, cm^{-3}
1	Si^{28}	$1{,}8\text{x}10^{14}$	$1{,}5\text{x}10^{18}$
2	Si^{nat}	$1{,}8\text{x}10^{14}$	$3{,}3\text{x}10^{18}$
3	Si^{28}	$1{,}8\text{x}10^{15}$	$1{,}1\text{x}10^{19}$
4	Si^{nat}	$1{,}8\text{x}10^{15}$	$9{,}1\text{x}10^{18}$

In fig. 1 the dependencies of inverse intensity of conduction electrons EPR line from temperature are shown. From the behavior of dependence it can be concluded that the samples with high concentration of impurity have the dependence of inverse intensity on temperature which reveals the saturation, and does not correspond to the Curie law. For the samples with low dose of irradiation the dependencies of inverse intensity follow to the Curie law. Hence, due to inhomogeneous distribution of impurity in the layer the electron gas in samples 3 and 4

Spin Relaxation of Conduction Electrons in Ion Implanted Layers of Si with Modified Isotopic Composition

A.A. Ezhevskii, D.V. Guseinov, A.V. Soukhorukov

N.I. Lobachevsky State University of Nizhni Novgorod, 603950, 23 Prospekt Gagarina,
Nizhni Novgorod, Russia

e-mail: hatagus@mail.ru

In a present work the spin relaxation processes of conduction electrons in silicon with different isotopic composition were studied. The films of silicon single crystal doped under ion implantation by phosphorous with concentration averaged over irradiated layer from $1.5*10^{18}$ cm^{-3} to $1.1*10^{19}$ cm^{-3} were used for investigations. The concentration of impurity was calculated from intensity of EPR line. The contribution of several mechanisms to spin relaxation processes connected with electron-impurity, electron-electron and electron-phonon interactions is considered. The electron-phonon interaction is less observable in comparison with the electron-impurity and electron-electron interactions in the used range of impurity concentrations.

Experimental Procedures and Results

The investigations were carried out on monocrystalline epitaxial layers of natural and monoisotopic (^{28}Si - 99.99 at. %) silicon grown from silane on natural silicon wafers. The thickness of layer were ~11 μm. The layer was doped with phosphorous by mean of ion implantation (E=40 KeV) at doses $1.8x10^{14}$ and $1.8x10^{15}$. For the purposes of electrical activation and annealing of defects the samples were hold at 1000 °C for an hour. Thus, the samples of natural and monoisotopic silicon with different concentration of phosphorous in the maximum of impurity distribution were obtained.

All measurements of conduction electron spin resonance spectrums were done on Bruker EMX spectrometer at the temperature range 95-300K.

From the intensity of EPR line of conduction electrons the bulk concentrations of impurity in irradiated by phosphorous layer were calculated. In Table 1 the irradiation doses and corresponding mean values of concentration of impurity for studied samples are shown. For sample 3 we suggest that since the inhomogeneous distribution of impurity the concentration in the maximum can reach the value close to 10^{20} cm^{-3}.

Table 1

№	Si type	D, ions/cm^2	N, cm^{-3}
1	Si^{28}	$1,8x10^{14}$	$1,5x10^{18}$
2	Si^{nat}	$1,8x10^{14}$	$3,3x10^{18}$
3	Si^{28}	$1,8x10^{15}$	$1,1x10^{19}$
4	Si^{nat}	$1,8x10^{15}$	$9,1x10^{18}$

In fig. 1 the dependencies of inverse intensity of conduction electrons EPR line from temperature are shown. From the behavior of dependence it can be concluded that the samples with high concentration of impurity have the dependence of inverse intensity on temperature which reveals the saturation, and does not correspond to the Curie law. For the samples with low dose of irradiation the dependencies of inverse intensity follow to the Curie law. Hence, due to inhomogeneous distribution of impurity in the layer the electron gas in samples 3 and 4

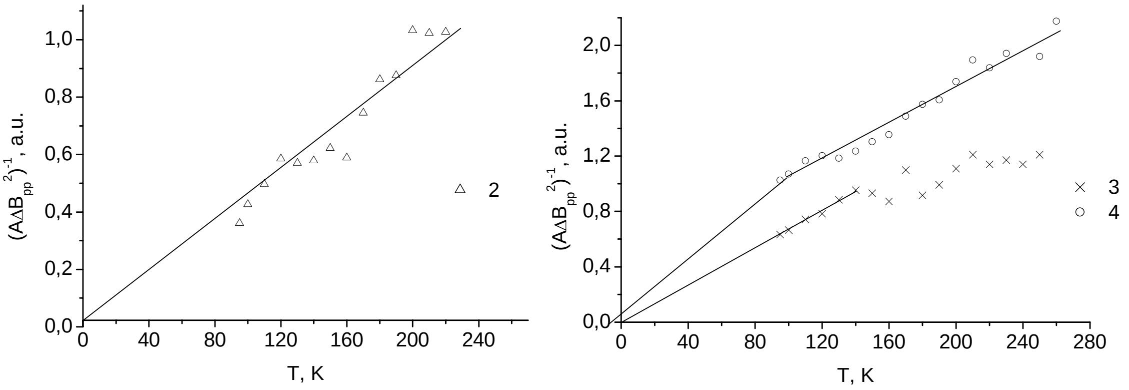

Fig. 1. Temperature dependence of the inverse intensity for the samples 2,4 of natural silicon and 3 of monoisotopic silicon with different doping dose.

is partially degenerated and nondegenerated in samples 1 and 2 in the full range of temperatures studied.

Temperature dependencies of conduction electron EPR line width were measured in order to investigate the spin relaxation processes. These dependencies are shown at fig. 2.

The main broadening mechanism for conduction electrons is the Elliot-Yafet one [3]. From figure 2 it can be shown that in the studied range of concentrations the dominant scattering mechanism is scattering by impurity. In comparison with it the electron-phonon scattering is less observable. Therefore even for the samples with low phosphorous concentration (samples 1, 2) scattering by impurity is dominant. At increasing of phosphorous concentration (samples 3, 4) the electron-electron interactions become more important, but scattering by impurity still remains. Hence, for the samples with the highest concentration scattering mechanisms by the impurity and electron-electron intervalley scattering are reliable.

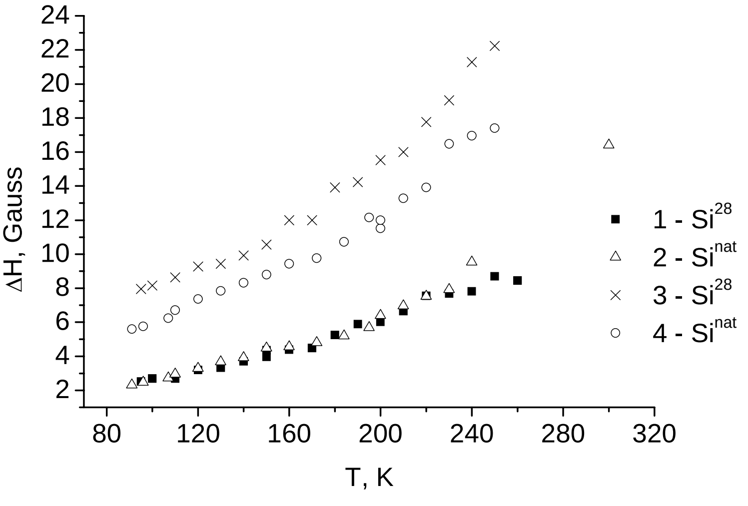

Fig. 2. Temperature dependencies of conduction electrons EPR line width in the silicon layers with different phosphorous concentration.

In silicon due to dominant scattering of electrons by deformation potential in the studied temperature interval to describe temperature dependencies one should use an expression that can be derived from that one shown in the work [5] for single valley model and for nondegenerated electron gas with six valley of silicon taking into account [4]:

$$1/\tau_s = 6\cdot 0.088\left(\frac{C_2}{C_1}\right)^2\left(\frac{\lambda}{\Delta E}\right)^2\left(\frac{k_bT}{\Delta E}\right)\frac{1}{\tau_p}\,, \tag{1}$$

$$\text{or:}\, 1/\tau_s \propto T^m \tag{2}$$

where C_1 и C_2 – constants of deformation potential for electrons in conduction band and intervalley one, for acoustic phonons accordingly (C_1=6.5eV и C_2=30eV), λ - parameter of spin-orbit coupling (~100 cm^{-1}), ΔE – band-to-band distance (4 eV), $1/\tau_p \sim T^n$ - n determined by the acting scattering mechanism. For the degenerated electron gas in the expression (1) k_bT substituted by E_F.

We have studied parameter m for the obtained dependencies. They are for the sample 1 - *m =1.8*; 2 – *m = 1.8, m = 2.5*; 3 – *m = 2.5;* 4 – *m = 2.1* in the temperature interval up to 240K. The value *m =1.8* for the samples 1 and 2 can be explained by presence of electron-impurity interaction, in other words the electron suffers strong scattering on impurity. It is typical, that at low temperatures such mechanism leads to inverse temperature dependence of line width [2], i.e. the line width increases at decreasing of temperature. For the samples 3 and 4 besides scattering on impurity there is an additional mechanism via electron-electron interaction, as the concentration of impurity is sufficient for its initiation. At the temperature interval T > 240 K *m>2* due to additional electron-phonon interaction, which ought to enlarge *m*. It is confirmed by observing the increase of the slope with rise of temperature, that is, probably, connected with participation of short-wavelength phonons in scattering, which lead to transfer of the electrons from the one valley to the other.

The obtained experimental data are evidence of the fact that at the studied concentrations range the isotopic effects is negligible in comparison with strong scattering mechanisms on impurity and electrons, when the electrons and impurity concentration is comparable with that one of isotopic impurity.

The decreasing of g-factor of conduction electrons with increasing of temperature (fig. 3) that well correlates with dependencies shown at fig.2 was observed.

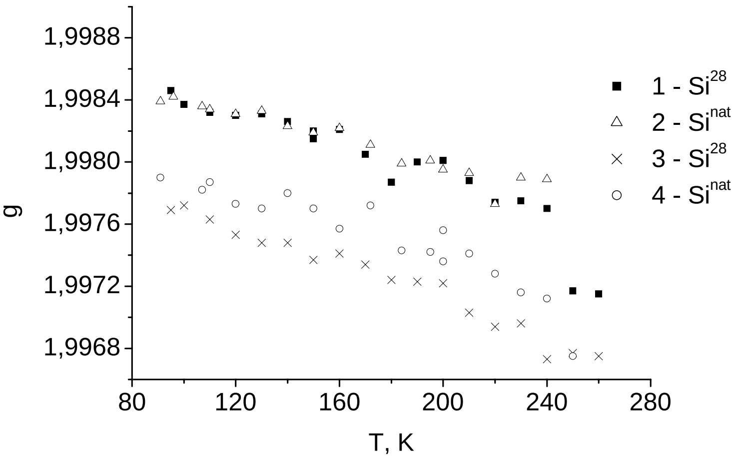

Fig. 3. Modification of conduction electrons g-factor in the silicon layers with different concentration of phosphorous impurity.

It is well known decreasing of g-factor with increasing of donor concentration []. In that case electron gets the additional spin-orbital contribution from interaction with impurity. In case of samples 3 and 4 there is also can be contribution from the electron-electron interaction. It remains unexplained how the decreasing of g-factor is connected with rising of the temperature, as the probability of scattering on impurity is diminished. The possible explanation is the contribution of the intervalley electron-electron interaction, which is temperature dependent.

Conclusion

In a present work the layers of natural and monoisotopic silicon doped by phosphorous were investigated. As a result of doping two types of samples were obtained with partially degenerated electron gas and with nondegenerated one. For the heavy doped samples the spin relaxation mechanisms are connected with scattering of electrons on impurity and electron-electron interaction. In the samples with lower concentration of phosphorous the scattering on impurity becomes dominant. To estimate the contribution of superhyperfine interaction it is necessary to carry out the investigation on the silicon samples with lower donor concentration and enriched by isotope with ½ nuclear spin, i.e. ^{29}Si.

References

[1] Lepine D.J. // Spin resonance of localized and delocalized electrons in phosphorus doped Silicon between 20 and 30 K, Phys. Rev. V. 2, N. 7, 1970

[2] Lancaster G., Van Wyk J.A., Schneiders E.E. // Spin-lattice relaxation of conduction electrons in Silicon, Proc. Phys. Soc, V. 84, 1964

[3] Elliot R.J. // Theory of the effect of spin-orbit coupling on magnetic resonance in some semiconductors, Phys. Rev. V. 96, N. 2, 1954

[4] Ежевский А.А., Гусеунов Д.В., Сухоруков А.В., Хомицкий Д.В. Кузнецов О.А., Гусев А.В. // Вклад различных механизмов в спиновую релаксацию электронов проводимости в кремнии с различным изотопным составом, XI международный симпозиум «Нанофизика и наноэлектроника», 2007

[5] Захарченя Б.Н., Майер Ф. // Оптическая ориентация, Л.: Наука. 1989. 408 с.

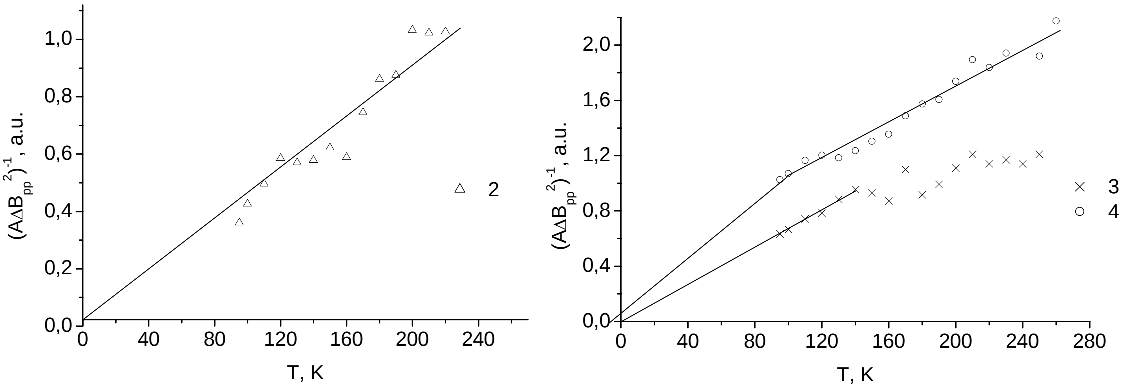

Fig. 1. Temperature dependence of the inverse intensity for the samples 2,4 of natural silicon and 3 of monoisotopic silicon with different doping dose.

is partially degenerated and nondegenerated in samples 1 and 2 in the full range of temperatures studied.

Temperature dependencies of conduction electron EPR line width were measured in order to investigate the spin relaxation processes. These dependencies are shown at fig. 2.

The main broadening mechanism for conduction electrons is the Elliot-Yafet one [3]. From figure 2 it can be shown that in the studied range of concentrations the dominant scattering mechanism is scattering by impurity. In comparison with it the electron-phonon scattering is less observable. Therefore even for the samples with low phosphorous concentration (samples 1, 2) scattering by impurity is dominant. At increasing of phosphorous concentration (samples 3, 4) the electron-electron interactions become more important, but scattering by impurity still remains. Hence, for the samples with the highest concentration scattering mechanisms by the impurity and electron-electron intervalley scattering are reliable.

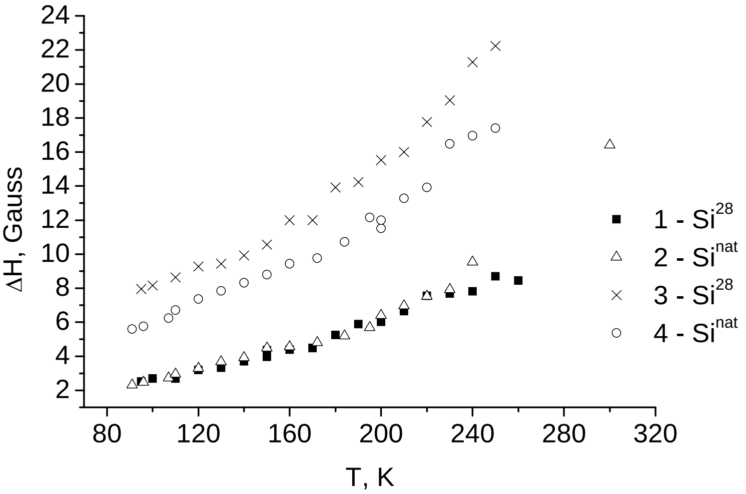

Fig. 2. Temperature dependencies of conduction electrons EPR line width in the silicon layers with different phosphorous concentration.

In silicon due to dominant scattering of electrons by deformation potential in the studied temperature interval to describe temperature dependencies one should use an expression that can be derived from that one shown in the work [5] for single valley model and for nondegenerated electron gas with six valley of silicon taking into account [4]:

$$1/\tau_s = 6\cdot 0.088\left(\frac{C_2}{C_1}\right)^2\left(\frac{\lambda}{\Delta E}\right)^2\left(\frac{k_bT}{\Delta E}\right)\frac{1}{\tau_p}\ , \tag{1}$$

$$\text{or:}\, 1/\tau_s \propto T^m \tag{2}$$

where C_1 и C_2 – constants of deformation potential for electrons in conduction band and intervalley one, for acoustic phonons accordingly (C_1=6.5eV и C_2=30eV), λ - parameter of spin-orbit coupling (~100 cm^{-1}), ΔE – band-to-band distance (4 eV), $1/\tau_p \sim T^n$ - n determined by the acting scattering mechanism. For the degenerated electron gas in the expression (1) k_bT substituted by E_F.

We have studied parameter m for the obtained dependencies. They are for the sample 1 - $m = 1.8$; 2 – $m = 1.8$, $m = 2.5$; 3 – $m = 2.5$; 4 – $m = 2.1$ in the temperature interval up to 240K. The value $m = 1.8$ for the samples 1 and 2 can be explained by presence of electron-impurity interaction, in other words the electron suffers strong scattering on impurity. It is typical, that at low temperatures such mechanism leads to inverse temperature dependence of line width [2], i.e. the line width increases at decreasing of temperature. For the samples 3 and 4 besides scattering on impurity there is an additional mechanism via electron-electron interaction, as the concentration of impurity is sufficient for its initiation. At the temperature interval T > 240 K $m>2$ due to additional electron-phonon interaction, which ought to enlarge m. It is confirmed by observing the increase of the slope with rise of temperature, that is, probably, connected with participation of short-wavelength phonons in scattering, which lead to transfer of the electrons from the one valley to the other.

The obtained experimental data are evidence of the fact that at the studied concentrations range the isotopic effects is negligible in comparison with strong scattering mechanisms on impurity and electrons, when the electrons and impurity concentration is comparable with that one of isotopic impurity.

The decreasing of g-factor of conduction electrons with increasing of temperature (fig. 3) that well correlates with dependencies shown at fig.2 was observed.

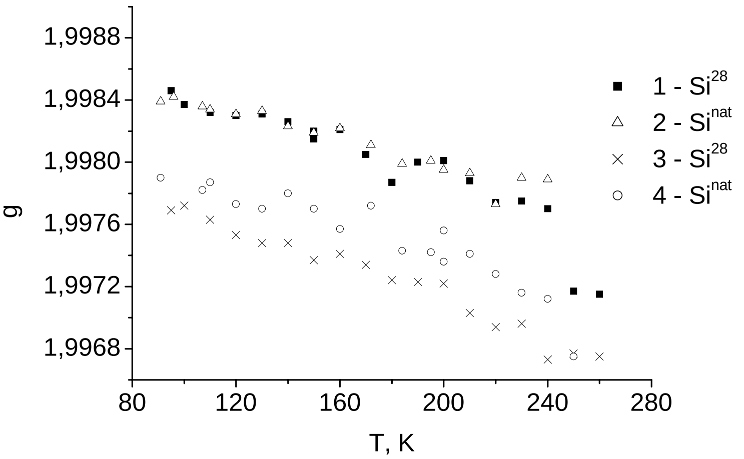

Fig. 3. Modification of conduction electrons g-factor in the silicon layers with different concentration of phosphorous impurity.

It is well known decreasing of g-factor with increasing of donor concentration []. In that case electron gets the additional spin-orbital contribution from interaction with impurity. In case of samples 3 and 4 there is also can be contribution from the electron-electron interaction. It remains unexplained how the decreasing of g-factor is connected with rising of the temperature, as the probability of scattering on impurity is diminished. The possible explanation is the contribution of the intervalley electron-electron interaction, which is temperature dependent.

Conclusion

In a present work the layers of natural and monoisotopic silicon doped by phosphorous were investigated. As a result of doping two types of samples were obtained with partially degenerated electron gas and with nondegenerated one. For the heavy doped samples the spin relaxation mechanisms are connected with scattering of electrons on impurity and electron-electron interaction. In the samples with lower concentration of phosphorous the scattering on impurity becomes dominant. To estimate the contribution of superhyperfine interaction it is necessary to carry out the investigation on the silicon samples with lower donor concentration and enriched by isotope with ½ nuclear spin, i.e. ^{29}Si.

References

[1] Lepine D.J. *// S*pin resonance of localized and delocalized electrons in phosphorus doped Silicon between 20 and 30 K, Phys. Rev. V. 2, N. 7, 1970

[2] Lancaster G., Van Wyk J.A**.**, Schneiders E.E. // Spin-lattice relaxation of conduction electrons in Silicon, Proc. Phys. Soc, V. 84, 1964

[3] Elliot R.J. // Theory of the effect of spin-orbit coupling on magnetic resonance in some semiconductors, Phys. Rev. V. 96, N. 2, 1954

[4] Ежевский А.А., Гусеунов Д.В., Сухоруков А.В., Хомицкий Д.В. Кузнецов О.А., Гусев А.В. // Вклад различных механизмов в спиновую релаксацию электронов проводимости в кремнии с различным изотопным составом, XI международный симпозиум «Нанофизика и наноэлектроника», 2007

[5] Захарченя Б.Н., Майер Ф. // Оптическая ориентация, Л.: Наука. 1989. 408 с.

Usage of Low-Field Extremity MRI for Wrist Bone Erosions Detection and Evaluation in Comparison with Plane Radiography Data in the Diagnostics of Patients with Early Rheumatoid Arthritis

I.E. Rapoport, E.Yu. Pogozheva, A.V. Smirnov

Department of Radiology, Institute of Rheumatology RAMS, Kashirskoe sh., 34A, Moscow, Russia

e-mail: rapoport@inbox.ru

Introduction

Rheumatoid arthritis (RA) is an inflammatory rheumatic disease of unknown etiology, characterized by symmetric chronic erosive arthritis (synovitis) of peripheral joints (such as joints of wrists, metacarpophalangeal (MCP) and proximal interphalangeal joints and others) and systemic inflammatory lesion of internal organs. [1]

The diagnosis is often difficult, and the disease course is difficult to predict in individual patients. Recent data suggest that early and aggressive treatment is better than the more conservative strategies used previously [2-4]. This implies a need for development of methods which can better define patients with a high risk of developing erosive disease and patients with a more favorable prognosis. An X-ray examination is well established in the assessment of disease severity but does not describe ongoing inflammatory activity. Joint X-ray examination depicts lesions which have arisen as a result of past inflammatory processes, but has limited value in detecting early structural damage [5]. Within recent years, magnetic resonance imaging (MRI) has been shown to be better than clinical and X-ray examinations for the identification of inflammatory and destructive processes in RA joints.[6-8] Some studies suggest a role for MRI as prognostic indicator in early RA.[6, 9-10]. However, most previous studies have been performed by using high field, whole body MR units. But there is a growing need in less expensive, more comfortable and more convenient alternatives. This study reports the results of MRI performed on patients with early rheumatoid arthritis by a low field dedicated MRI system specifically designed for the examination of peripheral joints. As well, correlation between MRI, X-ray and standard laboratory investigations data (rheumatoid factor – RF, C-reactive protein – C-RP, erythrocyte sedimentation rate – ESR) are evaluated.

Patients and methods

Patients

One hundred consecutive patients with rheumatoid arthritis of less than 24 months' duration were recruited from the RADIKAL research list from the patients, consequently admitted to the Institute of Rheumatology RAMS, Moscow, Russia. All patients fulfilled the ACR (American College of Rheumatology) 1987 revised criteria of RA.[11] Their median age was 52 years (range 19-81). The female/male ratio was 9/2. The median disease duration since the first onset of arthritis or joints pain or swelling was 169 days (range 15-450). Twenty seven were seronegative for rheumatoid factor, (evaluated by A. Speransky method modification). None of the patients had received corticosteroids or disease modifying antirheumatic drugs before inclusion in the study. The study was conducted in accordance with local ethics committee approval obtained before starting the general research project.

Clinical examination

All clinical examinations were done by the same rheumatologist. The examinations included assessments of joint swelling and joint tenderness, as recommended by EULAR.[12] Clinical synovitis in a joint was considered in the presence of joint swelling or tenderness, or both.

Extremity MRI

MRI of the wrist and 2nd-5th MCP joints was performed by a 0.2 T Artoscan system (ESAOTE Biomedica, Italy). The patients were placed in comfortable scanning chair with the both hands positioned consecutively in the magnet in neutral rotation with the thumb up and the fingers extended The imaging protocol consisted from a coronal and axial T_1 and T2 weighted spin echo images. I.v. enhancing by gadolinium was not used. The imaging parameters For the T_1 weighted spin echo sequences were as follows: TR 500 ms, TE 18 ms, matrix size 256 × 192, FOV 200 mm, slice thickness 1 mm, and distance factor 0.1. The approximate imaging time for each patient was approx. 30 minutes.

The MR images were all scored by a rheumatologist experienced in reading MR images of the RA joints, who was unaware of the clinical and radiographic findings. Synovitis, erosions and bone marrow oedema were evaluated by OMERACT-RAMRIS scoring reference atlas, by Ejbjerg B. et. al. [13].

Plane X-ray examination

Radiographs of the wrist and hand were made in the antero-posterior projection. Cumulative radiation dose per patient was 0.04 msv.

A second observer, an experienced radiologist who was unaware of the MRI and clinical findings, evaluated all the radiographs for the presence and number of bony erosions by Sharp / Van Der Heijde method – wrist bones, ulna and radius distal junction area and foot bones bilaterally. .

Laboratory analyses

Serum C reactive protein (CRP), erythrocyte sedimentation rate (ESR), and rheumatoid factor (RF) were measured by standard methods (Speransky modification in last case).

Statistical analysis

Correlations were assessed by Spearman's test of rank correlation. Values $p<0.05$ by a two tailed test were considered to be significant.

Results

Bone erosions

Extremity MRI (E-MRI) was made of a total 4000 hand bones (20 bone each hand) and plane X-ray studies was made of a total of 7400 hand and foot single bones (+17 bones each foot). In the wrist, E-MRI detected erosions in 70 patients, number of erosions per patient was usually more then 2 (only 2 patients had one erosion), whereas by X-ray examination only 20 erosions were detected (table 1). Similar by ratio picture was received when calculated MCP and wrist joints erosions detected separately. The resulting MRI to X-ray erosion detection ratio was 7:1. 2 radiographic erosion was not detected by MRI.

Table 1 Comparison of amount of erosions detected by MRI and X-ray of hand (distal area of radius& ulna, art. radiocarpalis, wrist joints and bones, MCP joints) (erosions detected at foot films are not included)

	X-ray	E-MRI
Erosions (n=4000) detected	10	70
Erosions (n=4000) not detected	90	30

Difference is significant ($p<0.05$)

Synovitis evaluation

According to OMERACT-EULAR scoring system [13], synovial membrane hypertrophy grades ranged from 0 to 3, Clinical assessment data and MRI data were evaluated. MRI synovitis, defined as marked signal increase in the synovium, in both T1 and T2 regimes, was found in 95 patients, while clinical synovitis (joint swelling and/or tenderness) was diagnosed in 48 patients. None of MCP joints with clinical synovitis did not show MRI synovitis, $p<0.001$. 47% of the joints without clinical soft tissue swelling or effusion showed synovitis on E-MRI. No one joint with clinical signs of inflammation was recognized as synovitis on E-MRI.

Evaluation of correlation between ESR, C-RP, rheumatoid factor titer, X-ray and MRI Erosions Score

After implementation of range correlation analysis, and split of 100 patients into groups, according to their clinical investigations data, following results were received (table 2). Spearman's coefficient of range correlation (r_s) was calculated in each case, according to the method described [14].

Table 2. Results of correlation check among clinical investigations data and radiological erosions score.

	Compare with X-ray	Compare with MRI
ESR (erythrocyte sedimentation rate) n = 7	$r_s = 0.893$ Correlation is significant ($p<0.01$)	$r_s = 0{,}74$ Correlation is significant, $p<0.05$
C-RP n=26	$r_s = 0.178$ Correlation results are not significant = $p<0.5$	$r_s = 0{,}25$ Correlation results are not significant = $p<0.2$
RF (rheumatoid factor) n=7	$r_s = 0{,}634$ Correlation results are not significant = $p<0.2$	$r_s = 0{,}36$ Correlation results are not significant = $p<0.5$

Discussion

There are a lot of existing evidences, that MRI is more sensitive in identifying joint abnormalities than clinical and conventional X-ray examination [6-9, 13-17]. There were a lot of investigations on this matter since last years, but none of them was performed in former USSR territory, as we know. So, we would like to consider ourselves as pioneers in this area of investigations.

In our study, an extremity-dedicated, low-field MRI unit was used to obtain MR images of the hands in untreated patients with early rheumatoid arthritis. Our study showed, that X-ray examination only disclosed about 10% of the erosions visible on MRI. This figure is comparable to other studies data.[6-9, 14-18]. However, the exact accuracy of MRI detection of erosions and synovitis has not been verified yet.

In our study a positive correlation was found between X-ray, MRI erosions score and ESR. A similar correlation was not found for RF and C-RP data. This discrepancy may reflect absence of direct link between RF level and erosions appearance. Discrepancy between C-RP and erosions data, both in X-ray and MRI investigations remains unclear and demand further investigation. Also, data received confirms once again existing evidences that plane X-ray and low-field E-MRI has, at least, similar characteristics of correlation with clinical data, taking into account only erosions scoring data.

Recent discoveries of anti-cyclic citrullinated peptide antibody (A-CCP) role in pathogenesis of rheumatoid arthritis [19] requires investigation of it’s possible correlation with MRI and X-ray data.

Recent studies have suggested that MRI is an indicator of subsequent erosive progression.[9, 20-21]. Works of F. McQueen and coworkers indicated that baseline MRI findings may be of prognostic value for later joint destruction [20]. In contrast, Klarlund et al, found no correlation between baseline MRI and erosive progression, but a very low progression rate in their cohort in combination with a relatively short follow up period may account for this discrepancy [21].

The relation between MRI lesions and erosions detected by X-ray examination is still an opened question [22]. Our study has shown that even at a very early stage of the disease affected joints are destructively damaged at multiple sites. Probably, these lesions will grow and fuse into erosions which can be detected by X-ray examination, in case of no treatment will be done. Longitudinal studies are still needed to clarify issue of their fate, with and without treatment.

In summary, low field E-MRI gave possibility of detailed visualization of inflammatory and destructive lesions in patients with early RA. Further studies and comparisons with other techniques – high field MRI, CT, USE etc are needed, but the combination of low costs, more comfortable patient positioning, and the promising preliminary results (sensitivity, accuracy and specificity) [6] suggests a big potential for the E-MRI technique in the evaluation of early rheumatoid and unclassified arthritis.

References

[1] Nasonova V.A., Nasonov E.L., ed. Rationale for drug therapy of rheumatic diseases. In: Rationale for drug therapy series, vol. III. Moscow, Litterra Publishers, 2003; 86.

[2] van der Bijl AE, Goekoop-Ruiterman YP, de Vries-Bouwstra JK, et al.. Infliximab and methotrexate as induction therapy in patients with early rheumatoid arthritis. Arthritis Rheum 2007 Jul;56(7):2129-34

[3] Emery P. Early rheumatoid arthritis: therapeutic strategies. Scand J Rheumatol Suppl 1994;100:3-7

[4] Emery P. Therapeutic approaches for early rheumatoid arthritis. How early? How aggressive? Br J Rheumatol 1995;34(suppl 2):87-90.

[5] Matsuda Y, Yamanaka H, Higami K, Kashiwazaki S. Time lag between active joint inflammation and radiological progression in patients with early rheumatoid arthritis. J Rheumatol 1998;25:427-432

[6] Ejbjerg BJ, Narvestad E, Jacobsen S, et al Optimised, low cost, low field dedicated extremity MRI is highly specific and sensitive for synovitis and bone erosions in

rheumatoid arthritis wrist and finger joints: comparison with conventional high field MRI and radiography. Ann Rheum Dis. 2005 Sep;64(9):1280-7. Epub 2005 Jan 13

[7] Jorgensen C, Cyteval C, Anaya JM, et al. Sensitivity of magnetic resonance imaging of the wrist in very early rheumatoid arthritis. Clin Exp Rheumatol 1993;11:163-168

[8] McQueen FM, Stewart N, Crabbe J, *et al*. Magnetic resonance imaging of the wrist in early rheumatoid arthritis reveals a high prevalence of erosions at four months after symptom onset. Ann Rheum Dis 1998;57:350-356

[9] Østergaard M, Hansen M, Stoltenberg M, *et al*. Magnetic resonance imaging-determined synovial membrane volume as a marker of disease activity and a predictor of progressive joint destruction in the wrists of patients with rheumatoid arthritis. Arthritis Rheum 1999;42:918-929

[10] Jevtic V, Watt I, Rozman B, Presetnik M, *et al*. Prognostic value of contrast enhanced Gd-DTPA MRI for development of bone erosive changes in rheumatoid arthritis. Br J Rheumatol 1996;35(suppl 3):26-30.

[11] Arnett FC, Edworthy SM, Bloch DA, *et al*. The American Rheumatism Association 1987 revised criteria for the classification of rheumatoid arthritis. Arthritis Rheum 1988;31:315-324

[12] Scott DL, van Riel PL, Van der Heijde, et al (on behalf of the EULAR Standing Committee for International Clinical Studies including Therapeutic Trials—ESCISIT (Chairman: PLCM van Riel). *EULAR handbook of clinical assessments in rheumatoid arthritis.* The Netherlands: Van Zuiden Communications, 2000.

[13] Ejbjerg B, McQueen F, Lassere M, et al. The EULAR-OMERACT rheumatoid arthritis MRI reference image atlas: the wrist joint.. Ann Rheum Dis 2005 Feb;64 Suppl 1:i23-47.

[14] Glantz S. A. Primer of biostatistics, 4th edition. McGraw-Hill Inc, 1994, Praktika, Moscow, 1999

[15] McGonagle D, Conaghan PG, O'Connor P, Gibbon W, Green M, Wakefield R, *et al*. The relationship between synovitis and bone changes in early untreated rheumatoid arthritis: a controlled magnetic resonance imaging study. Arthritis Rheum 1999;42:1706-1711

[16] Ejbjerg BJ, Vestergaard A, Jacobsen S, et al Conventional radiography requires a MRI-estimated bone volume loss of 20% to 30% to allow certain detection of bone erosions in rheumatoid arthritis metacarpophalangeal joints. Arthritis Res Ther. 2006;8(3):R59. Epub 2006 Mar 15.

[17] Lindegaard H, Vallø J, Hørslev-Petersen K, et al. Low field dedicated magnetic resonance imaging in untreated rheumatoid arthritis of recent onset. Ann Rheum Dis. 2001 Aug;60(8):770-6.

[18] Østergaard M, Stoltenberg M, Gideon P, et al. Changes in synovial membrane and joint effusion volumes after intraarticular methylprednisolone. Quantitative assessment of inflammatory and destructive changes in arthritis by MRI. J Rheumatol 1996;23:1151-1161

[19] del Val del Amo N, Ibanez Bosch R, Fito Manteca C, et al. Anti-cyclic citrullinated peptide antibody in rheumatoid arthritis: relation with disease aggressiveness. Clin Exp Rheumatol 2006 May-Jun;24(3):281-6

[20] McQueen FM, Benton N, Crabbe J, Robinson E, et al What is the fate of erosions in early rheumatoid arthritis? Tracking individual lesions using x rays and magnetic resonance imaging over the first two years of disease. Ann Rheum Dis. 2001 Sep;60(9):859-68

[21] Klarlund M, Østergaard M, Jensen KE, et al, and the TIRA group. Magnetic resonance imaging, radiography, and scintigraphy of the finger joints: one year follow up of patients with early arthritis. Ann Rheum Dis 2000;59:521-528

[22] Østergaard M. MRI bone erosions and MRI bone lesions in early rheumatoid arthritis [letter], with reply by McGonagle, Conaghan and Emery. Arthritis Rheum 2000;43:949-950

Radiological Diagnostics of Pancreatic Pseudocysts

O.V. Masina, M.L. Chehonatskaja, V.N. Priezzheva, E.B. Iljasova, V.V. Zuev

Saratov State Medical University, 410012, Bolshaya Kazachya str, 112, Saratov, Russia
e-mail: masinaoksana@mail.ru

Pseudocysts are best defined as a localized fluid collection that is rich in amylase and other pancreatic enzymes, that has a nonepithelialized wall consisting of fibrous and granulation tissue, and that usually appears several weeks after the onset of pancreatitis. The pathogenesis of pseudocysts seems to stem from disruptions of the pancreatic duct due to pancreatitis and extravasation of enzymatic material.Pancreatic pseudocysts can be single or multiple. Multiple cysts are more frequently observed in patients with alcoholism, and they can be multiple in about 15% of cases. Size varies from 2-30 cm [Nguyen B.L. et al, 1991]. About one third of pseudocysts manifest in the head of the gland, and two thirds appear in the tail. This volumetric formations displace and squeeze surrounding organs: shifts forward a stomach, moves apart two parts of duodenum loop, and squeezes the common bile duct.

The purpose of the present research was the evaluation of diagnostic opportunities and the relative characteristics of various diagnostic imaging modalities (conventional X-ray, ultrasound, computer tomography, MRI) in diagnostics and staging of pancreatic pseudocysts.

Materials of research: 15 patients with abdominal lesions evaluated by means of dynamic contrast material–enhanced MR imaging with serial breath-hold spoiled gradient-echo acquisitions in LDC-MIBS-Saratov with diagnoses: «pancreatic cysts» - (4), «retroperitoneal space cysts» - (8). "Pancreatonecrosis" - (3). 11 patients were male, and 4-female.

Methods of research: MRI was performed on device Siemens-Expert 1,0 Tl, abdominal CT scan on device " Somatom-CR " " Siemens ". Criterions of accuracy of diagnostic methods were operative treatment and pathological examinations results.

Findings: In conventional X-ray contrast investigation in 11 patients indirect attributes of volumetric formation in pancreas were fixed. Between 11 patients with fixed pancreatic pseudocysts in 7 patients formation was localized in the body of pancreas, in 4 patients – in the tail of pancreas. Imaging modalities allowed to reveal liquid formation at abdominal ultrasound as anechoic space, abdominal CT - hypodensive formation (9-12 HU), MRI- hypointensive on T1-weigted and hyper-on T2- weigted images unimodal signal.

Differential diagnosis with true cyst: connection with an acute pancreatitis (in 12 patients), an idiopathic pancreatonecrosis (in 3 patients); stages in process (1 stage – acute inflammatory-in 3 observations, 2 stage- stationary cyst in 8 observations); roughness of contours and bizarre shape- "stamp" of interorganic space in this anatomical area; the large dimensions up to 20 cm and more (in 6 patients). All these attributes have allowed the conclusion about pancreatic pseudocysts.

Organ of origin was fixed in MRI in 14 patients, i.e. in 100 % of cases (11- pancreatic pseudocysts, and 3- kidney cysts), in abdominal ultrasound in 7 patients- 50 % (5- pancreatic pseudocysts, 2- kidney cysts,), in abdominal CT without contrast in 1 patient in 11 % of cases, with contrast in 4 patients from 4 with performed evaluation-in 100 % (pancreatic cysts). Stages were fixed with MRI in 11 patients-in 100 % cases (3 observations -1stage, in 8 observations -2 stage), with abdominal ultrasound in 2 patients- in 22 % (2 stage), at abdominal CT with contrast in 4 patients - in 100 % of cases (1 observation -1 stage, in 3 observations – 2 stage).

As an example it is resulted the following observation:
Patient L, age 34 male. History: complaints to pain in the top parts of abdomen, fever up to 38C, sense of abdominal distention. Abdominal ultrasound -acute pancreatitis.
Abdominal CT (fig. 1) total pancreonecrosis (it is marked by an arrow).
MRI (fig. 2) a pancreatonecrosis + pancreatic pseudocysts 1stage (it is marked by an arrow). The decision on conservative tactics of treatment was accepted, the conforming therapy is appointed.

Fig.1 Abdominal CT

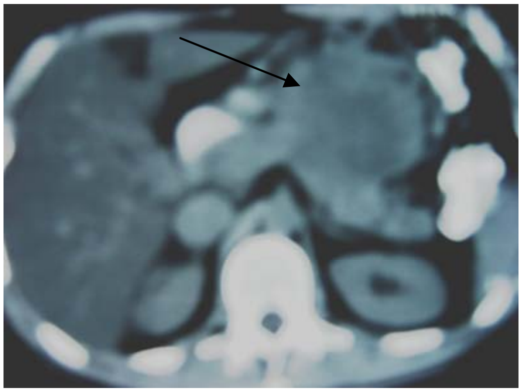

Fig.2 MRI (T2-weighted)

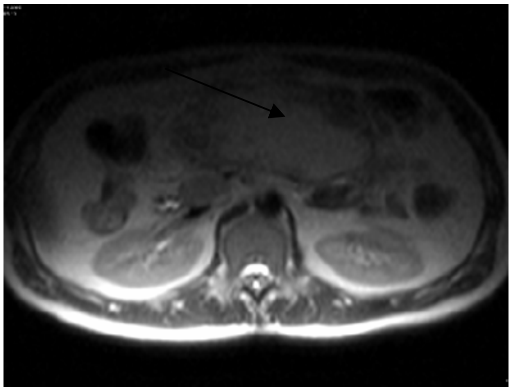

Through 3 months. Ultrasound data - liquid formation of retroperitoneal space. Abdominal CT data (fig. 3) - forming pancreatic pseudocysts.MRI data (fig. 4) pancreatic pseudocyst 1 stage.

Fig.3 Abdominal CT.

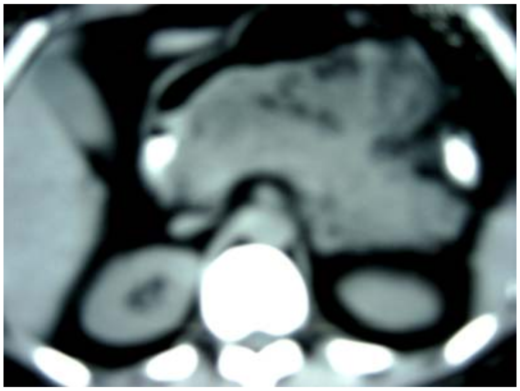

Fig.4 MRI (T1-weighted)

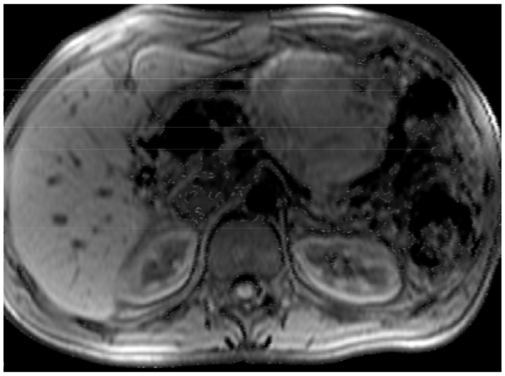

Through 6 months.
MRI (fig. 5) pancreatic pseudocysts 2 Stage.

This case has allowed to observe all stages of formation of pancreatic pseudocysts and to define that MRI allows receiving the greatest volume of the information in all stages of pseudocysts development.

Fig.5 MRI 3D-reconstruction (pancreatic pseudocyst is marked by an arrow)

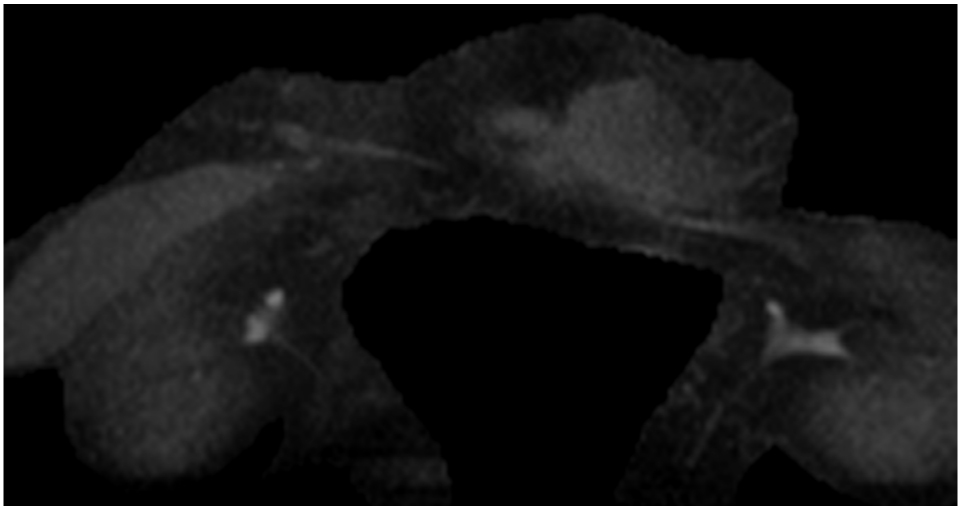

Conclusions

1. Abdominal ultrasound is screening method of inspection and allows to reveal in most cases liquid formation in retroperitoneal space, however, technique is limited by operator skill, the patient's habitus, and overlying bowel gas. As such, ultrasound is not the study of choice for diagnosis.
2. The roentgenoscopy of a stomach is a necessary part of diagnostic algorithm in all patients with suspicion on pancreatic pseudocysts. Technique helps to reveal topographical interrelations of a stomach and surrounding organs.
3. Abdominal CT with contrast enhancement and MRI are the most reliable diagnostic methods pancreatic pseudocysts revealing, allowing to estimate character of volumetric formation }, its stage, localization that is necessary for tactics of operative or conservative treatment choice. MRI is useful in detecting a solid component to the cyst and in differentiating between organized necrosis and a pseudocyst.
4. For specified diagnostics of pancreatic pseudocysts complex radiological research including above algorithm of methods is necessary.

References

[1] V.V.Mitkov. A clinical management{manual} on ultrasonic diagnostics.-Moscow.-1996.-356c.

[2] N.S. Ignashin Diagnostics and treatment. - Moscow.-1997.-165c

[3] П.Е.С. Пальмер the Management{Manual} on ultrasonic diagnostics. - Женева.-2000.-375c.

[4] S.A. Panfilov, E.V. Panfilova. Diagnostika of diseases of a liver, a pancreas, a lien and paranephroses with a course pathological анатомии.-Moscow.-2000.-175c.

[5] M.G. Prives, N.K. Lysenkov, V.I. Bushkovich Anatomy.-Ленинград.-1969.-814c.

[6] R.D. Sinelnikov the Atlas of anatomy the person-Moscow.-1968.-.-394c.

[7] T.N. Trofimova .Luchevaja anatomy человека.-2005.-493с.

[8] Nguyen BL, Thompson JS, Edney JA: Influence of the etiology of pancreatitis on the natural history of pancreatic pseudocysts. Am J Surg 1991 Dec; 162(6): 527-30

[9] Sahani D.V., Kadavigere R., Saokar A.: Cystic pancreatic lesions: a simple imaging-based classification system for guiding management. Radiographics 2005 Nov-Dec; 25(6): 1471-84.

[10] Yeo C.J., Bastidas J.A., Lynch-Nyhan A.: The natural history of pancreatic pseudocysts documented by computed tomography. Surg Gynecol Obstet 1990 May; 170(5): 411-7.

MRI Cystourethrography

V.V. Zuev, M.L. Chehonatskaja, V.N. Priezzheva, E.B. Iljasova,. O.V. Masina

Saratov State Medical University, 410012, Bolshaya Kazachya st 112, Saratov, Russia

e-mail: zuev.viktor.sgmu@mail.ru

Last three decades are characterized with wide occurrence in diagnostic medicine the large group of new highly effective techniques of a MRI and MRS. MRI allows an accurate study of the different components of the pelvic floor by means of following techniques: standard MRI, diffusion - weighed MRI, dynamic research with application paramagnetic contrast materials and fiber tracing, MRS with visualization of relative concentration of various substances in different tissues. We suggest adding two variants of MRI cystourethrography – voiding and ascending. The following similar techniques are known: X-ray cystourethrography — method of the conventional x-ray image of urethra after filling by his{its} liquid or gaseous contrast substance. Cystourethrography has been offered by Cunningham in 1910. In Russia cystourethrography has been introduced into practice by A.P. Frumkin in 1924. Liquid or gaseous contrast substances could be used for artificial contrasting. The contrast substance should be inserted into the urethra by Jane syringe with Tarnovsky rubber tip slowly, without big pressure for reflux avoidance. For best image of a back urethra the bladder is filled with a contrast liquid in amount of 150-200 ml and force the patient to urinate, making a x-ray picture during voiding time. This technique-descending cystourethrography. Besides of back urethra evaluation during this research functional changes of the pelvic floor could be revealed.

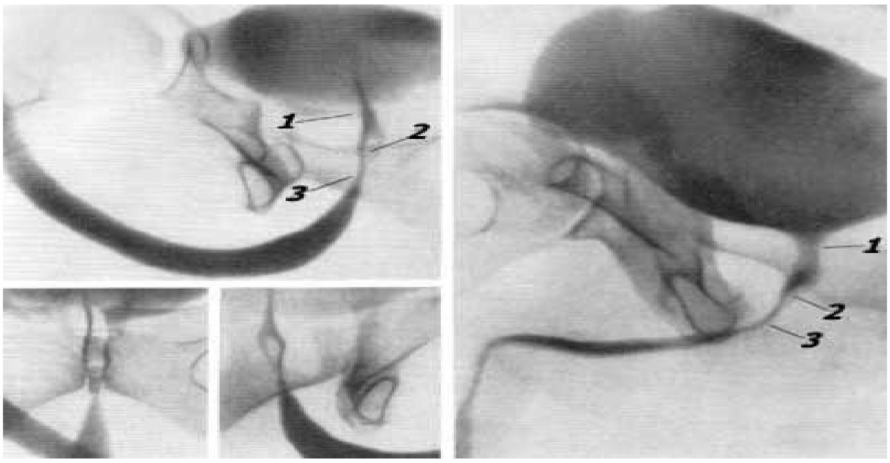

Normal x-ray cystourethrogram: 1 - internal sphincter; 2 – seed tuberculum; 3 - external sphincter.

The functional ultrasound method-« real time» research of bladder and back urethra with the help of rectal probe during voiding time, allowing to estimate not only sizes of bladder and urethra, but also their dynamic changes and a condition of wall.

Disadvantages of these techniques and a standard MRI are:

1. Impossibility of display and a complex estimation of all parts of the urinal channel during voiding time.
2. Invasive character of these techniques, infection complications and allergic reactions possibility. Additionally in young people high radiation dose in genitals zone is

undesirable.

3. With pelvis MRI it is impossible to estimate: a functional condition of a bladder and a urethra, a condition and change of all bodies and fabrics of a small basin during time мочеиспускания.

We develop methods voiding and ascending cystourethrography. Voiding cystourethrography method: during voiding time researches are performed with super fast sequences not sensitive to impellent artifacts, with scans direction in saggital planes, with an opportunity of the subsequent computer processing and formation of the video clip displaying in a mode of pseudo-real time dynamic changes of pelvic tissues and organs during voiding act.

Bladder filling occurs physiologically or is accelerated by means of water loading. This technique is truly functional because investigates the basic function of a bladder and a urethra - removing liquid. Procedure technique: plastic basin is given to the patient. Research begins since programs and the received images allow features of an anatomical structure of pelvic organs of this exact patient to be defined. Proceeding this information to focus in saggital plane scan package; the patient is offered to urinate and simultaneously series of programs are made (duration of each program — 2 seconds, amount of recurrences 30); processing of parameters is carried out on end of all series; images are processed by means of the program and the videoloop is formed of received "staff". This method could be performed independently, but it is more expedient to use it in complex with all MR methods of pelvis research.

Ascending cystourethrography techniques consists in introduction in a urethra isotonic solution or a weak solution of a paramagnetic contrast using Jane syringe with rubber tip with reception T2 - weighed images in case of isotonic solution or T1 -weighed images in case of Gd-DTPA. In the closed types of MRI it is necessary to use for instillation lengthened Foley catheter or special clips on a urethra, outcoming of the entered solution avoidance; in open types of MRI tomographs it is possible to perform this procedure with Jane syringe with rubber tip. This method allows to diagnose pathological processes in urethra, processes in bladder and urethra in pelvic traumas, communication with voiding channel and a bladder liquid masses in pelvis.

To advantage of this method - possibility of data processing and dynamic virtual urethrocystoscopy and virtual urofluometry.

Principles put in a basis of methods voiding and ascending cystourethrography allow applying their analogues to research motor function of different organs and systems. Development already known and new techniques of medical visualization based on the phenomenon of MRI gives the increasing amount of the diagnostic information. To understand opportunities and the importance of techniques - the main purpose of work engaged MRI practical doctors and scientists.

Voiding MRI cystourethrography.

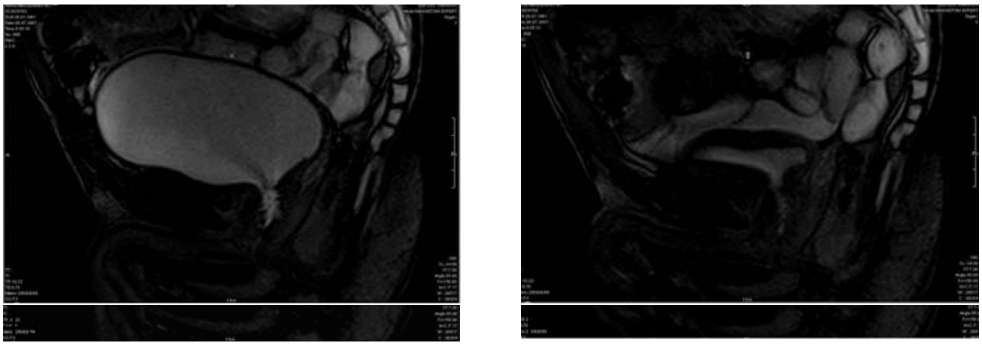

2 s

12 s

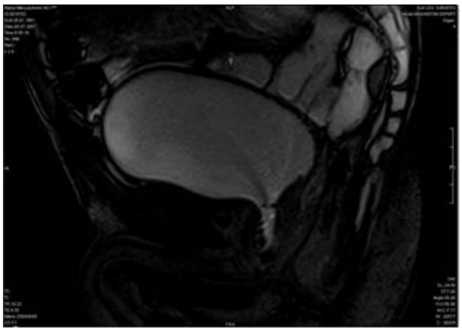

6 s

16 s

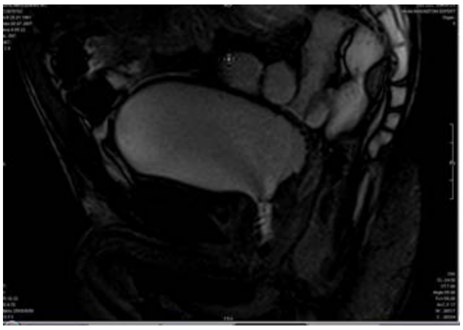

8 s

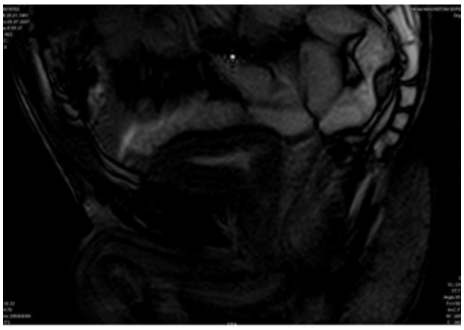

18 s

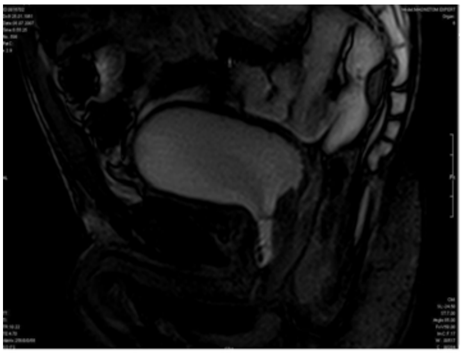

10 s

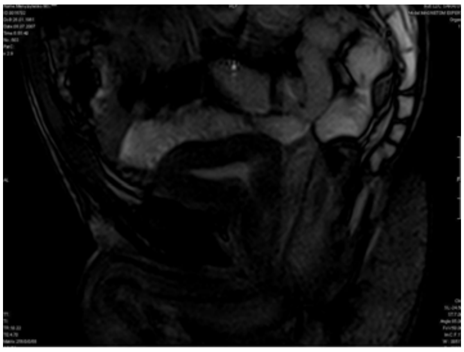

20 s

References

[1] V.V.Mitkov. A clinical management{manual} on ultrasonic diagnostics.-Moscow.-1996.-356c.

[2] N.S. Ignashin Diagnostics and treatment. - Moscow.-1997.-165c

[3] П.Е.С. Пальмер the Management{Manual} on ultrasonic diagnostics. - Женева.-2000.-375c.

[4] M.G. Prives, N.K. Lysenkov, V.I. Bushkovich Anatomy.-Ленинград.-1969.-814c.

[5] R.D. Sinelnikov the Atlas of anatomy the person-Moscow.-1968.-.-394c.

[6] T.N. Trofimova .Luchevaja anatomy cheloveka.-2005.-493c.

[7] Hricak H., Williams R.D. et al. Anatomy and pathology of the male pelvis by magnet resonance imaging.- AJR,1983, 1441, 1101.

[8] Pytel' A.Ya., Pytel' Yu.A. Rentgendiagnostika urologicheskih zabolevaniy. M.: Meditsina, 1966.

Novel Cyclic Derivatives of Substituted Iminoquinones or Aminophenols: NMR Study

A.S. Shavyrin, Yu.A. Kurskii, N.O. Druzhkov

G. A. Razuvaev Institute of Organometallic Chemistry of Russian Academy of Sciences, 603600 49 Tropinina str., Nizhny Novgorod, Russian Federation

e-mail: andrew@iomc.ras.ru

Aryl substituted iminoquinones are quinone derivatives with several reaction centres capable to enter into various chemical reactions. These compounds are used as a chelating agents, dyes and ligands in compounds with coordination to metal. Possibility of iminoquinones and aminophenols application in various reactions explains interest to their chemical properties and reactivity. Reactions of some substituted iminoquinones and aminophenols leading to heterocycles were investigated in this study. Tendency of iminoquinones to form heterocyclic compounds is already known. One of examples is shown below.

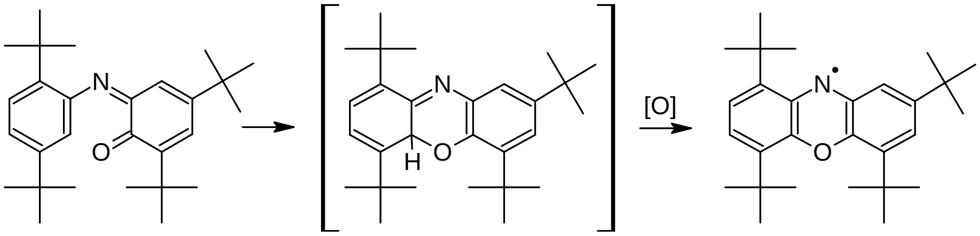

Iminoquinone cyclization leads to derivative of phenoxazine which easily oxidized to stable radical [1]. Examples of *N*-aryl-phenantren-*o*-iminoquinones cyclizations are shown in article [2].

Heterocycles formed from substituted iminoquinones often have complicated structure with asymmetric centers. 1D and 2D NMR is one of the most informative and useful method for investigating such compounds. NMR spectra are highly dependent on symmetry of molecule and exhibit a lot of information in case of compound with asymmetric elements, such as iminoquinone derivatives.

A successful application of 1D (^{1}H, ^{13}C, DEPT) and 2D (COSY, NOESY, CHCORR, COLOC) NMR methods to elucidation of structure of complicated heterocyclic derivatives of N-aryl substituted iminoquinones were conducted for compounds **2a**-**b** [3].

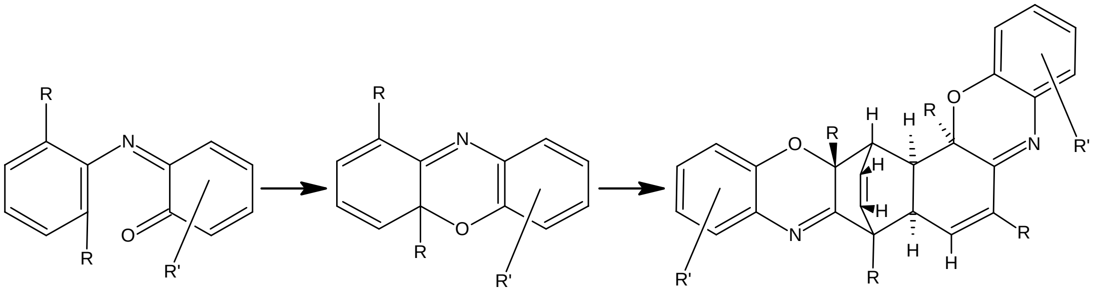

1a R=2,5-Me, R=3,5-di-*tert*-Bu
1b R=2,5-*iso*-Pr, R=3,5-di-*tert*-Bu
1c R=2,5-Me, R=3-Cl-4,6-di-*tert*-Bu
1d R=2,5-Me, R=3,4,6-*iso*-Pr

2a-d

It was shown that cyclization of iminoquinones **1a-d** is followed by Diels-Alder reaction with formation of **2a-d**. 2D NMR NOESY spectrum of **2b** contain a lot of information about structure of compound and exhibit some patterns characteristic to compounds with chiral elements. One of them is a nonequivalence of methyl substituents in *iso*-propyl group in NMR spectra, as shown on ^{1}H NMR spectrum (above NOESY spectrum). Difference of chemical shift for methyl substituents of each *iso*-propyl group is often dependent on distance from chiral center.

All methyl groups of all *iso*-propyl substituents of **2b** are nonequivalent. This is a clear mark of chiral elements presence.

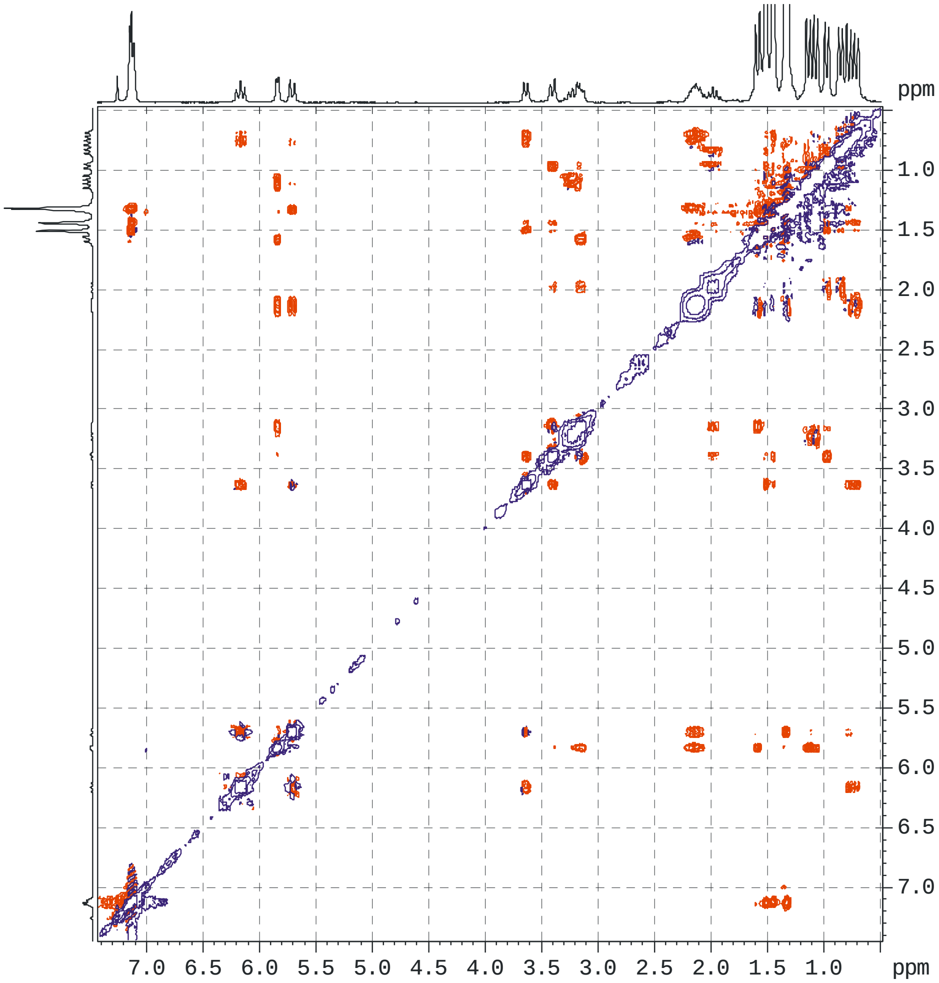

NOESY spectrum of compound **2b**. t_{mix}=250ms. NOESY and COSY spectra were used for elucidation of structure and assignment of 1H spectra of **2a-d**.

NOESY NMR spectra allowed us to find relative configuration of all chiral centers. Despite of complicated structure of products, NMR spectra proved as that compounds **2a-d** share the same structure and configuration of chiral centers. The reaction leads to only one of many possible products with definite chiral centers configuration. No any other isomers or diastereomers were found in cases **2a-d**. Therefore this reaction is typical for appropriate iminoquinones and features high yields and high stereoselectivity.

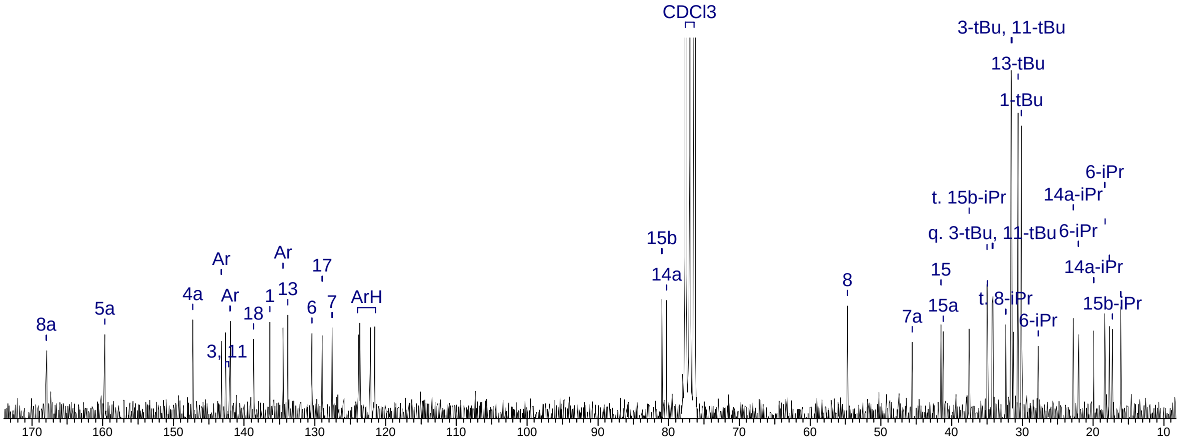

13C NMR spectra of **2b** and assignment according to COLOC and CHCORR spectra.

Aminophenols are closely related to iminoquinones and may be obtained by their reduction. We have investigated formation of benzoxazole or bezoxazine compounds (**3**,**4**) from N-substituted aminophenols. Structures of such compounds may be easily determined even by 1H NMR spectrum, since NMR spectra of source and product are clearly different in a point of cyclization.

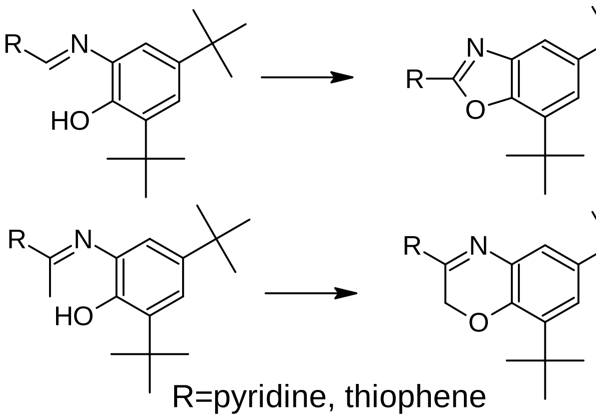

3

4

R=pyridine, thiophene

Another cyclization was studied for compounds **5a,b**. Structures of **6a,b** were elucidated by 1D and 2D NMR. Products **6a,b** have 2 chiral centers, but their NMR spectra are relatively simple since molecules have no any group sensitive to chiral elements.

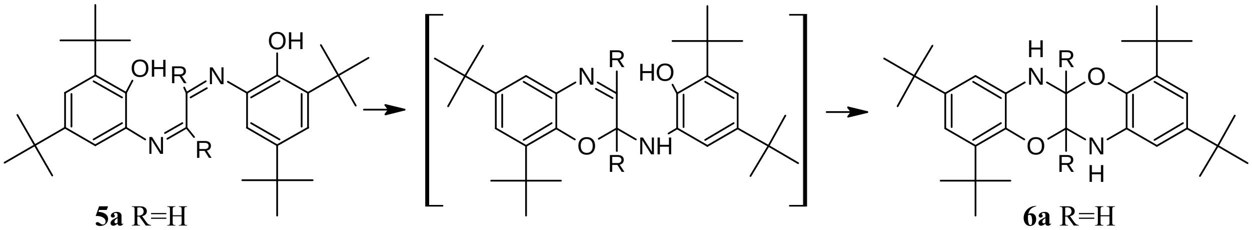

5a R=H

5b R=Me

6a R=H

6b R=Me

There are 2 diastereomers possible, but ^{13}C NMR shows no splitted signals. This means that only 1 diastereomer exist and reaction goes stereospecifically.

Other compounds were produced from **7** and **9**.

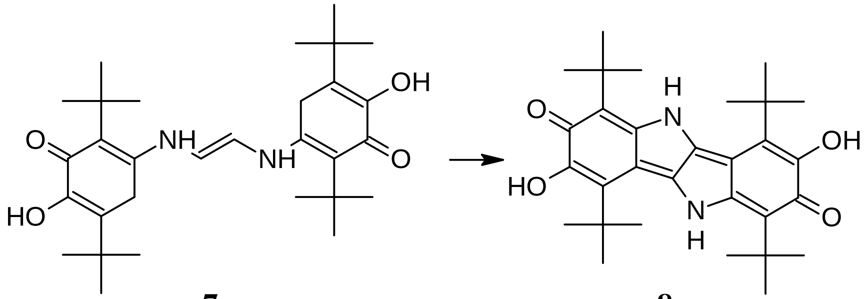

7 **8**

Despite of similar structures of compounds **8** and **10** their NMR spectra are quite different due to difference in symmetry of molecules and double bond placement. Structures of **8** and **10** were determined by 1D and 2D NMR.

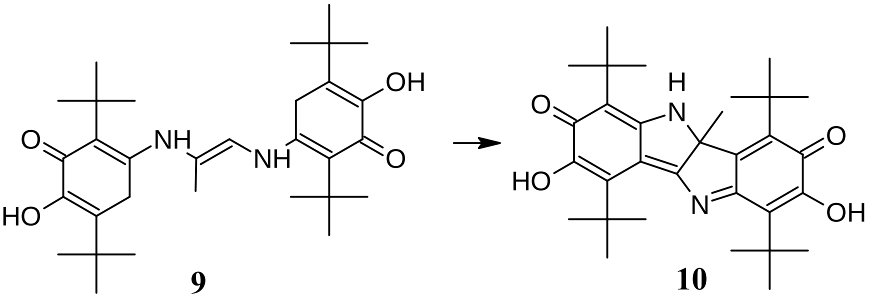

9 **10**

NMR spectra of compounds with two or more chiral elements exhibit one more interesting pattern. Since diastereomers are chemically nonequivalent, their NMR spectra are different. It's clearly visible in ^{13}C NMR spectra since some signals are usually divided into group of signals belonging to different diastereomers.

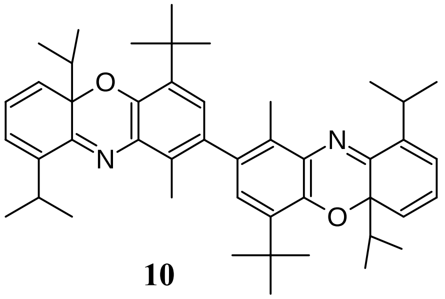

10

Product **10** contains 2 chiral centers and one chiral axis. ^{13}C NMR signals of **10** are divided into groups of lines. This NMR spectrum allows us to distinguish between signals belonging to different diastereomers, since integral intensity between lines in each groups is almost same in each group.

Almost all structures revealed in this paper were elucidated by 1D and 2D NMR spectroscopy and approved by other methods. Obtained results showed not only a moderate potential of iminoquinones and related aminophenoles as a precursors of heterocyclic compounds, but also ability of modern NMR methods to solve complex structure problems.

Acknowledgements

This research was supported by Russian President's grant supporting scientific schools: 4947.2006.3 and Russian Foundation of Basic Research (grant: 07-03-00711-a).

[1] G.A. Abakumov, N.O. Druzhkov, Yu.A. Kurskii, L.G. Abakumova, A.S. Shavyrin, G.K. Fukin, A.I. Poddelskii, V.K. Cherkasov, L.S. Okhlopkova Quinoneimines and aminophenols as precursors of new heterocycles. Russ. Chem. Bull. Int. Ed., 2005, V. 54, №11, p 2571

[2] G.A. Abakumov, V.K. Cherkasov, N.O. Druzhkov, Yu.A. Kurskii, G.K. Fukin, L.G. Abakumova, T.N. Kocherova. Synthesis, structures, and properties of novel *N*-aryl-phenantren-*o*-iminoquinones. Synthetic Commun. 2006, V.36, p.3241.

[3] A.S. Shavirin, G.A. Abakumov, Yu. A. Kurskii, N.O. Druzhkov NMR study of products of thermal transformation of substituted N-aryl-o-quinoneimines. Russ. Chem. Bull. Int. Ed., 2003, V.52, №3, p 712

Models of Paramagnetic Centres Gd^{3+} in Tetrahedral Yttrium Clusters in Cadmium Fluoride

A.V. Fokin, V.B. Guseva, M.Yu. Artyomov

Ural State University, 620083, pr. Lenina 51, Yekaterinburg, Russia

e-mail: andrey.fokin@rambler.ru

The electron paramagnetic resonance spectrum contains unique data about structure of impurity ion nearest environment in crystal which are concluded in values of Zeeman and zero field splittings (ZFS). The volume of this information grows with increase in spin of the paramagnetic defect. The following analysis (construction of the spin-Hamiltonian) allows determining a symmetry class of the paramagnetic ion position and in case of existence anisotropic external influence its symmetry group.

Table 1. Spin-Hamiltonian parameters for monoclinic and trigonal Gd^{3+} centers in $Y_xGd_yCd_{1-x-y}F_{2+x+y}$. (standard deviation *f* and parameters *bnm* are given in MHz). T=300K.

	C_S	C_{3V}	C_S
g_x	1.988(6)	1.992(5)	1.992
g_y	1.991(6)	1.992(5)	1.992
g_z	1.991(3)	1.992(5)	1.992
b_{20}	-345(4)	-200(6)	-600
b_{21}	287(24)		
b_{22}	87(14)		
b_{40}	25(2)	80(3)	
b_{41}	3(12)		
b_{42}	17(10)		
b_{43}	-554(40)	2300(60)	
b_{44}	-30(15)		
b_{60}	-2.4(15)	-17(3)	
b_{61}	-7(14)		
b_{62}	-4(14)		
b_{63}	1(30)	-270(50)	
b_{64}	-5(20)		
b_{65}	-60(80)		
b_{66}	7(25)	490(50)	
f	12	25	

The EPR spectrum of $Y_xGd_yCd_{1-x-y}F_{2+x+y}$ (x = 0.03, y ≤ 0.001) single crystals was studied in works [1-2]. Besides already known cubic center, trigonal and two monoclinic centers of Gd^{3+} ions which have been not observed earlier in these crystals were found. Spin-Hamiltonian parameters are listed in Table 1 ($z \| C_3$, $y \| C_2$).

It is necessary to note, at rotation of coordinate system around of the axis *y* the value ($b_{21}^2+b_{22}^2$) of the intensive monoclinic center has a minimum near of orientation defined by Euler's angles $\alpha = 0$, $\beta = -7.17°$, $\gamma = 0$ (b_{21} changes a sign), thus $|b_{20}|$ shows a maximum. These facts: maximization of the parameter b_{20} and b_{21} tend to zero determine orientation of the pseudo-symmetry axis of the fine structure second-rank tensor. The nearness of this axis to C_3 means that observable monoclinic center most likely originate due to distortions of the C_{3v} symmetry center.

In works [3-4] CdF_2–RF_3 (*R* = Sm – Lu, Y) solid solutions with high contents (~10%) of the rare-earth (RE) metal trifluorides were studied by using x- ray diffraction. It was found that tetrahedral RE (or yttrium) clusters exist in these solid solutions (Fig.). There is an opportunity of the incomplete replacement of the matrix cations by RE or yttrium ions in clusters, so for a part clusters the problem of the extra charge compensation is solved. On the basis of these data a conclusion has been made, that the found centers are caused by Gd^{3+} ions in tetrahedral clusters: $[Y_3GdF_{26}]^{1+}$ (C_{3V}), $[CdY_2GdF_{26}]^0$ (C_S), $[Cd_2YGdF_{26}]^{1-}$ (C_S), where in round brackets it is the

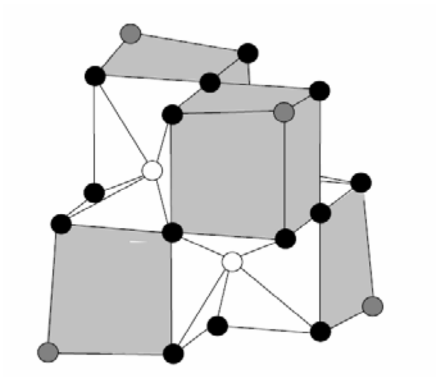

Fig. The structure of tetrahedral rare earth cluster.

symmetry group of the Gd^{3+} ion. The superscripts specify difference between a charge of defective cluster and a fragment of a lattice replaced by it. So, it's possible correlate found trigonal center Gd^{3+} with cluster $[Y_3GdF_{26}]$, but to determine correspondence between the remained types of clusters and two monoclinic centers it is not possible without calculation of the fine structure parameters. In other words application of the microscopic model describing relation between structure of the defect environment and values of its ZFS parameters is necessary.

At the solving of this problem the superposition model of the ground state zero field splitting with approximation from work [5] was used,

$$b_{2m} = \sum_{d} K_{2m}(\theta_d, \varphi_d) \cdot \bar{b}_2(R_d), \tag{1}$$

$$\bar{b}_2(R_d) = Z_d \cdot \bar{b}_{2p}(R_0)(R_0/R_d)^3 + \bar{b}_{2s}(R_0)(R_0/R_d)^{10},$$

where the first and second terms are the contributions of the electrostatic field of the ligand point charge and the short-range metal–ligand interaction respectively, $K_{2m}(\theta_d, \varphi_d)$ is the angular structure factor, R_d, θ_d, and φ_d are the spherical coordinates of the ligands; R_0= 2.37 Å is the sum of the ionic radii of the impurity and ligand; the values of the semiempirical parameters $\bar{b}_{2p} = -\chi_p \bar{A}_{2p}$, $\bar{b}_{2s} = \chi_s \bar{A}_{2s}$, χ_p= -2.14 χ_s= -2.70 can be found in [5, 6]; Z_d is the ligand charge. Values $\bar{A}_{2p,2s}$ according to [5] determine parameters of the crystal field:

$$A_{2m} = \sum_{d} K_{2m}(\theta_d, \varphi_d)[\bar{A}_{2p}(R_0)(R_0/R_d)^3 + \bar{A}_{2s}(R_0)(R_0/R_d)^{10}] \tag{2}$$

For the solving of this problem the knowledge about coordinates of the environment of the paramagnetic ion is necessary. Structure of the tetrameric clusters of cadmium fluoride was obtained by V.A. Chernyshev as a result of minimization of the lattice energy with an RE-ion cluster. Calculation was executed in approximation of the pair-potential [7] and with use the shell model which allows to consider polarization of a lattice that is important in case of charged impurity defects.

Parameters of the model, except for short-range interaction, considering only point charges of the nearest ions F-, are resulted in work [5]: $\bar{b}_{2p}$ = 6210 MHz, $\bar{b}_{2s}$ = 4273 MHz at R_0 = 2.37 Å. Calculation results of fine structure b_{20} parameters for Gd^{3+} ions localized in clusters of three types, with using formulas (1), with intrinsic parameters from work [5] and coordinates of anion and cation environments are given in Table 2. The contribution from dipole fields was considered by summation on charges of cores and shells of ions. Nondiagonal parameters of the spin-Hamiltonian which values depend on azimuthal coordinates of ligands were not calculated. Generally speaking, using in the calculations which deal with polarized anion and cation environment the superposition parameters [6] which obtained for model considering only not polarized the nearest ions F- is wrongfully. However Table 2 data very clear show a ratio of contributions from point charges, dipole fields and cation environments. At the same time pay attention to essential influence on result the contribution from polarized anion environment.

Table 2. Calculated b_{20} parameters for Gd^{3+} ions in clusters (in MHz) with intrinsic parameters from work [5].

cluster	b_{20} (point charges, 11anions)	b_{20} (point charges and dipoles, 11 anions)	b_{20} (point charges and dipoles, 11 anions and 12 cations)
GdY_3F_{26} (C_{3V})	820	-3191	-93
GdY_2CdF_{26} (C_S)	1086	-2732	-120
$GdYCd_2F_{26}$ (C_S)	1328	-2236	-121

For obtaining more appropriate (taking into account charged cation defects and polarization of the ions) empirical model parameters experimental data about zero field splitting of the well known tetragonal and trigonal Gd^{3+} centers connected with charge compensation of the Gd^{3+} extra charge by fluorine ion in the nearest neighbour or next nearest neighbour interstitial sites in calcium, strontium and barium fluoride [8-11] were used. The structure of these centers has been calculated by V.A. Chernyshev in the same way that was used for a finding of ion coordinates of tetrahedral clusters.

By means of formulas (1-2) the equations at the account short-range interaction, electrostatic interaction with the polarized 11 ions of fluorine and contributions of cores and shells of 12 cations have been obtained. Using the obtained coordinates by least-squares method the solution of the equations set which are values of intrinsic parameters: $\bar{b}_{2p}$ = 13670 MHz, $\bar{b}_{2s}$ = 5670 MHz has been obtained. The description quality of the experiment [8-11] by these parameters is showed in Table 3. The calculation result of the b_{20} parameters of the Gd^{3+} ions, localized in three types of the tetrahedral clusters are brought in Table 4. For comparison and an estimation of the contribution values the parameters calculated without taking into account influence of the cation environment and dipole interaction also are brought in Table 4.

Table 3. Experimental and calculated ZFS parameters of centers Gd^{3+} -F with superposition parameters: $\bar{b}_{2p} = 13670$ MHz, $\bar{b}_{2s} =$ 5670 MHz.

	b_{20} (exp.), MHz	b_{20} (cal.), MHz
CaF_2, C_{4V}	-4452(3) [22]	-4500
SrF_2, C_{4V}	-3367(25) [23]	-3200
SrF_2, C_{3V}	-406(2) [24]	-280
BaF_2, C_{3V}	-407(3) [25]	-470

The sets of the computed b_{20} parameters for Gd^{3+} ions in clusters of three types which are brought in tables 2 and 4 show a small range of absolute values and a constancy of signs. In this connection to b_{20} parameters (table. 1) of weakly-intensive Gd^{3+} centers at which hardly probably direct determination of the energy level order we assigned the negative sign.

It is clear, that b_{20} parameters from table 4 which absolute values in some times exceed values from table 1 cannot explain experiment. However, it is possible to assume that errors

Table 4 Calculation results of the b_{20} parameters (in MHz) Gd3+ ions in tetrahedral clusters with empirical parameters: $\bar{b}_{2p} = 13670$ MHz, $\bar{b}_{2s} =$ 5670 MHz.

cluster	b_{20} (point charges, 11 anions)	b_{20} (point charges and dipoles, 11 anions)	b_{20} (point charges and dipoles, 11 anions and 12 cations)
GdY_3F_{26} (C_{3V})	483	-8342	-1525
GdY_2CdF_{26} (C_S)	950	-7450	-1704
$GdYCd_2F_{26}$ (C_S)	1450	-6393	-1740

of the used models lead to strong common displacement of calculated parameters but the tendency of change along series of clusters remains constants. Then on the base of the comparison results of the behaviour of the calculated and experimental b_{20} values of the observable centers it is possible to conclude that intensive monoclinic Gd^{3+} center with b_{20} = -345 MHz should be related to [CdY_2GdF_{26}] cluster with charge equal to one of the substituted fluorite structure fragment and less widespread monoclinic center can be related to [Cd_2YGdF_{26}] cluster.

In work [1] it has been shown, that existence the cubic Gd^{3+} center which typical to low-doped CdF_2 in crystals $Y_xGd_yCd_{1-x-y}F_{2+x+y}$ (x=0.03, y≤0.001) is possible to explain only in the assumption of existence of the big enough clusters associations. In this case EPR spectrum belonging to the gadolinium ions in clusters which have in the nearest environment other clusters will be detected. At modelling of the tetrahedral cluster structure the account of neighbour clusters influence is rather important since except for the solving of the computation problems demands construction of the association model. In the given work these problems were not solved and apparently it is the main reason of the bad agreement of the calculation results and experiment.

References

[1] V.A. Vazhenin, A.P. Potapov, A.D. Gorlov, A.E. Nikiforov, S.A. Kazanski, A.I. Ryskin. Physics of the Solid State **47**, 8, 1450 (2005).

[2] V.A. Vazhenin, A.P. Potapov, A.D. Gorlov, V.A. Chernyshev, S.A. Kazanski, A.I. Ryskin. Physics of the Solid State, Vol. **48**, 4, 686 (2006).

[3] E.A. Ryzhova, V.N. Molchanov, A.A. Artyukhov, V.I. Simonov, B.P. Sobolev. Kristallografiya (in Russian) **49**, 1 (2004).

[4] E.A. Sulyanova, A.P. Shcherbakov, V.N. Molchanov, V.I. Simonov, B.P. Sobolev. Kristallografiya (in Russian) **50**, 235 (2005).

[5] L.I. Levin. Phys. Stat. Solidi (b) **134**, 275 (1986).

[6] L.I. Levin, V.I. Cherepanov. Fizika Tverdogo Tela (in Russian) **25**, 700 (1983).

[7] V.A. Chernychev, A.D. Gorlov, A.A. Mekhonoshin, A.E. Nikiforov, A.I. Rokeakh, S.Yu. Shashkin, A.Yu. Zaharov. Appl. Magn. Reson. **14**, 37 (1998).

[8] K. Zdansky, A. Edgar. Phys. Rev. **23**, 2133 (1971).

[9] J. Sierro. Helv. Phys. Acta **36**, 505 (1963).

[10] A. Edgar, D.J. Newman. J. Phys. C: Solid State Phys. **8**, 4023 (1975).

[11] L.A. Boatner, R.W. Reynolds, M.M. Abraham. J. Chem. Phys. **52**, 1248 (1970).

The Application of EPR and NMR Spectroscopy for the Reversible $^3O_2$ Binding by Complexes With Redox Active Ligands

A.I. Poddel'sky, E.V. Volkova, Yu.A. Kurskii, V.K. Cherkasov, G.A. Abakumov

G.A. Razuvaev Institute of Organometallic Chemistry of Russian Academy of Sciences, 603950, 49 Tropinina str., Nizhny Novgorod, Russia

e-mail: aip@iomc.ras.ru

Introduction

The coordination of dioxygen to transition metals is a subject of extreme interest due to its utilization by biological systems [1,2]. The development of redox-processes in biochemistry, and technology requires the synthetic analogues of nature dioxygen carriers. A wide range of transition metal complexes will bind dioxygen reversibly. However, in many cases the realization of this process needs the combination of some condition like low temperature, sterical hindrances in these complexes and immobilization to prevent irreversible oxidation of dioxygen-adducts. The search of stable transporters and carriers of O_2 maintains its importance.

Results

o-Benzoquinones (Q) and *o*-iminobenzoquinones (IQ) take an especial position among O,O- and O,N-chelating ligands due to their ability to reversible one-electron reduction steps leading to radical-anion (SQ$^{\bullet -}$ or ISQ$^{\bullet -}$) and dianion (Cat^{2-} or AP^{2-}) forms. Such transformation (Scheme 2) are easily accessible in different complexes and can occur as intramolecularly (due to the change of an oxidation level of the central atom) [8-11], and under influence of an external oxidizer etc [12-14].

Scheme 1

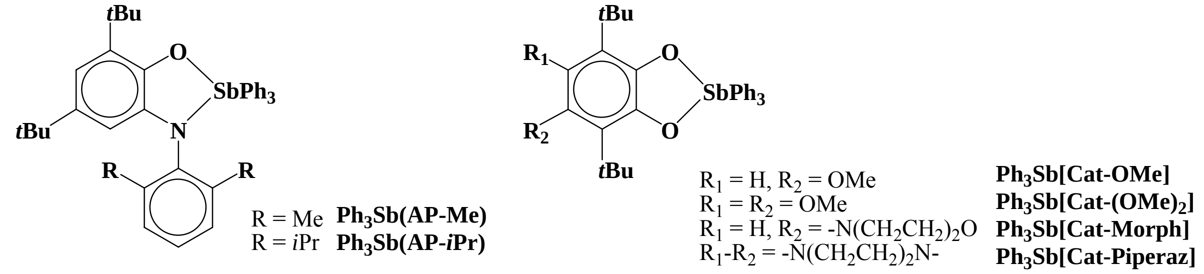

R = Me **Ph$_3$Sb(AP-Me)**
R = *i*Pr **Ph$_3$Sb(AP-*i*Pr)**

R_1 = H, R_2 = OMe	**Ph$_3$Sb[Cat-OMe]**
R_1 = R_2 = OMe	**Ph$_3$Sb[Cat-(OMe)$_2$]**
R_1 = H, R_2 = -N(CH$_2$CH$_2$)$_2$O	**Ph$_3$Sb[Cat-Morph]**
R_1-R_2 = -N(CH$_2$CH$_2$)$_2$N-	**Ph$_3$Sb[Cat-Piperaz]**

Scheme 2

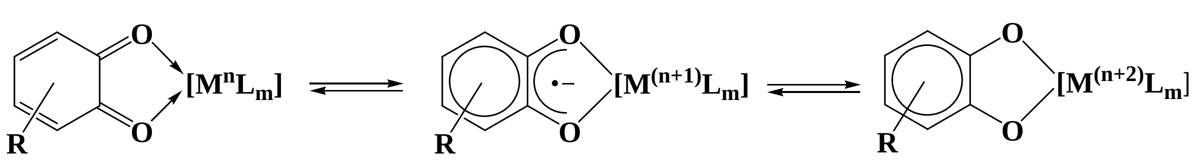

(Q)M^nL_m (SQ)$M^{n+1}L_m$ (Cat)$M^{n+2}L_m$

The unique ability of antimony complexes to bind dioxygen reversibly is caused by the redox activity of the catecholate (*o*-amidophenolate) ligand. We have proposed the mechanism of O_2-binding [3]. The crucial stage of mechanism is one-electron oxidation of dianions Cat^{2-} (AP^{2-}) to radical-anion SQ$^{\bullet -}$ (ISQ$^{\bullet -}$) with the formation of molecular cation [Ph$_3$Sb^{V}(SQ)]$^{\bullet +}$ and superoxide anion $O_2^{\bullet -}$. The recombination of cation and anion yields a neutral diradical complex in triplet state. Inter-spin conversion of a triplet state to a singlet one in this radical pair is facilitated by the presence of heavy antimony atom with great constant of spin-orbital interaction. The subsequent recombination of radical centers in this singlet intermediate results the final bicyclic endoperoxide of 1,2,4,3-trioxastibolane type (Scheme 3).

Scheme 3

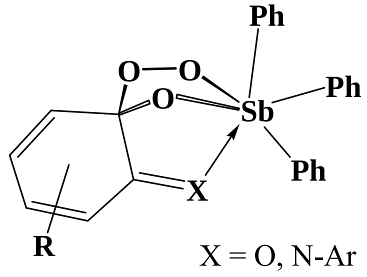

Such type systems are grateful objects for NMR investigations. The dioxygen-bound form, trioxastibolane, is clearly detected by ^{1}H and ^{13}C NMR spectroscopy.

All complexes shown in Scheme 1 reveal changes in NMR spectra being stored on air. In each case, molecular oxygen inserts into initial complex molecule as the additional linker between antimony and C(O) carbon atoms. It creates the breaking of one valent Sb-O (in catecholates) or Sb-N (in *o*-amidophenolates) bond and the formation of peroxide Sb-O and C-O bonds in Sb-O-O-C fragment. As a result, one carbon atom of catecholate fragment

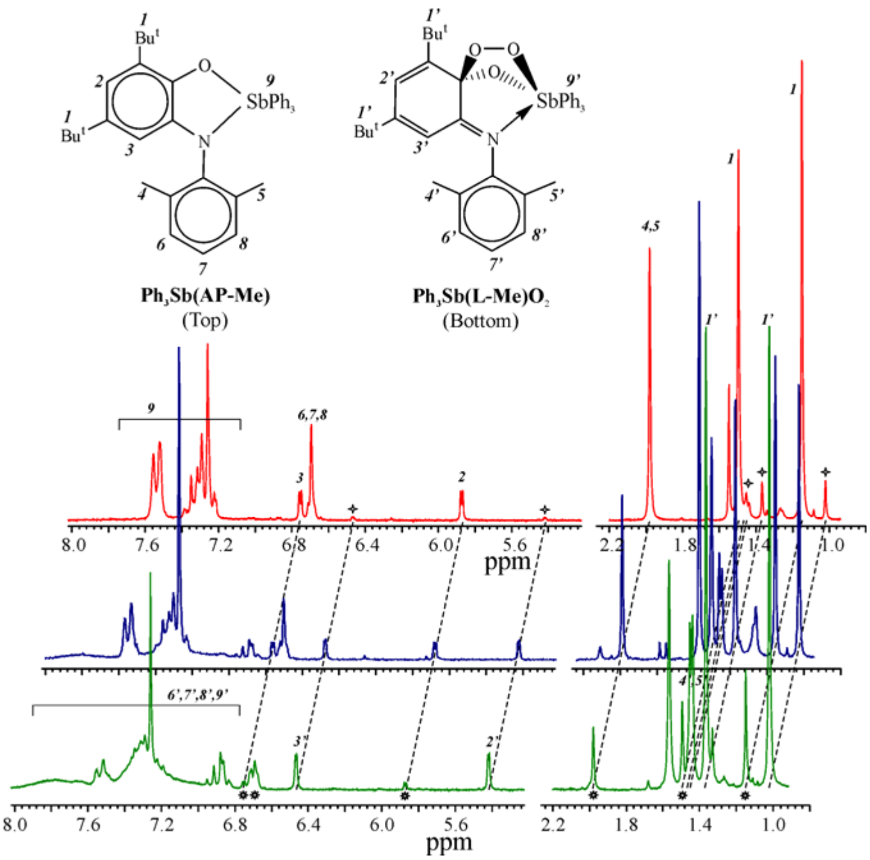

Fig.1 ^{1}H NMR spectra of Ph$_3$Sb(AP-Me) (top), its spiroendoperoxide Ph$_3$Sb[L-Me]O$_2$ (bottom) and 1:1 mixture (middle) (D-acetone, 298K). ✢ and ✻ indicates admixtures of Ph$_3$Sb[L-Me]O$_2$ and Ph$_3$Sb(AP-Me) correspondingly.

changes itself hybridization from sp^2 to sp^3 and the aromaticity of the six-membered C-C ring is lost; the formation of double N=C or C=O bond and correspondingly to the formation of donor-acceptor Sb…O or Sb…N bond which vary in the wide range of values whereas other geometrical parameters in the coordinating sphere of Sb atoms are close to each other. The corresponding changes are shown in Fig. 1 for *o*-amidophenolate complex Ph_3Sb(AP-Me).

We have earlier found that pentacoordinated manganese complex with sterically hindered *o*-iminobenzoquinonato ligands Mn(ISQ-*i*Pr)(AP-*i*Pr)THF is also able to reversible dioxygen binding [6]. A similar tetracoordinated manganese complex Mn(ISQ-*i*Pr)(AP-*i*Pr), i.e. without solvent molecule in coordination sphere, binds dioxygen irreversibly. However, this process becomes reversible as soon as coordinating solvent (THF, methanol etc.) is added to the system [7]. Noteworthy, in most cases the presence of transition metal and radical ligands leads to high spin multiplicity of system and the application of EPR is quite restricted there due to a number of conditions. Manganese complexes Mn(ISQ-*i*Pr)(AP-*i*Pr)THF and Mn(ISQ-*i*Pr)(AP-*i*Pr) have quadruplet spin state (S=3/2) that is corroborated by low-temperature X-band EPR in solid state: EPR spectra of these complexes are typical for manganese(III) complexes with S = 3/2 [15] and have parameters $g_1 = 4.37$, $g_2 = 2.83$, $g_3 = 1.93$ for Mn(ISQ-*i*Pr)(AP-*i*Pr)THF and $g_1 = 4.94$, $g_2 = 2.79$, $g_3 = 1.74$ for Mn(ISQ-*i*Pr)(AP-*i*Pr). These complexes don't have EPR in solution. Themselves, we have shown that the monitoring of interaction between manganese complexes and dioxygen can be carried out by means of EPR because the ground state of manganese-dioxygen complexes is doublet and it is easily fixated by EPR in solution at ambient temperature [6,7].

So, manganese complex Mn(ISQ-*i*Pr)(AP-*i*Pr)THF was used as the dioxygen trap in the system with *o*-amidophenolate antimony complex (Scheme 4).

Scheme 4

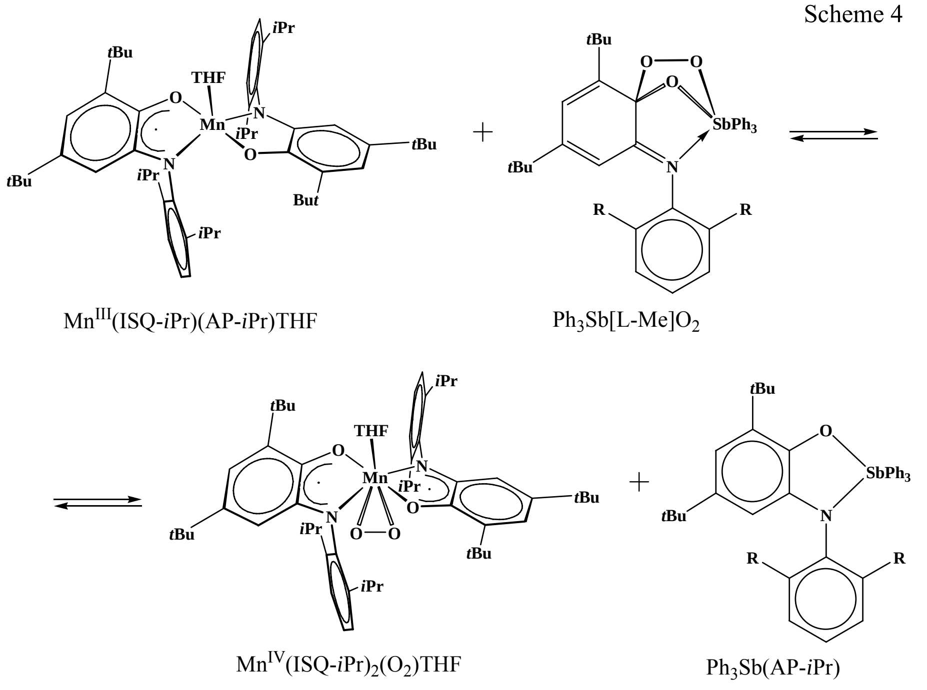

X-band EPR spectrum of dioxygen complex is a sextet (1:1:1:1:1:1) of quintets (1:2:3:2:1) due to HFC with ^{55}Mn (I = 5/2, 100%, $\mu_N = 3.4687$, $A_i(^{55}Mn)$ = 106-107 G) and two equivalent ^{14}N nuclei (I = 1, 99%, $\mu_N = 0.40376$, $A_i(^{14}N1) = A_i(^{14}N2)$ = 3.5 G) of two ISQ ligands with $g_{iso} = 2.006$ (toluene, 290K). Figure 2 shows the increase of EPR signal (only the fourth component of EPR spectrum is shown) in magnitude as the function of reaction time (up to 30 min. with a time interval of 2 min.).

EPR experiment shows that reaction of dioxygen exchange between manganese and antimony complexes (Scheme 4) is reversible and can be realized in both directions.

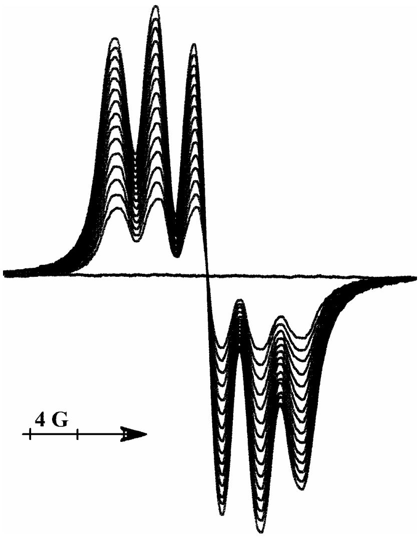

Fig.2 X-band EPR spectra (the fourth component of sextet) of manganese-dioxygen complex Mn(ISQ-*i*Pr)$_2$(O$_2$)THF as the time function of reaction between Mn(ISQ-*i*Pr)(AP-*i*Pr)THF and spiroendoperoxide Ph$_3$Sb[L-Me]O$_2$ (toluene, 298K). Time period is 2 minutes.

Acknowledgements

We are grateful to the Russian Foundation for Basic Research (grants 07-03-00711, 07-03-00819), Russian President Grants (NSh-4947.2006.3, MK-3523.2007.3) for financial support of this work.

References

[1] Solomon E.I., Brunold T.C., Davis M.I., Kemsley J.N., Lee S.-K., Lehnert N., Neese F., Skulan A.J., Yang Y.-S., Zhou J., *Chem. Rev.* **100**, 235 (2000).

[2] Simándi L.I., *Advances in Catalytic Activation of Dioxygen By Metal Complexes, Catalysis By Metal Complexes. Vol. 26.* Boston Kluwer Academic Publishers (2003).

[3] Abakumov G.A., Poddel’sky A.I., Grunova E.V., Cherkasov V.K., Fukin G.K., Kurskii Yu.A., Abakumova L.G., *Angew. Chem. Int. Ed. Engl.* **44**, 2767 (2005).

[4] Abakumov G.A., Cherkasov V.K., Grunova E.V., Poddel’skii A.I., Abakumova L.G., Kurskii Yu.A., Fukin G.K., Baranov E.V., *Doklady Chemistry* **405**, 222 (2005).

[5] Cherkasov V. K., Abakumov G.A., Grunova E.V., Poddel'sky A.I., Fukin G.K., Baranov E.V., Kurskii Yu.A., Abakumova L.G., *Chem. Eur. J.* **12**, 3916 (2006).

[6] Abakumov G.A., Cherkasov V.K., Poddel’sky A.I., Bubnov M.P., Abakumova L.G., Fukin G.K., *Doklady Chemistry* **399**, 207 (2004).

[7] Abakumov G.A., Poddel’sky A.I., Bubnov M.P., Fukin G.K., Abakumova L.G., Ikorskii V.N., Cherkasov V.K., *Inorg. Chim. Acta.* **358**, 3829 (2005).

[8] Pierpont C. G., *Coord. Chem. Rev.* **415**, 219-221 (2001).

[9] Dei A., Gatteschi D., Sangregorio C., Sorace L., *Acc. Chem. Res.* **37**, 827 (2004).

[10] Sato O., Tao J., Zhang Yu.-Zh., *Angew. Chem. Int. Ed.*, **46**, 2152 (2007).

[11] Abakumov G.A., Razuvaev G.A., Nevodchikov V.I., Cherkasov V.K., *J. Organomet. Chem.* **341**, 485 (1988).

[12] Abakumov G.A., Lobanov A.V., Cherkasov V.K., *Dokl. Akad. Nauk SSSR* **266**, 361 (1982).

[13] Bill E., Bothe E., Chaudhuri P., Chlopek K., Herebian D., Kokatam S., Ray K., Weyhermüller T., Neese F., Wieghardt K., *Chem. Eur. J.* **11**, 204 (2005).

[14] Chun H., Verani C.N., Chaudhuri P., Bothe E., Bill E., Weyhermüller T., Wieghardt K., *Inorg. Chem.*, **40**, 4157 (2001).

[15] Weyhermüller T., Paine T.K., Bothe E., Bill E., Chaudhuri P., *Inorg. Chim. Acta* **337**, 344 (2002).

Phosphorus - 31 Spin-lattice Relaxation in Aqueous Solutions Digidrophosphate Sodium

E.V. Morozov

Siberian Federal University, 660041, av. Svobodny 79; Krasnoyarsk Regional Multi-Access Center of SB RAS, 660036, Akademgorodok 50; Krasnoyarsk, Russia

e-mail: morozov_sfu@mail.ru

Introduction

Last years an active interest to studying an opportunity of use in medicine of new biologically compatible cements on the basis of phosphates of calcium is displayed. The given materials have high porosity that allows a tissue of an organism to fill implant and so to eliminate consequences of defects (fractures, cracks, etc.). Biocements have ability to completely filling the defect with convenient rate of concreting and required mechanical characteristics [1, 2].

It is necessary to note, that wide possibilities of nuclear magnetic resonance (NMR) are practically not used up to the present when studying of cement systems and kinetics of their hardening. Therefore the author offers to test different NMR techniques in this field.

As an illustration some proton magnetic resonance imaging (MRI) slices are presented for system $Ca(H_2PO_4)_2 - Ca_3(PO_4)_2$ (see Figure 1). The given system is cemented with formation of $CaHPO_4$. With MRI it is possible to observe processes of inspissation, compaction, crystallization through whole volume in different sites for a long time without sample destruction (see Fig. 2).

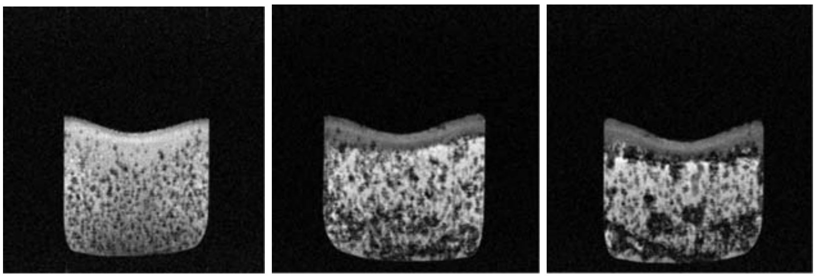

Fig.1 The central vertical slice of a sample in a glass tube (diameter 15 mm) (was obtained with intervals about one day).

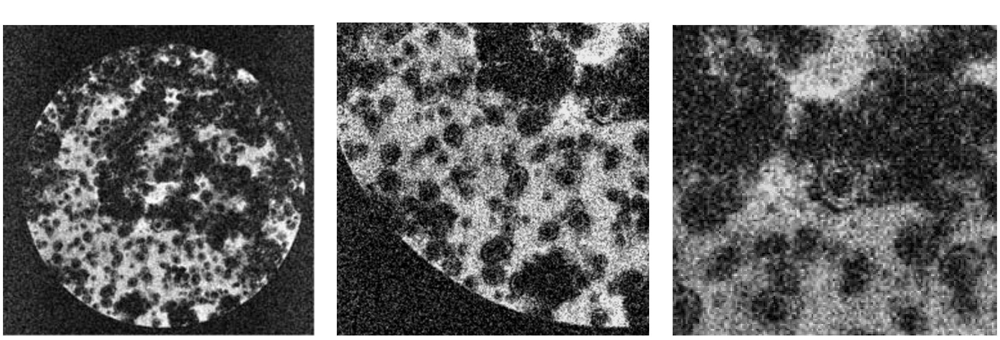

Fig.2 Formation of a microcrystalline structure (a horizontal slice with consecutive magnification and displacement of the interesting site to the center of figure).

For development of concrete NMR techniques for investigation of considered systems it is necessary to study, first of all, NMR relaxation (on various nuclei) not only in complex mixtures, but also in solutions of their separate components. In particular, the spin-spin relaxation measured in different sites of the considered system (with multiple spin-echo technique) during the cementation displays the tendency of T_2 decreasing, which requires to be interpreted. First attempts to use the data on proton relaxation of individual component solutions now, yet have not resulted in clear results.

The most interpretive results were obtained on nucleus ^{31}P which reflects behavior of the orthophosphate-ion with its key role in the given problem. In the report the results of measuring of spin-lattice relaxation for solutions NaH_2PO_4 in D_2O are submitted. Despite of similar works (for example, [3]), the information on concentration dependences is absent. In this case such data are especially important, because polycrystallization processes when cementing is accompanied by structural change of solutions and their concentration in local sites of system.

Experimental part

The Fourier NMR spectrometer Avance 200 DPX with the MRI equipment was used. The times of spin-lattice relaxation $T_{1,}$ of spin-spin relaxation, T_2^* , as well as the chemical shifts in solutions NaH_2PO_4 in D_2O were measured by standard techniques for ^{1}H, ^{23}Na, ^{31}P. In particular ^{31}P T_1 were measured by the inversion-recovery technique.

Results

Experimental values T_1 and T_2^* for ^{31}P in dependence on concentration at room temperature are given on Figure 3. As seen, these concentration dependences have the same view reflecting a sharp change of slope in the region about 0.4 mol^{-1}.

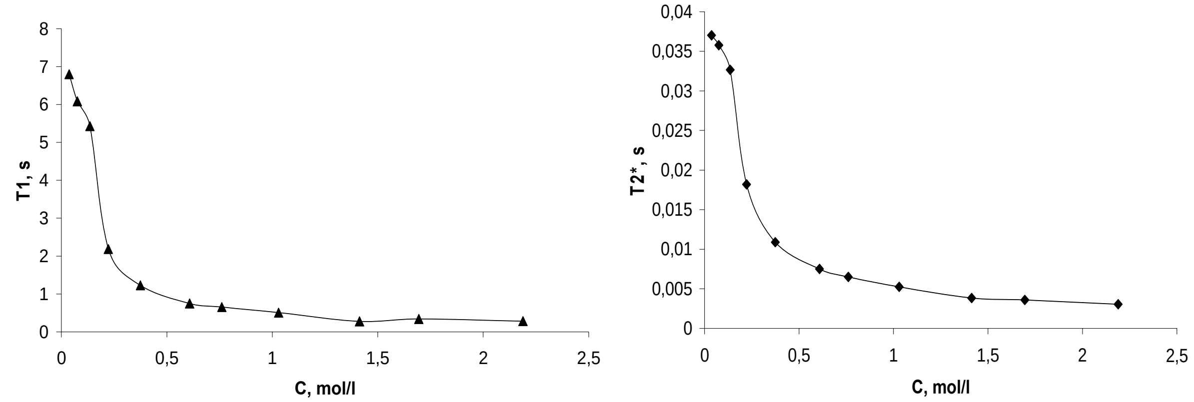

Fig.3 ^{31}P spin-lattice relaxation times (at the left) and T_2^* (on the right) as a function of concentration.

The results of measuring of spin-lattice relaxation for solutions of various concentrations depending on temperature are submitted on Figure 4. For convenience, very small values at high concentration are shown separately. These curves have identical character with the alone minimum. But when proceeding to low concentrations this character becomes quite another, namely the maximum appears and prevails. As for T_2^* (see Figure 5), the differences are not so significant, nevertheless the dependences also shown separately to underline them. In particular the curve for the minimal C is practically the straight line.

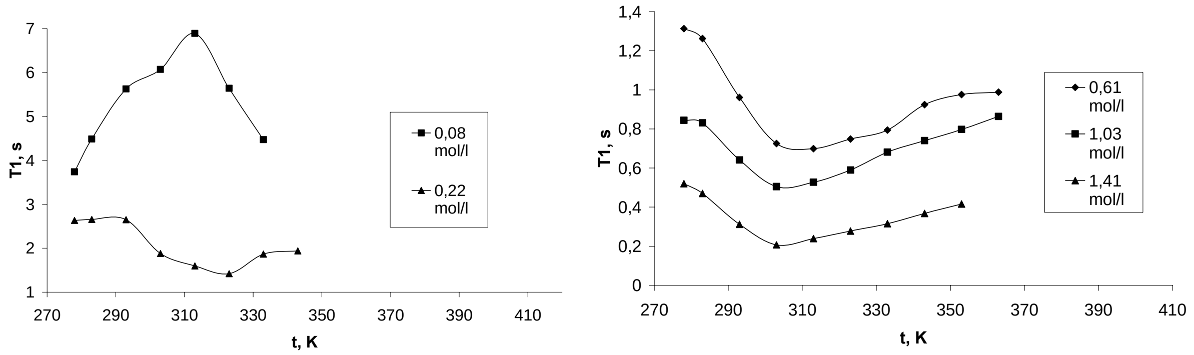

Fig. 4 ^{31}P spin-lattice relaxation times as a function of temperature.

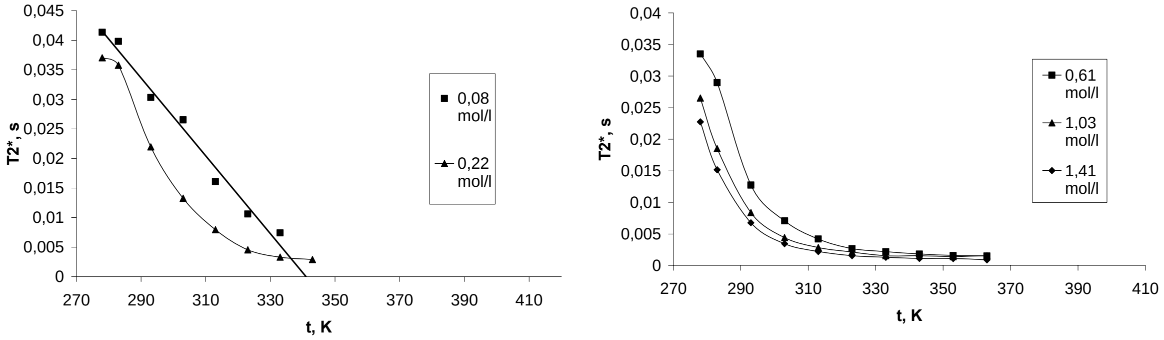

Fig.5 T_2^* as a function of temperature for ^{31}P

Discussion

The temperature interval of measurements T_1 in our case corresponds to such times of correlation τ_R that approach $\omega^2\tau_R^2 << 1$ is applicable. From this the conclusion follows, that the minimum on curves T_1=f(t) is not caused by the dipole-dipole relaxation mechanism. In similar cases a transition from spin-rotation mechanism to dipole-dipole one was actively discussed [4]. Note that spin-rotation relaxation is easy to define – a relaxation time is inversely proportional to temperature.

Relaxation at dipole-dipole intramolecular interaction (for spins ^{31}P and ^{1}H when $\omega^2\tau_R^2 << 1$) can be described by the equation [3-5]

$$\frac{1}{T_1}=\frac{4}{3}\hbar^2\gamma_H^2\gamma_P^2 S(S+1)R^{-6}\tau_R\,,\ \tau_R=\frac{4\pi\eta r^3}{3kT}. \qquad (1)$$

The calculated dependences of the dipole-dipole relaxation times vs. temperature are shown on Figure 6 (on the right). Here the temperature change of solution viscosity is not taken into account.

The other contribution in the relaxation which can be calculated is the spin-rotation mechanism. For a spherical molecule the rate of spin-rotation relaxation is equal [4, 5] to

$$\frac{1}{T_1}=\frac{8\pi^2 kT}{\hbar^2}IC^2\tau_{sr}\,,\ \tau_{sr}=\frac{I}{8\pi\eta a^3}. \qquad (2)$$

The estimated theoretical curves are represented on Figure 6 (at the left) in which the change η from temperature are also not taken into account (underline that η is the same in (1) and (2)). The next values of parameters were used: a=2.22Å, I =9.2·10^{-45} kg·m^2, η =10^{-3} Pa·s (for concentration 1.41 mol·l^{-1}), C=14 kHz. Parameters η and C were fitted to describe the main peculiarities of the experimental date.

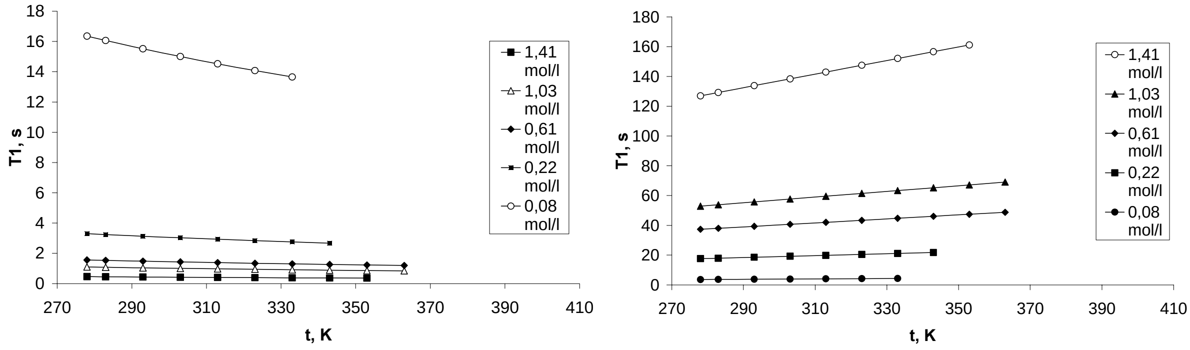

Fig.6 Theoretical curves for spin-rotation relaxation times (at the left) and dipole-dipole relaxation (on the right) as a function of temperature.

From such consideration the dependence viscosity vs. concentration becomes inverse that seems not to be typical. Nevertheless, it can be possible as a matter of principle, if to take into account a local viscosity which decreases when the concentration of solution increases. This is in accordance with the theory of solutions by Samoilov [6] as well as with the fact of quasi-spin-rotation character of relaxation mechanism for orthophosphate-ion [3].

On the basis of concentration dependence time of spin-lattice relaxation ^{31}P it is possible to draw a conclusion that for high concentrations (more 0.1 mol·l^{-1}) the basic contribution belongs to the spin-rotation mechanism, but for low ones – to the dipole-dipole mechanism.

The obtained concentration dependences for ^{1}H and ^{23}Na chemical shifts (see Figure 7) seem to give additional arguments that in the region about 0.4 mol·l^{-1} some significant reconstructions of the discussed system take a place.

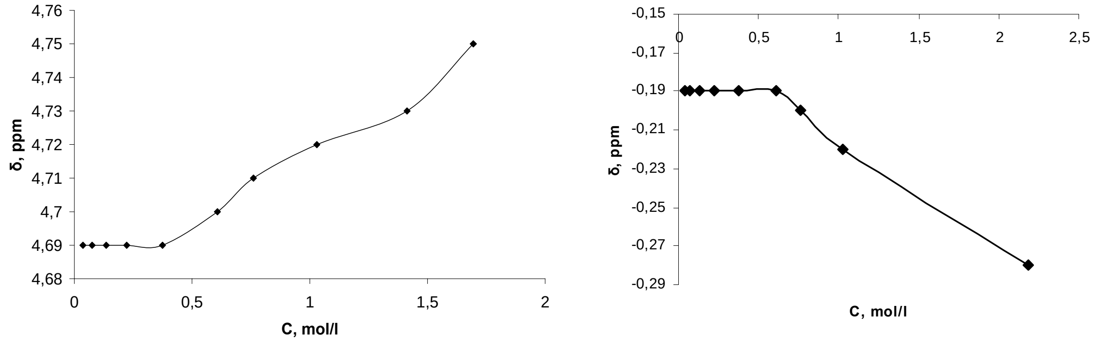

Fig.7 ^{1}H (at the left) and ^{23}Na (on the right) chemical shifts (CS) as a function of concentration (CS for the last nucleus is measured be relative 1M solution NaCl).

At the same time CS for ^{31}P as well as T_2^* for ^{1}H and ^{23}Na show only a monotonous deviations in the region of interest.

The author is grateful to scientific advisers: A.A. Shubin (SFU) and O.V. Falaleev (KRMAC of SB RAS) for active help in experimental process and discussion of results.

References

[1] B.R. Constantz et al, “Skeletal repair by in situ formation of the mineral phase of bone”, Science, **267**, 1796 (1995).

[2] M. Komath, H.K. Varma, R. Sivakumar, “On the development of an apatitic calcium phosphate bone cement”, Bull. Mater. Sci., **23**, 135-140 (2000).

[3] D.C. McCain, J.L. Markley, “Phosphorus-31 spin-lattice relaxation in aqueous orthophosphate solution”. J.Am. Chem. Soc., **102**, 5559-5565 (1980).

[4] A.A. Washman, I.S. Pronin, “Nuclear magnetic relaxation spectroscopy”, Energoatomizdat, Moscow, 1986 (in Russian).

[5] V.I. Chizhik, “Nuclear magnetic relaxation”, St.-Pb. University, St. Petersburg, 2004 (in Russian).

[6] O.Ya. Samoilov, “Structure of aqueous solution”, AS USSR, Moscow, 1957 (in Russian).

Ni-Catalyzed Phenylthiol Addition to Alkynes: Identification of Products Structure by Means of NMR Spectroscopy

S.S. Zalesskiy1), N.V. Orlov1), V.P. Ananikov1), I.P. Beletskaya2)

1)Zelinsky Institute of Organic Chemistry, Russian Academy of Sciences, 119991, Leninskiy prosp. 47, Moscow, Russia.
2)Department of Chemistry, Moscow State University, 119899, Vorob`evy Gory, Moscow, Russia.

e-mail: s.zalesskiy@gmail.com

In previous studies we reported nickel complexes to show high catalytic activity in vinylsulphide synthesis via arykthiol addition to alkynes [1]. But the NMR spectrum of the reaction mixture showed, that besides vinylsulphides formation of some side products also took place. After studying the model reaction (addition of phenylthiole to 2-methyl-3-butyn-2-ol, 40°C, solvent free) we found that yield of side products increased when we had used the excess of alkyne.

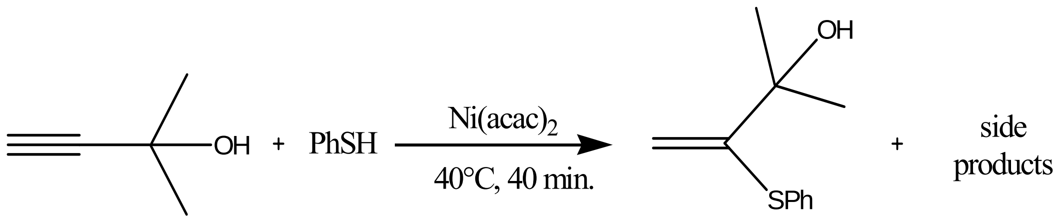

1a **Scheme 1** **2a**

Analysis of the ^{1}H NMR spectrum of the reaction mixture with doublefold excess of alkyne we showed that, in addition to the signals of product **2a**, the spectrum exhibits a large number of signals in the 4.9—7.0 range corresponding to olefinic protons. To determine the structures of products, they were chromatographed on silica gel. The yield of product **2a** with spectral characteristics identical to reported data[8] was 40%. The by-products were mainly conjugated 1,3-dienes **3a**, **4a**, and **5a** (Scheme 2). A mixture of these compounds was isolated in an overall yield of 31%; according to ^{1}H NMR data, the yields of compounds **3a**, **4a**, and **5a** were 15, 9, and 7%, respectively.

The low-field region of the ^{1}H NMR spectra of these compounds (**Fig. 1**) exhibits three groups of signals corresponding to the olefinic protons of each diene fragment:

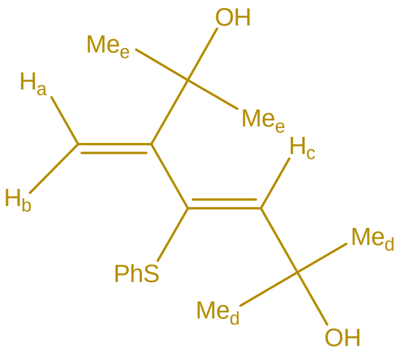

3a

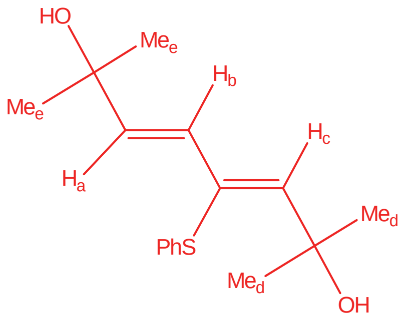

4a

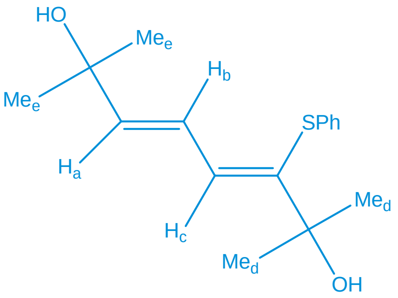

5a

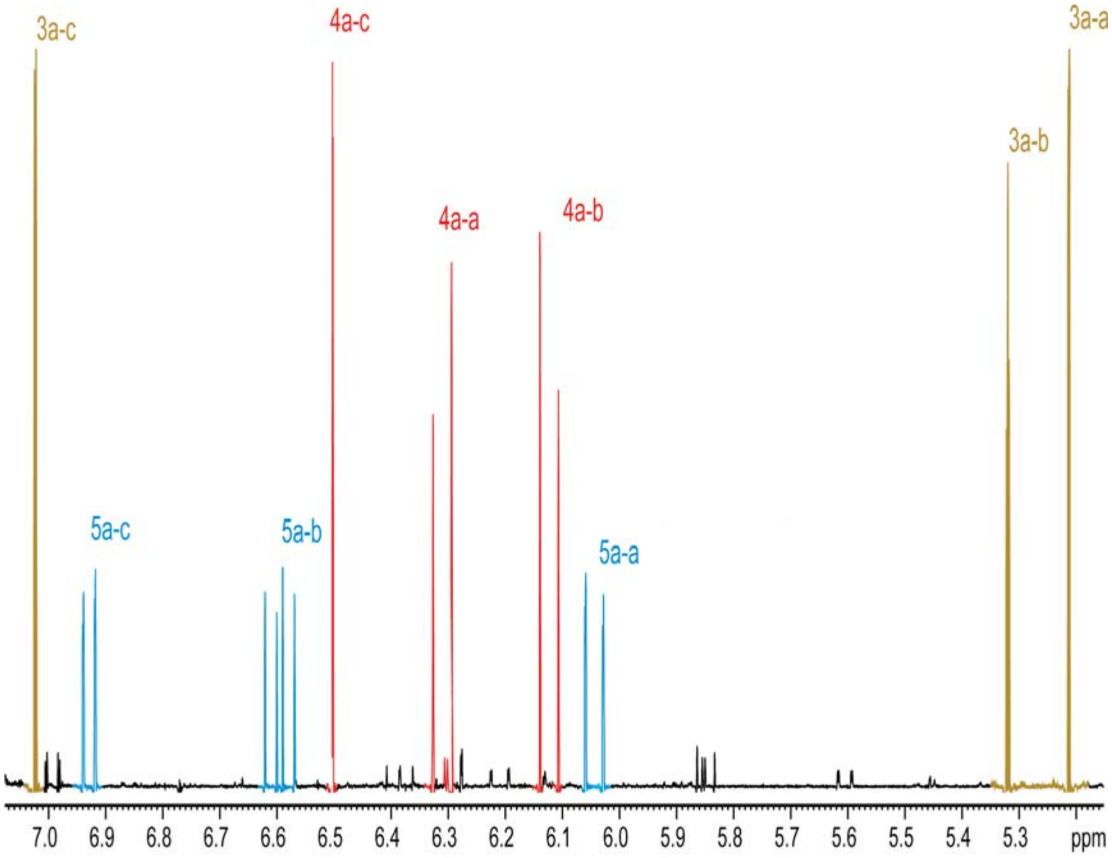

Fig.1

In the case of diene **3a**, only small spin-spin coupling constants are observed ($J < 2$ Hz). The spectrum of compound **4a** contains the coupling constant J(H—C=C—H$_{trans}$) = 16.1 Hz, and for diene **5a**, the spectrum shows the coupling constants J(H—C=C—H$_{trans}$) = 15.6 Hz and J(H—C—C—H) = 10.5 Hz and the far-range coupling constant $^4J = 0.7$ Hz.

The stereochemistry of dienes **5a—7a** was established using 2D NOESY experiments.

The methyl group signals in the high-field part of the spectrum were assigned using the

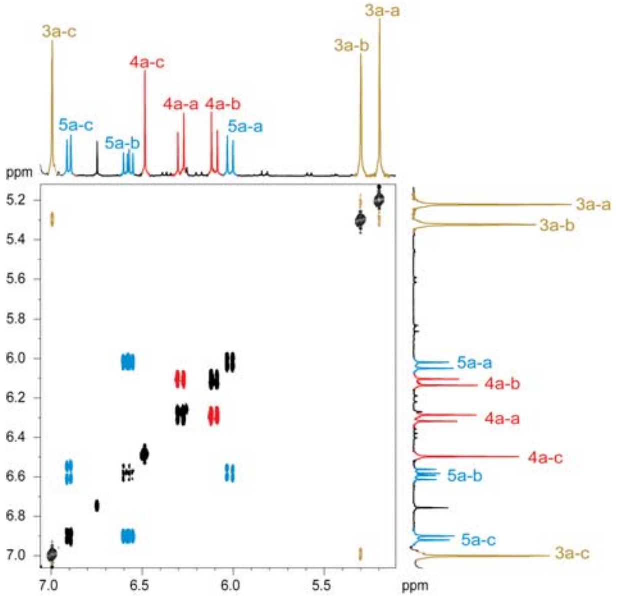

Fig.2 COSYgp

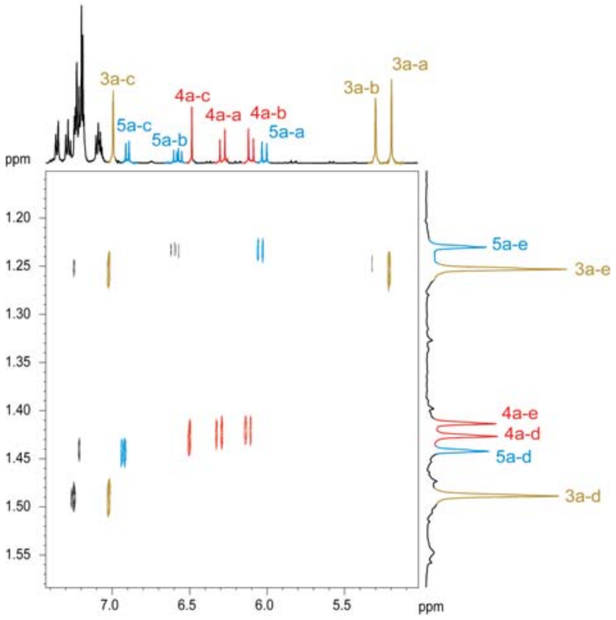

Fig.3 NOESY; 0.5 s

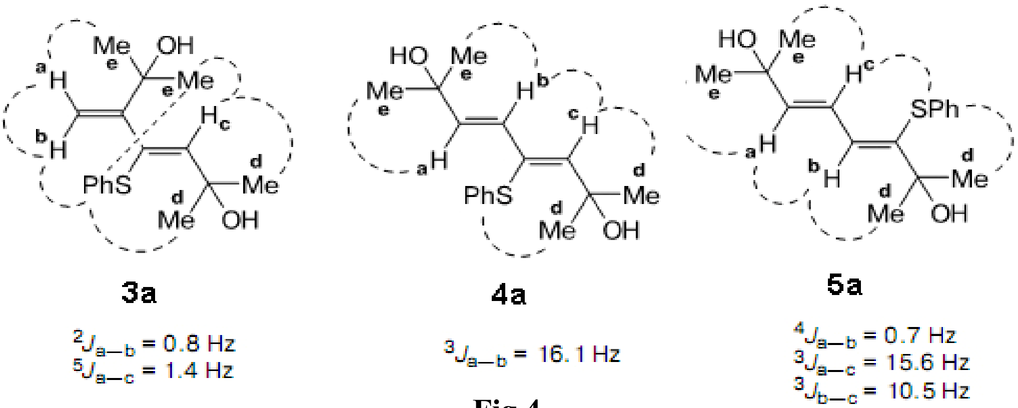

3a

$^{2}J_{a-b}$ = 0.8 Hz
$^{5}J_{a-c}$ = 1.4 Hz

4a

$^{3}J_{a-b}$ = 16.1 Hz

5a

$^{4}J_{a-b}$ = 0.7 Hz
$^{3}J_{a-c}$ = 15.6 Hz
$^{3}J_{b-c}$ = 10.5 Hz

Fig.4

key H^a—Me^e, H^c—Me^e, and H^c—Me^d contacts for **3a**; H^a—Me^e, H^b—Me^e, and H^c—Me^d contacts for **4a**; and H^a—Me^e, H^c—Me^e, and H^b—Me^d contacts for **5a** (for designations, see **Fig. 4**).

In addition, the mixture contained triene **6a** (yield 7%) and, somewhat unexpectedly, 1,3,5-tris(1-hydroxy-1-methylethyl)benzene **7a** (yield 12%). Aromatic derivative **7a** was identified based on ^{1}H and ^{13}C NMR and mass-spectrometry data. Previously,[2-4] the formation of symmetrical trisubstituted benzene **7a** from alkyne **1a** in a transformation catalyzed by nickel phosphine complexes has been reported; however, a catalytic activity of the sulfide nickel complexes toward trimerization is quite unusual.

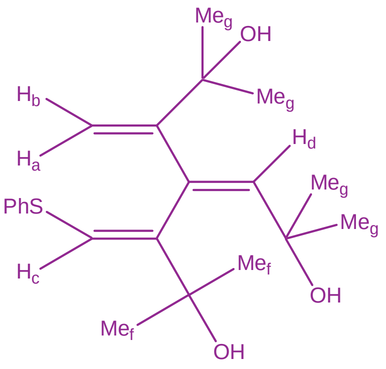

6a

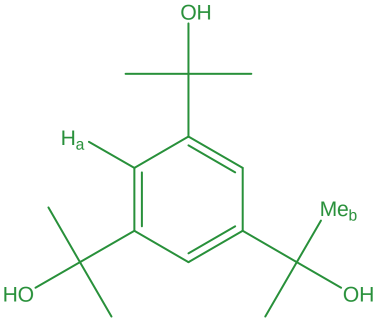

7a

The remaining byproducts fraction (~10%) could not be reliably identified, apparently, this comprised oligomers with higher molecular weights The structure of compound **6a** was proposed based on analysis of 2D NOESY and COSY spectra (similarly to the procedure described previously) (**Fig. 4**).

We investigated if the reaction was appliable to different thiols and selenols (**Table 2**).

Table 1. Diene yields.

Reagent	Product, %					
	2	**3**	**4**	**5**	**6**	**7**
PhSH **(a)**	40%	15%	9%	7%	7%	12%
CySH **(b)**	47%	-	7%	-	-	10%
PhSeH **(c)**	45%	12%	1%	3%	-	-

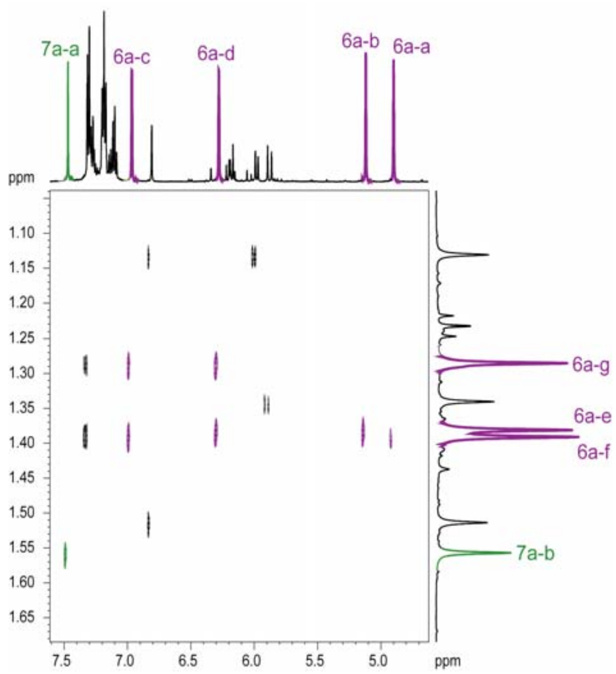

Fig.5 NOESY; 0.5 s.

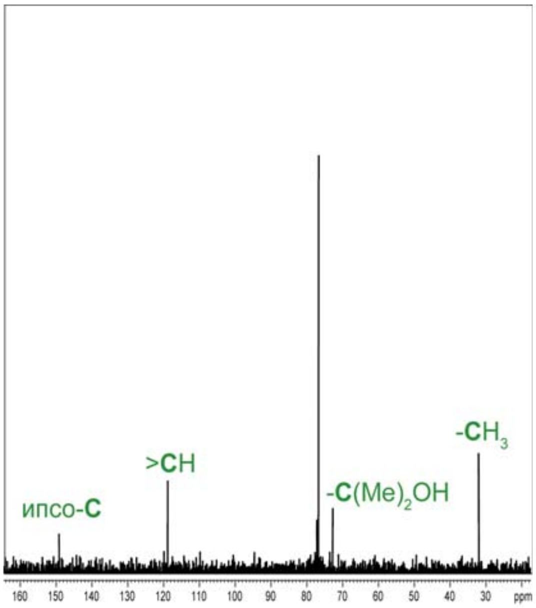

Fig.6 $^{13}C\{^{1}H\}$ NMR

Main products of cyclohexylthiol addition were diene **4b** and aromatic compound **7b**. The rest of reaction mixture could not be reliably identified. In case of phenylselenole vinylsulphide was obtained with 45% yield, among the byproducts dominated diene **3c**. structure of **3c** was confirmed by ^{1}H and $^{1}H - ^{77}Se$ NMR spectra (**Fig. 6**):

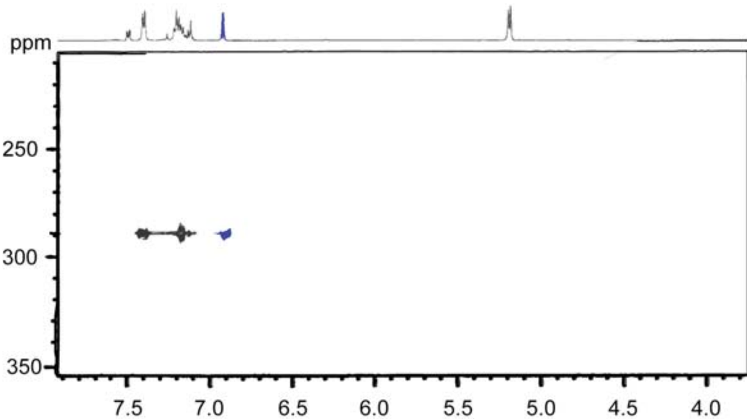

Fig.7 gpHMQC ^{1}H-^{77}Se

References

[1] V.P. Ananikov, N.V. Orlov, I.P. Beletskaya; Organometallics, 2006, 25, 1970-1977.

[2] P. Bicev, A. Furlani, G. Sartori, Gazz. Chim. Ital., 1973, 103, 849.

[3] P. Chini, A. Santambrogio, N. Palladino, J. Chem. Soc., 1967, 830.

[4] W. Hartmann, K. D. Preuss, H. Singer, J. Organomet. Chem., 1983, 258, 235.

Configurational Assignment and Conformational Analysis of Azomethines Based on their $^{13}C–^{13}C$, $^{13}C–^{1}H$ and $^{15}N–^{1}H$ Spin-Spin Coupling Constants

K.A. Chernyshev[1)], S.S. Khutsishvili[1)], N.A. Scherbina[2)], N.V. Istomina[2)], L.B. Krivdin[1,2)]

[1)]A.E. Favorsky Irkutsk Institute of Chemistry, Siberian Branch of the Russian Academy of Sciences, Favorsky St. 1, 664033 Irkutsk, Russia

[2)]Department of Chemistry, Technical Academy of Angarsk, Tchaikovsky Avenue 60, Angarsk 665835, Russia

e-mail: kirill@irioch.irk.ru

Many chemical transformations and rearrangements of oximes, hydrazones and other imines utilized in the synthesis of azoles and larger nitrogen-containing heterocycles occur stereoselectively, which makes the problem of the configurational assignment at the C=N bond to be of crucial importance.

In the present paper, configurational assignment and conformational analysis of a number of azomethines (aliphatic and alicyclic oximes [1], silicon and germanium containing propynal oximes [2], 2,5-dihydro-2-iminofuranes [3], azomethines of the α,β-unsaturated aldehydes [4], methylglyoxal *bis*-dimethylhydrazones [5], aminosulfonylamidines [6], *N*-arylsulfonylimines of α–polychloroaldehydes [7] and *N*-arylsulfonylformamidines) has been performed based on the experimental measurements and high-level *ab initio* calculations of their $^{13}C–^{13}C$, $^{13}C–^{1}H$ and $^{15}N–^{1}H$ spin-spin coupling constants showing marked stereospecificity dealing with the orientational nitrogen lone pair effect in the diverse isomers of azomethines [8].

For example, comparison of the experimental values of $^{1}J(\text{C-1,H}^{\alpha})$, $^{1}J(\text{C-1,C-2})$ and $^{2}J(\text{N,H}^{\alpha})$ measured in arylsulfonylimines of α-polychloroaldehydes **1**–**7** synthesized by the one-pot interaction of *N*,*N*-dichloroamides of sulfonic acids with 1,2-polychloroethanes or phenylacetylene with their theoretical values calculated in model structure (Table 1) leaves no doubt that all synthesized arylsulfonylimines of α-polychloroaldehydes under study have the *E* configuration at the C=N bond.

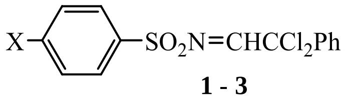

1 - 3

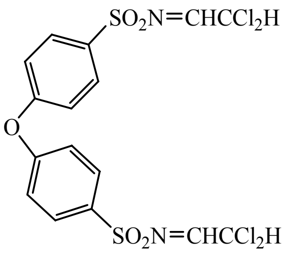

4

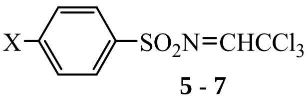

5 - 7

X = H (**1**, **5**), CH_3 (**2**, **6**), Cl (**3**, **7**).

It follows from the data presented in Table 1 that $^{1}J(\text{C-1,C-2})$, $^{1}J(\text{C-1,H}^{\alpha})$ and $^{2}J(\text{N,H}^{\alpha})$ spin–spin coupling constants demonstrate a remarkable stereospecificity in the configurational isomers of arylsulfonylimines of α-polychloroaldehydes. Indeed, $^{1}J(\text{C-1,C-2})$ are by *ca*. 11–15 Hz larger in *E* isomers while $^{1}J(\text{C-1,H}^{\alpha})$ are by *ca*. 8-11 Hz larger in the diverse hypothetical *Z* isomers. Accordingly, $^{2}J(\text{N,H}^{\alpha})$ couplings are small (*ca*. 3.2 Hz) in *E* isomers while they are large and negative being of *ca*. –(13-18) Hz in the diverse hypothetical *Z* isomers.

Table 1. Spin-spin coupling constants $^{13}C{-}^{13}C$, $^{13}C{-}^{1}H$ and $^{15}N{-}^{1}H$ in *E* and *Z* isomers of the model *N*-sulfonylimines of di- and trichloroaldehydes calculated at the SOPPA level

Model compounds	Isomer	Coupling constant	J_{calc}	J_{exp}
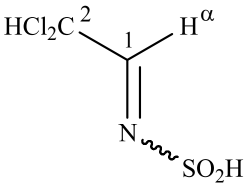	*E*	$^{1}J(\text{C-1,C-2})$	52.7	53.9
		$^{1}J(\text{C-1,H}^{\alpha})$	179.5	183.0
		$^{2}J(\text{N,H}^{\alpha})$	3.2	2.8
	Z	$^{1}J(\text{C-1,C-2})$	41.9	
		$^{1}J(\text{C-1,H}^{\alpha})$	187.4	
		$^{2}J(\text{N,H}^{\alpha})$	-18.6	
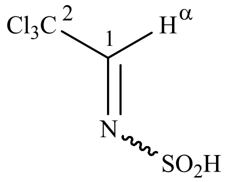	*E*	$^{1}J(\text{C-1,C-2})$	59.0	60.3
		$^{1}J(\text{C-1,H}^{\alpha})$	189.2	187.4
		$^{2}J(\text{N,H}^{\alpha})$	3.3	2.9
	Z	$^{1}J(\text{C-1,C-2})$	43.9	
		$^{1}J(\text{C-1,H}^{\alpha})$	200.6	
		$^{2}J(\text{N,H}^{\alpha})$	-13.0	

What is most remarkable, methylglyoxal bisdimethylhydrazone contains two azomethine functions, each providing the nitrogen lone-pair effects (LPE) upon the values of ^{1}J(C,C) and ^{1}J(C,H) couplings – a positive contribution to J_{cis} (+LPE) and the negative one to J_{trans} (–LPE) of the adjacent either C–C or C–H bond, as shown below:

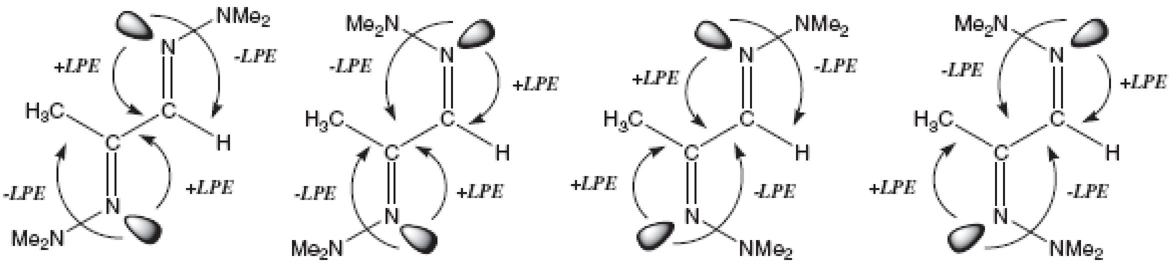

EE *EZ* *ZE* *ZZ*

The lone-pair effects on ^{1}J(C,C) and ^{1}J(C,H) in methylglyoxal bisdimethylhydrazone

Comparison of the calculated total values of ^{1}J(C,C) and ^{1}J(C,H) couplings in all four possible isomers of methylglyoxal bisdimethylhydrazone (Table 2) demonstrates the marked stereochemical dependence of these couplings upon the orientation of the lone pairs of both nitrogen atoms in the different isomers, in accord with the additive arguments. Established manifestation of the LPE in the values of ^{1}J(C-1,C-2), ^{1}J(C-2,C-3), and ^{1}J(C-3,H) of the four different isomers of methylglyoxal bisdimethylhydrazone provides unambiguous reasoning that the major observed isomer is *EE* while the minor one is *ZE*, both adopting predominant *s-trans* conformations.

Calculated dihedral angle dependences of ^{1}J(C-3,C-4) and ^{1}J(C-4,C-5) in respect to the internal rotation around the C(4)–CO and C(4)–N bonds accordingly in a iminodihydrofurans substituted with either amido or amino groups at the C(4) position of the 2,5-dihydro-2-iminofuran moiety demonstrate the marked stereochemical behavior which is due to the orientational effects of the C=O bond (Fig. 1a) and the amino nitrogen lone pair (Fig. 1b).

Table 2. ^1J(C,C) and ^1J(C,H) couplings (in Hz) of methylglyoxal bisdimethylhydrazone calculated at the SOPPA(CCSD) level compared with experimental values, whenever possible

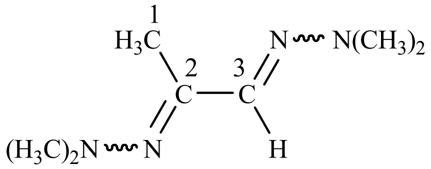

Isomer	Predominant conformation	Relative energy (kcal/mol)	^1J(C-1,C-2)		^1J(C-3,C-3)		^1J(C-3,H)	
			Calc	Exp	Calc	Exp	Calc	Exp
EE	*s-cis*	7.6	41.7		74.8		154.1	
	s-trans	0.0	41.8	41.5	74.5	75.3	162.1	162.7
EZ	*s-cis*	10.8	40.8		62.3		169.8	
	s-trans	9.7	39.3		57.3		178.6	
ZE	*s-cis*	7.8	51.1		63.9		154.0	
	s-trans	0.6	50.2	50.3	64.3	64.8	166.4	166.8
ZZ	*s-cis*	7.7	53.0		51.7		171.4	
	s-trans	10.6	51.8		44.5		171.4	

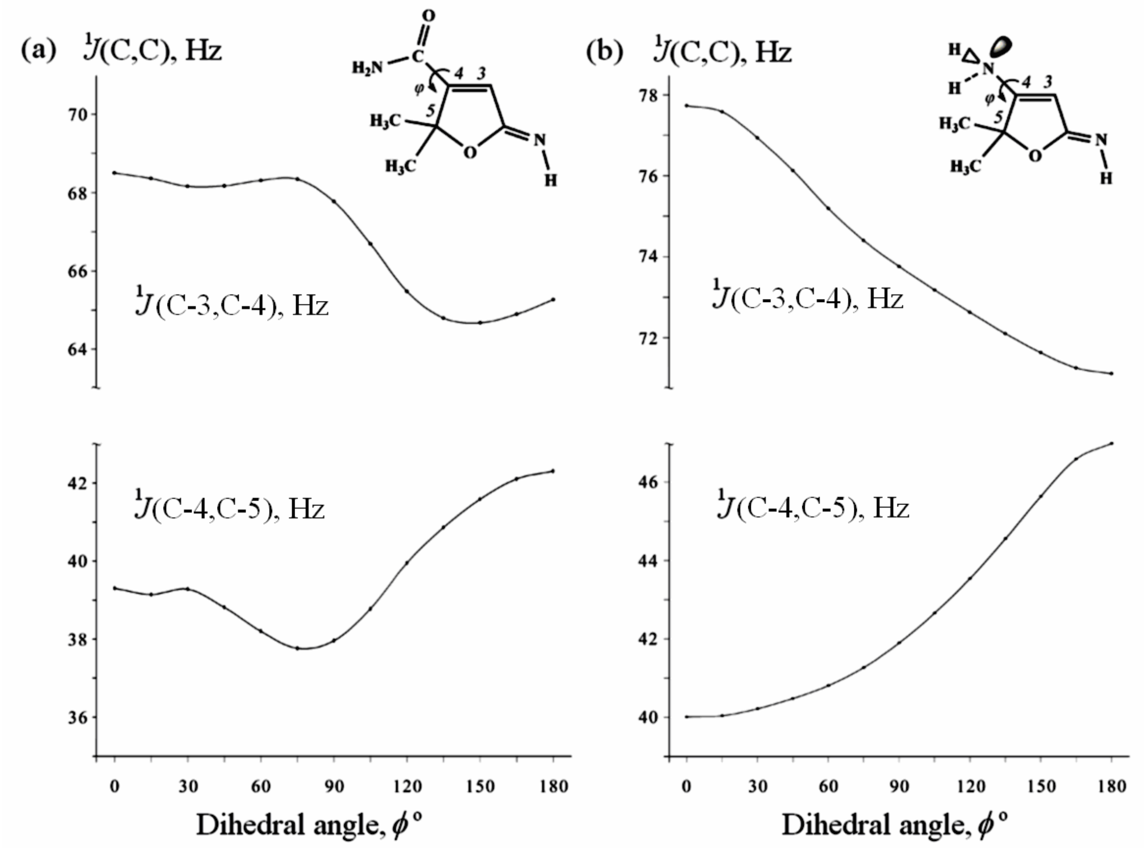

Fig. 1. Dihedral angle dependences of ^1J(C-3,C-4) and ^1J(C-4,C-5) in respect to the internal rotation around the C(4)–X (X = CO, N) bonds calculated at the SOPPA level with the MP2/6-311G* geometry optimizations in all rotational points.

It is noteworthy that ^1J(C-3,C-4) and ^1J(C-4,C-5) couplings in 4-amino-2,5-dihydro-5,5-dimetil-2-iminofuran (Fig. 1b) show the most remarkable stereochemical behavior. Indeed, the decrease of ^1J(C-3,C-4) from 78 to 74 Hz and increase of ^1J(C-4,C-5) from 40 to 43 Hz with the increase of φ from 0 to 90º is due to the decrease of the positive lone pair contribution to the former and decrease of the negative lone pair contribution to the latter, as follows from the very nature of the orientational lone pair effect. Further decrease of ^1J(C-3,C-4) from 74 to 71 Hz and increase of ^1J(C-4,C-5) from 43 to 47 Hz with the increase of φ from 90 to 180º is accounted for the increase of the negative lone pair contribution to the former and increase of the positive lone pair contribution to the latter. Taking into consideration these results, it follows from the experimental values of ^1J(C-3,C-4) = 73.5 Hz and ^1J(C-4,C-5) = 42.4 Hz that all amino iminodihydrofurans with the amino, alkylamino and dialkylamino groups at C^4 under study have mostly the orthogonal orientation of the amino nitrogen lone pair towards the plane of the iminodihydrofuran moiety.

On the other hand, the orientational effect of the C=O bond upon ^1J(C-3,C-4) and ^1J(C-4,C-5) in 4-carbamoyl-2,5-dihydro-5,5-dimethyl-2-iminofuran (Fig. 1a) governing their dihedral angle dependences is accounted for the effect of the hyperconjugative interactions on the Fermi contact term. Indeed, ^1J(C-3,C-4) decreases from 68 to 65 Hz while ^1J(C-4,C-5) increases from 39 to 42 Hz when increasing φ from 0 to 180º, i.e. when going from *s-cis* to *s-trans* conformer. Comparison of the calculated couplings with their experimental values, ^1J(C-3,C-4) = 65.1 Hz and ^1J(C-4,C-5) = 41.7 Hz leaves no doubt that 4-carbamoyl-2,5-dihydro-5,5-dimethyl-2-iminofuran adopts predominant *s-trans* conformation, in line with thermodynamic reasoning: *s-trans* conformer is by 3.8 kcal/mol more stable than the *s-cis* conformation, as calculated at the MP2/6-311G** level.

It thus follows that experimental measurements of ^{13}C–^{13}C, ^{13}C–^{1}H and ^{15}N–^{1}H spin-spin coupling constants in a series of azomethines in combination with their high-level non-empirical calculation provides a new guide to their stereochemistry including configuration at the C=N bond together with conformational structure.

References

[1] L.B. Krivdin, N.A. Scherbina, N.V. Istomina. *Magn. Reson. Chem.* 2005, **43**, 435.

[2] K.A. Chernyshev, L.B. Krivdin, L.I. Larina, T.V. Konkova, M.M. Demina, A.S. Medvedeva. *Magn. Res. Chem*. 2007, **45**, 661.

[3] L.B. Krivdin, S.S. Khutsishvili, O.A. Shemyakina, A.G. Mal`kina, B.A. Trofimov, R.H. Contreras. *Magn. Reson. Chem.* 2007, **45**, 758.

[4] L.B. Krivdin, L.I. Larina, K.A. Chernyshev, A.Yu. Rulev. *Magn. Reson. Chem.* 2006, **44**, 178.

[5] L.B. Krivdin, L.I. Larina, K.A. Chernyshev, N.A. Keiko. *Austr. J. Chem.* 2006, **59**, 211.

[6] L.B. Krivdin, L.I. Larina, K.A. Chernyshev, I.B. Rozentsveig. *Magn. Reson. Chem.* 2005, **43**, 937.

[7] L.B. Krivdin, K.A. Chernyshev, G.N. Rosentsveig, I.V. Ushakova, I.B. Rosentsveig, G.G. Levkovskaya. *Magn. Res. Chem*. In press.

[8] V. Barone, J.E. Peralta, R.H. Contreras, A.V. Sosnin, L.B. Krivdin. *Magn. Reson. Chem.* 2001, **39**, 600; L.B. Krivdin, S.V. Zinchenko, V.V. Shcherbakov, G.A. Kalabin, R.H. Contreras, M.F. Tufro, M.C. Ruiz de Azua, Giribet. *J. Magn. Reson.* 1989, **84**, 1; R.H. Contreras, C.G. Giribet, M.C. Ruiz de Azua, C.N. Cavasotto, L.B. Krivdin. *J. Mol. Struct. (Theochem)* 1990, **210**, 175; L.B. Krivdin, S.V. Zinchenko, G.A. Kalabin, M.F. Tufro, R.H. Contreras, A.Y. Denisov, O.A. Gavrilyuk, V.I. Mamatyuk. *J. Chem. Soc., Faraday Trans.* 1992, **88**, 2459; S.V. Zinchenko, R.Y. Kiselev, L.B. Krivdin. *J. Org. Chem. USSR (Engl. Transl.)* 1991, **27**, 1074.

NMR Assignments of the C-Terminal Domain of Human Polypeptide Release Factor eRF1

A.B. Mantsyzov[1)], E.V. Ivanova[2)], B. Birdsall[3)], P. Kolosov[2)], L.L. Kisselev[2)],
V.I. Polshakov[1)]

[1)]Center for Magnetic Tomography and Spectroscopy, M.V. Lomonosov Moscow State University, 119992, Moscow, Russia;
[2)]Engelhardt Institute of Molecular Biology, Russian Academy of Sciences, 119991, Vavilova str., Moscow, Russia;
[3)]Division of Molecular Structure, National Institute for Medical Research, The Ridgeway, Mill Hill, London NW7 1AA, U.K.

e-mail: mants@inbox.ru

Abstract

We report NMR assignments of the protein backbone of the C-terminal domain (163 a.a.) of human class 1 translation termination factor eRF1. It was found that several protein loop residues exist in two slowly interconverting conformational states.

Introduction

Termination of translation is governed by the cooperative action of two interacting polypeptide chain release factors, class-1 eRF1 and class-2 eRF3 [1]. The human eRF1 in the crystal [2] and in solution [3] consists of three domains. The N- terminal domain of the release factor eRF1 is involved in the recognition of one of the three stop codons, UAA, UAG or UGA [4,5]. The M-domain of eRF1 participates in the subsequent hydrolysis of the ester bond in peptidyl-tRNA [2,5]. The C-terminal domain of eRF1 interacts with the C-domain of eRF3 [6, 7] and the binding of both factors is essential for fast kinetics of the termination of translation [1]. At the same time, removal of this domain from human eRF1 enhances, rather than reduces, the termination activity *in vitro* [7,8]. The eRF3 is a ribosome- and eRF1-dependent GTPase which is encoded by an essential gene and belongs to class-2 release factors [9]. The mechanism of the interaction of eRF1 and eRF3 and its role in translation termination requires further elucidation. It is known that residues GILRY (411-415) of eRF1 are crucial for the interaction of eRF1 with eFF3 [7]. It is supposed, that the interaction between eRF3, GTP and eRF1 increases the affinity of eRF1 in forming the pretermination complex [1]. It is shown [1], that the binding of eRF1, eRF3 and GTP with the ribosome is accompanied by their cooperative interaction *in vitro* and it is suggested that this leads to significant conformational changes in the whole pretermination complex. These results are in good agreement with the fact, that both ternary (eRF1-eRF3-GTP) and quaternary complexes (eRF1-eRF3-GTP-Mg^{2+}) exist in solution even in the absence of the ribosome [10].

The structure of the C-domain of human eRF1 is still poorly known. The published crystal structure of eRF1 [2] has relatively low resolution of 2.8 Å and the C-domain has vast unresolved fragments. These unresolved highly mobile loops may have a functional role in interaction of eRF1 with eRF3. Earlier NMR assignments have been reported for the N-terminal domain (BMRB-6116) and the middle (M) domain (BMRB-6763) of the human eRF1. The solution structure and dynamics of the M-domain of human eRF1 have also been studied [11]. In order to elucidate the structure, dynamics and function of the C-domain of human eRF1, NMR assignments for the protein backbone of the C-domain of human eRF1 have been obtained.

Methods and experiments

The full-length cDNA encoding human eRF1 with the C-terminal His_6-tag fusion was cloned into pET23b(+) vector (Novagen) under the phage T7 RNA polymerase promoter. The C-domain (residues 276-437 of eRF1) was overproduced in *E. coli*, strain BL21(DE3), in M9 minimal medium and isolated using Ni-NTA resin (Qiagen). The protein was further purified by cation exchange chromatography using HiTrap SP columns (Pharmacia). For ^{13}C and/or ^{15}N-isotope labeling, [$^{13}C_6$]-D-glucose and/or $^{15}NH_4Cl$ (Cambridge Isotope Laboratories Inc.) were used as the isotope sources in M9 minimal medium.

The samples for NMR (approximately 1 mM) were prepared in either 95% H_2O/5% D_2O or in 100% D_2O and 10 mM potassium phosphate, 50 mM KCl, pH 7.0. Mercaptoethanol (final concentration ~2 mM) was added to the final solution in order to prevent oxidation of the free cysteine residue Cys-302.

All spectra were acquired at 25°C on Varian INOVA 600 and 800 MHz and Bruker AVANCE 600 MHz spectrometers equipped with triple resonance z-gradient probes. Spectra were processed by NMRPipe [12], and analyzed using SPARKY (from Goddard and Kneller). Sequential assignments for the backbone were obtained using the following spectra: 3D HNCO, HNCA, HN(CO)CA, HNCACB, CBCA(CO)NH, HNHAHB and HBHA(CO)NH.

Assignments and data deposition

In total, chemical shifts assignments were made for 89% of all the possible protein backbone amide resonances (Fig. 1); 89% of $^1H^N$ and non-prolyl ^{15}N resonances, 95% of $^{13}C^{\alpha}$ and 88% of $^{13}C'$ resonances. It was found that several residues (between a.a. 333 and 362) of protein loop that is invisible in crystal structure [2], exist in two slowly interconverting conformational states.

The ^1H, ^{15}N and ^{13}C chemical shifts have been deposited in the BioMagResbank database

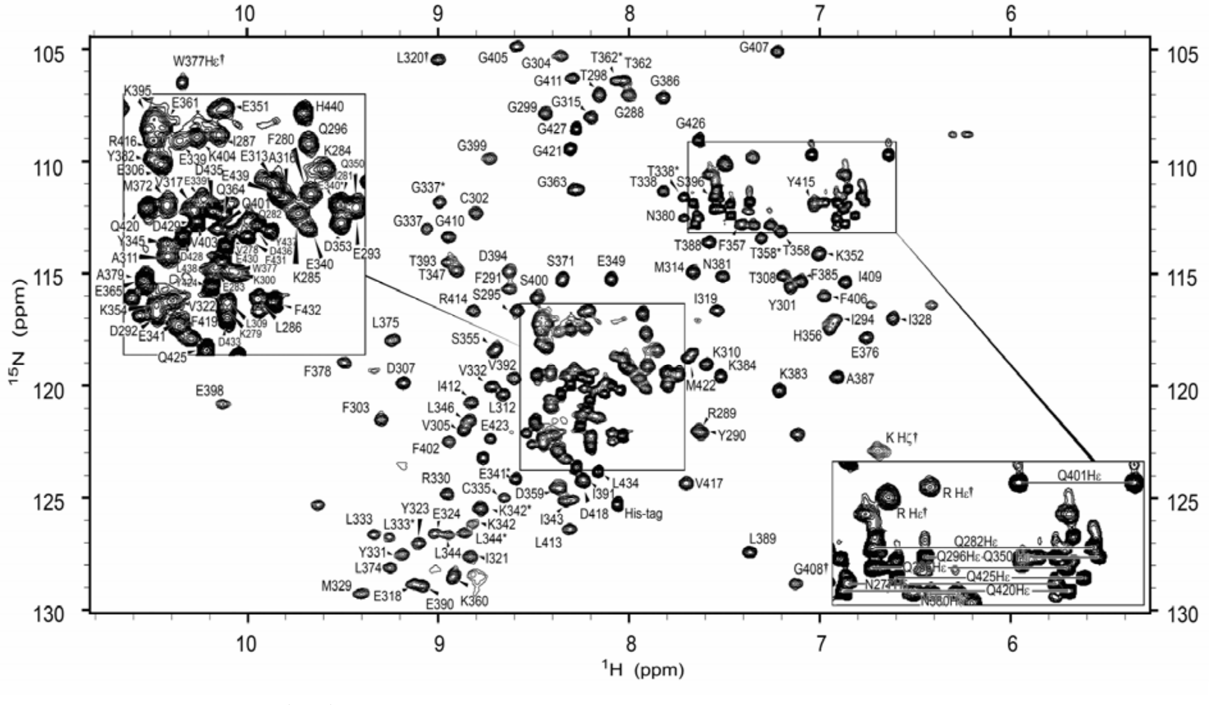

Fig.1 The ^1H,^{15}N-HSQC spectrum for the C-terminal domain of human eRF1. The numbering of the residues corresponds to that of the whole eRF1 protein. Asterisks (*) indicate resonances arising from the second conformational state of the amino acids 333-344 and 358-362. Peaks marked with the symbol (†) correspond to folded resonances, which would otherwise appear outside the spectral region shown.

(http://www.bmrb.wisc.edu) under the accession number BMRB-15366.

Acknowledgements

This work was partly supported by grants from the Presidium of the Russian Academy of Sciences (Program “Molecular and Cell Biology” to L.K.), the Russian Foundation for Basic Research (03-04-48943, to L.K. and 05-0888/04, to V.P.), the Presidential Program for Supporting the Leading Russian Scientific Schools (via Ministry of Education and Science to L.K.).

References

[1] Alkalaeva E.Z., Pisarev A.V., Frolova L.Y., Kisselev L.L. and Pestova T.V. (2006) In vitro reconstitution of eukaryotic translation reveals cooperativity between release factors eRF1 and eRF3, *Cell. 125*, 1125-36

[2] Song H., Mugnier P., Das A.K., Webb H.M., Evans D.R., Tuite M.F., Hemmings B.A. and Barford D. (2000) The crystal structure of human eukaryotic release factor eRF1--mechanism of stop codon recognition and peptidyl-tRNA hydrolysis, *Cell. 100*, 311-21.

[3] Kononenko A.V., Dembo K.A., Kisselev L.L. and Volkov V.V. (2004) Molecular morphology of eukaryotic class I translation termination factor eRF1 in solution, *Mol Biol (Mosk). 38*, 303-11.

[4] Bertram G., Bell H.A., Ritchie D.W., Fullerton G. and Stansfield I. (2000) Terminating eukaryote translation: domain 1 of release factor eRF1 functions in stop codon recognition, *RNA. 6*, 1236-47.

[5] Kisselev L., Ehrenberg M. and Frolova L. (2003) Termination of translation: interplay of mRNA, rRNAs and release factors? *EMBO J. 22*, 175-82.

[6] Ito K., Ebihara K. and Nakamura Y. (1998) The stretch of C-terminal acidic amino acids of translational release factor eRF1 is a primary binding site for eRF3 of fission yeast, *RNA. 4*, 958-72.

[7] Merkulova T.I., Frolova L.Y., Lazar M., Camonis J. and Kisselev L.L. (1999) C-terminal domains of human translation termination factors eRF1 and eRF3 mediate their in vivo interaction, *FEBS Lett. 443*, 41-7.

[8] Frolova L.Y., Merkulova T.I. and Kisselev L.L. (2000) Translation termination in eukaryotes: polypeptide release factor eRF1 is composed of functionally and structurally distinct domains, *RNA. 6*, 381-90.

[9] Frolova L., Le Goff X., Zhouravleva G., Davydova E., Philippe M., Kisselev L. Eukaryotic polypeptide chain release factor eRF3 is an eRF1- and ribosome-dependent guanosine triphosphatase. 1996, *RNA* 2, 334-341.

[10] Mitkevich V.A., Kononenko A.V., Petrushanko I.Y., Yanvarev D.V., Makarov A.A. and Kisselev L.L. (2006) Termination of translation in eukaryotes is mediated by the quaternary eRF1*eRF3*GTP*Mg2+ complex. The biological roles of eRF3 and prokaryotic RF3 are profoundly distinct, *Nucleic Acids Res. 34*, 3947-54.

[11] Ivanova E.V., Kolosov P.M., Birdsall B., Kelly G., Pastore A., Kisselev L.L. and Polshakov V.I. (2007) Eukaryotic class-1 translation termination factor eRF1: the NMR structure and dynamics of the middle domain involved in triggering ribosome-dependent peptidyl-tRNA hydrolysis, *FEBS Journal* 274, 4223-4237.

[12] Delaglio F., Grzesiek S., Vuister G.W., Zhu G., Pfeifer J. and Bax A. (1995) NMRPipe: a multidimensional spectral processing system based on UNIX pipes, *J Biomol NMR. 6*, 277-93.

Dynamic Nuclear Polarization: From Solids towards to Liquids, Biomolecules, and High Frequencies

M. Gafurov[1)], V. Denysenkov[1)], M. Prandolini[1)], S. Lyubenova[1)], B. Endeward[1)],
M Bennati[2)], T. Prisner[1)]

[1)]Department of Physical and Theoretical Chemistry and Center for Biomolecular Magnetic Resonance, J.W. Goethe-University, Frankfurt am Main, Germany,
[2)]Max-Planck Institute for Biophysical Chemistry, Goettingen, Germany

e-mail: gafurov@prisner.de

The sensitivity of NMR experiments can be enhanced orders of magnitude by polarization the nuclear spin system via a coupled electron spin reservoir. In dynamic nuclear polarization (DNP) experiments a diamagnetic sample is doped with paramagnetic molecules. The procedure involves microwave irradiation of the EPR spectrum of the paramagnetic species and results in the transfer of the larger electron spin polarization (due to the larger gyromagnetic ratio) to the nucleus spins.

We briefly review the mechanisms that are currently employed for DNP experiments (Overhauser Effect, Solid Effect, Cross Effect, and Thermal Mixing) and their applicability for solid and liquid probes at high magnetic field values.

We build a 9.4 Tesla DNP spectrometer to investigate the possibility of DNP on biomolecules at room temperature. For this a 400 MHz Bruker NMR spectrometer was extended with a 260 GHz microwave setup including microwave sources (50-300 mW), metallodielectric waveguide transmission system for decoupling of microwave excitation and reflection (which can be also used for EPR detection), and special double resonance structures which have been developed to avoid microwave heating of aqueous samples during DNP experiments. First test results are presented.

References

[1] Jeffries C. *Dynamic Nuclear Orientation* Interscience Publishers, **1963**

[2] В.А. Ацаркин *УФН.* **1978**, 126, 3

[3] R.Wind *Prog. Nucl. Magn. Reson. Spectrosc.* **1985**, 17, 33

[4] K.H. Hausser and D. Stehlik, *Adv.Magn.Res.* **1968**, 79

[5] Kan-Nian Hu, Vikram S.Bajaj, M.Rossay, and R.Griffin *J.Chem.Phys.* **2007**, 126, 044512 and references therein

NMR ^{1}H and ^{7}Li in $Li_{2-x}H_xMO_3$ (M=Ti, Zr)

Ya.V. Baclanova

Institute of Solid State Chemistry UB RAS, 620041, Pervomaiskaya str. 91, Ekaterinburg, Russia

e-mail: yana.2007@mail.ru

The aim of the present work was to investigate the peculiarities of replacement of lithium atoms by protons in Li_2MO_3 (M=Ti, Zr). Phases $Li_{2-x}H_xMO_3$ ($0<x\leq 2$) were prepared from a Li_2MO_3 samples, calcined at 700 °C, through ion exchange in 0.05 M acetic acid at 60°C. The final exchange products are the new compounds H_2MO_3 (or $MO(OH)_2$) with individual crystal structure. They are stable below 170-200^{o}C and above these temperatures transform into the known hydrous oxides $MO_2 \cdot nH_2O$.

The ordered crystal lattices of Li_2MO_3 (M=Ti, Zr) are derivatives from lattice NaCl with monoclinic distortion In Li_2TiO_3 lithium ions occupy positions Li(1), Li(2) between layers from octahedrons TiO_6 and positions Li(3) located in layers of TiO_6-octahedrons (fig. 1, a). In the lattice of Li_2ZrO_3 octahedron positions in the most dense cubic packing from oxygen ions are occupied with ions of lithium Li(1), Li(2) and zirconium (fig. 1, b).

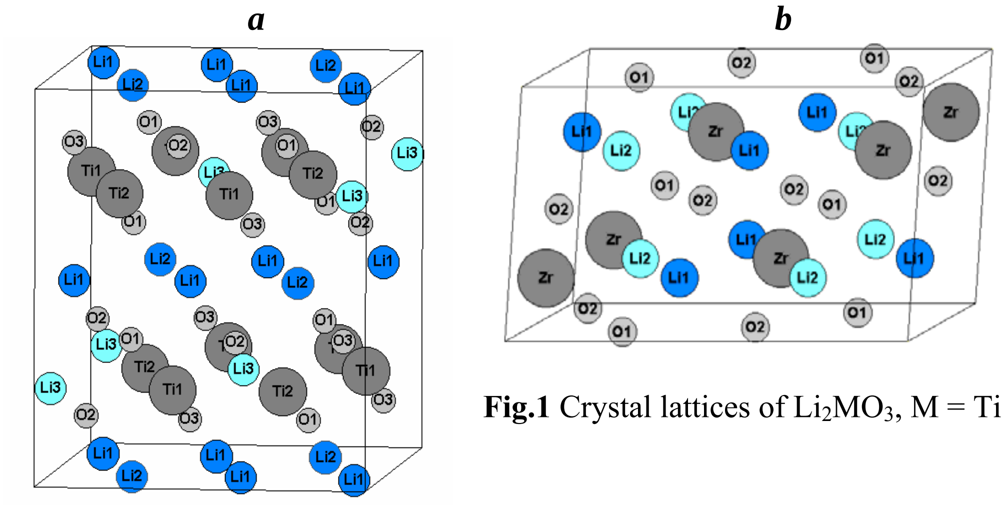

Fig.1 Crystal lattices of Li_2MO_3, M = Ti (*a*); Zr (*b*)

In order to determine the changes occurring in the nearest neighborhood of lithium ions when they are replaced by protons, we measured wide-line 7Li NMR spectra (Fig. 2), on which except for the central signal the satellite lines caused by quadrupole effects on lithium nucleus are observed. For reference of signals to the certain positions of lithium in a crystal lattice parameters of distortion (α) of LiO_6 octahedrons were calculated:

$$\alpha = \sqrt{\sum_{i=1}^{N}\left|1-\frac{R_i}{\sum_{i=1}^{N} R_i \Big/ N}\right|^2}\,; \qquad (1)$$

where R_i – distances Li – O in LiO_6 *i*-octahedron.

Values of parameters α can be considered as a first approximation for an estimation of size of a gradient of electric field (EFG) on ^{7}Li nucleus. Quadrupole coupling constant values (ν_q), relative areas of separate lines (S_i) and values of parameters α for various lithium positions are resulted in table.

Definition of quadrupole coupling constants in Li_2TiO_3 were carried out by decomposition of experimental spectra on two components: a line responsible for positions Li (1) and Li (2) with close values α and on a line from lithium in position Li (3). As follows from the table data, the signal areas from different lithium coincide with relative populations of corresponding positions. NMR ^{7}Li spectrum of Li_2ZrO_3 was superposition of two lines with approximately equal contribution and different constants ν_q. This result corresponded to equal population of two positions Li (1) and Li (2). The analysis of spectra of $LiHTiO_3$ and $Li_{0.3}H_{1.7}ZrO_3$ has shown that replacement of Li^+ by protons occurred equiprobably on all Li_i positions.

Results of the analysis of wide-line spectra NMR ^{7}Li of Li_2MO_3

M	Li$_i$, %	α	ν_q, MHz	*S*, % (±5)
Zr	Li1- 50%	0.166	51.5	51.4
	Li2 - 50%	0.050	28.5	48.6
Ti	Li1 - 50%	0.069	21	74.3
	Li2 - 25%	0.076		
	Li3 - 25%	0.243	44.5	25.7

^{1}H NMR wide-line spectra of $Li_{2-x}H_xMO_3$ ($0<x\leq 2$) samples recorded at –150°C (Fig. 3) are broad singlets with half-widths of Δh = 3.0–4.5 G, which is intrinsic to protons in $M(OH)_n$ groups, where $n \geq 2$. The spectra of the final exchange products H_2TiO_3 and H_2ZrO_3 are similar and different radically from the NMR spectra of $MO_2{\cdot}nH_2O$ samples [1], to which H_2MO_3 transforms when heated to 170–200 °C (Fig. 4, spectrum *c*). In hydrous titania and zirconia water molecules and protonic groups reside on grain surfaces of metal oxides, while the OH groups in H_2MO_3 are structural.

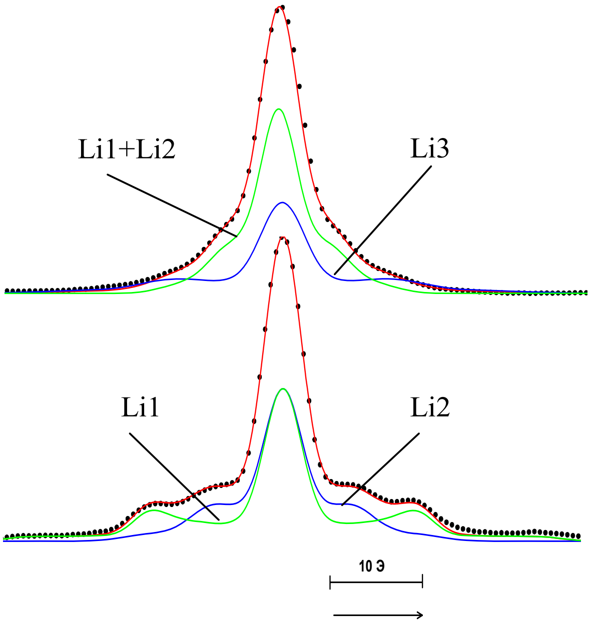

Fig. 2. Experimental (points) and calculated (continuous lines) spectra of a NMR ^{7}Li Li_2TiO_3 (a), Li_2ZrO_3 (b).

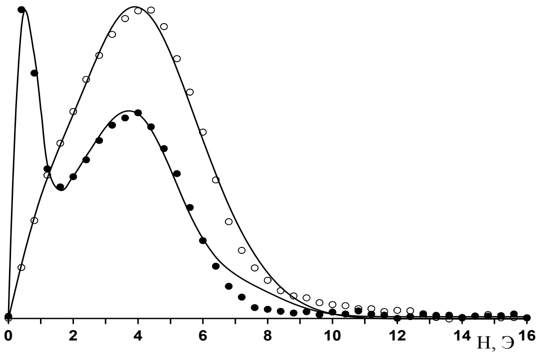

Fig.3 Experimental (circles) and calculated (continuous lines) ^{1}H NMR wide-line spectra of H_2TiO_3 at -150 °C (empty circles) and +30 °C (black circles)

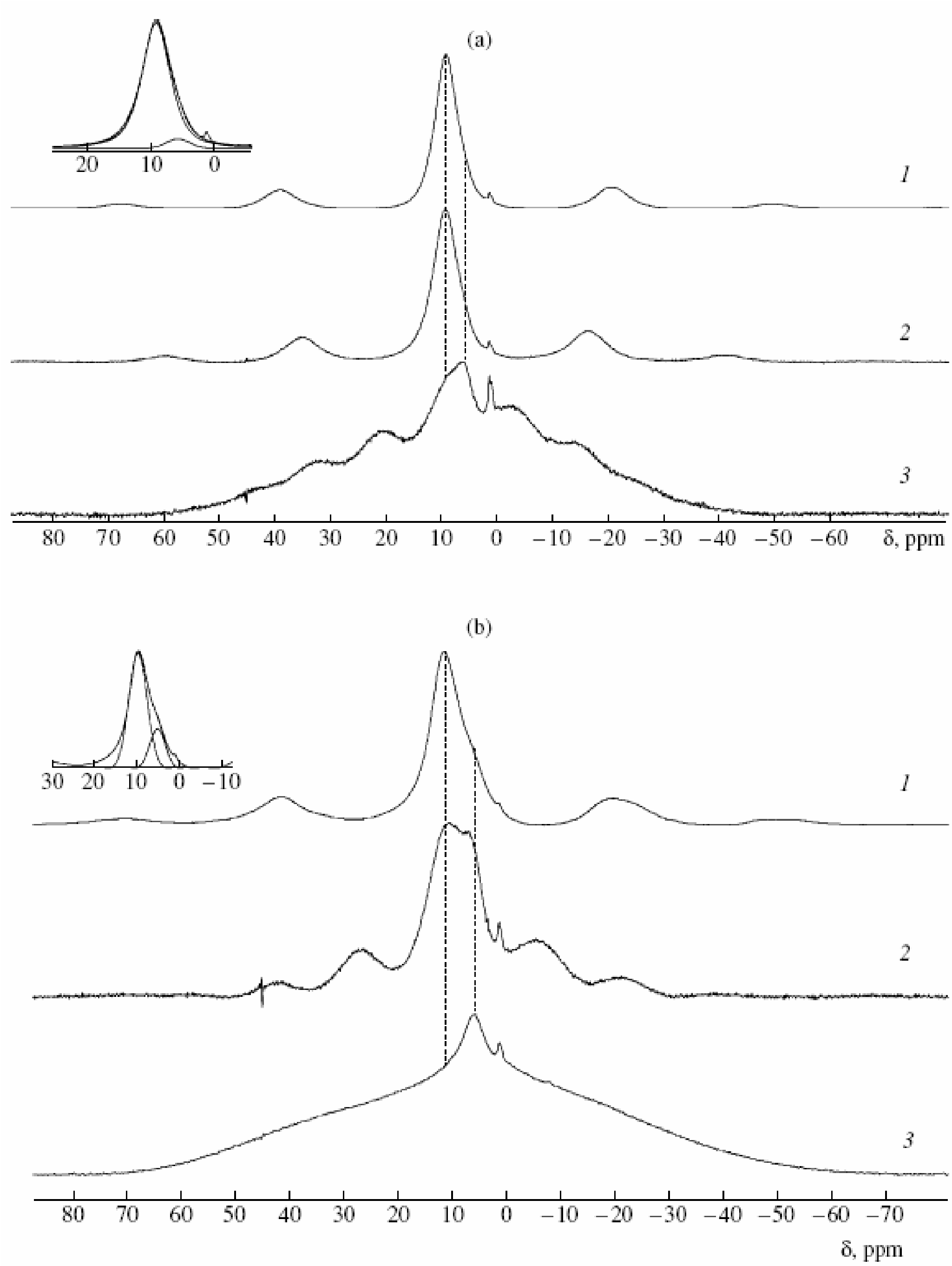

Fig.4 ^{1}H MAS NMR spectra for (a) $LiHTiO_3$ recorded at spinning rates of (*1*) - 12, (*2*) - 10, and (*3*) - 4.5 kHz; (b) H_2TiO_3 at (*1*) - 12 and (*2*) - 6.5 kHz; and (3) - a static spectrum. Isotropic lines are shown in dash. In the insets, decomposition of the major signal into components.

The high-resolution (MAS) ^{1}H NMR spectra of the samples having the compositions $LiHTiO_3$ and H_2TiO_3, shown in Fig. 4, are a superposition of two lines with isotropic chemical shifts of $\delta_1 = 5.7$ ppm and $\delta_2 = 9.7$ ppm for $LiHTiO_3$ and $\delta_1 = 5.8$ ppm and $\delta_2 = 11.4$ ppm for H_2TiO_3. The appearance of two lines signifies a chemical inhomogeneity of protons in the samples. The isotropic shift δ_2 of the strongest signal increases in transfer from $LiHTiO_3$ to H_2TiO_3 this proves that the acidity of the protons increases as a result of the strengthening of hydrogen bonds [2]. On the other hand, δ_1 remains nearly unchanged for both compositions; however, its fraction increases from 0.10 in $LiHTiO_3$ to 0.24 in H_2TiO_3.

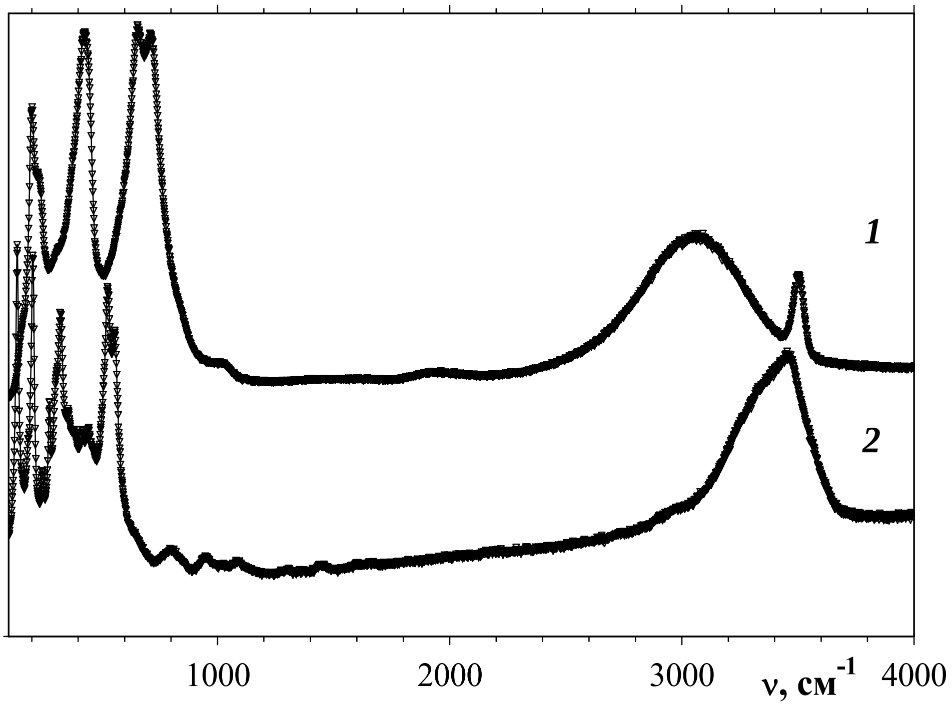

Fig.5 Raman spectra of H_2ZrO_3 (*1*) и H_2TiO_3 (*2*)

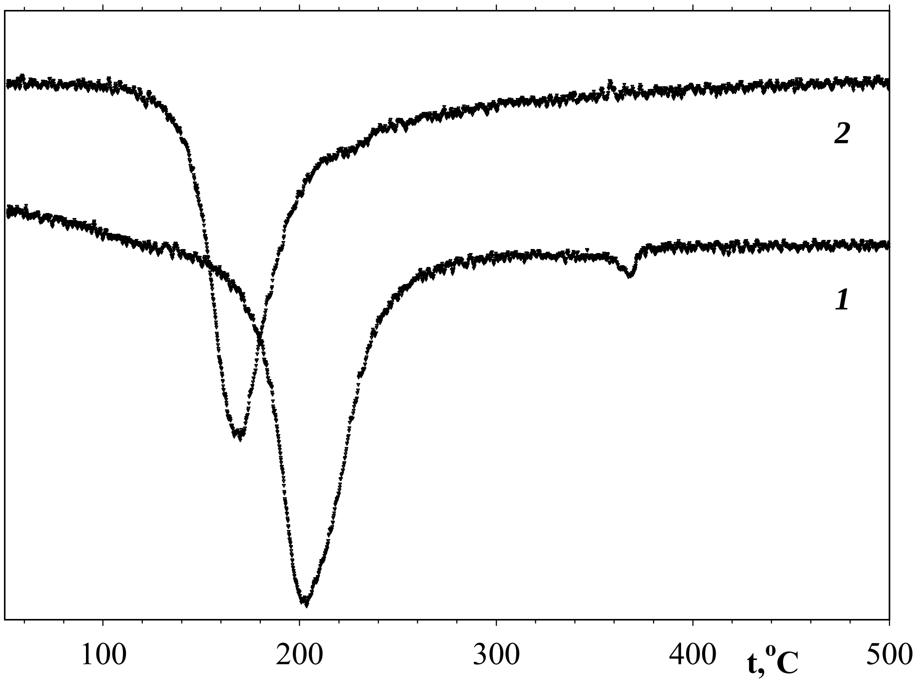

Fig.6 DTG curves of H_2ZrO_3 (*1*) and H_2TiO_3 (*2*)

The above features allow us to assign the lines with δ_1 to the protons of isolated OH groups which are not hydrogen-bonded either with each other or with other OH groups.

The Raman spectra of H_2TiO_3 and H_2ZrO_3 are shown in Fig. 5. Two lines are observed in H_2TiO_3 in the region 2000–4000 cm^{-1}, where O–H stretching vibrations appear. The broad line at 3000 cm^{-1} is due to hydrogen-bonded OH groups. The narrow line at 3500 cm^{-1} is due to short, isolated O–H bonds uninvolved in the interaction with other oxygen–hydrogen groups. In H_2ZrO_3 O–H stretching vibrations are shown as a wide line at 3400 cm^{-1} which asymmetric form allows to make the conclusion about presence of two types of the structural

OH - groups differing by bond energy with a crystal lattice. In comparison with H_2TiO_3 O–H stretching vibrations of H_2ZrO_3 are shifted in high-frequency area that testifies to weaker hydrogen bonds. It is possible to explain this fact in the bigger sizes of an elementary cell of H_2ZrO_3 according to radiuses of Ti (IV) and Zr (IV).

Weaker hydrogen bonds of OH groups in H_2ZrO_3 lead to the greater thermal stability of the compound in comparison with H_2TiO_3 (Fig.6).

The fact that up to about 75% of the OH groups in H_2TiO_3 are hydrogen-bonded allows us to classify this compound as a metatitanic acid. H_2ZrO_3 should be attributed to hydroxides and the chemical formula should be written down as $ZrO(OH)_2$.

The electronic structure and chemical bonding parameters in lithium titanate and zirconate and their protonated analogues were compared using the band quantum-chemical techniques. It was shown that covalent bonds M-O in the H_2MO_3 lattice are weaker, whereas H-O bonds are stronger as compared with M-O and Li-O bonds in Li_2MO_3. The calculated results are in good agreement with the data on thermal stability of the compounds.

This work was supported by the Russian Foundation for Basic Research, project no. 06-08-00847; the Program for the Support of Leading Scientific Schools, project nos. NSh 5138-2006-3 and NSh 8380-2006-3; and the joint program for interdisciplinary projects of the Ural and Siberian Divisions of the Russian Academy of Sciences.

References

[1] R. N. Pletnev, A. A. Ivakin, D. G. Kleshchev, et al., Hydrated Oxides of the Group IV and V Elements (Nauka, Moscow, 1986).

[2] V. M. Mastikhin and K. I. Zamaraev, Heterogeneous Catalysis as Probed by Solid-State High-Resolution NMR (Inst. of Catalysis, Novosibirsk, 1990).

Relaxation of ^{2}H, ^{23}Na, and ^{35}Cl Nuclei in Binary and Ternary Aqueous Solutions

A.V. Donets, V.I. Chizhik

Faculty of Physics, Saint-Petersburg State University, 198504, Ulyanovskaya str., 1, Petrodvorets, Saint Petersburg, Russia.

e-mail: aldonets@mail.ru

The method developed in the Department of Quantum Magnetic Phenomena (SPbSU) makes it possible to determine important parameters of the microstructure of electrolyte solutions using measurements of magnetic relaxation rates of solvent nuclei as functions of concentration and temperature [1]. The fact that many ions keep their coordination within wide ranges of concentration and temperature of the solution was experimentally proved. However, when solutions containing the Cl^- ions were studied [2], a peculiar temperature dependence of the relaxation rates was detected: within 30-40°C the nearest environment of the Cl^- ion changes. For the temperatures lower than 30°C the tetrahedral structure of the chlorine hydration shell appears to be more energetically effective. When the temperature exceeds 40°C, the Cl^- hydration shell consists of 8 solvent molecules. The changes of the Cl^- hydration shell in the temperature interval 30-40°C reflects the change of the water microstructure.

The investigation of the aqueous solutions of salts, containing the Cl^- anions and different organic compounds, has been carried out in a wide range of concentration and temperature. The biological components β-alanin, glutathione, BSA, γ-globulin were used. The examples of the experimental data are presented in Fig. 1 and Fig. 2. The slope of experimental curve is proportional to the activation energy, the bends occur at the temperature in which the microstructure near Cl^- anions changes. The results confirm the supposition about the reorganization of the nearest environment of chlorine anions. The effect occurs within the relatively narrow temperature interval between 30 and 35°C.

The structure of the nearest vicinity of chlorine ion in the aqueous salt solution with organic molecules can be described as superposition of "free" and solvated substructures. If the exchange of the ^{35}Cl between these substructures is fast, the analysis of the experimental results leads to the formulation of some rules for the formation of the solvation shells of different organic compounds. One can write

$$p_f = \frac{\dfrac{1}{T_1^{A}} - \dfrac{1}{T_1^{A'}}}{\dfrac{1}{T_1^{OA}} - \dfrac{1}{T_1^{OA'}}} \tag{1}$$

$$\frac{1}{T_1^{bA}} = \frac{\dfrac{1}{T_1^{A}} - \dfrac{p_f}{T_1^{OA}}}{1 - p_f} \tag{2}$$

where p_f – the relative concentration of “free” chlorine ions in solution (with protein); T_1^{A} and $T_1^{A'}$ – the relaxation times of the ^{35}Cl, which can be determined in the experiments with simple electrolyte solutions (without protein); T_1^{OA} and $T_1^{OA'}$ – the relaxation times of the ^{35}Cl (solution with protein); T_1^{bA} – the relaxation time of solvated chlorine ion (see, Fig. 2).

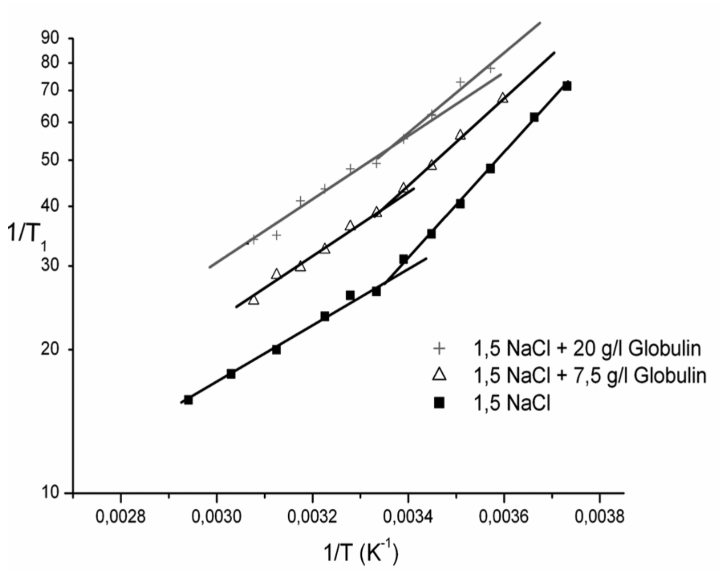

Fig.1 Temperature dependence of the ^{35}Cl spin-lattice relaxation rates

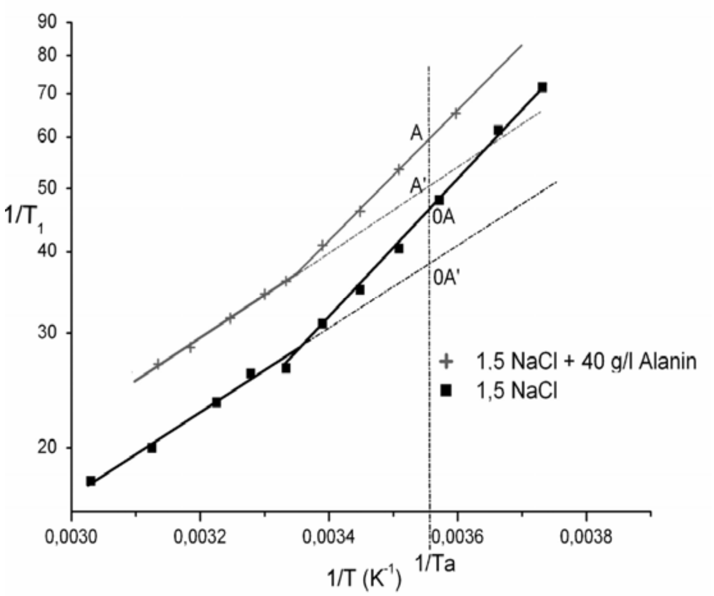

Fig.2 Temperature dependence of the ^{35}Cl spin-lattice relaxation rates

Much attention has been paid to the investigation of the similar systems by very complicated methods. In our case, equations 1 and 2 allow the determination of the concentrations and relaxation rates of "free" and solvated chlorine in the structure of solution.

This work is supported by the Russian Foundation for Basic Research (07-03-00735) and the Government of St. Petersburg.

References

[1] Chizhik V.I. Molec. Phys. 1997. V. 90 № 4. P. 653-659.

[2] Donets A.V., Chizhik V.I. 2005. Rus. J. Phys. Chem. V.79. №6. P.893-897.

Reorientation mobility of NH_3-group and thermodynamic parameters of glycine polymorphs

I.V. Drebushchak[1)], S.G. Kozlova[1)], S.P. Gabuda[1)], E.V. Boldyreva[2,3)], A. R. Semyonov[1)]

[1)]Nikolaev institute of inorganic chemistry SB RAS, Lavrentiev prospect 3, Novosibirsk 630090, Russian Federation

[2)]Novosibirsk state university, research and education center for Molecular Design and Ecologically Safe Technologies, Pirogova 2, Novosibirsk 630090, Russian federation

[3)]Institute of solid state chemistry and mechanochemistry, Kutateladze 18, Novosibirsk 630128, Russian Federation

e-mail: dairdre@gmail.com

One of the most important problems in condensed matter physics and chemistry is the problem of polymorphism, which arises when the same compound crystallizes into different crystal structures. A widely used drug, glycine, under the ambient conditions crystallizes into three polymorph modifications that have different piezoelectric and optical properties. Structure investigations [1–3] show that in crystals glycine appears as zwitterions $\left({}^{+}NH_3 - CH_2 - COO^{-}\right)$ connected to each other via the network of N–HO hydrogen bonds. Each polymorph has its own unique hydrogen bond system. The stability of glycine polymorphs was studied in the series of papers [4-6]. Recent calorimetric studies of β-glycine [6] have shown that it has a second order phase transition near the temperature of 252 K. However, X-ray data [6] and IR spectra [7] at this temperature range don't contain any information that may clarify the mechanism behind the phase transition. One can suppose that this phase transition may be related to disorder effects of NH_3 group reorientation process. If the process involves additional states, the system entropy may change. That will lead to the second order phase transition. The reorientation process can easily be characterized by ^1H NMR data. Moreover, there were no detailed studies of proton mobility in β-polymorph of glycine.

In this work we used powder samples obtained by recrystallizing various unsorted glycine samples [8]. The polymorph purity was controlled by X-ray powder diffraction. The continuous wave ^1H NMR spectra for the three glycine polymorphs were registered using the homemade solid state NMR spectrometer operating at 23 MHz. The measurements were performed within the temperature interval 140350 K. We also measured the temperature dependence of spin-lattice relaxation time (T_1) for the β-from at 25 MHz. Because of the saturation effects that appear at temperatures lower than the phase transition temperature on the one hand, and the increased possibility of β transforming into other forms with increasing temperature on the other hand, these measurements were held between 294 K and 316 K.

Fig. 1 shows low temperature spectra for α-, β- and γ-polymorphs of glycine. Protons in zwitterions are organized in CH_2 and NH_3 groups. This makes possible to simulate the spectra as superposition of three-spin and two-spin functions. For the two-spin group we used the Pake function and for three-spin group we used functions from papers [9] and [10]. The proton-proton distance for CH_2 group was set to 1.7 Å and we only varied the distances between protons for NH_3 group. Because of the saturation effects that distort the central part of the spectrum line, we were able only to fit the outer parts of the spectra starting from 30 kHz. Fig. 2 shows the example for β-form spectrum. Table 1 shows values for ammonium group proton-proton distances in three forms of glycine. These values agree with structure data [11].

Table 1. The proton-proton distances for amino-group in three forms of glycine.

	α	β	γ
D_{HH} (NH_3), Å	1.58±0.03	1.62±0.03	1.63±0.02

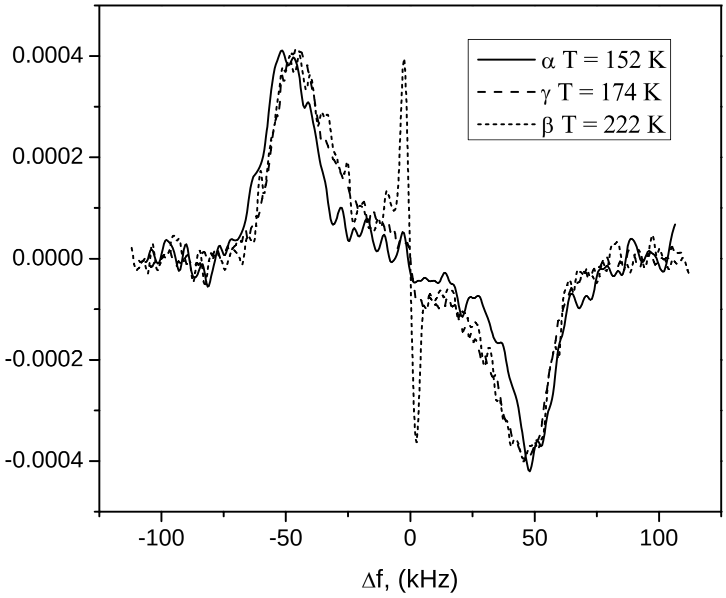

Fig.1 The low temperature ^{1}H NMR spectra for α-, β- and γ-polymorphs of glycine.

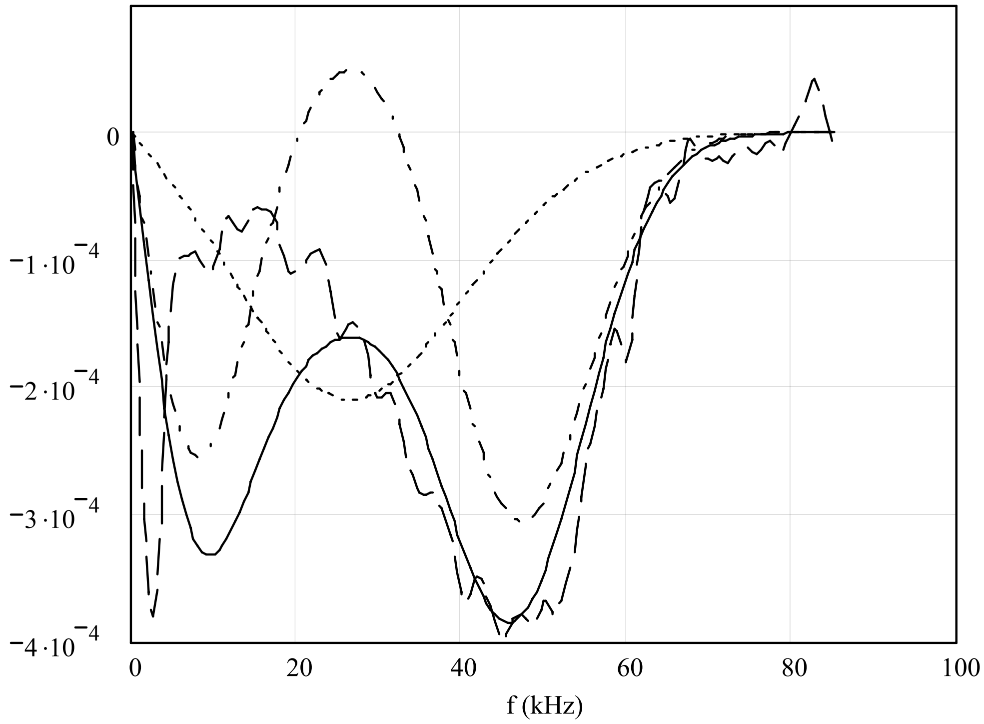

Fig.2 Fitting the ^{1}H NMR spectrum for β-polymorph of glycine (222 K). Dashed line represents experimental data, solid line represents theoretical curve, dotted and dash-dotted lines represent two-spin and three-spin components respectively.

Fig. 3 shows the temperature dependence of the second momentum for glycine spectra. All three curves show the development of some activation process. Note that for β-glycine the temperature, where the narrowing of the spectrum starts, is close to the temperature of the phase transition. The temperature dependence of the second moment *$M_2(T)$* may be described by the following equation [12]:

$$M_2(T) = M_2^{\min} + \Delta M_2 \arctan\left(\exp\left(\frac{E_a}{RT}\right)\frac{\sqrt{M_2(T)}}{\tau_c^{-1}}\right), \qquad (1)$$

$$\tau_c = \tau_0 \exp(E_a/kT)\exp(-\Delta S/R), \qquad (2)$$

where M_2^{min} is the minimum value of the second momentum, ΔM_2 is the difference between minimum and maximum values of the second momentum, τ_c is the correlation time that characterizes the reorientation process, E_a is the activation energy for the process, k is the Boltzmann constant, and τ_0 is the librational frequency. For glycine, τ_0^{-1} = 1.46x10^{13} Hz [unpublished data by S.V. Goryainov (Raman spectroscopy)]. Equation (1) allows to determine the activation energy for the reorientation process. The resulting values are shown in the Table 2. The activation barrier for amino-group reorientation in β-glycine is the highest among all polymorphs. In case of powder samples the transition region is widened, thus the correlation time values found by equation (1) are not correct.

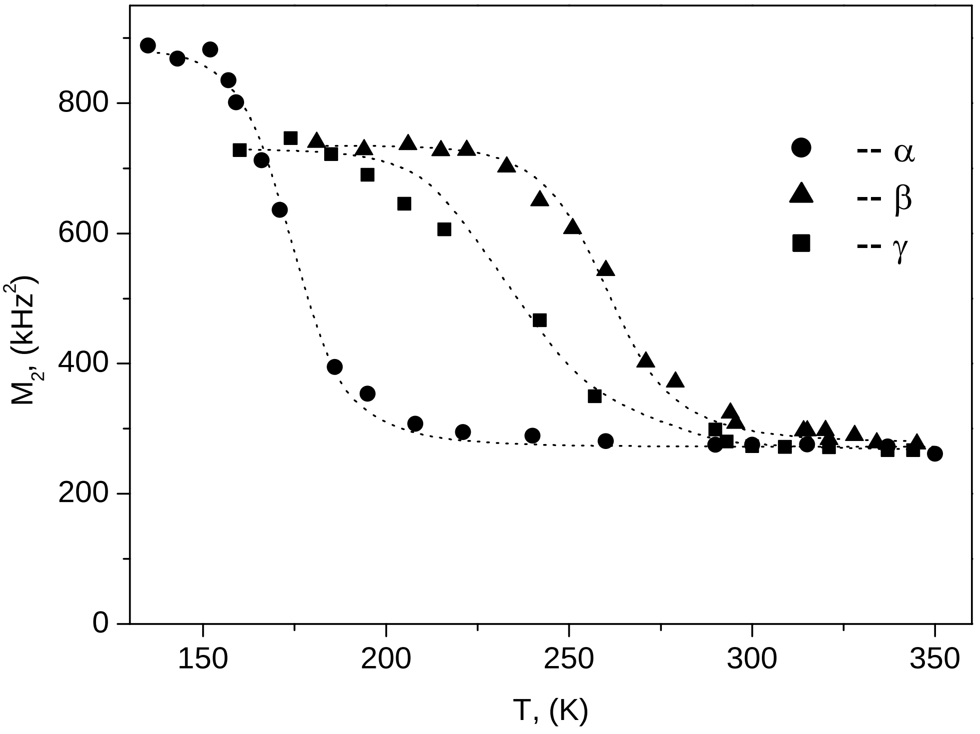

Fig.3 Temperature dependence of the second moment M_2 of the ^{1}H NMR spectra for three glycine polymorphs. Dotted lines represent the best fit theoretical curves (equation (1)).

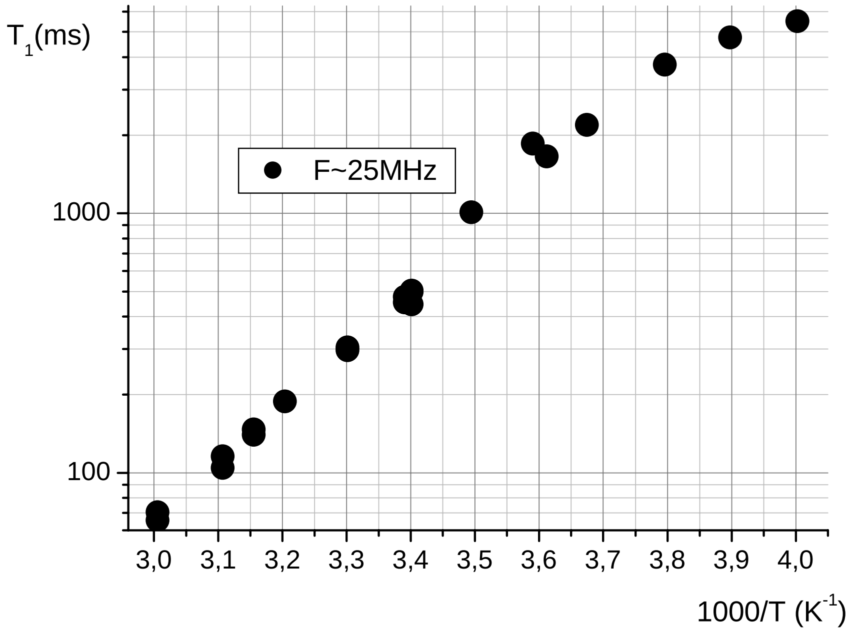

Fig.4 Temperature dependence of the spin-lattice relaxation time T_1 for the β-glycine.

Correct values for the correlation time τ_c may be found by measuring the temperature dependence of the spin-lattice relaxation time T_1 (Fig. 4 shows $T_1(T)$ for β-glycine)with the help of the following equation [13]:

$$T_1^{-1} = \frac{2}{3}\gamma_H{}^2 \Delta M_2 \left(\frac{\tau_c}{1+(\tau_c\omega_0)^2} + \frac{4\tau_c}{1+4(\tau_c\omega_0)^2} \right), \tag{3}$$

where γ_H is the gyromagnetic ratio for proton and ω_0 is the Larmor frequency. Knowing the τ_c value, we may also calculate the entropy contribution for the reorientation process ΔS using equation (2). Table 2 shows NH_3 reorientation process parameters for three glycine polymorphs, $\tau_a = \tau_0 \exp(-\Delta S/R)$ is the inverse for the so called "attempt rate".

Table 2. Amino-group reorientation parameters: activation energy, correlation time and exponential entropy factor.

	E_a, kJ/mol	τ_a, s x10^{-13}	exp($-\Delta S/R$), ($\Delta S/R$)
α-glycine	~ 23	*0.83	1.21, (-0.19)
γ-glycine	~ 29	*0.61	0.82, (0.2)
β-glycine	~ 43	0.77	0.89, (0.12)

* – data from the paper [14].

For all three polymorphs entropy contribution from amino-group reorientation process is $\Delta S \sim 0$. That means that no additional states are involved in the process. It also shows that the second order phase transition in β-glycine is not the result of the process activation. We assume that the phase transition may be a result of small proton displacements that were not registered by X-ray analysis in paper [6].

The work was supported by Interdisciplinary integration projects № 49 and №110 and RFBR projects 05-03-32468 and 05-03-32263.

References

[1] Marsh RE. Acta Crystallogr 11:654–663. (1958).

[2] Iitaka Y. Acta Crystallogr 13:35– 45. (1960).

[3] Iitaka Y. Acta Crystallogr 11:225–226. (1958).

[4] E.V. Boldyreva, V.A. Drebushchak, T.N. Drebushchak, I.E. Paukov, Y.A. Kovalevskaya, E.S. Shutova. Journal of Thermal Analysis and Calorimetry, Vol. 73 (2003) 409-418.

[5] E.V. Boldyreva, V.A. Drebushchak, T.N. Drebushchak, I.E. Paukov, Y.A. Kovalevskaya, E.S. Shutova. Journal of Thermal Analysis and Calorimetry, Vol. 73 (2003) 419-428.

[6] V.A. Drebushchak, E.V. Boldyreva, Yu.A. Kovalevskaya, I.E. Paukov and T.N. Drebushchak. Journal of Thermal Analysis and Calorimetry, Vol. 79 (2005) 65-70.

[7] Chernobay G.B., Chesalov Yu.A., Burgina E.B., Drebushchak T.N., Boldyreva E.V. Journal of Structural Chemistry, 2007, 48(2), 339-347.

[8] V.A. Drebushchak, E.V. Boldyreva, T.N. Drebushchak and E.S. Shutova, J. Crystal Grouth, 241 (2002) 266.

[9] E.R. Andrew, B. Bersohn, Journal of Chemical Physics, Vol. (1950), 159-161.

[10] E.R. Andrew, N.D. Finch. Proc. Phys. Soc., Vol. 70(B) (1957), 980-990.

[11] L.F. Power, K.E. Turner, F.H. Moore, Acta Cryst. B32 (1976) 11.

[12] A. Losche, Kerninduktion, Deutscher Verlag der Wissenschaften, Berlin, 1957.

[13] R. Kubo and K. Tomita, J. Phys. Soc. Jpn., 9 (1954) 888-919.

[14] Zhengtian Gu, Kazuyoshi Ebisawa, Ann McDermott. Solid State Nuclear Magnetic Resonance, Vol. 7 (1996) 161-172.

Analysis of the Radical Formation in Electron Irradiated Synthetic Carbonate-Containing Hydroxylapatite by IR, EPR and ESE Spectroscopy

Yu.I. Yakimenko1), M.K. Rodionov1), A.A. Sitnikov1), Yu.S. Borisov2), J. Hoentsch3),
A. Pöppl3), D.V. Savchenko4), E.N. Kalabukhova4)

1)Faculty of Electronics, National Technical University of Ukraine "Kyiv Polytechnic Institute", 03056, Pr. Peremohy 37, Kiev, Ukraine
2)Department of protective coatings, E.O. Paton Electric Welding Institute, NASU, 03650, Bozhenko Str. 11, Kiev, Ukraine
3)Faculty of Physics and Earth Sciences, Institute of Experimental Physics II, Leipzig University, D-04103, Linnéstrasse 5, Leipzig, Germany
4)Institute of Semiconductor Physics NASU, 03028, Pr. Nauki 45, Kiev, Ukraine

e-mail: katia@i.kiev.ua

Abstract

Radical formation in irradiated synthetic carbonate-containing hydroxylapatite (CHAp) were analyzed by electron paramagnetic resonance (EPR), field-sweep electron spin echo (ESE) and Fourier-transformed infrared (FT-IR) spectroscopy. Comparison of the X-, Q-band EPR and ESE results allows us to resolve five paramagnetic species in CHAp electron irradiated with a dose of 10 kGy in air at 300 K demonstrating the advantages of multi-frequency EPR and ESE techniques in the case of multi-component spectra. Three paramagnetic species were identified as the already known CO_2^-, PO_4^-, NO_3^{2-} radicals while two others were assigned to the NO? and CO? radicals which were not observed previously. Simulations of the experimental EPR, ESE spectra in the two frequency bands by using the Easyspin-2.6.0 toolbox and the FT-IR data support this assignment.

Introduction

Synthetically carbonated hydroxyapatite (CHAp) as well as biological apatites have been intensively investigated with EPR, after X-, γ-ray or heavy ion beam irradiation [1, 2]. The EPR spectrum of CHAp in the region near $g = 2$ was found to be highly composite, i.e. consisting of several contributions arising from radicals differing both in location (hydroxyl (A-type), phosphate (B-type) or surface location) and molecular structure (CO_3^-, CO_3^{3-}, CO_2^-, O^-, O_3^- etc.). Since the EPR signals of the different radicals overlap considerably, the overall EPR spectrum is very complex. In this case a multi-frequency EPR approach has been proven to be an effective tool for increasing the spectrum resolution and for distinguishing between the individual components of EPR spectrum [3]. Furthermore combination of X-, Q-band EPR and ESE techniques enable to disentangle overlapping EPR lines by taking advantage of differences in spin relaxation time of the paramagnetic species. However, very little has been reported about application of the pulse EPR techniques to decompose complex EPR spectra in irradiated apatites, whether biological or synthetically prepared.

In this paper we present an analysis of the radical compositions in irradiated synthetic CHAp by EPR, ESE along with FT-IR spectroscopy to demonstrate that the combination of these techniques are a powerful tool for studying of the irradiated CHAp.

Experimental details

Samples were synthesized from aqueous solutions of $Ca(NO_3)_2$, $(NH_4)_2HPO_4$, and NH_4OH. The resulting deposit was washed with the distilled water. Drying was performed at

200^0C until moisture content reached 1-2 wt. % with following heating in a dry CO_2 flow. The synthesis of hydroxyapatite is described in Ref. [4].

EPR spectra were measured at X- and Q- band frequencies. Field-sweep ESE measurements were performed on the X-band Bruker ESP 380E FT-EPR- Spectrometer and Q-band Bruker EMX EPR-Spectrometer with home-built pulse equipment using a $\pi/2$-τ-π pulse sequence. FT-IR spectra were measured at Perkin Elmer Fourier Transform Infrared Spectrometer Spectrum One in the range of 4000-400 cm^{-1}. The EPR, ESE and FT-IR measurements were performed on CHAp samples electron irradiated with the doses of 10 kGy at T=300 K and 100 kGy at T=370 K.

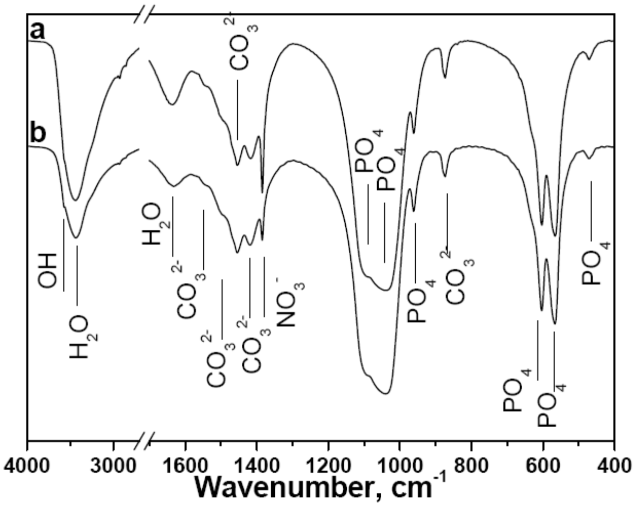

Fig. 1 The FT-IR spectra of CHAp sample measured at T = 300K. **a**- irradiated by 10 kGy, **b** - irradiated by 100 kGy

Experimental results

The FT-IR spectra (Fig. 1) revealed a typical apatite bands from PO_4^{3-} and carbonate ions, OH groups and H_2O [2, 5-7]. The broad bands observed at 1635 cm^{-1} and 3430 cm^{-1} were assigned to the adsorbed H_2O. The CHAp samples irradiated with the lower dose showed more intense absorption indicating more contamination due to water molecules. The band at 3430 cm^{-1} due to adsorbed water overlaps with the weak band at 3570 cm^{-1} which is due to structural OH and is not clearly visible. The fact that the absorption band at 630 cm^{-1} was not clearly observed in IR spectrum gave us the suggestion that the O-H stretching is very weak in CHAp as was previously concluded in [6].

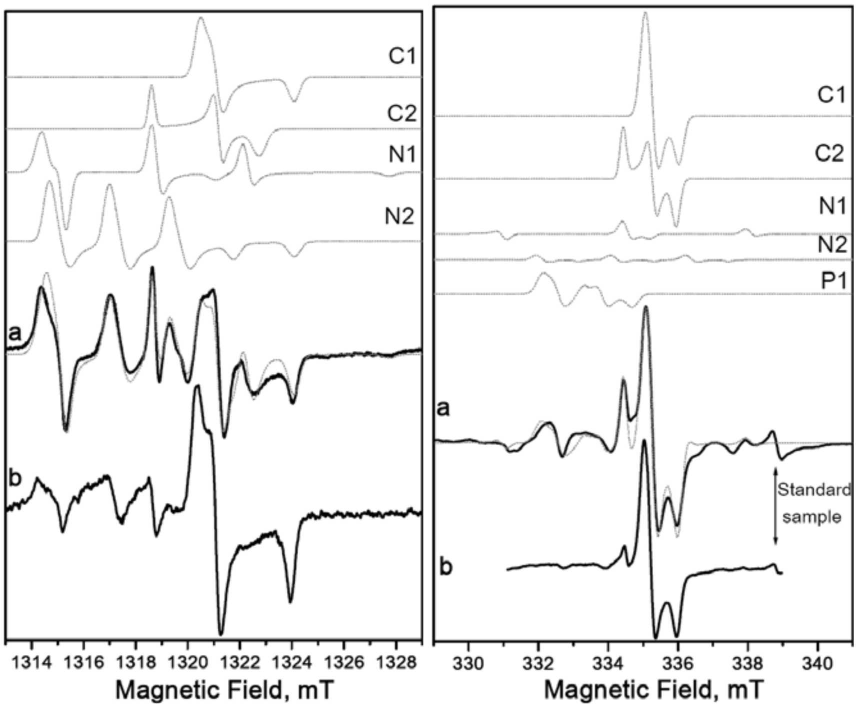

(1) **(2)**

Fig. 2 EPR spectra of CHAp sample (solid line) along with their simulations (dotted line) involving the four and five line profiles from Table 1. T=300 K. **a** - irradiated by 10 kGy, **b** - irradiated by 100 kGy, **(1)** – Q-band **(2)** – X-band

The IR absorptions at 1498 cm^{-1} and 1417 cm^{-1} indicates the presence of CO_3^{2-} ions located at PO_4^{3-} sites (B sites) while the IR absorptions at 1545 and 1454 cm^{-1} indicated the presence of CO_3^{2-} ions located at OH sites (A sites). The IR spectra in Fig. 1a and b show the band at 1385 cm^{-1} which was previously attributed to NO_3^- [5, 7].

Fig. 2 shows the Q- and X- band multi-component EPR spectra of CHAp sample irradiated by 10 kGy and 100 kGy measured at T=300 K. As can be seen in Fig. 2, several components contribute to the spectrum.

The Q- and X-band field-sweep ESE spectra of CHAp sample irradiated by 10 kGy and 100 kGy measured at T=300 K are shown in Fig. 3. As was seen from Fig. 3, ESE spectra mostly resemble the EPR spectrum of irradiated CHAp but with different relative contributions of the components due to various spin-relaxation times of the radical species that facilitates the spectrum decomposition.

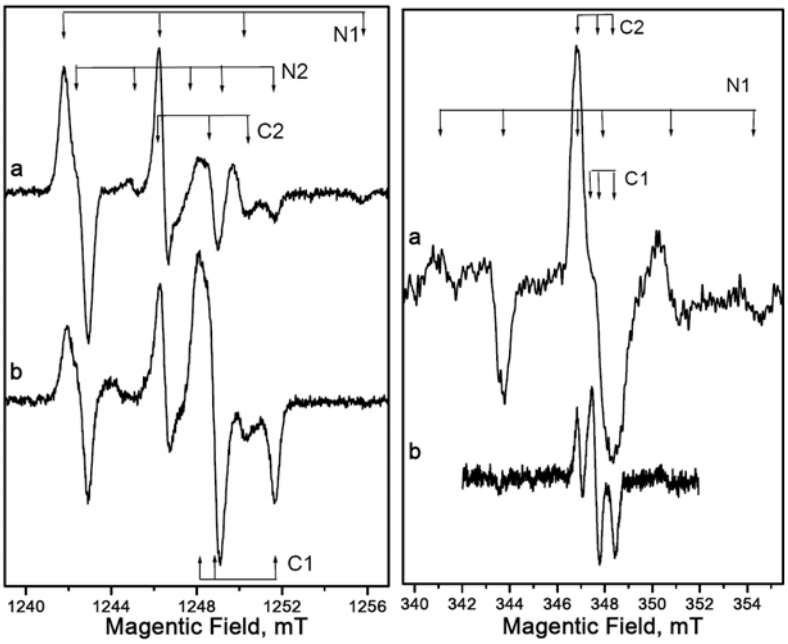

(1) **(2)**

Fig.3 First derivatives of field-sweep ESE spectra of CHAp sample. T=300 K. **a** - irradiated by 10 kGy, **b** - irradiated by 100 kGy, **(1)** – Q-band, **(2)** – X-band.

The simulation of the experimental EPR, ESE spectra was performed by using Easyspin-2.6.0 toolbox program [9]. It was found that the Q-band EPR spectrum is composed of four components labeled as C1, C2, N1, N2 while in the X-band an extra component labeled as P1 is present in EPR spectrum. Four (C1, C2, N1, N2) and three components (C1, C2, N1), contribute to Q- and X-band ESE spectra, respectively. The different number of components in the ESE spectra and different relative intensities of them are explained by the fact that the Q-band ESE spectra were measured by longer pulses than those at X-band.

After irradiation of the sample with dose of 100 kGy, as was seen from Fig. 2 and Fig. 3, C1 component dominates the EPR and ESE spectra while intensity of other components decreases and only N2 could be detected in Q-band EPR and ESE spectrum showing that radiation dose response of the individual radicals might be different. The reduction of the signals could also be due to the heating of the sample during the irradiation with dose of 100 kGy. The essential difference in intensity of the components in EPR spectrum may also account for the different microwave power level used in X and Q-band frequencies.

The best results of simulation, where all essential features of the spectrum are reproduced, were obtained with linear combination of five and four components with spin Hamiltonian parameters listed in the Table 1.

The evidence supporting the spectrum decomposition made here is that the basic components with the same spin Hamiltonian parameters were used to simulate the experimental EPR and ESE spectra in both frequency bands.

As was seen from Table 1, the spin Hamiltonian parameters confirm identity of the radical species labeled C1 and C2 with carbonate radicals, based on the similarity with the parameters obtained from earlier work on synthetic apatites [8]. At the same time, no definite conclusion can be made in a view of the type of CO? responsible for the C2 radical species, which was firstly revealed in irradiated synthetic CHAp in [8] and in this work, from a literature study.

Table 1. Spin Hamiltonian parameters of the EPR and ESE components derived from computer simulation in irradiated CHAp.

Label	Radical	g			A, mT			Ref.
		xx	yy	zz	xx	yy	zz	
C1	CO_2^-	2.0026(2)	2.0014(4)	1.9970(2)	-	-	-	[2]
C2	CO?	2.0058(3)	2.0014(3)	1.998(1)	-	-	-	[8]
N1	NO_3^{2-}	2.0053(2)	2.0053(2)	2.0013(2)	3.50(2)	3.50(2)	6.64(2)	[10]
N2	NO?	2.0084(2)	2.0074(2)	2.0009(2)	2.3(1)	2.3(1)	2.3(1)	This study
P1	PO_4^-	2.0164(2)	2.0135(2)	2.0082(2)	1.30(2)	1.30(2)	1.30(2)	[3]

It is obvious that the identification of the radical species would be easier when hyperfine information is available. Three other radical species P1, N1, N2 show the clearly resolved hyperfine structure. The triplet HF structure verifies the presence of nitrogen nucleus with spin I = 1 in N1, N2 radical species that gave us evidence that N1 and N2 are originated from nitrate radical ions.

Comparison with [10] showed that N1 is originated from nitrate radical ions NO_3^{2-}. This conclusion is supported by the fact that the band due to nitrate impurity was observed in FTIR spectrum of CHAp.

Nitrate radical ions NO? with parameters given in the Table 1 were not reported earlier. HF splitting due to interaction with a nuclear spin of I = 1/2 indicates that a phosphorus nucleus which has a spin I = 1/2 is responsible for the hf interaction of P1 radical species and therefore it can be classified as phosphate PO_4^- radicals [11].

Summary and Conclusions

As was previously stated, the multi-frequency magnetic resonance techniques applied in this work offer the opportunity to decompose multi-component EPR spectra in irradiated synthetic CHAp. The results of the present study, thanks to the multi-frequency approach and selectivity of ESE methods allows us to resolve five paramagnetic species in electron irradiated CHAp. Two radical species were attributed to the carbon-centered radical ions CO_2^- and CO?. It appears that CO? with parameters obtained in this study was not observed before. It was found that two nitrate radical ions NO_3^{2-} and NO? are coexisting in irradiated synthetic CHAp. Apart from carbon and nitrate radicals further signals with small intensity due to phosphate PO_4^- radicals were resolved in the EPR spectra. The elucidation of the chemical nature of the carbonate CO? and nitrate NO? radical ions observed for irradiated synthetic CHAp in this work remains a real challenge for future studies.

References

[1] S. Amira, G. Vanhaelewynl, F. Callens: Phys. Chem. Chem. Phys. **3**, 1724-1728 (2001).

[2] D.U. Schramm, A.M. Rossi: Appl. Radiat. Isot., **52**, 1085-1091 (2000).

[3] F. Callens, G. Vanhaelewyn , P. Matthys: Spectrochimica Acta Part A **58**, 1321–1328 (2002).

[4] T. Kanazawa: Inorganic Phosphate Materials, in Materials Science Monographs **5**, Kodanska-Elsevier, Tokyo 1989.

[5] D. Martini, M. Fini, V. De Pasquale at. al.: Biomaterials **24**, 1309-1316 (2003)

[6] N. Sahai, J.A. Tossell: J. Phys. Chem. B **104**, 4322, (2000).

[7] S. Raynaud, E. Champion, D. Bernache-Assollant, P. Thomas: Biomaterials **23**, 1065-1072 (2002)

[8] A.A. Sitnikov, M.K. Rodionov, D.V. Savchenko, Yu.S. Borisov, A. Pöppl, J. Hoentsch, E.N. Kalabukhova: Proc. of the Int. Conf. "Modern Development of Magnetic Resonance", Russia, Kazan', 24-29 September 2007 – in Press.

[9] S. Stoll, A. Schweiger: J. Magn. Reson., **177**, 390-403 (2005)

[10] T. Murata, K. Shiraishi, Y. Ebina, T. Miki: Appl. Radiat, Isot., **47** (11-12), 1521-1527 (1996)

[11] R.A. Peckauskas, I. Pullman: Calcif. Tiss. Res. **25**, 191-195 (1978)

EPR, ESE and Pulsed ENDOR Investigations of Nitrogen Aggregated Center in 4H-SiC Wafers Grown by Different Technologies

D.V. Savchenko1), S.N. Lukin1), A. Pöppl2), E.N. Kalabukhova1)

1)V.E. Lashkaryov Institute of Semiconductor Physics NASU, 03028, Pr. Nauki 45, Kiev, Ukraine
2)Faculty of Physics and Earth Sciences, Institute of Experimental Physics II, Leipzig University, D-04103, Linnéstrasse 5, Leipzig, Germany

e-mail: katia@i.kiev.ua

Abstract

Nitrogen aggregated center labeled N_x with $g_{||}=2.0055$, $g_\perp=2.0010$ was studied by field-sweep ESE and pulsed ENDOR in n-type 4H-SiC wafers grown by different techniques with different C/Si ratios and nitrogen concentration which were preliminary tested by EPR at high frequency. Based on ENDOR data obtained it was concluded that N_x nitrogen related center should be attributed to $N_{C,c}$–$N_{C,h}$ pairs with S=1 which were observed in the samples with low concentration of nitrogen as triplet line and in the sample with high nitrogen concentration as a single line. This conclusion was also supported by nutation frequency experiments from which the spin state of the N_x nitrogen related center was determined as S = 1.

Introduction

The recent high frequency EPR, ESE and pulsed ENDOR study of the 4H SiC wafers grown by different techniques showed that depending on the nitrogen concentration the n-type 4H-SiC wafers revealed, besides a triplet due to nitrogen residing on the cubic site (N_c), two nitrogen (N) related EPR spectra with $g_{||}=2.0055$, $g_\perp=2.0010$ and $g_{||}=2.0063$, $g_\perp=2.0005$ with different intensities [1]. In the samples with low nitrogen concentration the EPR line with the smallest hyperfine (hf) interaction and $g_{||}=2.0063$, $g_\perp=2.0005$ dominates the EPR spectrum and was attributed to N on the hexagonal lattice site (N_h). The triplet lines labeled N_x with $g_{||}=2.0055$, $g_\perp=2.0010$ lying exactly at half of the hf splitting of the $N_{C,h}$ spectrum and having half of the hf splitting of the N_c have low intensity in the samples with low nitrogen concentration and were transformed into one structureless line of high intensity in the samples with high nitrogen concentration. The microscopic origin of the N_x EPR-lines was discussed in [2] on the base of EPR parameters calculated from first principles. It was concluded that next nearest neighbour $N_{C,k}$–$N_{C,h}$ pairs which are coupled to S=1 centers are able to explain EPR experimental parameters of N_x center. In this work we used high frequency EPR, X-band ESE detected EPR and pulsed ENDOR to study the n-type 4H-SiC wafers with different nitrogen concentration to verify the electronic model for N_x center proposed in [2].

Experimental Details

A series of n-type 4H-SiC wafers grown by physical vapor transport (PVT), sublimation sandwich method (SSM) and modified Lely method with different C/Si ratios and nitrogen concentration which were preliminary tested at 140 GHz were investigated by ESE and pulse ENDOR. Donor concentrations in 4H-SiC were determined from temperature dependent Hall effect measurements. EPR measurements at 140 GHz were performed on a D-band EPR setup at 4.2 K. Spin-echo detected EPR and pulsed ENDOR measurements were performed in temperature range from 6 K to 50 K on the Bruker ESP 380 X-band spectrometer using modified Davies pulse sequence to enhance the sensitivity and nuclear spin relaxation [3].

In the modified Davies pulse sequence an additional rf pulse applied after echo detection helps the total spin system to recover to a thermal equilibrium in a much shorter time limited only by T_{1e} instead of T_{1n} as in case of the original Davies ENDOR experiment. So, the signal averaging can be performed at a much faster rate and an enhanced signal/noise ratio can be achieved in a shorter experimental time.

Experimental results

Fig. 1 and Fig. 2 show a typical D-band EPR and X-band field-sweep ESE spectrum observed in n-type 4H-SiC wafers with low donor concentration of about 10^{17} cm^{-3}. The EPR and X-band field-sweep ESE spectrum consists of triplet lines due to nitrogen residing cubic site and (N_c), single line with unresolved hf interaction due to nitrogen residing hexagonal site (N_h) and a low intensity triplet labeled N_x with $g_{||}$=2.0055, $g_{\perp}$=2.0010.

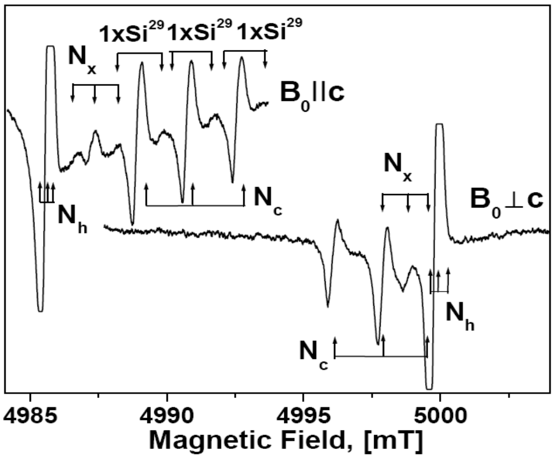

Fig.1. EPR spectrum observed in n-type 4H-SiC wafers grown at T<2000°C by SSM and PVT method. (N_D–N_A)≈10^{17}cm^{-3}. T=4.2 K

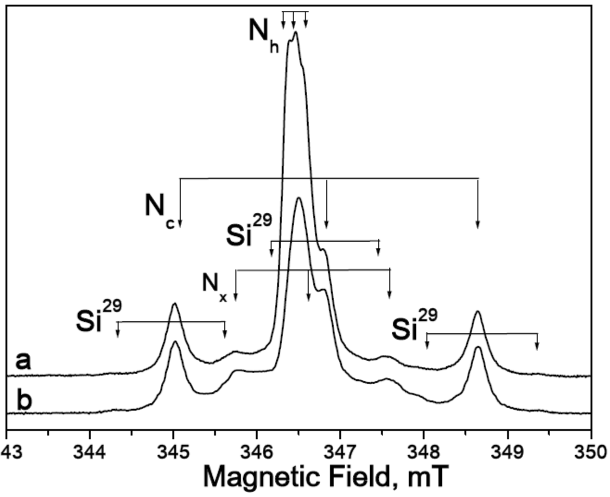

Fig.2. X-band field-sweep ESE spectra detected in 4H SiC samples grown by SSM method with different compensation degree. (N_D–N_A)≈10^{17}cm^{-3}, $\mathbf{B_0}$||**c**, T = 6 K. **a** – low compensation, **b** – high compensation

As was seen from Fig. 2, the intense single line N_h with $g_{||}$=2.0063, $g_{\perp}$=2.0005 and central triplet line of N_x coincides at low frequency with the central line of the triplet N_c. In addition, each triplet line of the N_c EPR and ESE spectrum is accompanied by two hf lines, identified as due to 1 x Si^{29} in accordance with [1, 4] with a splitting of 1.46 mT. At high frequency the two Si^{29} hf lines positioned between the triplet lines are barely resolved due to broadening.

Fig. 3 and 4 show D-band EPR and X-band field-sweep ESE spectrum observed in n-type 4H-SiC wafers with donor concentration of about 10^{18} cm^{-3}. As is seen from Fig. 3 and 4, the X-band ESE and D-band EPR spectra detected in the n-type 4H-SiC wafers with high nitrogen concentration have substantial differences. X-band ESE spectrum consists of triplet lines due to nitrogen residing cubic site and N_x triplet lines of low intensity with $g_{||}$=2.0055, $g_{\perp}$=2.0010 having half the hf splitting in respect to the nitrogen residing cubic site. The intensive single EPR line N'_x observed in D-band EPR spectrum was not detected in ESE spectrum due to the short spin-relaxation time demonstrating its exchange nature. Therefore following [2], it could be proposed that the broad single line N_x observed in samples with nitrogen concentration (N_D–N_A)≈10^{18}cm^{-3} is due to $N_{C,k}$–$N_{C,h}$ pairs with the average value of the N_c and N_h spectrum g-tensor: $g(N_x)\approx½[g(N_c)+g(N_h))]$, which is observed in the samples

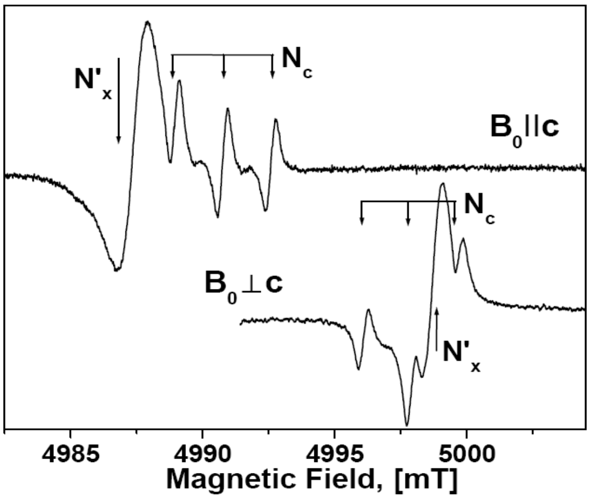

Fig.3 EPR spectrum observed in n-type 4H-SiC wafers grown at T=2200°C by SSM and Lely method. $(N_D - N_A) \approx 10^{18}$ cm^{-3}. T = 4.2 K

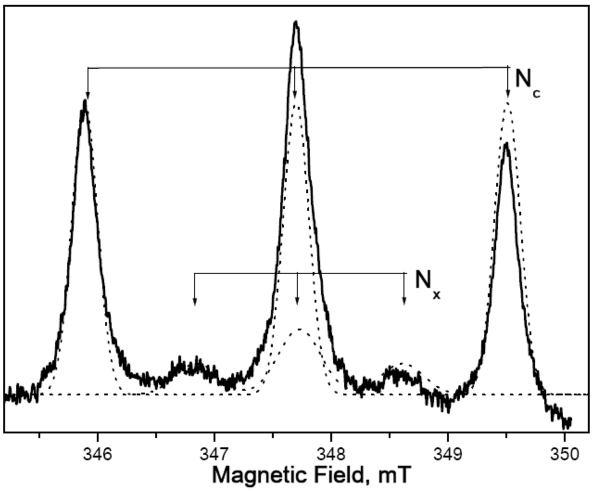

Fig.4 X-band field-sweep ESE spectra detected in 4H SiC samples grown at T=2200°C by SSM and Lely method. $(N_D - N_A) \approx 10^{18}$ cm^{-3}. $\mathbf{B_0} \perp \mathbf{c}$, T = 6 K

with low concentration of nitrogen as N_x triplet line [2].

Fig. 5 shows the X-band Davies pulsed-ENDOR spectra measured in highly compensated 4H SiC sample with $(N_D - N_A) \approx 10^{17}$ cm^{-3} when magnetic field ($\mathbf{B}_0$) was set to the position of the central N_c triplet lines (a) coincided with the intense single line with $g_{\|}=2.0063$, $g_{\perp}=2.0005$, low-field N_c triplet lines (b), low-field of N_x triplet lines (c) and ^{29}Si lines (d) at T = 6 K.

With $\mathbf{B_0}$ at the central N_c triplet line ENDOR lines at 2.41 MHz and between 24 and 27 MHz with small quadrupole splitting were observed in the X-band ENDOR spectra. The lines at 2.41 MHz were attributed to the nitrogen on the hexagonal lattice site (N_h) [1]. The ENDOR lines observed between 24 and 27 MHz are due to N_c. All other lines are related to ^{29}Si and ^{13}C hf interactions. Among them the lines observed in the range of 8–14 MHz have been assigned to the ^{13}C nuclei in the NNN and outer shells of N_c by Son et al. [4]. Furthermore the ENDOR signals observed at 6 MHz were attributed to the three Si(2–4) atoms in the NN of N_c. When $\mathbf{B}_0$ is set to the position of the low-field of N_x triplet lines and ^{29}Si lines two lines at 17.65 and 23.43 MHz are observed in ENDOR spectrum and identified as ^{29}Si hf lines, corresponding to the transitions: $A_{Si}/2-\nu(^{29}Si)$ and $A_{Si}/2+\nu(^{29}Si)$, were A_{Si} is the hf constant of ^{29}Si and $\nu(^{29}Si)$ is the nuclear Zeeman frequency of ^{29}Si. The deduced A_{Si} value is 41.07 MHz,

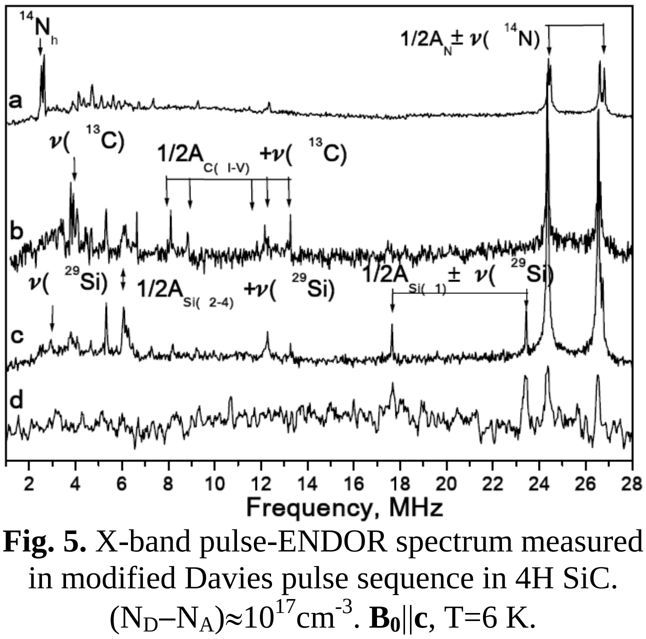

Fig. 5. X-band pulse-ENDOR spectrum measured in modified Davies pulse sequence in 4H SiC. $(N_D - N_A) \approx 10^{17}$ cm^{-3}. $\mathbf{B_0} \| \mathbf{c}$, T=6 K.
a - $\mathbf{B_0}$ is set at the position of the N_h line, coincided with the central N_c triplet line; **b** - $\mathbf{B_0}$ is set at the position of low-field of N_c triplet lines; **c** - $\mathbf{B_0}$ is set at the position of low-field of N_x triplet line, **d** - $\mathbf{B_0}$ is set at the position of low-field of Si^{29}

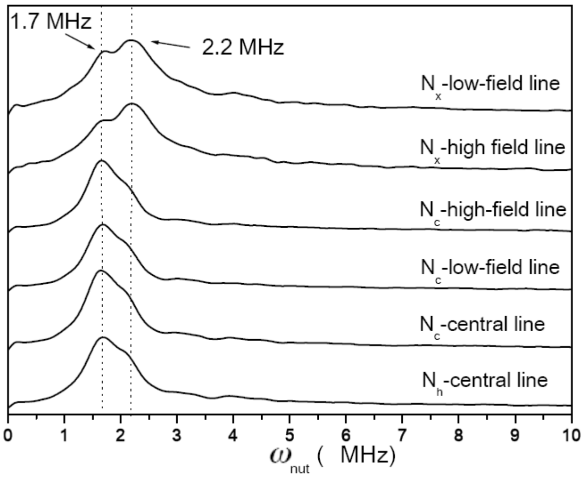

Fig.6. ESE nutation spectra observed in 4H SiC at different field-sweep ESE spectrum observer positions. $(N_D\text{-}N_A)\approx10^{17}cm^{-3}$, T=6K. Pulse sequence: t-π/2- τ-π-τ-echo with π/2=100ns, π=200ns, τ=800 ns, t=1500 ns. $\mathbf{B_0}||\mathbf{c}$.

which is close to the hf value of 40.9 MHz determined by EPR for the Si (1) atom in the nearest neighbour (NN) of N_c and therefore confirms the identification made in [4].

We have to stress that no addititional lines due to N_x center having half the hf splitting with respect to the N_c (A=25.6 MHz) were observed in ENDOR spectrum. The equation for frequency of an ENDOR line $\upsilon(m_S)=|\nu_N\pm m_SA|$ immediately shows that in X-band we should expect the lines for N_x center at ENDOR frequencies $\upsilon(m_s=1)=26.6$ MHz, $\upsilon(m_s=-1)=24.6$ MHz, $\upsilon(m_s=0)=1$ MHz. The first two ENDOR lines are coincided with those observed due to N_c, while the third line at 1 MHz could not be observed in X-band ENDOR spectrum.

Hence, the fact that no additional lines could be expected due to N_x center with S = 1 and A = 25.6 MHz in X-band ENDOR spectrum is not in contradiction with the model proposed in [2] for N_x center.

In addition the nutation frequency experiments were undertaken to evaluate the electron spin S of the N_x center using the equation for the nutation frequency:

$$\omega_{nut}(m_S,m_S+1)=\frac{g\beta_e B_1}{\hbar}\left[(S(S+1)-m_S(m_S+1)\right]^{1/2}=\omega_1\left[(S(S+1)-m_S(m_S+1)\right]^{1/2} \qquad (1)$$

Fig. 6 shows nutation spectra recorded at ESE observer positions of Nx and Nc lines which exhibited two nutation signals at 2.2 MHz and 1.7 MHz, respectively. The ratio between nutation frequency 2.2 MHz and 1.7 MHz is found to be $\omega_{nut}(N_x)/\omega_{nut}(N_c)=1.3$ which agrees well with the ratio between nutation frequency expected for the centers having S=1 and S=1/2:

$$\frac{\omega_{nut}(S=1)}{\omega_{nut}(S=1/2)}=\frac{\omega_1\cdot2^{1/2}}{\omega_1}=2^{1/2}. \qquad (2)$$

This indicates that N_x center should be attributed to a center with S = 1.

Summary and Conclusion

Nitrogen related centers were studied by field-sweep ESE and pulsed ENDOR in n-type 4H-SiC wafers grown by different techniques with different C/Si ratios and nitrogen concentration which were preliminary tested by EPR at high frequency. The lines due to nitrogen at the hexagonal, cubic sites, hf lines with A = 41.07 MHz due to ^{29}Si (1) and lines due to ^{29}Si (2–4) nuclei located in the NN of N_c were observed in pulse ENDOR spectrum. In contrast to the results obtained in [4, 5] both lines due to nitrogen at the hexagonal and cubic sites revealed the quadrupole splitting. The absence of the additional ENDOR lines due to N_x center could be explained by the fact that for N_x center with S=1 and A=25.6 MHz the two among three expected ENDOR lines are coincided with those observed due to N_c at X-band, while the third line which was estimated at 1 MHz is hardly could be observed in X-band ENDOR spectrum. Spin state of the N_x nitrogen related center was also determined as S=1 from nutation frequency experiments.

Acknowledgements

This work was supported by DFG project No GZ 436 UKR 17/23/06.

References

[1] E.N. Kalabukhova, S.N. Lukin, D.V. Savchenko, W.C. Mitchel, S. Greulich-Weber, U. Gerstmann, A.Pöppl, J. Hoentsch, E. Rauls, Yu.Rozentzveig, E.N. Mokhov, M. Syväjärvi, R. Yakimova: Mat. Sci. Forum, 2007 (accepted to publication)

[2] U. Gerstmann, E. Rauls, S. Greulich-Weber, Kalabukhova, D.V. Savchenko, A. Pöppl, F. Mauri: Mat. Sci. Forum, 2007 (accepted to publication)

[3] A.M. Tyryshkin, J. J. L. Morton, A. Ardavan, S.A. Lyon: J. Chem. Phys., Vol. 124, p. 234508 (7 p.), 2006.

[4] N.T. Son, E. Janzén, J. Isoya, S. Yamasaki: Phys. Rev B, Vol. 70, p. 193207, 2004

[5] A.V. Duijn-Arnold, R. Zondervan, J. Schmidt, P.G. Baranov, E.N. Mokhov: Phys. Rev.B, Vol. 64, p. 085206 (17 p.), 2001

EMR and Optical Absorption Studies of Vanadyl Doped L-Asparagine Monohydrate

R. Kripal1), I. Mishra1), A.K. Shukla2)

1)Department of Physics, University of Allahabad, Allahabad, India, 211002.
2)Physics Department, Ewing Christian College, Allahabad, India, 211003.

e-mail: akshukla10@rediffmail.com

X-band EMR study of vanadyl doped L-Asparagine monohydrate has been performed at room temperature. Spin-Hamiltonian parameters have been determined and location of impurity in the host lattice has also been estimated. UV-Visible optical absorption study has also been performed at room temperature. Bonding parameters has been determined and nature of bonding in the complex has been discussed using EMR and optical data.

Magnetic Properties of Chemically Deposited Ferromagnetic Semi-Conducting $CuCr_2S_4$ Thin Films on Si(100) and YSZ(100) Substrates

M. Erdem1), A.C. Başaran2), S. Kazan2), H. Yüzer3), M. Ozdemir1)

1)Marmara University, Faculty of Science and Letters, Department of Physics, 34722 Ziverbey, Goztepe, Kadıköy ISTANBUL TURKIYE
2)Gebze Institute of Technology, Faculty of Science, Department of Physics, Cayirova Gebze KOCAELI TURKIYE
3)TUBITAK Marmara Research Center, Chemistry and Environment Institute P.K. 21 41470 Gebze / KOCAELİ TURKIYE

e-mail: abasaran@gyte.edu.tr

Ferromagnetic thin films of $CuCr_2S_4$ compound were independently deposited onto Glass, Si(100), and YSZ(100) substrates by simple chemical bath deposition (CBD) method. The films were found to be uniform and adherent to substrates. The samples were characterized by structural, optical and magnetic measurements techniques.

The XRD and Scanning Electron Micrographs (SEM) studies revealed that the films are polycrystalline and well-covered the substrate without any cracks or pinholes.

The optical constants of the deposited films were obtained from the analysis of the experimentally recorded absorption and transmission spectral data in the wavelength range 300–800 nm. An analysis of the optical absorption data of the as-deposited films revealed an optical direct transition with an estimated band gap E_g of about 2.5 eV lying in the range of common semi-conducting materials.

$CuCr_2S_4$ films exhibit ferromagnetism up to Curie temperature, T_C of 380K. Coercive field increases with decreasing temperature. Some magnetic anomalies are observed at the temperatures around 220K and 150K for $CuCr_2S_4$/Si(100) and $CuCr_2S_4$/YSZ(100), respectively. These temperatures were defined as melting temperature T_m of these ferromagnetic thin films. This anomalous behavior could be attributed to either the coexistence of both the ferromagnetism and spin-glass-like phases or structurally different phase inclusion like $CuCrS_2$.

This work was supported in part by Marmara University, and TUBITAK, TBAG-105T458.

Research of Molecular Dynamics of 4-methyl-2-allylphenol Derivatives in Solution by NMR Spectroscopy Method

I.G. Mammadov, A.M. Maharramov, M.R. Bayramov

Baku State University, Z.Khalilov, 23, Baku, Azerbaidjan

e-mail: ib.nmrlab@list.ru

In this report by NMR spectroscopy method has been investigated the formation of hydrogen bond and molecular dynamics of 4-methyl-2-allylphenol derivatives containing aminomethyl fragment in orto-position. The results of research confirm the importance of relaxation time in very sensitive test at studying molecular dynamics.

The investigation of relaxation time of various compounds gives the valuable information about molecular reorientation, molecular dynamics, high-speed intramolecular rotations, space interactions and etc. in a liquid [1-3].

For studying hydrogen bond and molecular dynamics firstly by us the investigation has been carried out by NMR spectroscopy method of 4-methyl-2-allylphenol. The investigations have been carried out at various cosentrations. In ^{1}H NMR spectrum the signal of hydroxyl group of 4-methyl-2-allylphenol (without solvent) is observed at 6.5 ppm, and in its 1 % solutions in CCl_4 at 4.72 ppm. These results confirm formation of intermolecular hydrogen bond (I):

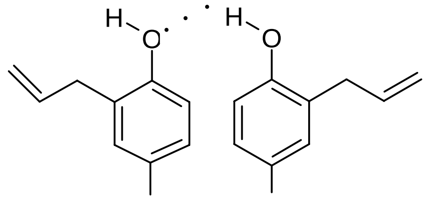

(I)

However result of interaction with in 5 % acetone–d_6 solution the signal of hydroxyl group of the given compound is observed at 8.57 ppm.

Further have been investigated derivatives of 4-methyl-2-allylphenol, containing in the structures aminomethyl fragment.

The signal of hydroxyl group in ^{1}H NMR spectrum of compound 6-diethylaminomethyl-4-methyl-2-allylphenol (II) (without solvent) is observed at 10.77 ppm and in 0.1% solution in CCl_4 at10.21 ppm.

The dependence of the signal hydroxyl group from temperature has been investigated. Without solvent the signal of hydroxyl group is observed at 22^{0}C at 10.77 ppm, at 80^{0}C at 10.42 ppm and in 0.1 % solution in CCl_4 at 22^{0}C at 10.21 ppm, at 70^{0}C at 10.03 ppm. It wasfound out by us no shift of hydroxyl group signal to more stronger field confirms the formation of intramolecular hydrogen bond.

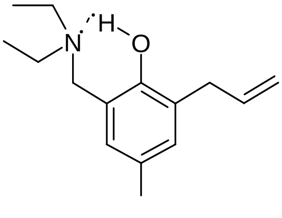

(II)

The spin-lattice relaxation time (T1) of two methyl groups for nucleus ^{1}H in compound (II) (5 % not degassed sample in acetone-d_6) also has been investigated at various temperatures. The obtained results are given in tab.1.

Table 1 Spin-lattice time of compound (II) T_1 (sec.) at various temperature

fragment	22^{o}C	30^{0}C	40^{0}C
CH_3 (in ethyl fragment)	2.27	2.76	3.29
CH_3 (in aromatic fragment)	3.10	3.53	4.07

From the given Table 1 it is visible, that value relaxation time of methyl group in ethyl fragment is less, than value relaxation time of methyl group in aromatic fragment. To weaken movement of methyl group in ethyl fragment allows to explain the formation of intramolecular hydrogen bond of type N·H.

With the purpose of revealing the influence of various aminomethyl fragments on formation of hydrogen bond and molecular movement also other aminomethylated derivatives of 4-methyl-2-allylphenol have been investigated.

The signal of hydoxyl group in ^{1}H NMR spectrum of compound of 6-*tret*-buthylaminomethyl-4-methyl-2-allylphenol (III) (without solvent) is observed at 4.67 ppm. The fact gives a basis to tell, that not formation inter- and intramolecular hydrogen bond, probably connected by the steric factor tretbuthyl fragment.

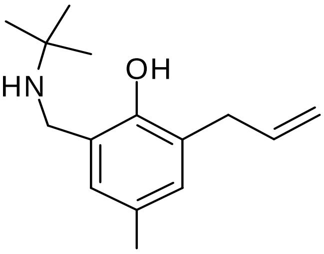

(III)

6-Morfolinomethyl-4-methyl-2-allylphenol (IV) also has been investigated. The signal of hydroxyl group in ^{1}H NMR spectrum of compound (IV) (without solvent) is observed at 9.78 ppm and in 0.1% solution in CCl_4 at 9.37 ppm. It was also investigated the dependence signal of hydroxyl group from temperature. Without solvent the signal of hydroxyl group is observed at 22^{0}C at 9.78 ppm, at 80^{0}C at 9.04 ppm and in 0.1 % solution in CCl_4 at 22^{0}C at 9.37 ppm, 70^{0}C at 8.69 ppm. Comprehensive investigation confirms the formation of intramolecular hydrogen bond in compound (IV).

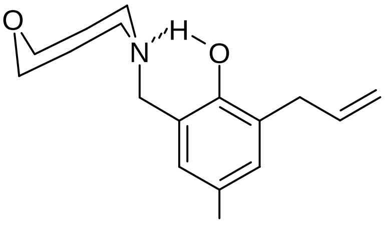

(IV)

In not degassed sample (5% solution in acetone-d6) of compound (IV) spin-lattice relaxation time (T1) of methyl and of some CH_2 groups for nucleus ^{1}H has been calculated (Table 2).

Thus, as the sensitive test for molecular dynamics the relaxation time can be used for obtaining of information about configuration of molecule.

Table 2 Spin-lattice time of compound (IV) T_1, sec.

fragment	T_1, sec.
$_3$HC-Ar	2.39
$_2$HC-Ar	2.63
N-CH_2-Ar	1.29
$(CH_2)_2$-O	1.42
$(CH_2)_2$-N	1.30

References

[1] K. Nakanshi. One dimensional and two dimensional NMR spectra by modern pulse techniques. Tokyo-Kaliforniya, 1990, p. 56-58.

[2] Kashaev P.S., Idiatullin Z.Sh. JPh.Ch, 2001, 75, 2, 352-355

[3] N.K.Andreev. IV All-Russian conference " New achievement NMR in structural researches ". Kazan, 2005, p. 30

Synthesis and EPR-investigation of Iron (III) Containing Dendrimeric Complex of Second Generation, Derivative of 3,4-*n*-Decyloxybenzoyl Poly(Propylene Imine)

M.S. Gruzdev[1,2], G. Lattermann[2], N.E. Domracheva[3]

[1]Institute of Solution Chemistry, Russian Academy of Science, Ivanovo, Akademicheskay str. 1, 153045, Russian Federation
[2]Bayreuth University, D-95447 Bayreuth, Universitaetstrasse 30, Germany
[3]Zavoisky Kazan Physical-Technical Institute, Russian Academy of Science, Sibirsky tract 10/7, Kazan, 420029, Russian Federation

e-mail: gms@isc-ras.ru

Recently metal containing dendrimers have attracted much attention in many research groups. It can be easily explained by the fact that dendrimers have a large number of potential coordination sites. This is the reason why this type of materials can be used as catalysts and as components of sensors. [1]. In this connection it will be very interesting to synthesize new organometallic dendrimers or complexes of dendrimers with metals [2]. In the last ten years some complexes were prepared using dendrimers of poly(alkylen imin) as ligands for the complexation of transient metals: Co, Ni, Cu and Zn [3]. Recently, complexes of poly(propylene imine) dendrimers with salts of bivalent copper have been obtained and their structure and mesomorphic properties were investigated [4 - 6]. Our aim was to synthesize a stable complex of the ligand poly(propylene imine) dendrimer with iron (III) salts and to investigate the structure of this compound.

Synthesis of iron containing complex of 2nd generation dendrimer

The synthetic pathway of the Fe (III) complex with a 2nd generation dendrimer, 3,4-*n*-decyloxybenzoyl poly(propylene imine) derivative (**2-K2,10**), as organic ligand, the structure and property investigations are described below.

$$\textbf{2-K2.10} + x\,\mathrm{FeCl_3}\ _{\text{anh.}} \xrightarrow[\text{THF}]{\text{18 hours/RT}} \textbf{2-K2.10-}(\mathrm{FeCl_3})_{4.7} + (x-4.7)\,\mathrm{FeCl_3}$$

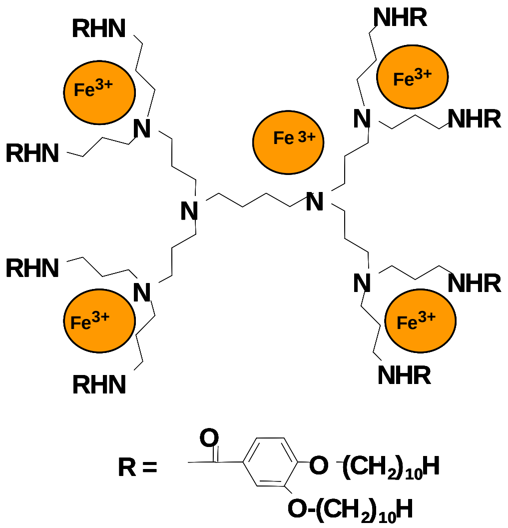

Fig.1 The structural model of **2-K2,10-(FeCl$_3$)$_{4.7}$** compound.

The complex, fig. 1, was obtained with respect to the number of potential coordination places in dendrimeric core of ligand **2-K2,10** by using five times excess of dry FeCl$_3$.

The general scheme of the synthesis of iron complex is given below. The complexation reaction was carried out in a tetrahydrofuran solution under argon atmosphere. After the synthesis, free FeCl$_3$ was removed by cooled ethanol and the residue was dissolved in benzene and filtered through teflon mesh filters (0.200 μ). The desired product was isolated by freeze drying from benzene solution. The complex results as a yellow-ochre amorphous powder. The yield of iron containing compound was 74.67%. The purity of the synthesized complex was checked using gelpermeation chromatography (GPC). The elution volume and molar mass of the complex is larger than that for the free ligand. The chromatograms indicate the purity of the 2nd generation complex to the largest extent. It has the following characteristics, Mn = $6.1258*10^3$ g/mol; Mp = $2.3548*10^4$ g/mol; FI = $9.179*10^{-1}$ ml*V, (UV-detector date, Standard: poly(styrene)). The ligand **2-K2.10** has quite differen characteristics: Mn = $5.6725*10^3$ g/mol; Mp = $2.0883*10^4$ g/mol; FI = $1.154*10^{-1}$ ml*V (UV-detector). The presence of iron and complex stability is demonstrated by means of mass-spectroscopy *MALDI-ToF-MS*. There are four main stable molecular ions present in the spectrum which indicate the presense of iron in the complex structure: m/Z^+ 4107.66; 4166.04; 4219.69; 4325.81. The iron content was calculated using formulas which use as a standard the amount of carbon in the macromolecule as well as the data of elemental analysis for carbon [6]. In our case in complex present 4.7 atoms of iron.

EPR investigation of 2-K2,10-(FeCl$_3$)$_{4.7}$ complex

EPR spectroscopy was used to identify the local structure and geometry of iron(III)-complexing sites in PPI - dendrimer ligand. **2-K2,10-(FeCl$_3$)$_{4.7}$** complex was studied in a wide temperature (300-4.2) K range in *X*- and *Q*- bands. The EPR spectrum (*X*-band, $h\nu_1$=0.3 cm^{-1}) of iron-dendrimeric complex contains two lines (Fig. 2) with effective *g*- factor g_1 = 4.3 (signal **B**) and more intensive line (signal **A**) with g_2 = 2. On the left wing of signal **B** a weak line with effective *g*- factor g_3 = 9.6 is additionally observed.

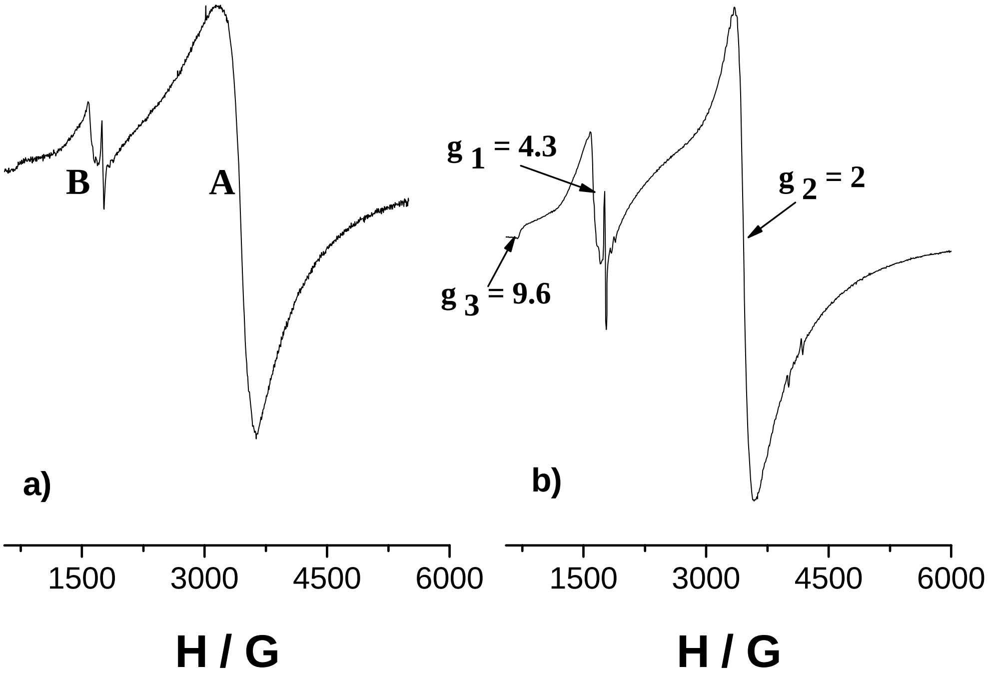

Fig.2 *X*- band EPR spectra of **2-K2,10-(FeCl$_3$)$_{4.7}$** complex at 300 K (a) and 20 K (b).

It is well known that such an EPR spectrum belongs to high spin Fe(III) ions with ground term $^6S_{5/2}$ (3d^5) and is described by the spin - Hamiltonian [7-9] :

$$H = g\beta \mathbf{HS} + D[S^2_z - 1/3S(S+1)] + E(S^2_x - S^2_y) \quad (1)$$

with $g = 2$ and $S = 5/2$. The parameters D and E characterize, respectively, the axial and and orthorhombic part of the distortion of the crystal field of iron ion from octahedral (or tetrahedral) symmetry, the relation $0 < E / D \leq 1/3$ holding. When the parameter E of spin - Hamiltonian (1) is large compared with $g\beta H$ ($E >> g\beta H$) and $D = 0$, the energy levels in zero magnetic field are three Kramer's doublets. The middle doublet has an isotropic g value of 4.29, whereas the upper and lower Kramer's doublets have strongly anisotropic g-values: 9.6, 0.86 and 0.61.

The signals $g_1 = 4.3$ and $g_3 = 9.6$ according to theoretical calculations [7 - 9] are due to the strong rhombic distortion of the Fe(III) environment and these signals might result from Fe^{3+} in a tetrahedral site. The EPR spectrum of the sample (Fig. 3) taken in the Q- band ($h\nu_2 = 1.2\ cm^{-1}$) does not contain the line with $g_1 = 4.3$ which make it possible to estimate the range of variation of the orthorhombic part of the distortion of the crystal field: $0.3\ cm^{-1} \leq E \leq 0.6\ cm^{-1}$. The signal with effective g factor $g_2 = 2$ belongs to complexes with weakly distorted ($h\nu_1 >> 2D$, E=0) octahedral crystal field [7 - 9].

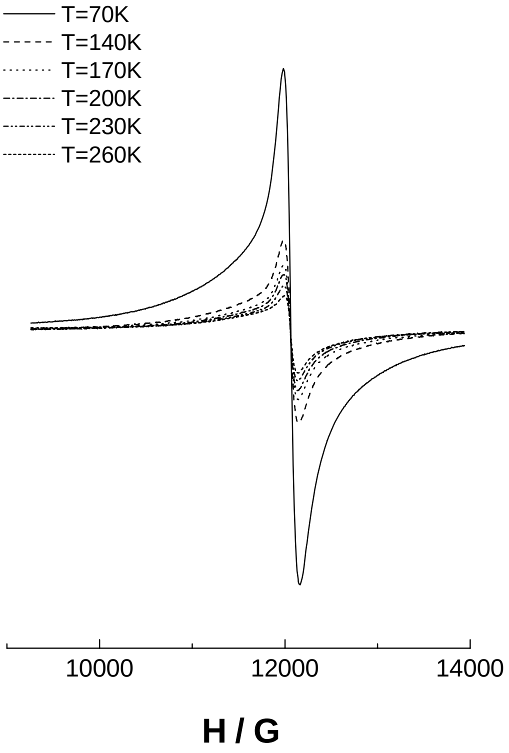

Fig.3 Q-band EPR spectra of **2-K2, 10-($FeCl_3$)$_{4.7}$** complex at different temperatures.

Thus, in accordance with the EPR results, there evidently exist two types of Fe (III) paramagnetic centers in **2-K2,10-($FeCl_3$)$_{4.7}$** compound: iron(III) centers in tetrahedral environment with strong orthorhombic (E) distortion of the coordination site (g_1 = 4,3) and iron(III) ions in octahedral environment with weak distortion ($h\nu_1 >> 2D$) from octahedral symmetry ($g_2 = 2$) of the coordination site. The integrated intensity ratio of these signals shows that the fraction of the first type iron centers is about 9 % at room temperature.

We suppose that the first type of the iron(III)-complexing site may be formed by one tertiary amine nitrogen atom of dendrimer ligand and three chlorine counterions coming from the starting ($FeCl_3$) salt used in the synthesis of compound. The second type of the iron(III)-complexing site is formed by coordination of three nitrogen atoms, two of which belong to amido groups, and the third one – to amino groups. Three other atoms of octahedral coordination are the chlorine counterions. The octahedral paramagnetic centers are located on the periphery (outside of) the dendrimer, whereas the tetrahedral one – inside the dendrimer "framework". Therefore, the Fe(III) ion of the second type of the centers has a flexible first coordination sphere that changes strongly with temperature variation, whereas that of the first one has a "harder" first coordination sphere. The ratio of high-to-low symmetry centers depends from the thermal history of the sample. A number of low-symmetry centers increase with temperature decrease, owing to the growth of the distortions (the growth of D and E parameters' values) in the octahedral crystal field for "soft" centers located on the periphery.

The EPR spectrum of the mesomorphic sample contains only one broad line with effective *g*- factor $g_2 = 2$. Our attempts to resolve a fine structure failed for the complex investigated.

The ability of iron dendromesogenic complex to form lyotropic mesomorphic system with some inert solvents was investigated too. It has been shown that the complex studied can self-organize in columnar structure in mixtures of inert solvents at the room temperature. The ability of these complexes to be oriented in a high magnetic field (similar to that reported in [10]) was not revealed.

Results and Conclusions

1) A dendrimeric complex of 2nd generation has been synthesized by complex formation between metal salt and organic ligand.
2) The purity of the synthesized compound has been checked by GPC chromatography. The presence of iron(III) has been established by mass-spectroscopy. The iron content in the complex was calculated and the result agreed excellently with the experimental data.
3) The local structure and geometry of dendrimeric complex of 2nd generation **2-K2,10-**$\mathbf{(FeCl_3)_{4.7}}$ have been investigated by EPR.

Acknowledges

M.S. Gruzdev gratefully acknowledges a PhD Student Grant of The President of The Russian Federation for financial support. N.E. Domracheva thank for receiving support from RFBR, grand № 06-03-32387. Authors wish to thank Dr. Markus Bate (Bayreuth University, Germany) for measuring mass-spectroscopy MALDI-ToF-MS.

References

[1] Frechet J.M.J., // *Science* **1994**, *263*, P. 1710-1715.

[2] Tomalia D.A., // Aldrichimica Acta **1993**, *26*, P. 91-101.

[3] Stebani U., Lattermann G., Wittenberg M. // Angew. Chem. **1996**. 108. P. 1941-1944.

[4] Barberá J., Marcos M., L.Serrano J. // Chem.Eur.J. **1999**, 5, P. 1834-1840.

[5] Domracheva N., Mirea A., Schwoerer M., Torre-Lorente L., Lattermann G. // ChemPhys Chem, **2005**, 6, P. 110-119.

[6] Gruzdev M.S. Usol'seva N.V., Torre-Lorente L., Lattermann G., Domracheva N.E. // Liqiud crystals and their aplication, **2006**, №4, P. 89-98.

[7] Wickman H.H., Klein M.P., Shirley D.A. // J. Chem. Phys. **1965,** 42, P. 2113-2117.

[8] Kurkjian C.R., Sigety E.A. // Phys. Chem. of Glasses, **1968,** 9, P. 73-83.

[9] Loveridge D., Parke S. // Phys. Chem. of Glasses, **1971,** 12, P. 19-27.

[10] Domracheva N., Mirea A., Schwoerer M., Torre-Lorente L., Lattermann G. // ChemPhys Chem. **2006**, 7, P. 2567 – 2577.

The Influence of Lysozyme on Self Diffusion of Monoolein in Cubic Phase

B.V. Munavirov, I.Y. Desyatnikova, A.V. Filippov

Kazan State University, 420008, Kremlyovskaya str. 18, Kazan, Russia

e-mail: bmunavirov@yahoo.com

When placed in water, lipids form various types of liquid crystalline phases, among all of them the most complex ones are cubic phases. The inner structure of cubic phase is formed by curved lipid bilayers which separate two no interconnecting water networks. It makes possible to “fill” lipid cubic phases with substances of different amphiphilicity, and so they are perspective to be used as in vivo drug delivery and controlled release systems [1]. It needed to be mentioned, that in such systems it is important to consider the influence of environment (e.g. temperature, pH) on condition of the system. In earlier works it was shown, that interaction of protein with lipids in cubic phases is commonly explained by means of electrostatic (in the case of charged molecules) and hydrophobic (if protein molecule has hydrophobic parts) interactions [2, 3]. Presence of macromolecules (drugs) may vary cubic phase symmetry, water channel sizes and permeability [3, 9]. When comparing such two-component systems with pure cubic phases, it is important to mention that stability of the system also may vary. Thus, investigation of properties of cubic phase in the presence of drug is very actual physical problem. Earlier, properties of such systems were studied by means of NMR spectroscopy, electron microscopy, X-ray diffraction [3, 4]. In this work we studied translational mobility of lipid molecules forming cubic phase in the presence of protein. Experiments have been performed by means of the ^{1}H NMR pulsed magnetic field gradient technique; method’s details are described in literature [5]. The diffusion decays were obtained using stimulated echo pulse sequence. The diffusion time was fixed at 7 ms and the maximum amplitude of pulse field gradient was 30 T/m.

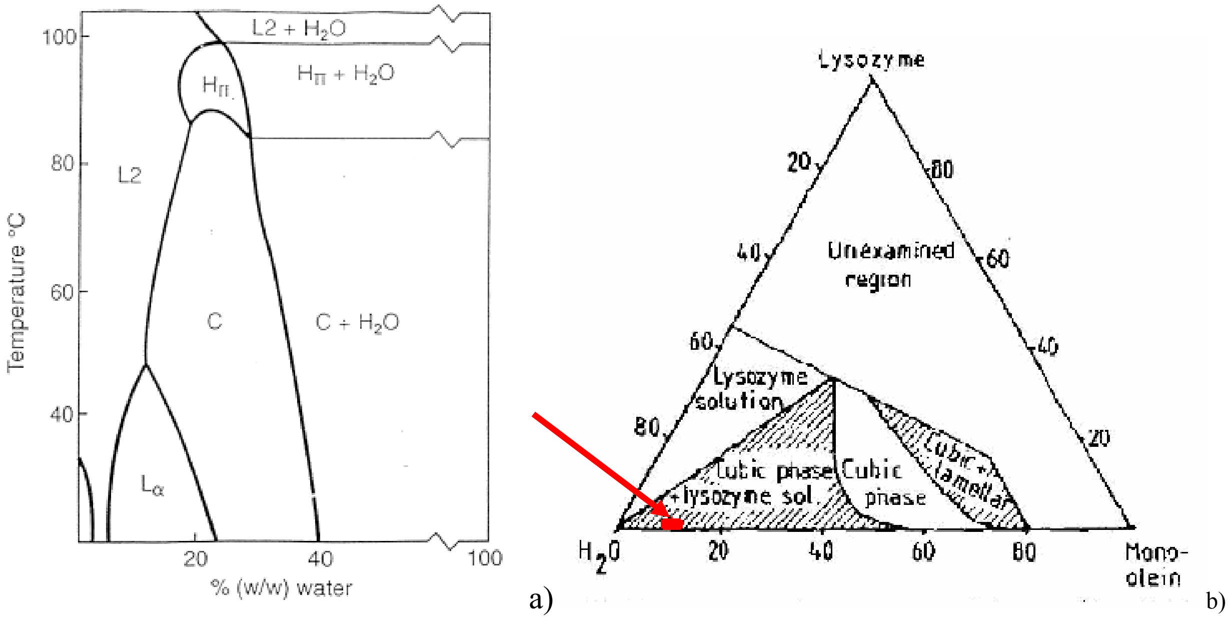

a) b)

Fig.1 Phase diagrams of studied systems: a) monoolein-water. L2 – inverted micellar phase, Lα - lamellar phase, C – cubic phase, H_{II} – inverted hexagonal phase [1], b) Monoolein-water-lysozyme [6]

1-MONOOLEOYL-rac-GLYCEROL(C18:1) (monoolein) was used as a lipid component to form cubic phase in water solution at certain hydration level. Hen egg-white lysozyme was chosen as a protein, because its common properties, such as structure, conformation, dynamics in solution etc. are known [8]. Lysozyme is a natural antibiotic, the globular protein with pH dependent conformation in solution. All of these and other properties make lysozyme suitable for our experiments. Materials were purchased from SIGMA CHEMICAL CO., St. Louis, MO, USA and used without further purification.

Monoolein-water and monoolein-water-lysozyme phase diagrams (fig.1) were taken from literature [1,6].

Samples were prepared according to the method, described in literature [3, 7]. Lysozyme was dissolved in 0.05M sodium acetate buffer solution, pH=4.5±0.05. Reference samples with pure cubic phases were prepared in D_2O. Samples hydration level was kept at ≈30% (w/w).

As it can be seen from fig.2, the diffusion decays of cubic phases without protein were described with two diffusion coefficients. Further experiments showed that addition of lysozyme doesn't change the common view of the diffusion decays.

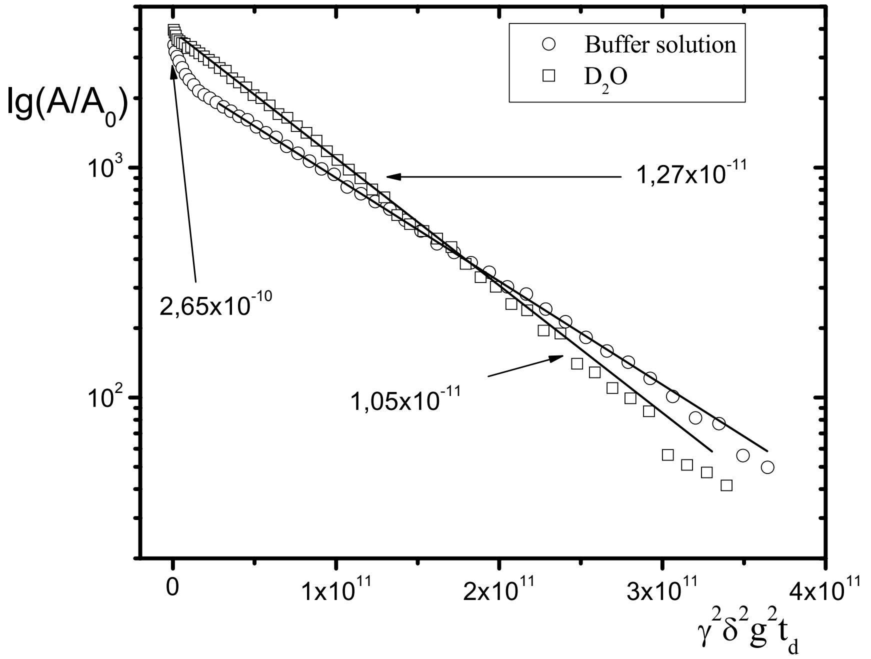

Fig.2 Diffusion decays, describing diffusion of source pure cubic phase in H_2O buffer solution and pure D_2O medium. T = 24°C

Analysis of ^1H NMR spectra, obtained at different values of the pulsed gradient, allowed us to conclude, that the smaller coefficients relates to diffusion of lipid molecules while larger ones describes the diffusion of water molecules.

It was observed (fig.3) that the self-diffusion coefficient of lipid molecules is rising with temperature increase.

Experiments performed with lysozyme containing systems showed that increasing of lysozyme concentration lead to rise of self-diffusion coefficients in the whole studied temperature interval (fig.3).

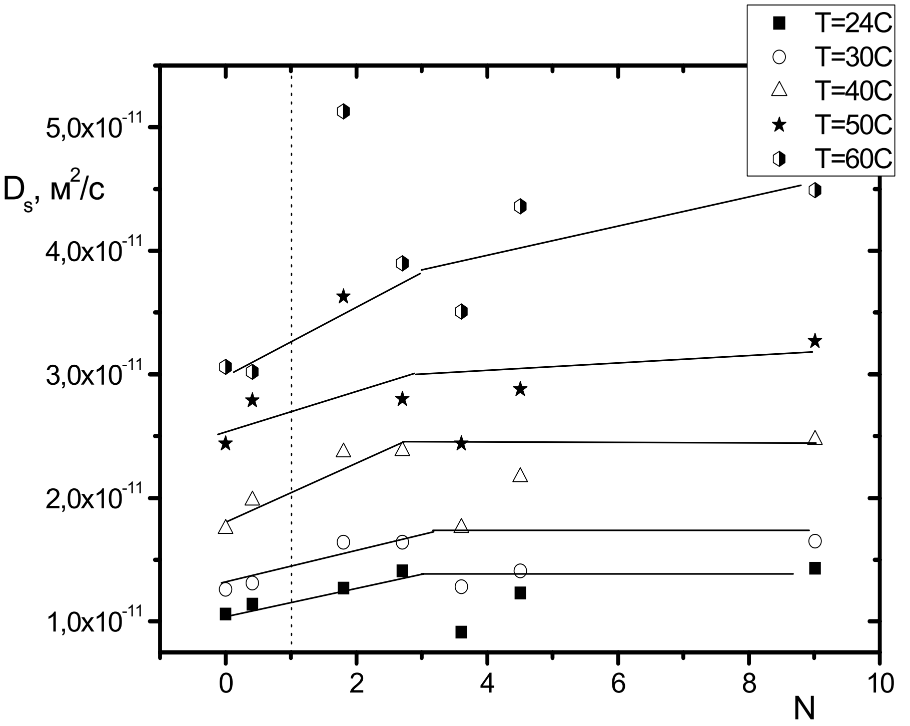

Fig.3 Lipid self-diffusion coefficients versus number of lysozyme molecules per cubic phase unit cell dependencies

It is known that T_2 relaxation time of lysozyme molecules ≤ 1 ms that is much faster than that of lipid molecules (≈ 100 ms); the weight concentration of lysozyme is more than 15 times less than concentration of the lipid. In such conditions lysozyme molecule's protons contribution is insignificant in comparison with protons of the lipid. So, the observed lipid's self-diffusion coefficient alteration is probably related with particular interaction of protein molecules with lipid bilayer. It is known from literature [3], that lysozyme is globular protein. However it can interact with the lipid membrane [10]. Else it is known [3] that at certain concentration level (marked with dotted line on fig.3) it crystallizes in cubic phase's water channels.

We suppose that observed lipid's self-diffusion coefficient alterations may be explained by one/all of the following effects:

- Lysozyme crystallization is followed with releasing of part of water from its hydrate shell, as a result the hydration level of bilayer forming lipids increases.
- An increase in number of lysozyme molecules in cubic phase unit cells changes bilayer curvature, this is followed by alterations in projection of lipid molecular motion trajectory on the direction of pulse gradient. Changes in bilayer curvature results in increasing of free volume per one lipid molecule (decrease in the density of bilayer lipid packing).

Real mechanism of the observed alteration of the lipid diffusion coefficient remain unknown, it will be studied soon applying techniques sensitive to the protein-membrane interaction. Anyway, our investigation showed that PFG NMR has a potential to study alteration in lipid dynamics conditioned by interaction with proteins confined in cubic phase channels.

Work was supported by CRDF REC-007-3 and RNP.2.1.1.3222 grants

References

[1] Shah J.C. Cubic phase gels as drug delivery systems. Adv. Drug Deliv. Rev.- 2001-47-P.229–250.

[2] Ipatova, O.M., Phosphogliv: mekhanizm deistviya i primenenie v klinike (Phosphogliv: Action Mechanism and Clinical Applications) - Moscow: Institute of Biomedical Chemistry - RAMS – 2005 – 318P.

[3] Tanaka S. Structural transitions of the monoolein bicontinuous cubic phase induced by inclusion of protein lysozyme solutions/Tanaka S., Maki S., Ataka M.// Phys. Rev.-2006-E 73-061510.

[4] Landau E.M. Lipidic cubic phases: A novel concept for the crystallization of membrane proteins/ Landau E.M., Rosenbusch J.P.// Proc. Natl. Acad. Sci. USA-1996-93-P.14532–14535.

[5] Maklakov A.I. Self-Diffusion in Polymer Solutions and Melts/ Maklakov A.I., Skirda V.D., Fatkullin N.F. // Kazan State University Press – Kazan - 1987.

[6] Larsson K. Cubic Lipid-Water Phases: Structures and Biomembrane Aspects.- J. Phys. Chern.-1989-93-P.7304-7314.

[7] Qiu H. The phase diagram of the monoolein/water system: metastability and equilibrium aspects/ Qiu H., Calrey M. // Biomaterials-2000-21-P.223-234.

[8] Chicken egg white lyzosyme [Internet] – Quid United Ltd – 2006 – http://lysozyme.co.uk/

[9] Clogston J. Controlling release from the lipidic cubic phase. Amino acids, peptides, proteins and nucleic acids/Clogston J., Caffrey M. // J. of Contr. Rel. – 2005 - V.107 – P.97-111.

[10] Gorbenko G. Binding of lysozyme to phospholipid bilayers: Evidence for protein aggregation upon membrane association/ Gorbenko G., Ioffe V.M., Kinnunen P.K.J. // Biophys. J. – 2007 – V.93 – P.140-153.

Part P_s of Solid Component in the ^{1}H NMR Signal as a New Oil Characteristic

N.V. Shkalikov, V.D. Skirda

Kazan state university, 420008, Kremlevskaya str. 18, Kazan, Russia

e-mail: Nikolay.Shkalikov@ksu.ru

At present, nuclear magnetic resonance (NMR) method is widely applied to research oil and its products. NMR method is closely integrated into the oil-extracting industry, so NMR logging method is applied to define oil saturation of oil-reservoir rock.

However, it is necessary to note, that the range of spin-spin relaxation times T_2, which widely applied in NMR of oil and its products, is limited by relaxation times from 1 ms up to 10 s and more. Thus, NMR method is widely used to study liquid phase of oil and gas dissolved in it.

But it is necessary to note, that oil is a colloidal solution by nature [1], which contains solid-state formations. These solid-state formations can be caused by asphaltenes, resins and paraffins. It is necessary to investigate the additional range of short spin-spin relaxation times T_2 (from several μs up to several hundred μs) for correct investigation of oil nature and structure by NMR methods, because ^{1}H NMR signal of oil solids possesses short spin-spin relaxation times T_2.

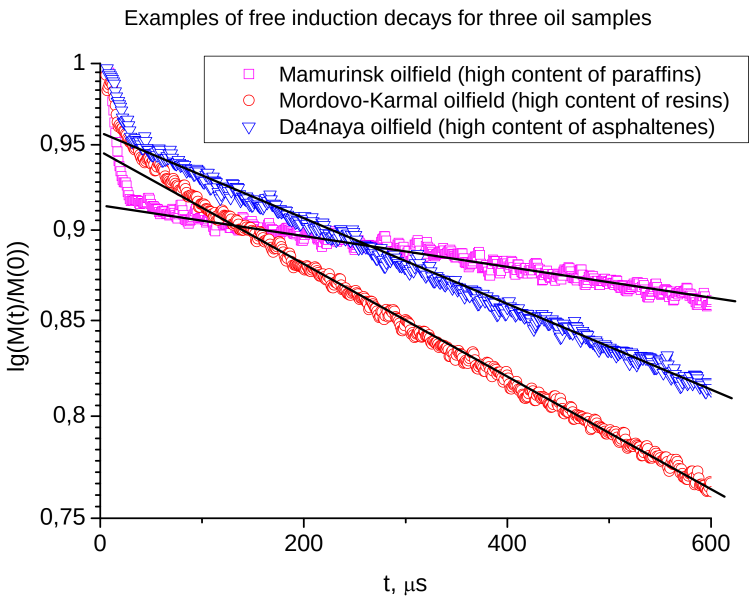

Fig.1 Typical FIDs of oil samples

Free induction decays (FID) of various oil samples contain Gaussian component with spin-spin relaxation times T_2 about 9÷30 μs (Fig.1). We believe, that crystalline and semicrystalline oil formations, containing hydrogen, can possess such short spin-spin relaxation times T_2. Since, among the standard NMR oil characteristics there is no parameter, which describes the content of solid-state formations in the oil, then it is possible to choose part P_s of solid component in the ^{1}H NMR signal of oil as such a parameter. Its measurement is complicated by direct measurement from FID, because NMR equipment has dead time τ_p (in our case τ_p=13 μs). Therefore it is necessary to use Solid-Echo pulse sequence ($90°_x$-τ-$90°_y$-τ) [2-4] for correct measurement of parameter P_s.

Transverse magnetization decay of oil in Solid-Echo pulse sequence is well described by equation:

$$M(t)=\sum_i M_{li}(0)\cdot e^{-\frac{t}{T_{2li}}}+M_S(0,\tau)\cdot e^{-\left(\frac{t}{T_{2s}}\right)^2}, \tag{1}$$

where $M_{li}(0)$ — magnetization of liquid component at the maximum of solid echo signal; $M_S(0,\tau)$ — magnetization of solid component at the maximum of solid echo signal, which depends from time interval τ between RF-pulses; T_{2li} — spin-spin relaxation time of liquid component; T_{2s} – spin-spin relaxation time of solid component.

Solid component magnetization dependence from time τ can be presented in the form:

$$M_S(0,\tau)=M_S(0,0)\cdot e^{-\left(\frac{\tau}{T_{nonrevers}}\right)^n}, \tag{2}$$

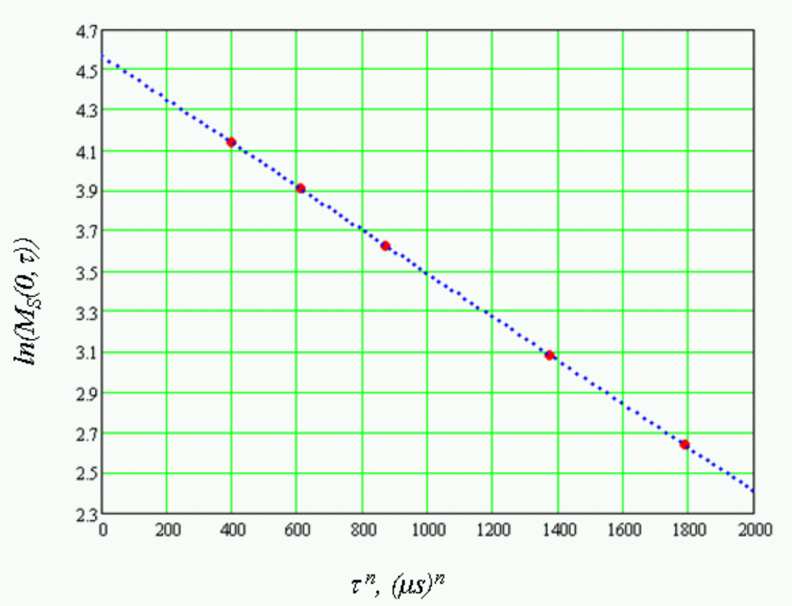

Fig.2 Dependence of solid component magnetization from time τ in Solid-Echo pulse sequence

where $T_{nonrevers}$ — relaxation time of solid component caused by irreversible processes (flip-flop transitions, multi-quantum transitions); n — power parameter, for which the dependence of $\ln(M_S(0,\tau))$ from τ^n is a linear function. The value of parameter n is defined by the properties of dipole-dipole interactions and the nature of oil solid-state formations. Figure 2 presents experimental dependence of solid component magnetization from time τ in Solid-Echo pulse sequence for Vietnamese heavy oil from the “White tiger” oilfield.

Thus, expressions to define part P_s of solid component in the ^{1}H NMR signal of oil can be written down as follows:

$$\begin{aligned} P_S &= \frac{M_S(t=0,\tau=0)}{M(0)}, \\ \sum_i p_{li} + P_S &= 1, \end{aligned} \tag{3}$$

where p_{li} – part of liquid component in the ^{1}H NMR signal of oil.

The work is supported by projects CRDF GAP № RUP 1331, РЦКП КГУ and ПВНШ.

References

[1] Fuks G.I.: Colloid Chemistry of Petroleum Crudes and Products [in Russian]. Moscow: Znanie 1984.

[2] Powles J.G., Mansfield P.: Phys. Letters, **2**, 2, 58 (1962)

[3] Mansfield P.: Phys. Rev., **137**, 3A, A961 (1965)

[4] Kimmich R.: NMR: tomography, diffusometry, relaxometry. Berlin, Heidelberg: Springer-Verlag 1997.

Antiferromagnetic Resonance in $LaTiO_3$ and $YTiO_3$

A.A. Mozhegorov, A.E. Nikiforov, L.E. Gontchar

Ural State University, 620083, 51 Lenin av., Ekaterinburg, Russia
e-mail: a_mozhegorov@mail.ru

Introduction

Magnetic properties of perovskite crystals with 3d-elements are recently under intent investigation due to their unusual properties. These are high-temperature superconductivity (HTSC) in cuprates, colossal magnetoresistance in manganites. And the investigation of rare-earth titanates is at the cutting edge of solid state physics because of strong spin-orbital entanglement in these compounds (see [1,2] for a review).

RTiO$_3$, where R is rare-earth element or Y, is the system, known to possess orthorhombic (*Pnma*) crystal structure [3, 4] in wide temperature range for different R. GdFeO$_3$-type distortions, which are present in these crystals, are believed to control magnetic structure and properties of the compounds through the influence on their orbital ground state [2]. That is why La and Y titanates are seemed to be of special interest for investigators as these two ions stand at the opposite ends of rare-earths and Y series with different ionic radii. The difference between LaTiO$_3$ and YTiO$_3$ becomes even more attractive and puzzling if one will try to realize their magnetic properties: lanthanum titanate is antiferromagnetic [4] with strong superexchange interactions of about 15.5 meV [5] and $T_N \approx 140$ K, whereas yttrium titanate is ferromagnetic with −2.75 meV superexchange [6] and $T_C \approx 27$ K [3].

(La,Y)TiO$_3$ compounds were already studied theoretically by several authors in order to reveal the interplay between their lattice, orbital and magnetic degrees of freedom [1, 7–10] and to investigate their dynamical magnetic properties. In particular, investigations of magnetic structure [1, 8–10] and spin wave spectra [9, 11] were made. Experimental studies of spin waves are reported in [5] for LaTiO$_3$ and in [6] for YTiO$_3$. But so far it was not paid any attention to such powerful and sensitive method of magnetic structure and couplings investigation as antiferromagnetic/ferromagnetic resonance (AFMR/FMR). The only attempt to observe electron spin resonance (ESR) below the magnetic transition temperatures (AFMR or FMR) and above them (EPR) was made by S. Okubo et al. [12]. This latter can’t be attributed as complete, because it was made only for powder samples (and thus all direction-dependent effects were wiped out) and for LaTiO$_3$ AFMR signals were not observed at all.

Having in view current situation in the field of perovskite titanates study we now turn our attention to the blanks in it. So we develop LaTiO$_3$ and YTiO$_3$ compounds model with complete investigation of interrelation of structural, electronic and magnetic properties of these crystals. Here we report the results of magnetic structure as well as spin-wave and AFMR/FMR spectra modeling.

The spin–Hamiltonian

First, our objective is to obtain spin–Hamiltonian for interacting Ti^{3+} ions in (La,Y)TiO$_3$ as these ions are the only magnetic ones in the compounds under consideration. It has already been declared [1, 8–10] and confirmed by first-principal calculations [10, 13] that Ti^{3+} in lanthanum and yttrium perovskite titanates is in non-degenerate orbital ground state, therefore, as it has only one electron on the 3d-t_{2g} shell, its magnetic behaviour may be described by the effective spin-½ Hamiltonian:

$$H_{eff} = \sum_{i\neq j}\left(J_{ij}(\mathbf{S}_i\cdot\mathbf{S}_j) + \mathbf{D}_{ij}(\mathbf{S}_i\times\mathbf{S}_j) + \sum_{\alpha,\beta} S_i^{\alpha} A_{ij}^{\alpha\beta} S_j^{\beta} \right) + \sum_{i,\alpha,\beta} H^{\alpha} g_i^{\alpha\beta} S_i^{\beta} . \qquad (1)$$

Here $\mathbf{S}_i$ ($\mathbf{S}_j$) denotes the spin of i-th (j-th) sublattice, *i* and *j* goes from 1 to 4 as there are four vectors of spins within the magnetic cell; α, $\beta = x$, y, z. J_{ij} is isotropic superexchange interaction, $\mathbf{D}_{ij}$ is anisotropic antisymmetric superexchange (Dzyaloshinskii–Moriya vector), $\boldsymbol{A}_{ij}$ stands for symmetric anisotropy tensor, $\boldsymbol{g}_i$ is g-factor and H^{α} are external magnetic field components.

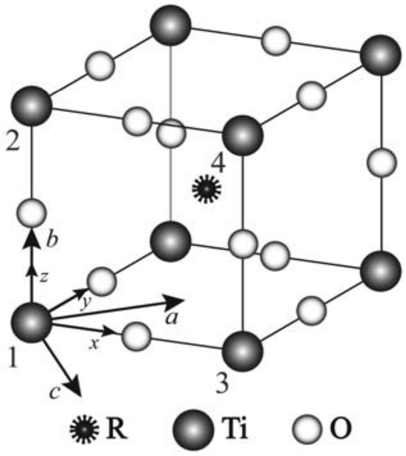

Fig. 1 $RTiO_3$ crystal structure. Pnma (*a*, *b*, *c*) and pseudocubic (*x*, *y*, *z*) axes are shown. Numbers denote Ti sublattices.

We argue that there are essentially 4 magnetic sublattices needed to be considered in $LaTiO_3$ as well as in $YTiO_3$. This is because of the fact that in the latter compound all three components of magnetic structure (A_x, F_y and G_z in *Pnma* notations) are observed [6] and, thus, they introduce 4-subblattice magnetic invariant of this space group [14,18].

Magnetic interactions parameters J_{ij}, $\mathbf{D}_{ij}$, $\boldsymbol{A}_{ij}$ and $\boldsymbol{g}_i$ are supposed to be dependent on Ti^{3+} ions orbital states. J_{ij} is determined within the P.W. Anderson's approach [15] using the Hubbard model parameters t_{mn}, U and J_H, which are taken from LDA–based calculation [10]. Indexes in t_{mn} denote 3d-t_{2g} orbitals, namely ξ, η, ζ. For $LaTiO_3$ $t_{mm} \approx 0.24$ eV, $t_{m\neq n} \approx 0.12$ eV, $U \approx 3.20$ eV, $J_H \approx 0.61$ eV. For $YTiO_3$ $t_{mm} \approx 0.21$ eV, $t_{m\neq n} \approx 0.10$ eV, $U \approx 3.45$ eV, $J_H \approx 0.62$ eV.

Two special features in J_{ij} are important for obtaining correct magnetic structure. First is considering Hund's coupling, which is J_H/U smaller then «common» superexchange, proportional to $\frac{t_{mn}^2}{U}$ for titanates [15]. The second is explicit introduction of the Ti–O–Ti bond angle (θ, see Fig. 1) dependence of t_{mn}: $t_{mn} \sim t_{mn}^{(0)}(p - \sin\theta)$. Here *p* is 1 for «active» and 0 for «inactive» orbitals [7, 8]; $t_{mn}^{(0)}$ is charge transfer integral in strictly cubic system. Without these two peculiarities one can not obtain experimentally observed magnetic structure in both compounds simultaneously as Schmitz et al. couldn't [8, 9]. Ti–O–Ti bond angle θ for lanthanum titanate is about 153° and 142° for $YTiO_3$.

As orbital state of Ti^{3+} is a singlet, anisotropic superexchange interactions $\mathbf{D}_{ij}$, $\boldsymbol{A}_{ij}$, as well as $\boldsymbol{g}_i$, may be obtained by perturbation expansion in spin-orbit coupling and isotropic superexchange interaction as it was described in classical works by T. Moriya [16] ($\mathbf{D}_{ij}$, $\boldsymbol{A}_{ij}$) and by A. Abragam with B. Bleaney [17] ($\boldsymbol{g}_i$). We used spin-orbit coupling parameter $\lambda \approx 0.15$ meV [17]. Final values of all magnetic parameters are listed in Table 1.

Averaged diagonal elements of $\boldsymbol{g}_i$, written in Table I, are 1.91 for $LaTiO_3$ and 1.92 for $YTiO_3$. They are in good agreement with experimentally obtained values of g-factors measured for polycrystals [12], these are near 2 for lanthanum crystal and 1.92 for yttrium.

Table 1. Magnetic interactions (meV) and magnetic structure components in $LaTiO_3$ and $YTiO_3$. All values are written *Pnma*.

R	A_x, F_y, G_z	***g***	J_{12}	J_{13}	$\mathbf{D}_{12}$ x,y,z	$\mathbf{D}_{13}$ x,y,z	$\boldsymbol{A}_{12}$		$\boldsymbol{A}_{13}$	
							xx,yy,zz	xy,xz,yz	xx,yy,zz	xy,xz,yz
La	0.0099 0.0316 0.9995	$\begin{pmatrix} 1.94 & -0.06 & 0.02 \\ -0.06 & 1.93 & 0 \\ 0.02 & 0 & 1.87 \end{pmatrix}$	13.11	16.88	0.515 0 −2.477	0 −0.365 −0.227	–0.052 –0.056 –0.304	0 0.054 0	–0.019 –0.025 0.030	0 0 –0.022
Y	0.0042 0.9980 0.0624	$\begin{pmatrix} 1.86 & -0.01 & 0.03 \\ -0.01 & 1.96 & -0.04 \\ 0.03 & -0.04 & 1.94 \end{pmatrix}$	−2.73	−2.74	1.148 0 −0.407	0 −0.229 −0.304	–0.393 –0.049 –0.110	0 0.115 0	–0.341 –0.049 –0.080	0 0 –0.043

The magnetic structure and spectra

Minimizing the energy (1) with parameters from Table I by the directions of spins one obtains ground state magnetic structure. For both compounds the magnetic structure is turned out to be of one type, that is (A_x, F_y, G_z) (*Pnma* notations). In excellent agreement with experiment [3, 4, 6], $LaTiO_3$ is mostly A-type antiferromagnet, whereas $YTiO_3$ is almost ferromagnetic (see Table I). Schematic magnetic structures of these compounds are shown in Fig. 2.

Magnons (or spin wave) dispersions were calculated utilizing the Hamiltonian (1) within the linear spin waves approximation [19]. The results together with experimental data [5, 6] are shown in Fig. 3.

As it was discussed in the introduction, there are no satisfactory magnetic resonance

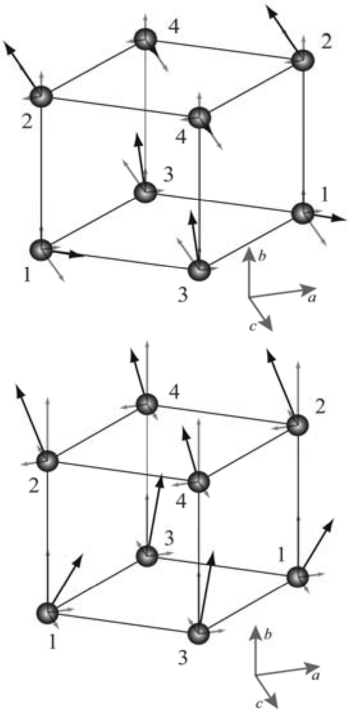

Fig. 2. Schematic magnetic structures of $LaTiO_3$ (up.) and $YTiO_3$ (bott.). Gray arrows denote magnetization projections (*Pnma*).

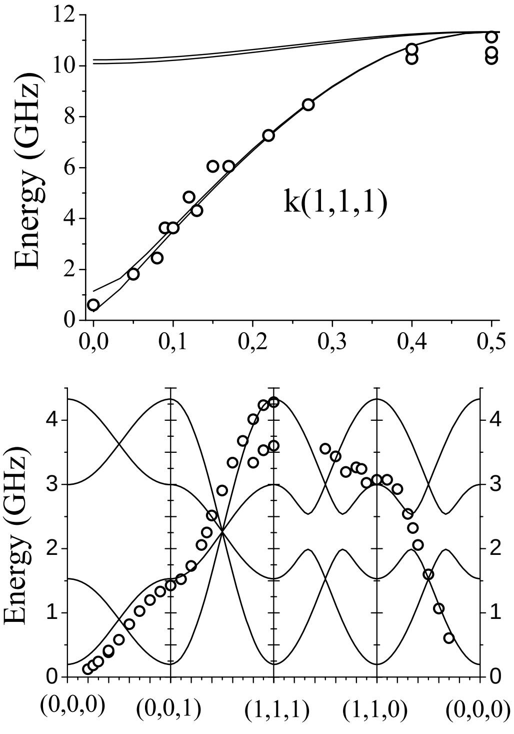

Fig. 3. Spin wave dispersions for $LaTiO_3$ (upp.) and $YTiO_3$ (bott.). Circles denote experimental data, taken from [5] for $LaTiO_3$ and [6] for $YTiO_3$.

experiments for both compounds under consideration in their ordered phases. So it seems to be important to estimate typical spectra, namely external magnetic field dependencies, and typical frequencies of AFMR in lanthanum titanate and FMR in $YTiO_3$. Such calculation was also performed within the linear theory of magnetic resonance [19]. The simulation results with **H** close to light axes directions are shown in Fig. 4.

Discussion

Within the realistic model with ab initio calculated parameters [10, 13] we obtained superexchange interactions in $LaTiO_3$ and $YTiO_3$. The values which may be estimated experimentally (that is J_{ij}, $|\mathbf{D}_{ij}| + \mathrm{Sp}(\boldsymbol{A}_{ij})$ and $\boldsymbol{g}_i$) are in good agreement with those reported in [5,6,12].

The simulation of spin wave spectra also gives excellent coincidence, excluding some particular regions of dispersion curves for $YTiO_3$. The latter discrepancy is due to overestimation of anisotropy parameters within the model. This discrepancy would become even smaller took we slightly different parameters of Hubbard model. That is really possible because of the variance of those reported by different authors [10, 20]. We claim that simple approximation, used in [6], for fitting SW data and therefore extracting superexchange parameters is not enough for making correct estimations of *anisotropic* interactions (for example, Dzyaloshinskii–Moriya interaction is not considered at all). If we chose slightly different Hubbard model parameters to fit experimental dispersions, we would get discrepancy in superexchange interactions. So we stop on the agreement in parameters instead of fitting the spectra. This choice does not make us modify values of t_{mn}, U and J_H from [10].

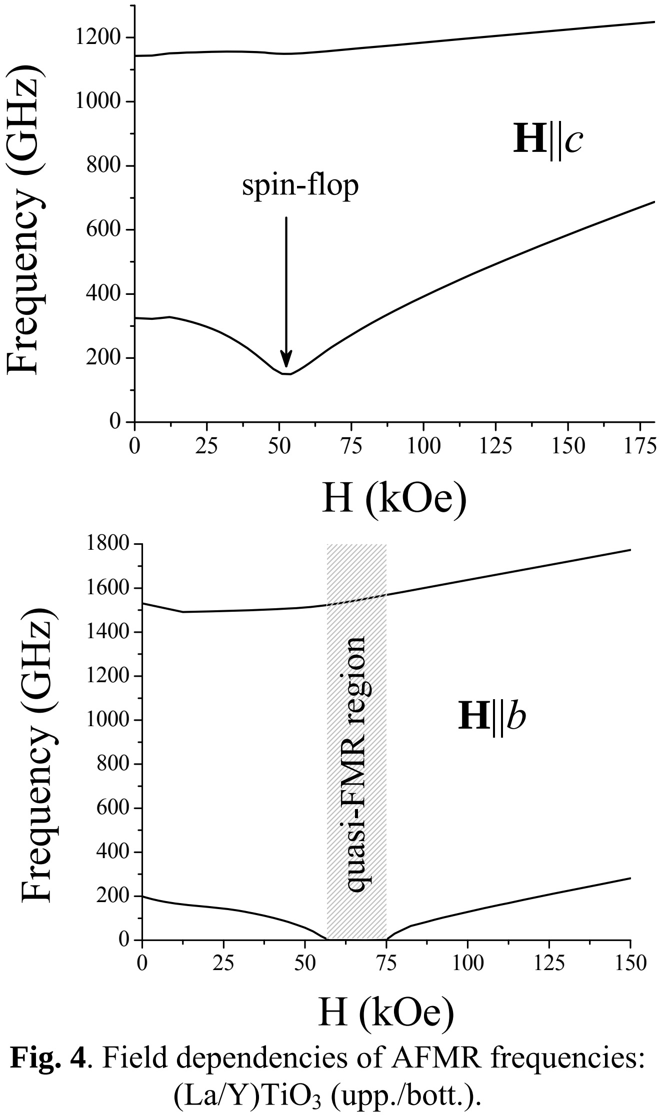

Fig. 4. Field dependencies of AFMR frequencies: $(La/Y)TiO_3$ (upp./bott.).

Finally, AFMR and FMR spectra are predicted. It is seen from our simulation of AFMR in $LaTiO_3$ (Fig. 4), why S. Okubo et al. could not observe the spectrum [12]. The resonance frequency is at the breaking point of their equipment.

Further experimental research is needed with use of high-quality single crystals of lanthanum and yttrium titanates to confirm estimations given. This would give the most accurate information on magnetic interactions and magnetic subsystem symmetry of these compounds.

The work is partially supported by the «Dynasty» foundation.

References

[1] Mochizuki M., Imada M., New J. of Physics, v. 6, no. 1, p. 154 (2004).

[2] Imada M., Fujimori A., Tokura Y., Rev. Mod. Phys., v. 70, p. 1039 (1998).

[3] Komarek A.C. et al., Phys. Rev. B, v. 75, p. 224402 (2007).

[4] Cwik M. et al., Phys. Rev. B, v. 68, p. 060401 (2003).

[5] Keimer B. et al., Phys. Rev. Lett., v. 85, p. 3946 (2000).

[6] Ulrich C. et al., Phys. Rev. Lett., v. 89, p. 167202 (2002).

[7] Oles A.M. et al., Phys. Rev. B, v. 72, p. 214431 (2005).

[8] Schmitz R. et al., Phys. Rev. B, v. 71, p. 144412 (2005).

[9] Schmitz R. et al., cond-mat/0506328 (2005) (unpublished).

[10] Solovyev I., Phys. Rev. B, v. 74, p. 054412 (2006).

[11] Schmitz R. et al., Phys. Rev. B, v. 71, p. 214438 (2005).

[12] Okubo S. et al., JMMM, v. 177-181, p. 1373 (1998).

[13] Submitted to The Physics of the Solid State (Fiz. Tverd. Tela – in Russian).

[14] Turov E.A., Kolchanov A.V., Menshenin V.V., Mirsaev I.F., Nikolaev V.V., «Symmetry and physical properties of antiferromagnets». Moscow: «Fizmatlit», 2001. 560 p. (in Russian).

[15] Anderson P.W., Phys. Rev., v. 115, no. 1, p. 2 (1959).

[16] Moriya T., Phys. Rev., v. 120, no. 1, p. 91 (1960).

[17] Abragam A., Bleaney B., «Electron paramagnetic resonance of transition ions», T. 2. Oxford: «Clarendon press», 1970. 351 p.

[18] Gontchar L.E., Mozhegorov A.A., The Physics of the Solid State, v. 47, no. 8, p. 1455 (2005) – Fiz. Tverd. Tela (in Russian).

[19] Gurevich A.G., «Magnetic resonance in ferrites and antiferromagnets». Moscow: «Nauka», 1973. 592 p. (in Russian).

[20] Streltsov S.V. et al., Phys. Rev. B, v. 71, p. 245114 (2005).

Using RF Pulses Sequences for Slice Selection in NMR Imaging

V.L. Parshina, V.V. Frolov

St.-Petersburg State University, 198504, St.-Petersburg, Petrodvorets, Ulianovskaya st.1
e-mail: parshenn@mail.ru

Introduction

Nearly all modern NMR imaging techniques contain imposing magnetic field gradients (MFG) to localize NMR signals. MGF can work by two ways: to produce a physical selection of some volume or to provide the spatial encoding of NMR signals. Despite of existence of three-dimensional Fourier imaging the most of techniques in current use are 2D imaging in an allocated slice. For quality of NMR image it is very important to have the clear boundaries of the slice to select. In this communication the results of theoretical analysis and simulation of implementation of modified series of radiofrequency pulses known as “DANTE” as well as experimental test with NMR imaging at very low (7 mT) magnetic field are presented.

Theory

To excite spins in an interested slice one applies a magnetic field with a gradient that is orthogonal of the slice. Ideally, the signals of spins throughout the all the width of slice are equal. Practically, the signals decrease according to moving from the plane in which the Larmor frequency coincides with the carrier of radiofrequency off. Thus, quality of slice selection is characterized by the profile of the dependence of transverse components of nuclear magnetization on the distance of a volume element from that plane. So, rectangular profile is desirable for a selected slice.

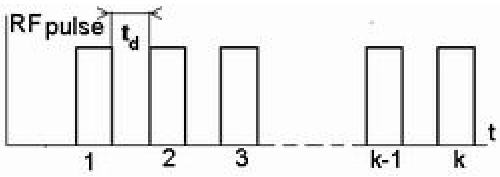

Fig.1 Diagram of DANTE sequence

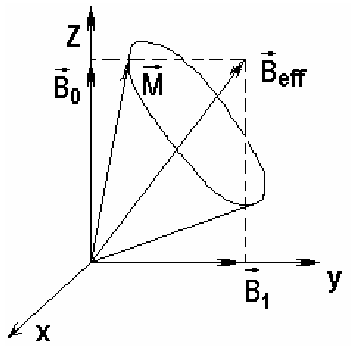

Fig.2 Transversal magnetization in Rotating frame of references

In the experiment quality of selection may be evaluated by comparing profile of the whole of a sample and one of a slice. In practice vague boundaries of the slice with different artifacts are got. Some techniques to improve the quality of selection profile is using of the specific form of envelope of radio frequency (RF) pulse [1]. Alternatively P.Mansfield and A.A. Maudsley have used a special sequence of square RF pulses to achieve the same target [2]. Earlier we attempted to use pulse sequence known as DANTE for slice selection in NMR-tomography [3]. The standard techniques DANTE consists in dividing of 90 degree RF impulse into several equal parts with equal intervals (Fig. 1). Selectivity of this sequence is provided by fact that magnetization of spines which frequency coincides with Larmor frequency stays in a plane *XZ* (Fig. 2) and DANTE influences on it like 90^0 RF pulse. Spines with another frequencies (with some offset (Ω)) during interval t_d are leaving plane *XZ* and can’t reach a plane *XY* (except spines with angular of precession in Rotating FR is ktheirs contribution in signal is artifact). Usually a signal dependence on Ω is identified with a spectrum of pulse sequence but it is not correct. Spin system is non-linear one and precise dependence should be counted with applying of Bloch equations.

Simulation

The simulation of modified techniques DANTE was made using soft “Mathcad 2001 Professional”. Effect of DANTE on transversal magnetization has come about through a multiplication of some matrices. There are matrix of rotation transversal magnetization around B_{eff} and matrix of free precession. A computer simulation demonstrates a narrowing of selected slice by DANTE but a great disadvantage of the method was the presence of intense adjacent lobes in a profile of selected slice (Fig. 3). In this research a modified impulse sequence is proposed as a way to suppress the lobes. The gist of modification of standard sequence DANTE consists in using of unequal random separation between parts of 90 degree RF pulse [3]. A program which simulates dependence of transversal nuclear magnetization on offset of radiofrequency pulse from NMR frequency was created in “Mathcad” too. This program (Fig. 4) pickes up intervals t_j using a random values generator. Parameters for selection were half-thickness of layer W, location of the first maximum L1, altitudes of the first and the second maxima (HM1 and HM2). In the program their compare with the same parameters of standard DANTE W_0,$L1_0$,$HM1_0$,$HM2_0$. The quantity of cycles N is incoming parameter, a sequence of intervals is out coming one.

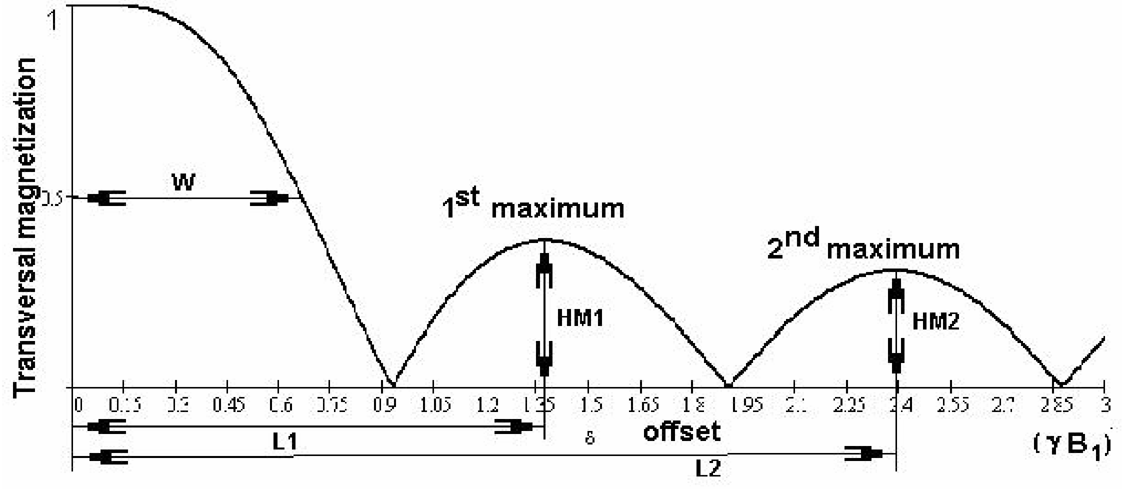

Fig.3 Dependence tr. magnetization on offset and parameters for selection.

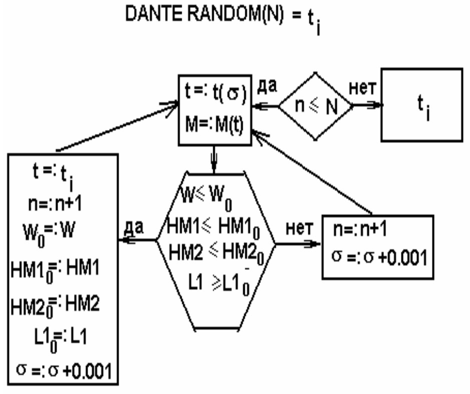

Fig.4 Algorithm of a program for picking up modified sequence.

Fig. 5 demonstrates magnetizations for one of modified sequence and standard DANTE. They are calculated dependences of transversal magnetization on non-dimensional offset in unit γB_1. Where B_1 is amplitude of RF pulse and γ is a gyromagnetic ratio.

It shows that modified sequence reduces the first maximum and moves away its location.

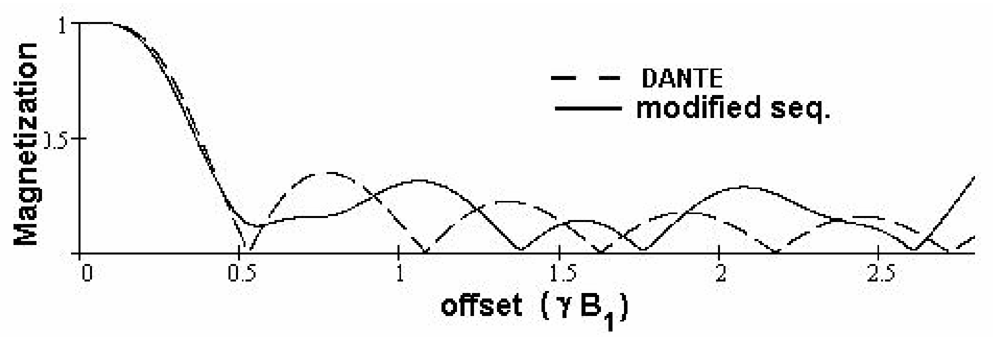

Fig.5 Dependence magnetization on offset for DANTE and for modification.

Experiment

Experiment was carried out using a homebuilt NMR mini-imager at 7 mT. Its scheme is shown in the Fig. 6. As a samples was taken container of 3.3 cm in diameter with three ampoules (d=8mm), filled with water doped with paramagnetic ions. Configuration of ampoules corresponds to 3 layers. The first layer is with one ampoule, the second one has no ampoules and the third layer contains two. Fig. 7 represents the diagram of pulse sequence was used to realize the method. The duration of rectangular RF pulse is 620mc sec.

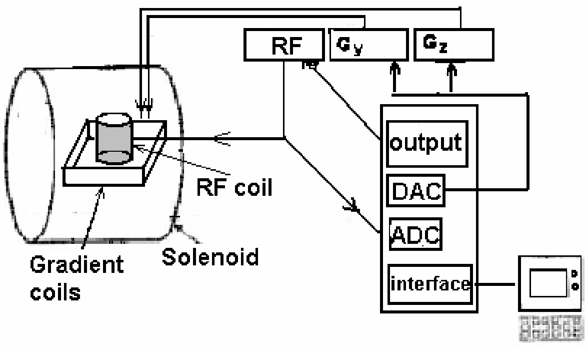

Fig.6 Homebuilt NMR mini-imager

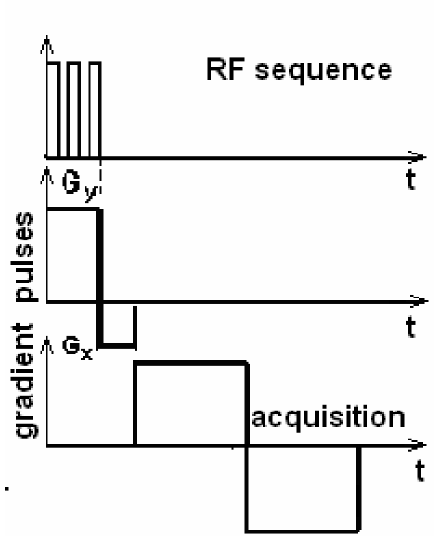

Fig.7 Diagram of pulse sequence for receiving profile along axis X

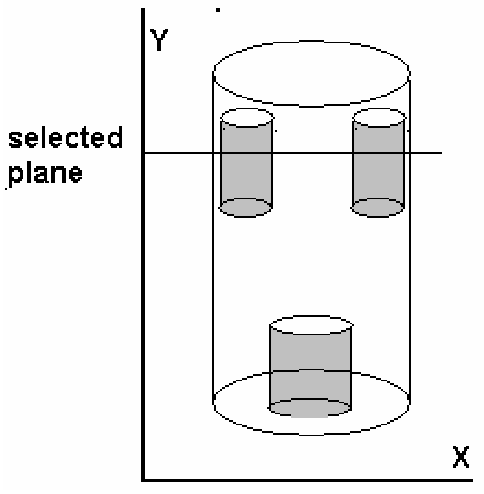

Fig.8 Scheme of position of a layer with 2 amp.

Magnetic field gradient (0.06mT/m) is acting along axis Y in the same time as RF sequence and narrow slice of a sample is selected in orthogonal plane. After RF sequence is off the gradient switches in the opposite direction. Gradient G_x along axis X (0.13mT/m) is used for receiving profile. Profiles along axis Y was received with 0.1mT/m gradient. Fig. 8

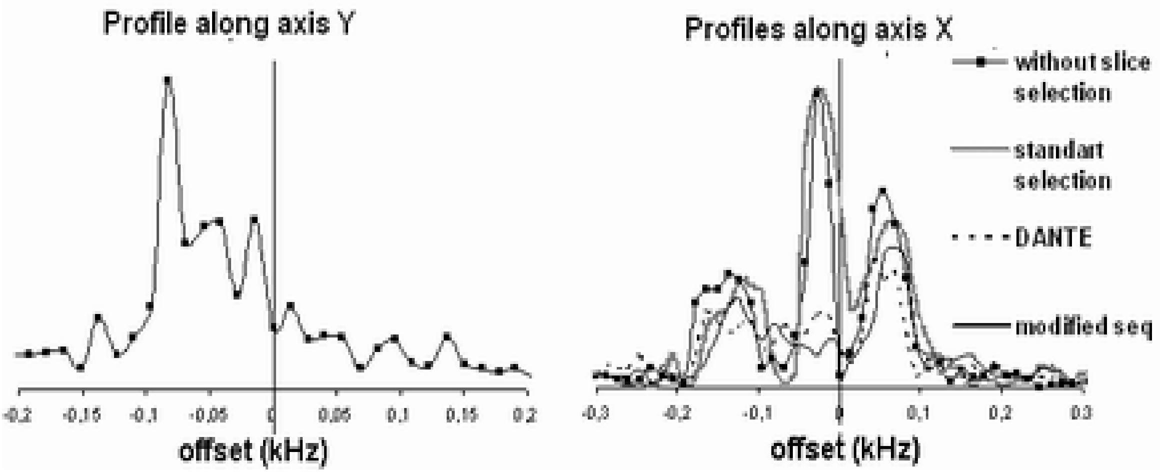

Fig.9 Experimental profiles of a sample along axes Y and X

shows position of the selected slice in the sample. In the left part of Fig. 9 is presented the vertical profile of the sample. Two highest picks on the graph mean two layers. In the right side are several profiles of ampoules along axis X. Line with marker is profile 3 ampoules. Profile of standard method selected layer is solid line, it can be seen that with this value of selecting gradient (0.06mT/m) standard method is not effective, and profile still consists of 3 ampoules. Profiles which were received with applying DANTE (dot line) and with modified sequence (wide black line) demonstrate well selection. Two picks on the graphs means that layer with two ampoules is selected. Fig. 10, 11 correspond a selection layer with one ampoule.

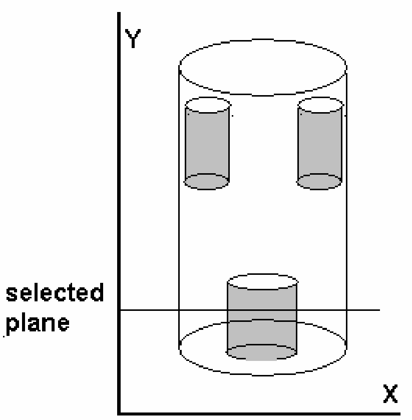

Fig.10 Scheme of position of a layer with 1 amp.

Conclusion

Pulse sequence DANTE and its modification can be used for slice selection. Experiment shows that applying of this sequences lets to narrow width of a layer with out increase of gradient amplitude. Modification of this sequence is decreasing of adjacent lobes.

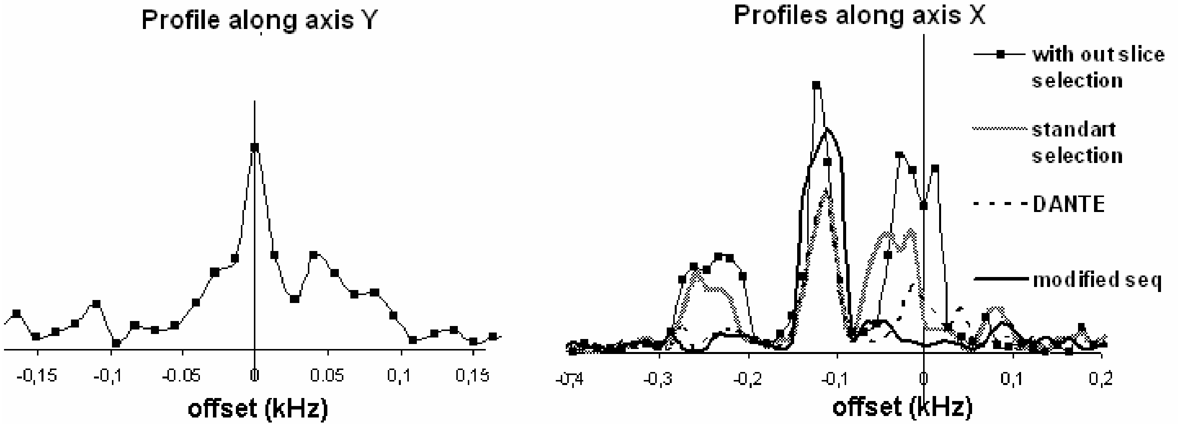

Fig.11 Experimental profiles of a sample along axes Y and X

References

[1] “NMR imaging: image recovery under magnetic field with large non-uniformities” J.M.S. Hutchison, R.J.Sutherland and J.R.Mallard, “Physics E: Science Instrument” vol.11 1978 p.217-221

[2] “Selective Excitation in Fourier Transform NMR” R.Freeman,G.Morris R.Freeman “Journal of Magnetic Resonance” 29,1980, p.433-462

[3] V. Parshina, K. Tutukin, V. Frolov. Slice selection in NMR imaging using modified pulse sequence "DANTE". Thesis book of International Symposium and Summer School in Saint Petersburg "Nuclear Magnetic Resonance in Condensed Matter" 2006, p. 88

High-Field EPR Study of the Exchange Interactions in Strongly-Coupled Spin Triads Undergoing Thermally-Induced Structural Rearrangements

S. Veber[1,2], M. Fedin[2], A. Potapov[3], V. Ovcharenko[2], D. Goldfarb[3], E. Bagryanskaya[2]

[1]Novosibirsk State University, 630090 Novosibirsk, Russian Federation

[2]International Tomography Center, Russian Academy of Science, 630090 Novosibirsk, Russia

[3]Department of Chemical Physics, Weizmann Institute of Science, Rehovot, 76100, Israel

e-mail: gs@tomo.nsc.ru

In recent years the molecular magnets have accumulated a large interest of scientists due to potential applications in magnetic data storage, spin electronics and quantum computers. Experimental investigation of their magnetic properties (especially exchange interactions) and following quantum-mechanical analysis are the key tools for the successful further directed synthesis of these materials with desired magnetic characteristics. In turn, EPR is the choice experimental technique capable for the high sensitivity and resolution study of paramagnetic systems and obtaining necessary information on their structural and magnetic parameters.

Recently a new family of polymer chain complexes (one-dimensional molecular magnets) based on copper(II) hexafluoroacetylacetonates ($Cu(hfac)_2$) and pyrazol-substituted nitronyl nitroxides (L^R) was synthesized (scheme 1) [1]. These compounds $Cu(hfac)_2L^R$ contain the alternating one-spin copper(II) and three-spin nitroxide-copper(II)-nitroxide paramagnetic clusters. They have attracted significant attention due to the observation of magnetic effects analogous to a spin-crossover. Such effects (so-called "nonclassical" spin transitions) arise from the changes of the exchange interaction values (J) in three-spin clusters resulting from structural rearrangements at low temperatures (typically $T \sim 50 \div 150$ K, $|J| \sim 100$ cm^{-1}).

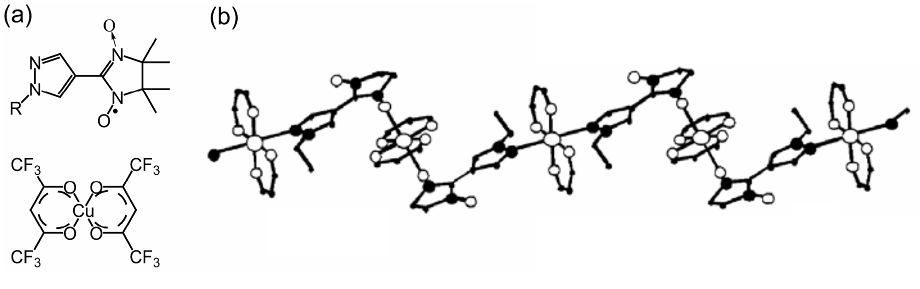

Scheme 1. (a) Chemical structure of $Cu(hfac)_2$ and the nitroxide ligand L^R and (b) Typical polymer-chain structure of $Cu(hfac)_2L^R$ complexes ($Cu(hfac)_2L^{Et}$ is shown).

The first EPR studies of the compounds of the $Cu(hfac)_2L^R$ family have shown that structural rearrangements can be monitored in EPR by a significant shift of the line corresponding to the three-spin clusters [2]. Unusual $g<2$ values of a spin triad have been explained by considering three exchange-coupled spins $S=1/2$ and taking the ratio between exchange coupling J and thermal energy kT into account. Later, the experimental observation of electron spin exchange processes between different multiplets of strongly-coupled spin triads has been reported [3]. These results allowed us to obtain the relationship between temperature dependences of the effective magnetic moment and the effective g-factor of three-spin clusters [4]. Thus, EPR can be used for studying the exchange interactions in three-spin clusters along with the magnetic susceptibility measurements. However, up to date only the estimations of the exchange interaction values in Cu(hfac)$_2$L^R using EPR have been done [4].

In this work we demonstrate the capability of the high-field EPR for the measurement of temperature dependence of the exchange interaction in strongly-coupled three-spin clusters. For this purpose the high-field CW EPR (W-band) was applied for investigation of the compounds Cu(hfac)$_2$L^{Pr} and Cu(hfac)$_2$L^{Bu}·0.5C$_8$H$_{18}$ (Pr=propyl and Bu=butyl). EPR spectra were recorded at T= 50 - 300 K with a temperature step of 3-5 K. The temperature dependences of the effective g-factor of the spin triad were obtained for both compounds. Different approaches for the exchange interaction measurements were compared, where disordered and oriented polycrystalline powder samples, as well as single crystals were used. It was shown that CW EPR spectra of powder samples contain mush more information about compounds in comparison with single crystal EPR spectra, but sufficient overlap of the signals of isolated copper and three-spin system in the case of powder spectra complicates following calculations of exchange interaction value (J) (fig.1).

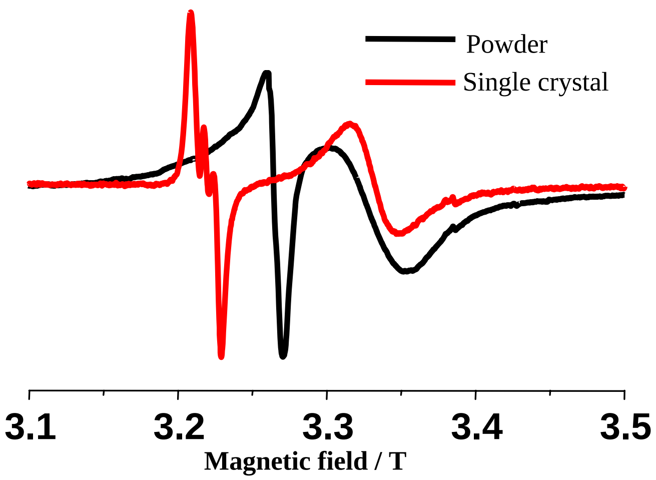

Fig.1 Single crystal and powder CW EPR spectra of Cu(hfac)$_2$L^{Pr} at 300K.

Calculations of the temperature dependence of the exchange interaction J using the dependence of the effective g-factor showed a good agreement with the magnetic susceptibility data. Several advantages of the EPR approach in comparison with magnetic susceptibility measurements were found and discussed.

This work was supported by INTAS (YSF No. 06-1000014-5915), RFBR (05-03-32264-a), grant of the President of Russian Federation (MK-6673.2006.3), Lavrentiev grant no. 79, and FASI state contract no. 02.513.11.3044.

References

[1] Ovcharenko, V. I.; Maryunina, K. Yu.; Fokin, S. V.; Tretyakov, E. V.; Romanenko, G. V.; Ikorskii, V. N. Russ. Chem. Bull. Int. Ed. **53**, 2406 (2004)

[2] Fedin, M.; Veber, S.; Gromov, I.; Ovcharenko, V.; Sagdeev, R.; Schweiger, A.; Bagryanskaya, E. J. Phys. Chem. A **110**, 2315 (2006)

[3] Fedin, M.; Veber, S.; Gromov, I.; Ovcharenko, V.; Sagdeev, R.; Bagryanskaya, E. J. Phys. Chem. A **111**, 4449 (2007)

[4] Fedin, M.; Veber, S. et.al. Inorg. Chem. (2007) submited

Magnetic Properties of Chemically Deposited Thin Films of Ferromagnetic-Semiconducting $CdCr_2S_4$ Compounds

M. Erdem[1)], H. Karaca[1)], S. Kazan[2)], A.C. Başaran[2)], M. Ozdemir[1)]

[1)] Marmara University, Faculty of Science and Letters, Department of Physics, 34722 Ziverbey, Goztepe, Kadıköy ISTANBUL TURKIYE
[2)] Gebze Institute of Technology, Faculty of Science, Department of Physics, Cayirova Gebze KOCAELI TURKIYE

e-mail: abasaran@gyte.edu.tr

Chalcogenide spinel of the $CdCr_2S_4$ has been investigated by dc magnetization and optical absorption methodes. $CdCr_2S_4$ thin films of 1500 A in thickness have been grown on various substrate such as single crystalline Si(100), YSZ(100) and amorphous glasses bu using chemmical bath deposition methodes. They were characterized by structural, optical and magnetic measurements techniques. The x-ray analysis revealed that the as-deposited films were polycrystalline and have cubic symmetry. The films were uniform and adherent to substrates. Scanning Electron Micrographs (SEM) showed that the substrates were well covered and continous with films; no cracks or pinholes were observed.

The optical constants of the deposited films were obtained from the analysis of the experimentally recorded transmission and absorption data over the wavelength range 300–800 nm. An analysis of the optical absorption data of the as-deposited films revealed an optical direct transition with an estimated band gap E_g of about 2.4 eV.

The Dc magnetic measurements have been carried out as a function af temperature in the range of 4-300 K. DC Magnetisation measurements were carried out on polycrystalline $CdCr_2S_4$/Si/YSZ/Glass films in the temperature range 5-150K. Magnetometry data confirm ferromagnetic order with a Curie temperature of 95 K, as in the bulk material. The magnetization exhibits hysteretic behavour with significant remenenace, and coercive field that is increasing with decreasing temperature and it has a value of about 250 Oe at lowest temperature. From the analysis of magnetic and optical data it has been concluded that the $CdCr_2S_4$/ films are ferromagnetic semiconductor and it is weakly ferromagnetic.

Interestingly the M-T curve of the films growth on YSZ(100) substrate exhibits an anomolies below about 30 K. Secondly, the branches of the curves, for instance, recorded with increasing absolute values of the external magnetic field are higher than those of recorded with decreasing filed in contrast to the usual behaviour of ferromagnetic hysteresis curves. (There seems to be a wery weak negative remnat magnetization.) This behaviour could be attributed to the negative exchange bias as rarely observed in the literature.

This work was supported in part by Marmara University, and TUBITAK, TBAG-105T458.

EPR of Ni^{2+} Impurity Centers in BaF_2 Crystal

A.D. Siraev[1)], E.R. Zhiteycev[2)], V.A. Ulanov[1)]

[1)]Kazan State Power Engineering University, Krasnoselskaya 51, Kazan, Russia
[2)]Kazan Physical Technical Institute, 420029, Sibirsky tract 10/7, Kazan, Russia

e-mail: lpee@yandex.ru

In our time a lot of attention is paying for synthesis and study the nanostructures embedded into various media. It is associated with the tendencies which arise in the fields of electronics and technology. Usually the nanostructures are formed by ten or more atoms or ions, and the gaseous or liquid media are used to synthesize them. But, up to now only some experimental studies were performed to find a possibility to synthesize the nanostructures in bodies of crystalline solids [1]. Such situation can be explained by the fact that solubility of admixed substances in most of crystals usually is limited. But it was found in our investigations that there are some ways to synthesize impurity nanostructures in the lattices of ionic crystals [2,3]. It seems to us that this technology is very promising. At first, a strong influence of a crystalline matrix on structure and properties of the impurity clusters arising in its volume due to synthesis process can results in a formation of absolutely new nanomolecules which cannot exist in a free condition. At second, the nanostructure, synthesized in a volume of chemically inert crystal lattice, appears to be perfectly protected from influence of atmosphere surrounding this crystalline sample. And finally, any nanostructure packed into the lattice of a crystalline matrix finds itself in a reliable contact (thermal, acoustic, etc.) with this matrix. As a result, there appear fine opportunities for changing the physical properties of the nanostructure by means of various external (in relation to nanostructure) influences [4].

The present work was devoted to research the formation conditions and physical properties of nickel impurity clusters arising in a fluorite type crystal, BaF_2, during a crystal growth process. It was shown that the interactions between admixed defects in the BaF_2:Ni crystals formed stable cluster structures containing two and more impurity ions. The investigation was performed by means of EPR method. The angular dependencies of the EPR line positions were studied and, as result, the spin-Hamiltonian parameters of the paramagnetic centers under investigation were established. Using the experimental facts got in the present investigation, the possible structures of the nickel impurity centers were proposed.

References

[1] Hayes W. Crystals with the fluorite structure / W. Hayes. - Clarendon: Oxford, 1974. – 414 p.

[2] EPR study of impurity iron ion clusters in BaF_2 crystals / E. R. Zhiteytsev, V. A. Ulanov, M. M. Zaripov, and E. P. Zheglov// Physics of the Solid State. – 2005. – V. 47, N. 7. – P. 1254.

[3] EPR of Trivalent Iron Centers in SrF_2:Fe Crystals / E. R. Zhiteytsev, V. A. Ulanov, M. M. Zaripov // Physics of the Solid State. – 2007. – V. 49, N. 5. – P. 845.

Jahn-Teller effect in the $[TiF_4F_4F_{int}]^{6-}(C_{4v})$ and $[NiF_4F_4F_{int}]^{7-}(C_{4v})$ clusters embedded into SrF_2 crystals / V. A. Ulanov, E. R. Zhiteytsev, A. G. Varlamov // Journal of Molecular Structure. – 2007. – V. 838. – P. 182.

EPR Spin Probe Study of Surface Properties of Magnetic-Heterogeneous Oxide Systems

S.B. Zikirin[1)], D.V. Stass[1)], O.N. Martyanov[2)], V.F. Yudanov[2)], N.V. Volkov[3)]

[1)]Institute of Chemical Kinetics and Combustion of Siberian Branch of the Russian Academy of Sciences, 630090, Institutskaya 3, Novosibirsk, Russia.
[2)]Boreskov Institute of Catalysis of Siberian Branch of the Russian Academy of Sciences, 630090, Pr. akademika Lavrentieva 5, Novosibirsk, Russia.
[3)]Kirensky Institute of Physics of Siberian Branch of the Russian Academy of Sciences, 660036, Krasnoyarsk, Russia.

e-mail: samat@kinetics.nsc.ru

Doped lanthanum manganite is very interesting from chemical viewpoint. Heterogeneous catalysts based on manganite are typically used in various processes of deep and partial oxidation. Unfortunately the connection between the unique electronic and magnetic properties of manganites and their catalytic properties is not yet clear [1]. This stimulates further development of adequate methods to study the properties of manganite surface.

This work is devoted to investigation into the process of adsorption of nitroxyl radical from liquid phase onto manganite surface. We used a 3-imidazoline radical, which is a typical stable nitroxyl radical, as a spin probe. Lunina et al. [2] have reported that it is possible to get qualitative information about translational and rotational freedom of adsorbed molecule by spin probe method. Due to adsorption molecular rotation become slower and we can observe a broadened inhomogeneous EPR spectrum which is a sum of spectra of differently oriented radicals. Correlation times then give qualitative information on surface properties.To determine experimental conditions in which adsorption of radicals can be observed, we, following Lunina, tested well-studied nitroxyl radical adsorption from liquid phase to □-Al_2O_3 surface, and obtained typical EPR spectra of hindered probe molecules (fig. 1a). But in case of manganite the shape of EPR spectra of nitroxyl radicals in solution in contact with surface is typical for pure liquid phase component with additional background from bulk manganite (fig. 1b). The spectrum of hindered rotation has not been registered.The absence of spectrum caused by hindered rotation of radical is interpreted by widening from magnetically heterogeneous manganite surface, because the solid has domains with various magnetic orders. This supposition is proved by temperature dependence of manganite EPR spectra. While temperature is increasing EPR spectrum slowly changes its shape finally coming to

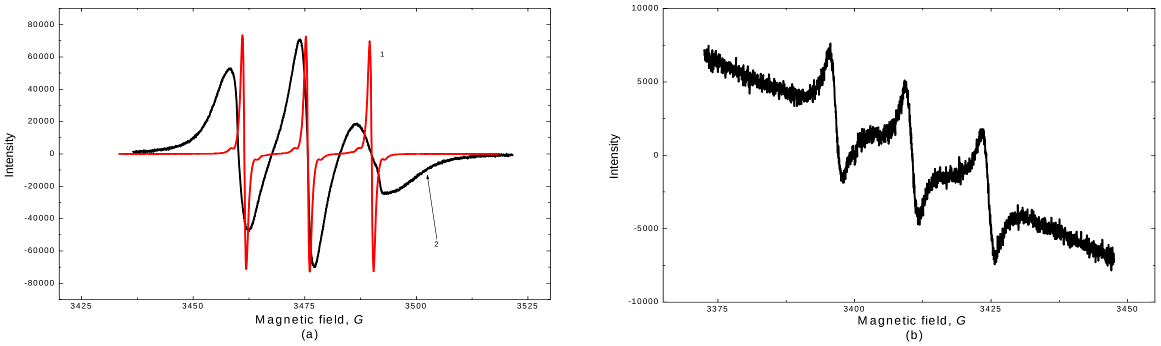

Fig.1 EPR spectrum of 3-imidazoline radical: (a) 1 – only solution in dodecane; 2 – solution with added (a) — Al_2O_3, (b) — solution with added manganite $La_{0.7}Ca_{0.15}Sr_{0.15}MnO_3$.

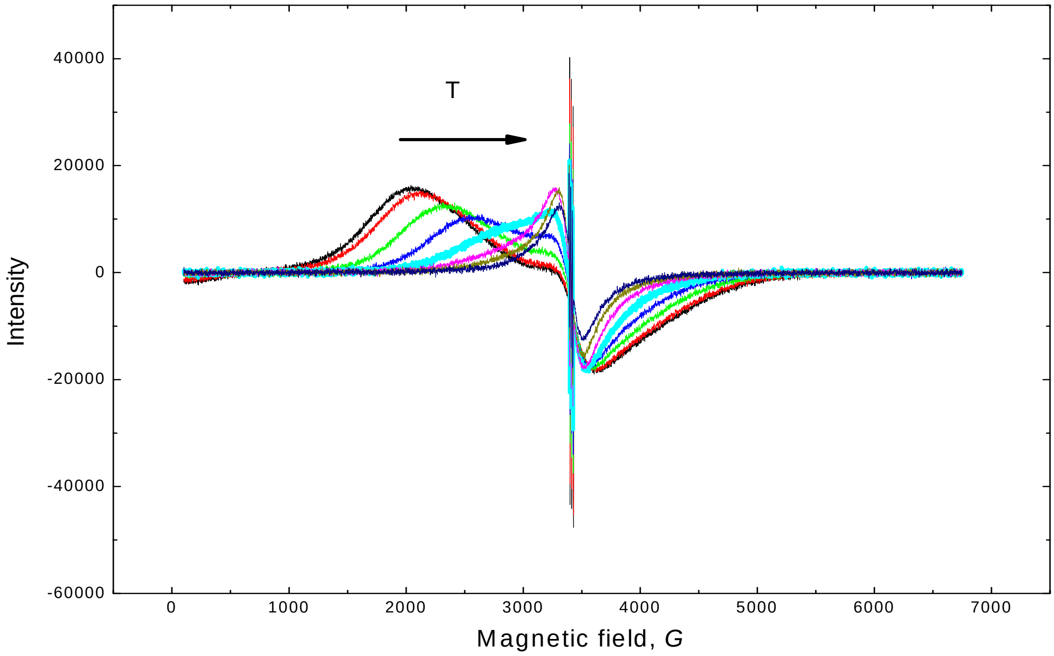

Fig.2 Temperature dependence of EPR spectrum of manganite $La_{0.7}Ca_{0.15}Sr_{0.15}MnO_3$. Temperature range 300-360 K. Narrow center line is reference signal of nitroxyl radical.

shape typical for EPR spectrum of paramagnetic sample (fig. 2).

Smooth variation of EPR spectrum is the evidence of coexistence of both ferromagnetic and antiferromagnetic phases in solid.

The EPR spectra were detected with Bruker X-band EMX spectrometer. The work is supported by Program of the Branch of Chemistry and Material Sciences of the Russian Academy of Sciences, project № 5.1.6.

References

[1] E. Dagotto, Open questions in CMR manganites, relevance of clustered states and analogies with other compounds including the cuprates // New Journal of Physics, 2005, v. 7, p. 67

[2] V.B. Golubev, E.V. Lunina, A.K. Selivanovskiy, Spin probe method in adsorption and catalysis // Uspekhi Khimii, 1981, V. 50, issue 5, p. 792 (in Russian)

Alignment of 1,2– and 1,3–Dichloronaphtalene and 1,2,3–Trichloronaphtalene Induced by Strong Magnetic Field

O.V. Smirnova, V.A. Chertkov

Department of Chemistry, Moscow State University, 119992,Vorobevy gory, Moscow, Russia

e-mail: olleys@rambler.ru

Introduction

NMR spectroscopy is a valuable method for studying of structure and properties of molecules in solution. Molecules with anisotropy of the magnetic susceptibility exhibit a small partial orientation in strong magnetic field. The resulting macroscopic anisotropy may become manifest anisotropic nuclear spin interactions, like the direct dipolar and quadruple coupling [1]. Methods based on this effect can provide information on the spatial structure of the compound. In the literature applications for DNA, peptides and their complexes are presented [2, 3].

Until recently, main source of information about orientation effects based on quadruple coupling in NMR ^{2}H for selectively deuterated species. However, some experimental factors: extra efforts for synthesis of the compounds, fast quadrupole relaxation of deuterium signals and complicated procedure of the data processing, - limited the feasibility of this technique.

Novel procedure for quantitative analysis of the orientation effect

The new procedure suggested for quantitative simultaneous analysis of a series of high resolution NMR spectra recorded on spectrometers with different magnetic field strength. This technique allows to separate the field-independent spin-spin and dependent dipole-dipole coupling constants.

Anisotropy and rhombicity as parameters of a magnetic susceptibility tensor for 1,2-, 1,3–dichloronaphtalene and 1,2,3-trichloronaphtalene.

This method was used for 1,2- , 1,3 –dichloronaphtalene and 1,2,3 –trichloronaphtalene for determination of anisotropy {$\Delta\chi$, m^3} and rhombicity {$\delta\chi$, m^3} as parameters of the magnetic susceptibility tensor.

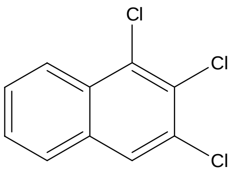

(I)

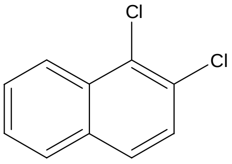

(II)

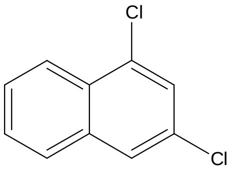

(III)

The series of NMR spectra recorded on four spectrometers with wide range of B_o (4.70, 9.39, 11.4 and 14.09 T, acetone-D_6, 303.5 K) was analyzed. Spin-spin and dipole-dipole coupling constants for all pair ^{1}H, anisotropy and rhombicity of the magnetic susceptibility tensor were received. Ab initio quantum calculation were performed using CSGT RHF approach with 6-311++G(df) basis.

Augmentation of the basis set with polarization functions affects the values of the calculated parameters to a lesser extent compared to augmentation with diffuse functions.

Calculated anisotropy and rhombicity of the magnetic susceptibility of molecules under investigation and experimental ones are in good agreement.

Acknowledgements

This work is supported by the RFBR (grant № 06-03-32800). A.K. Shestakova thanks the fond AVH (Germany).

References

[1] E.W. Bastiaan, J. Bulthuis, C. MacLean, *Org. Magn. Reson.,* v. 24, 723 (1986).

[2] B.N.M. Van Buuren, J. Schleucher, V. Wittman, C. Griesinger, H. Schwalbe, S.S. Wijmenga, *Angew. Chem., Int. Ed.*, v. 43, 187 (2004).

[3] D. Bryce, J. Boisbouvier, A. Bax, *J. Am. Chem. Soc.*, v. 126, 10820 (2004).

Magnetic Nanoparticles Influence on the Radical ESR Spectra

O.N. Sorokina, A.V. Bychkova, A.L. Kovarski

Emanuel Institute of Biochemical Physics, RAS 119334 Kosygin, 4 Moscow, Russia

e-mail: alsiona@gmail.com

Introduction

The presence of magnetic nanoparticles influences proton relaxation [1, 2], as a result they found a wide application as contrasting agents in tomography. In the field of ESR spectroscopy there are also studies investigating the influence of nanoparticles on paramagnets spectra [3-5]. These experiments model the interactions between low-molecular organic compounds and magnetic nanoparticles which can be used for understanding the drug delivery mechanisms.

ESR spectra of stable nitroxide radicals TEMPOL in the presence of the magnetite nanoparticles with mean diameter ~17 nm have been studied. Two parameters of radical spectrum are sensitive to the presence of magnetic nanoparticles: the spectra location and the linewidth. The radical spectrum shift depends on sample shape and its orientation in the magnetic field. This shift arises due to the demagnetizing field originating from the effect of external magnetic field on the magnetic system. The relaxation mechanisms of line broadening have also been studied. In the system under investigation, radical diffusion in the non-uniform magnetic field of nanoparticles is the main relaxation mechanism.

Materials and Methods

Magnetite hydrosol with particles concentration of 50 mg per ml (0.96 vol.%) in phosphate-citrate buffer, pH 4.0 has been used for experiments. Nanoparticles have been obtained by alkaline precipitation of the Fe(II) and Fe(III) salts mixture. Further the nanoparticles have been stabilized by phosphate-citrate buffer, pH 4.0. Nanoparticle sizes have been determined by photon correlation spectrometry. Particle size distribution followed Gaussian distribution with a maximum about 17 nm and standard deviation 12 nm.

Stable nitroxide radical 2,2,6,6-tetramethyl-4-hydroxy-piperidin-1-oxyl (TEMPOL) was used as a paramagnetic sensor. It was dissolved in the buffer solution, mentioned above, at concentration $1.7\ 10^{-2}$ M ($1\ 10^{19}$ cm^{-3}). No sensor degradation was observed during the experiment. Radical solution and hydrosol was mixed in 1:1 ratio.

The X-range “Bruker” (EMX-8/2.7) spectrometer was used for ESR spectra recording. Hydrosol spectra were placed in a quartz flat cell. The principal plane of the cell was orientated parallel and perpendicular toward the bias field. Microwave frequency power did not exceed 1 mW, and modulation amplitude was 0.5 G.

Results

Fig. 1 shows the ESR spectra of paramagnetic sensor in magnetite hydrosols. It is evident from fig. 1 that the radical spectrum position in the magnetic field depends on the flat cell orientation in spectrometer magnetic field (curves 3 and 4). This effect does not exist in the buffer without nanoparticles; cell rotation does not result in the spectra shift (fig. 1 curves 1 and 2). The direction of sensor spectra sift in hydrosol compared with the spectra in pure buffer is the following: it moves towards the lower fields with parallel cell orientation in the

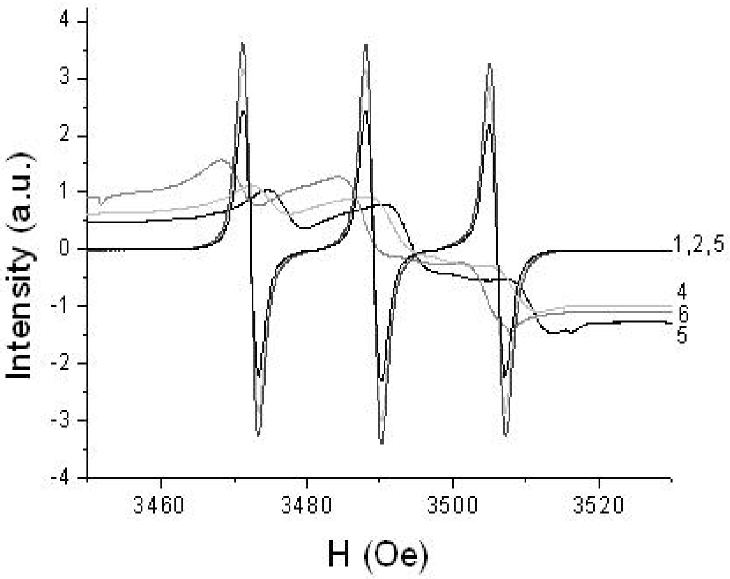

Fig.1 ESR spectra of sensor in buffer without nanoparticles at parallel (1) and perpendicular (2) orientation of flat cell and in capillary (5), and in magnetic liquid at parallel (3) and perpendicular (4) orientation of flat cell and in capillary (6).

magnetic field (curve 3), and towards higher fields at perpendicular cell orientation in the magnetic field (curve 4).

Here you can see the spectra of paramagnetic placed in the round capillary in fig. 1. Curve 5 corresponds to the radical spectrum in pure buffer without particles and the curve 6 to the spectrum in magnetic liquid. As expected curve 5 coincides with the other spectra in buffer without particles and curve 6 moves towards higher magnetic fields. The numerical data of spectra shifts are collected in table 1.

Table 1. ESR spectra parameters of the sensor: g-factor, central peak position H_{cent}, central peak shift δH.

Medium	Tube	Orientation	g-factor	Hcent, Oe	δH=Hcent - H0, Oe
Water	Flat cell	Parallel	2.0053	3508.2	0
		Perpendicular	2.0053	3508.2	0
	Capillary	-	2.0053	3508.2	0
Magnetic liquid	Flat cell	Parallel	2.0064	3487.3	-1.9
		Perpendicular	2.0027	3510.4	4.5
	Capillary	-	2.0039	3491.9	2.6

Moreover significant line broadening of sensor occurs in the magnetic liquid. Thus radical linewidth in water is ΔH = 2.2 ± 0.1 Oe and in magnetic liquid it is broader to ΔH = 5.2 ± 0.1 Oe the radical concentration ($8.5\ 10^{-3}$ M) and other conditions remain equal in both cases.

The radical spectra in hydrosol represent a triplet of hyperfine structure with equal intensities of lines. This characteristic corresponds to the fast nidroxide rotation with frequency ($10^{10} - 10^{11}$ Hz). There are no lines of slow rotation in spectra corresponding to nitroxides immobilized on the particle surface. Radical concentrations in the buffer and in the magnetic liquid defined by ESR spectra are equal. Consequently we may conclude that the number of radicals which are absorbed on the particles surface can be neglected.

ESR spectrum position in magnetic field

The shift of ESR spectrum of radicals with magnetic nanoparticles results in the resonance condition changes. There are internal demagnetizing fields in any magnetic system when an external magnetic field is imposed. As a result paramagnetic particles find themselves in magnetic fields that differ from the external magnetic field. ESR spectrum position varies in accordance with internal field magnitude and direction. The equation for resonance frequency shift $\Delta\omega$ in the framework of Weiss theory of magnetism have been made earlier. It was changed for nanoparticles and took the following form:

$$\Delta\varpi = \zeta\frac{\pi}{3}\gamma_e\mu n_\mu \tag{1}$$

where γ_e is gyromagnetic ratio, μ is magnetic moment of nanoparticles, n_μ s the nanoparticles concentration, ζ – is the coefficient depending on sample shape varied in the range $-1< \zeta <2$

In the case of infinitely elongate ellipsoid the field can be aligned along its principle axis, then $\zeta = -1$ and transversely to it then $\zeta = ½$. In the case of infinitely oblate ellipsoid coefficient $\zeta = 2$ when the external field is parallel to minor axis and $\zeta = -1$ when it is perpendicular to minor axis. The sign before the coefficient indicates the spectrum shift direction. The flat cell can be assumed as an oblate ellipsoid. As it can be seen from the fig.1 when the flat cell is parallel orientated and the external magnetic field is normal to minor axis then spectrum moves towards lower magnetic fields ($\omega\hbar=g\beta(H_0+H')$), and vice versa towards higher ones ($\omega\hbar=g\beta(H_0-H')$) when the orientation is perpendicular.

Spectrum shift depends only on sample shape and orientation for the same systems as it follows from eq.1. The sample shape and orientation are taken into account in ζ coefficient. Thus the shift of the parallel-orientated cell is approximately two times less than that of the transversal-orientated cell (fig.1, table 1).

The radical ESR spectrum shift towards higher magnetic fields is also observed in the capillary with magnetic liquid (fig.1 curve 6). The capillary can be considered as an infinitely elongate ellipsoid in which the principle axis is normal to external magnetic field and therefore ζ is equal $1/2$.

Therefore the spectrum shift results from the influence of demagnetizing magnetic field but not from dipole-dipole interaction between sensor and individual nanoparticles. The magnitude of this field depends on magnetic properties (magnetization), shape and orientation of sample in external magnetic field.

Linewidth analysis

Besides the radical spectra shift there is also the significant line broadening in magnetic particles presence (fig.1 curves 4, 5 and 6). This broadening arises due to dipole-dipole interaction between sensor's spin and particle's magnetic moment. It is directly proportional to the particle concentration [6].

The spin relaxation process is described using Roch – Muller (R-M) model designed for proton relaxation in media containing magnetic particles [9]. We use the cylindrical-symmetric model of R-M model. This approximation describes well, spin relaxation processes of low molecular particles in a liquid phase that contain rather large magnetic particles where thermal energy is not enough to overcome anisotropy energy barrier ($E_A \to \infty$) and also magnetization vector deviate greatly from easy direction. R-M model yields the equation for spin-spin relaxation time of protons in the media with magnetic particles. We use this equation for electron spin relaxation time calculation in the following form:

$$\frac{1}{T_2} = \left(\frac{32\pi}{135}\right)\gamma_e^4\hbar^2\left(\frac{n_\mu}{RD}\right)\times\left\{\left[\left(\frac{3}{2}\right)J^F(\omega_R,\tau_D,\tau_N)+2J^F(0,\tau_D,\tau_N)\right]\Delta S_z^2+\left[\left(\frac{3}{2}\right)J^A(\sqrt{2\omega_R\tau_D})+2J^A(0)\right]\langle S_z\rangle^2\right\} \tag{2}$$

where R is the nanoparticle radius, D is radical diffusion coefficient $D = kT/6\pi r_g\eta = 2.4\ 10^{-6}$ sm^2/sec, $\tau_D = R^2/D$, τ_N is the Neel relaxation time, ω_R is the radical resonance frequency, S is the spin of superparamagnetic crystal defined as S = Ns, s = ½ is electron spin N is the number of electrons in the crystal contributing to the magnetic moment. J^A and J^F are the spectral density functions.

There are two relaxation mechanisms taken into account in eq.2. acting in the systems with magnetic particles. The first expression describes thermal fluctuations of the nanoparticles' magnetic moment and the second expression, sensor motion in local magnetic fields of particles assuming that the particles on their own are observed as motionless. J^F and J^A terms of eq.2 are the spectral density functions, arising from magnetic moment fluctuations and radical diffusion in non-uniform magnetic fields.

Let's discuss the first relaxation mechanism where local magnetic fields are induced by fluctuations of magnetic moment μ. Its fluctuations are determined by the spin transition in the particle itself ($\tau_c \sim T_1^{\mu}$). It is necessary to find the magnetic moment deviation (ΔS_z) from z axis of external magnetic field to calculate fluctuation amplitude.

$$\frac{1}{T_{1,2}} \sim \Delta S_z^2(t) = \left\langle S_z^2 \right\rangle - \left\langle S_z(t) \right\rangle^2$$

is the root-mean-square deviation.$\langle S_z(t)\rangle$ is the magnetic moment projection on the z axis. It is the sum of constant component $\langle S_z \rangle$ and addition $\Delta S_z(t)$ depending on fluctuation time.

$$\left\langle S_z(t) \right\rangle \sim \left\langle S_z \right\rangle \cdot L\left(\frac{\mu H}{kT}\right) \tag{3}$$

where *L* is the Langeven function $L(\xi) = cth\xi - 1/\xi$, $\xi = \mu H/kT$, $\mu = MV$, *M* is saturation magnetization (for magnetite M = 500 kA/m) and V is the volume of the particle (for our system d_{NP} = 17 nm), H is external magnetic field ~3500 Oe, k is the Boltzmann constant, T = 298 K. Using this data the Langeven function is L(ξ) = 0.99 and $\langle S_z(t)\rangle = 0.99 \langle S_z \rangle$. Hence magnetic moment deviation is $0.02\langle S_z\rangle^2$ and $\Delta S_z^2 << \langle S_z\rangle^2$ therefore the fluctuation term in eq. 2 could be neglected.

The second relaxation mechanism results from radical diffusion in the nanoparticle field. In this way $T_{1,2}^{-1} \sim J^A(z)\left\langle S_z \right\rangle^2$. The spectral density function J^A represented in the original work of Roch-Muller is the following.

$$J^A(z) = \frac{1 + 5z/8 + z^2/8}{1 + z + z^2/2 + z^2/6 + 4z^4/81 + z^5/81 + z^6/648}, \tag{4}$$

where z is the function parameter which equals z = 0 ($J^A = 1$) and $\sqrt{(2\omega_R\tau_D)} = 17$ ($J^A \approx 0$) for the system under study when ω_R = 9.8 GHz and D = 2.4 10^{-5} cm^2/sec. As a result eq.1 would be the following:

$$\frac{1}{T_2} = \left(\frac{32\pi}{135}\right)\gamma_e^4\hbar^2\left(\frac{n_\mu}{RD}\right) \times 2\left\langle S_z \right\rangle^2 \tag{5}$$

The main relaxation mechanism is radical diffusion between nanoparticles. This contributes to sensor line broadening in the systems containing nanoparticles 17 nm size and external magnetic field 3.5 Oe

Conclusion

Radical ESR spectra shift in the presence of magnetic particles depends not only on the particle magnetic properties and concentration, but also on the sample shape as it has been shown in this work. This shift occurs due to internal demagnetizing fields in magnetic system influenced by external magnetic fields. Demagnetizing fields change the field acting on radical and as a result resonance conditions. The magnitude and direction of demagnetizing fields depends on sample shape and its orientation in magnetic fields, hence the radical shift depends on these parameters.

Relaxation processes affecting the broadening are defined by two mechanisms: particle magnetic moment fluctuations and radical diffusion in non-uniform magnetic fields. However, it was shown, that for 17 nm particles in magnetic field 3.5 kOe the second relaxation mechanism is dominating.

Acknowledgments

We thank V.I. Filippov for the hydrosols samples used in this study, prof. V.A. Atsarkin for valuable consultations. The work is supported by Russian Foundation of Fundamental Research No 05-03-32753 and State Contract No 02.513.11.3092.

References

[1] N Noginova, V A Atsarkin // J. Phys.: Condens. Matter **19** (2007) 10

[2] Y.K.Gun'ko; S.C.Pillai; D. McInerney J. Mat. Sci.: Materials in Electronics, 12, N 4-6, (2001) 299-302

[3] A.L. Kovarski, O.N. Sorokina. // JMMM, 311 (2007) 155

[4] P.C. Morais, A.Alonso, O.Silva, N. Buske // JMMM, 252 (2002) 53

[5] G.J. da Silva, P. de Morais, F. A. Tourinho // J. Phys. Chem. 100 (1996) 14269-14271

[6] A. Roch, R. Muller //. J. Phys. Chem, 110, N 11 (1999) 5403-5411

Paramagnetic Monitoring of Electrochemical Conversion of Some Free Radicals and Nickel Complexes

K.V. Kholin[1)], M.L. Valitov[1)], M.K. Kadirov[2)], Yu.G. Budnikova[2)]

[1)]Kazan State University, 420008, Kremlyovskaya str., 18, Kazan, Russia
[2)]Institute of organic and physical chemistry KSC RAS, 420088, Arbuzov str., 8, Kazan, Russia

e-mail: Kholin06@mail.ru

The combination of electrochemical techniques with methods of ESR spectroscopy allows to get the additional information about electrode processes, electronic structure, geometry and reactivity of depolarizers. In some cases ESR spectrum of a paramagnetic substratum allows to define area of localisation unpaired electron and geometry of disposition of magnetic nuclei.

Now in IOPC the new method - voltamperometry detected by an electronic paramagnetic resonance (DESR VA) is developed. This method unites two classical methods - VA and ESR, besides, uniting links are an original three-electrode cell of electrolysis-ESR (El-ESR) for research of paramagnetic particles and the computer with the interface connected to ESR spectrometer and electrochemical installation, consisting of programmer with potentiostat. The method allows to register simultaneously usual VA curves and curves when along with dependence of EPR signal strength s(E) from potential, its first-order derivative s'(E) is fixed also. The current is the first-order derivative of the charge which has passed through a cell, and level of ESR signal is proportional to the charge connected with investigated depolarizer.

Here are some results of research by means of method DESR VA of some free radicals and nickel complexes.

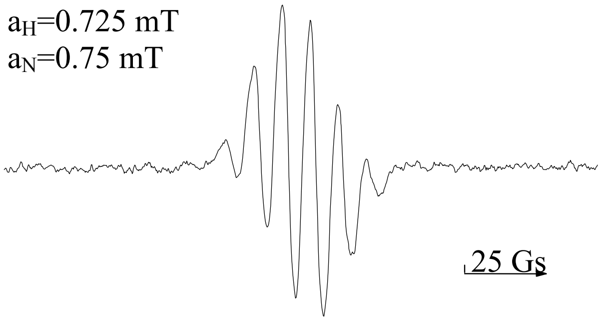

Fig.1 ESR signal 10-metilfenotiazin

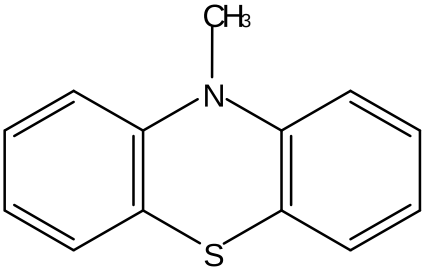

Fig.2 10-metilfenotiazin

On fig.3 CVA i(E), ESR signal strength s(E) and DESR CVA s'(E) 10-metilfenotiazin are shown.

On the CVA curve right after overlaying of potential final value of a current and its gradual increase is observed even before oxidation potentials of depolarizer that, mainly, is caused by charging of a double electric layer, adsorption effects and oxidation of impurity. Appreciable growth of values s'(E) is not observed before oxidation potentials of depolarizer. This results from the fact that during of DESR CVA rate of change in time of ESRsignal strength is registered. This change is connected with electrolysis of depolarizer, and double-layer currents, the adsorptive component of a current and impurity currents do not give contributions in s'(E). DESR CVA curve , basically, corresponds to CVA though does not

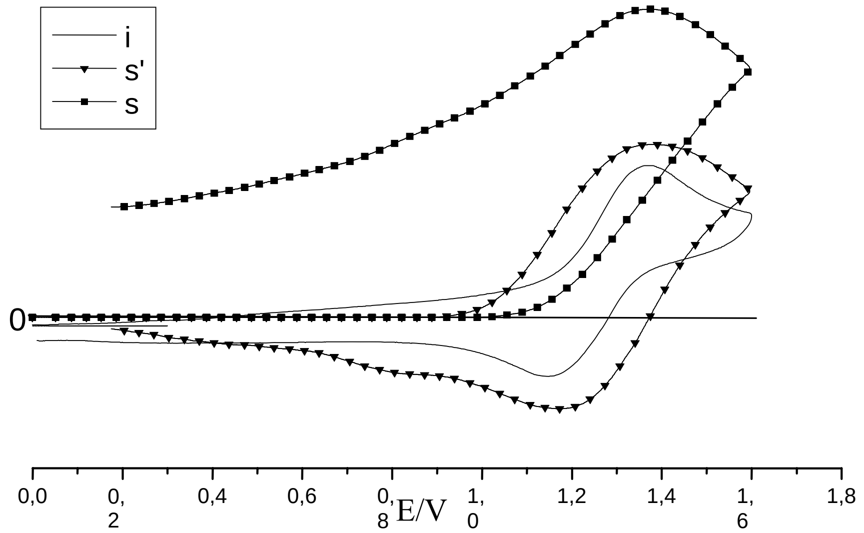

Fig.3. CVA i (E), ESR signal strength s(E) and DESR CVA s’(E) 10-metilfenotiazin ($n=5*10^{-3}$ M) in acetonitrile against the background of $5\cdot10^{-1}$ M $NaBF_4$; sweep rate of potential E (t) - 0,5 V/s; T=293 K. Potential sweep from 0 to -1.6 V.

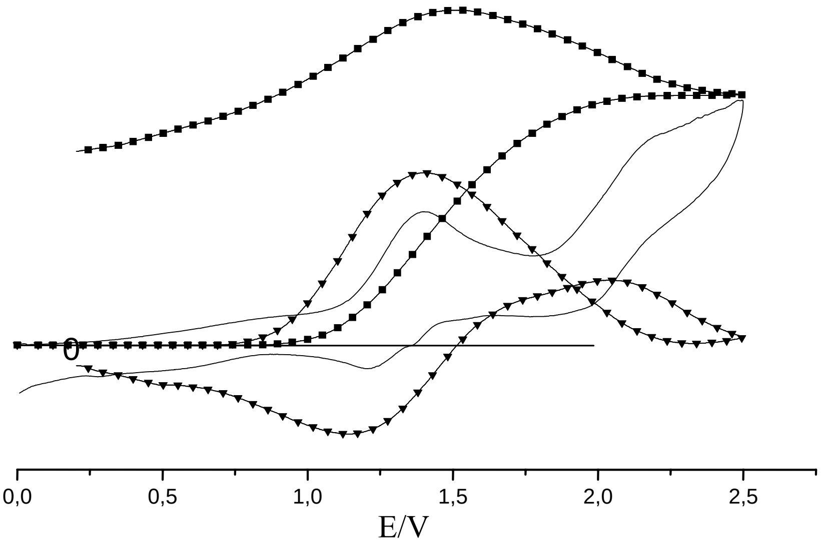

Fig.4. CVA i (E), ESR signal strength s (E) and DESR CVA s’(E) 10-metilfenotiazin ($n=5*10^{-3}$ M) in acetonitrile against the background of $5\cdot10^{-1}$ M $NaBF_4$; sweep rate of potential E(t) - 0,5 V/s; T=293 K. Potential sweep from 0 to -2.5 V.

repeat its form in details. We observe delay in time of anodic and cathodic DESR CVA peaks in relation to corresponding CVA peaks on 0,33 s . On fig.3 and 4 this delay is eliminated. Discrepancy of the form of curves and their shift in time from each other will be a subject of the further research and can give the information about adsorptive, diffusive mechanism, to a structure of a double electric layer etc. On fig.4 there are represented CVA i(E), ESR signal strength s(E) and DESR CVA s’(E) 10-metilfenotiazina in the most interval of working potentials that is when heterogeneous transfer of the second electron takes place also. Judging by CVA it is possible to conclude, that the first wave of oxidation is reversible, and reversibility of the second one is not shown on voltamperometry sweep under given conditions of the experiment. The result of DESR CVA represents a little bit different picture. To the first wave of oxidation i(E) corresponds a wave s'(E), fixing kation-radical formation. Shift of anode peaks in this case has made 0,38s. The second wave corresponds to oxidation of a cation-radical and, accordingly, formation of dication, that is clear from the character of s'(E), it has an anodic minimum and a cathodic maximum.

During the electrochemical oxidation of a complex of nickel (**I**):

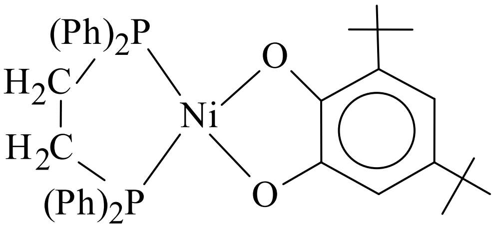

Fig.5 complex of nickel

ESR spectrum appears (potential — 0,6V).

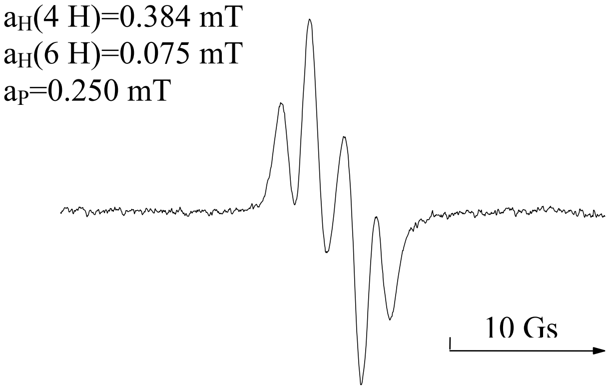

Fig.6 ESR spectrum of a complex of nickel (potential — 0,6V)

On fig.7 CVA i(E), and DESR CVA s'(E) compounds are shown. Judging by CVA it is possible to conclude, that the first wave of oxidation is reversible, and revesibility of the second one is not shown on the voltamperometry sweep under given conditions of the experiment. To the first wave (0,6B) oxidations i(E) there corresponds a wave s'(E), fixing kation-radical formation:

$$I \xleftrightarrow{-e} I^{+} \tag{1}$$

The second wave (1,2V) corresponds to oxidation of a kation-radical and, accordingly, formation of dication,

$$I^{+} \xleftrightarrow{-e} I^{2+} \tag{2}$$

that is seen from the character s'(E) which goes downwards. DESR CVA curve s' (E) answers to a question what causes irreversibility of the second wave of oxidation. After achievement of the second wave the curve s' (E) starts to go upwards. It testifies to presence of the process leading to the formation of kation-radicals after achievement of potentials of dication formation. And as a result of this third process the speed of kation-radicals formation exceeds

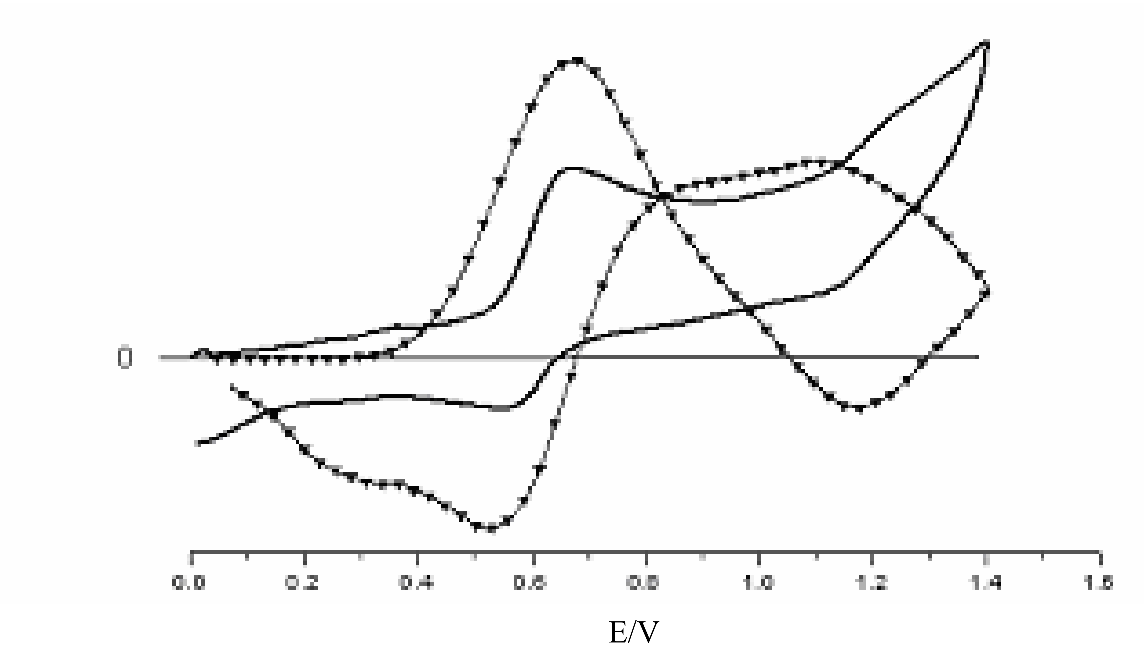

Fig.7. CVA i(E) and DESR CVA s'(E) complexes I ($n=5 \cdot 10^{-3}$ M) in acetonitrile against the background of $3*10^{-1}$ M $NaBF_4$; sweep rate of potential E(t)-0,5 V/s; T=293 K. Potential sweep from 0 to -1.4 V.

the speed of their expenditure by the reaction (2). This third process is reaction of comproportion of kation - radicals with participation of initial compound **I** and dication $\mathbf{I}^{2+}$:

$$I + I^{2+} \leftrightarrow 2I^{+} \tag{3}$$

Growth of speed of formation of kation-radicals proceeds after the potential reversibility. s'(E) starts to decrease at potentials of the first wave and reaches a minimum on cathodic peak.

In this way, DESR CVA method helped to clear up also the processes connected with heterogeneous transfer of the second electron.

Image-potential States in Small Metal Particles

M.A. Fayzullin[1], V.A. Zhikharev[2]

[1]Kazan State University, 420008, Kremlyovskaya str., 18, Kazan, Russia
[2]Kazan State Technological University, 420015, Karl Marks str., 68, Kazan, Russia

e-mail: fmrs@inbox.ru

Numerous physical effects based on specific states of ions and electrons at a surface of conductor have been the subject of large number of theoretical and experimental works and find expanding practical applications. One of the effects is an existence of image-potential states (IP states) which are the electron states localized at a metal surface in the field of image charge [1]. In a case of massive samples an electron bound to its own image does not penetrate the metal surface because of peculiarities of energy-band structure of the metal. IP states were widely investigated by low-energy electron diffraction (LEED), inverse photoemission (IPES) [2] and scanning tunneling spectroscopy (STS) [3]. In work [4] the transient processes signals have been observed after action of short SHF-pulse on a metal surface while static magnetic field was perpendicular to the surface. The origin and the properties of observed signals have been explained [5] in terms of combined magnetic resonance [6] of electrons localized in IP states.

Last decade a particular attention has been given to nanotechnologies. One of the systems widely used in micro- and nanoelectronics is an ensemble of small (nanosized) metal particles embedded into dielectrical or semiconducting matrix. In such a system electron states localized on the particle surface play significant role in particle interactions with surrounding matrix and interparticle interactions, in forming of system response to external electromagnetic radiation, in transfer of electrons throughout the system.

The aim of the present work is the investigation of electron IP states for small metal particle and their features determined by finite (nano) size of particle.

In the case of small spherical metal particle image potential causing an electron localization near particle surface can be approximated by the following formulae:

$$V_{image}(r) = \begin{cases} -\dfrac{\lambda a e^2}{r^2 - a^2}, & r \neq a \\ -\infty, & r = a \end{cases}, \tag{1}$$

where $\mathbf{a}$ is a radius of particle and λe is an effective image charge. To obtain energy spectrum and wave functions of electron IP states one must solve the Schrödinger equation for above mentioned potential

$$\left[-\frac{\hbar^2}{2m^*}\Delta + V_{image}(r)\right]\psi(r,\theta,\alpha) = E\psi(r,\theta,\alpha). \tag{2}$$

Here m^* is effective mass of electron in IP state. Due to spherical symmetry the wave function has the following form: $\psi(r,\theta,\alpha) = \psi^{(\ell)}(r)Y_{\ell m}(\theta,\alpha)$, where $\psi^{(\ell)}(r)$ is radial part of wave function and $Y_{\ell m}(\theta,\alpha)$ is the spherical function. Then the equation (2) is reduced to equation for radial function:

$$\frac{d^2\psi^{(\ell)}(\rho)}{d\rho^2} + \frac{2}{\rho}\frac{d\psi^{(\ell)}(\rho)}{d\rho} + \left[\tilde{\varepsilon} + \frac{b}{\rho^2 - 1} - \frac{c}{\rho^2}\right]\psi^{(\ell)}(\rho) = 0, \tag{3}$$

The dimensionless parameters in eq. (3) are: $\rho = r/a$, $\tilde{\varepsilon} = 2a^2E/e^2a_0$, $b = 2\lambda a/a_0$, $c = \ell(\ell+1)$, where a_0 is the Bohr radius and ℓ is orbital quantum number. The equation (3) can be solved by expansion of $\psi^{(\ell)}(r)$ in power series. The equation has two singular points: $\rho = 1$ - regular point, $\rho = \infty$ - essential singularity. The solution about a regular point ($\rho = 1$) can be written [7] in the form:

$$\psi_1^{(\ell)}(\rho) = A(\rho-1)\left[1+\sum_{n=1}^{\infty} a_n(\rho-1)^n\right], \tag{4}$$

where A is a constant and a_n are coefficients satisfy to the recurrence equation

$$a_n = -\left[p_n + q_n + \sum_{m=1}^{n-1} a_{n-m}[(n-m+1)p_m + q_m]\right]/n(n+1), \qquad a_1 = -(p_1+q_1)/2, \;\; n = 1,2,3,...,$$

with $p_{m(\geq 1)} = 2(-1)^{m+1}$, $\quad q_2 = (\tilde{\varepsilon} - c - b/4)$, $\quad q_{m(1,\geq 3)} = (-1)^m\left[c(1-m) - b/2^m\right]$.

The solution about infinity can be represented [8] as a power asymptotic expansion:

$$\psi_2^{(\ell)}(\rho) \sim Be^{-\alpha\rho}\rho^{-1}\sum_{m=1}^{\infty} b_m\rho^{-m}, \tag{5}$$

where $\alpha = \sqrt{-\tilde{\varepsilon}}$, B is a constant and expansion coefficients b_m are determined by the following expression:

$$b_{m-1} = -\frac{1}{2\alpha(m-1)}\left[(m-1)(m-2)b_{m-2} + \sum_{p=1}^{q} Z_p b_{m-2p}\right] \quad \text{for} \quad m = 1,2,3,...,$$

$$Z_1 = b - c, \qquad Z_{p(\geq 2)} = b, \;\; q = m/2 \;\text{ for even } m \text{ and } \; q = (m-1)/2 \;\text{ for odd } m$$

where b_0 is arbitrary constant. The asymptotic expansion (5) is the alternating series and so its maximal accuracy is achieved by cutting off the series on minimum module term [9].

Solutions (4) and (5) must be sewed at some point ρ^* in which the smoothness condition should be fulfilled:

$$\psi_1^{(\ell)}(\rho^*) = \psi_2^{(\ell)}(\rho^*), \qquad \psi_1^{(\ell)\prime}(\rho^*) = \psi_2^{(\ell)\prime}(\rho^*). \tag{6}$$

The set of equations (6) leads to the spectrum of IP states. The convergence of $\psi_1^{(\ell)}(\rho^*)$, $\psi_2^{(\ell)}(\rho^*)$ and their derivatives [7,10] at given point ρ^* strongly depends on particle radius a and dimensionless energy $\tilde{\varepsilon}$, orbital quantum number ℓ being of minor importance. For certain values of a and ℓ the series in set (6) will be convergent at point ρ^* only for $\tilde{\varepsilon}$ falls in some interval. The estimation made for limit case of metal plane [5] shows that $\tilde{\varepsilon} \in (-2363, 0)$. Below for definiteness the particle radius a was taken equal to 5 nm and $\ell = 0$. Then for $\rho^* = 1.4$ the solution convergence takes place when $\tilde{\varepsilon} \in [-2363, -250]$ and smoothness condition is fulfilled only for two values of energy: $\tilde{\varepsilon}_1 = -2185.4254$ and $\tilde{\varepsilon}_2 = -513.5375$ which are the first and second energy levels of IP state. The shift of point ρ^* to the value 1.7 leads to the interval $\tilde{\varepsilon} \in$ [-550,-200] and to $\tilde{\varepsilon}_2 = -513.5375$ and $\tilde{\varepsilon}_3 = -206.5863$. In similar way all energy levels of IP states may be calculated for given size of metal particle. The first four energy levels ($n = 1,2,3,4$) for different values of orbital number ℓ are presented in Fig 1.

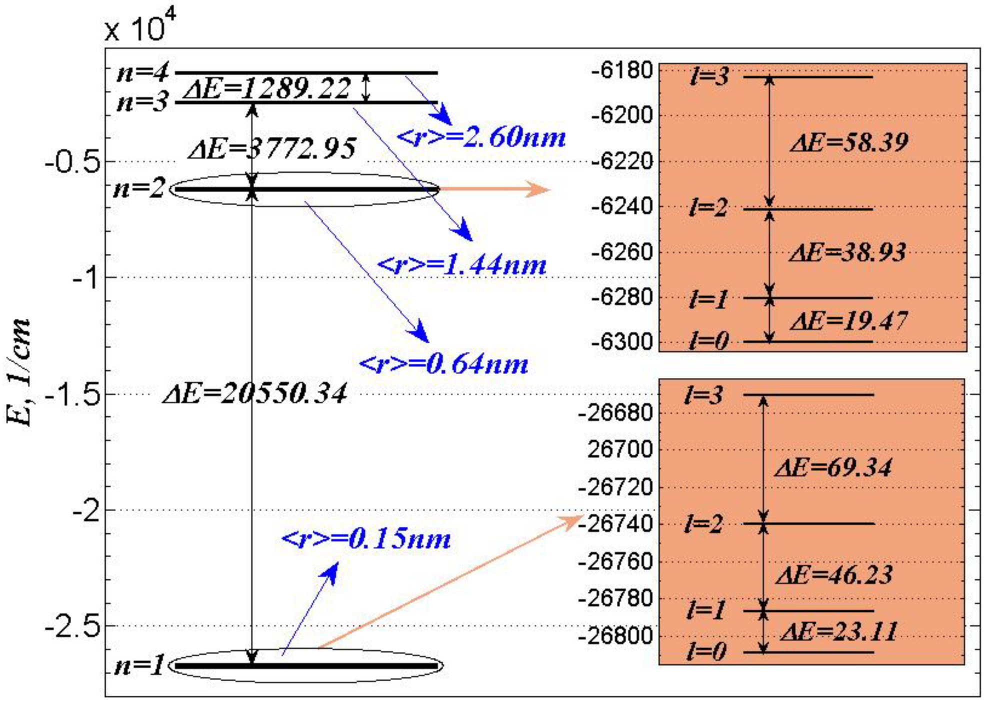

Fig.1 The energy diagram of IPS electron situated closed by spherically metal sample. The radius of particle is taken $\boldsymbol{a = 5nm}$. Here $\boldsymbol{n}$ is the principal quantum number and ℓ is the orbital quantum number. The average distances from the surface are denoted by blue for each of the states and they are depended on ℓ weakly.

A special interest is the possibility of investigation of IP states by magnetic resonance methods, in particular combined magnetic resonance. For this purpose the influence of static magnetic field on IP state should be taken into account. This essentially hinders the solving of the problem. A simple model was considered to gain insight into the behavior of real system: the energy spectrum and wave functions were calculated for an electron whose motion is constrained to the surface of a sphere of radius $\boldsymbol{a}$ in the magnetic field. To restrict an electron motion the term corresponding to infinitely deep and narrow well at $\boldsymbol{r = a}$ was included in Schrödinger equation. Because the radial motion is absent wave function can be expressed, as follows:

$$\psi(\theta,\varphi) = (1-x^2)^{n/2}\left[C_1\sum_{k=0}^{\infty} a_{2k}x^{2k} + C_2\sum_{k=0}^{\infty} a_{2k+1}x^{2k+1}\right]e^{i\varphi\ell_z}, \tag{7}$$

where $\boldsymbol{x = \cos\theta}$, $\boldsymbol{n = |\ell_z|}$ (ℓ_z is magnetic quantum number) and $\boldsymbol{C_1, C_2}$ are the constants. Series coefficients satisfy the recurrence equation:

$$\lambda^2 a_{k-2} + (k+1)(k+2)a_{k+2} - \left[k(k+1) + 2nk - B\right]a_k = 0, \quad k \geq 2, \tag{8}$$

$$a_0 = 1, \;\; a_1 = 1, \; B = 2ma^2E/\hbar^2 - \lambda^2 - 2\lambda\ell_z - n(n+1).$$

Here, $\lambda = \Phi/2\Phi_0$, where Φ is the flux through the equatorial plane and Φ_0 is a flux quantum.

From eq.(8) one can obtain the continued fractions the roots of which give the energy spectrum of considered problem. Field dependence of energy levels leads to the complex level crossing structure [11]. The calculated dependence of several low-lying energy levels on magnetic field is presented in Fig.2. The similar behavior in magnetic field can be expected for energy levels of real IP states for small metal particles.

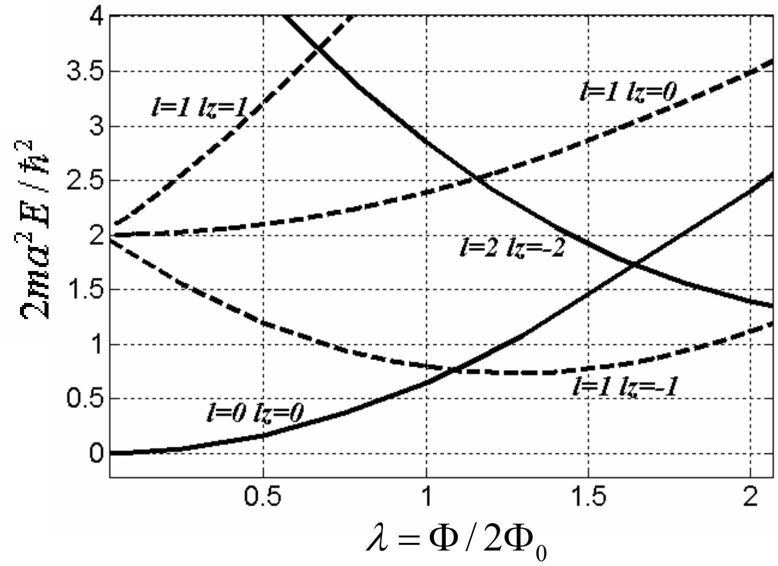

Fig 2 The energy spectrum of electron confined of sphere as function of magnetic field.

References

[1] D. Straub, F.J. Himpsel // Phys.Rev.Lett. 1984. V.52. P.1922.

[2] F.J. Himpsel, J.E. Ortega // Phys.Rev.B. 1992. V.46. P.9719.

[3] S.Yang, R.A. Bartynski, G.P. Kochanski, S. Papdia, T. Fonden, M. Persson // Phys. Rev. Lett. 1993. V.70. P.849.

[4] B.P. Smolakov, N.K. Solovarov // JETP. 1987. V.93. P.1039.

[5] V.A. Zhikharev, A.R. Kessel // Surface: Physics. Chemistry. Mechanics. 1988. № 5. P.13.

[6] E.I. Rashba, V.I. Sheka // SSP. 1961. V.3. P.1863.

[7] E.T. Whittaker, G.N. Watson, A course of modern analysis, edited by F.V. Shirokov (Editorial URSS, Moscow, 2002), P.279.

[8] E. Kamke, Handbook of Ordinary Differential Equations (Lan, St. Petersburg, 2003), P.124.

[9] I.S. Gradshteyn, I.M. Ryzhik, Tables of integrals, series and products (Moscow, Physmatlit, 1962), P.32.

[10] A. Erdelyi, Asymptotic Expansions (Physmatgiz, Moscow, 1962)

[11] J.H. Kim, I.D. Vagner, B. Sundaram // Phys.Rev.B. 1992. V.46. P.9501.

Observation of the Magnetic Coupling Between Nuclei of Liquid ^{3}He and ^{141}Pr in PrF$_3$ Crystal Powder

A.V. Egorov[1)], D.S. Irisov[1)], A.V. Klochkov[1)], A.V. Savinkov[1,2)], K.R. Safiullin[1)],
M.S. Tagirov[1)], D.A. Tayurskii[1)], A.N. Yudin[1)]

[1)]Physics Department, Kazan State University, 18 Kremlyovskaya St., Kazan, 420008, Russia
[2)]Kanazawa University, Kakuma-machi, Kanazawa 920-1192, Japan

e-mail: Murat.Tagirov@ksu.ru

For the first time resonance magnetic coupling in system “Van Vleck paramagnet – liquid ^{3}He” was found out in 1984 [1]. Cross-relaxation effect was observed between ^{3}He nuclei and ^{169}Tm of TmES single crystal. But observed effect wasn’t a replicable experimental result because of TmES surface instability. In preliminary studies of PrF$_3$ we suggested this Van Vleck paramagnet as a promising material for observing cross-relaxation effects in system “PrF$_3$ – liquid ^{3}He” [2].

It is known [3] that the nuclear spin Hamiltonian (1) describes observed ^{141}Pr (I=5/2) NMR spectrum in PrF$_3$ single crystal with parameters $\gamma_x/2\pi = 3.32(2)$ kHz/Oe, $\gamma_y/2\pi = 3.24(2)$ kHz/Oe, $\gamma_z/2\pi = 10.03(5)$ kHz/Oe, $|D/h| = 4.31(1)$ MHz, $|E/h| = 0.30(1)$ MHz.

$$H = -\hbar \sum_{i=x,y,z} \gamma_i H_i I_i + D\left[I_z^2 - \frac{1}{3} I(I+1)\right] + E\left(I_x^2 - I_y^2\right) \tag{1}$$

Computer simulation of ^{141}Pr nuclei NMR spectrum in PrF$_3$ crystal powder was made using method [14] with the nuclear spin Hamiltonian (1). According this simulation (fig. 1) the cross-relaxation effects probability that depends on ^{141}Pr NMR signal intensity have maximum value in magnetic field 2 kOe, which corresponds to the ^{3}He NMR frequency ~6.5

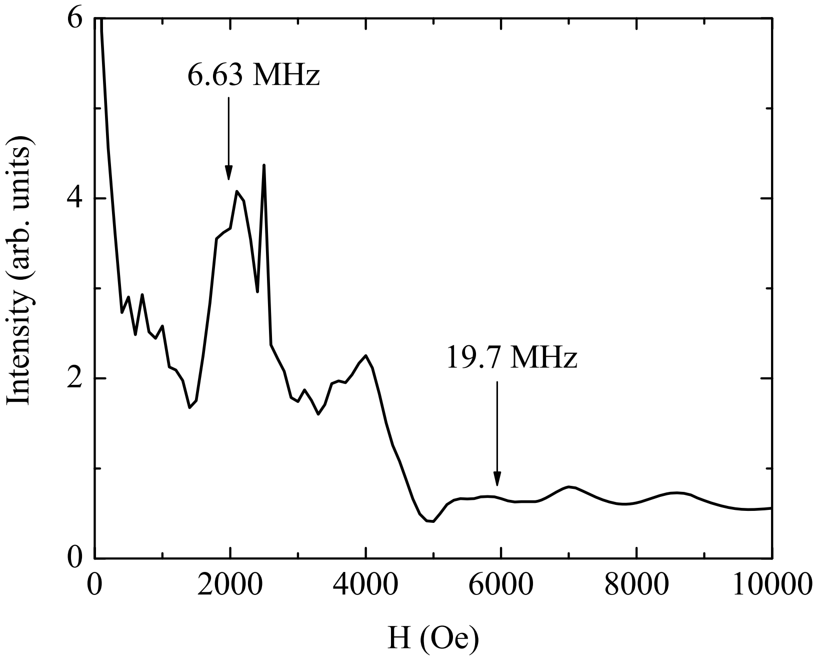

Fig.1 The simulation of the ^{141}Pr NMR signal intensity in PrF$_3$ crystal powder at the different ^{3}He Larmor frequencies.

MHz. In magnetic field 6 kOe (19.7 MHz for ^{3}He nuclei) cross-relaxation effects probability has on of its minimum values.

The PrF_3 crystal powder with medium size 10-45 mkm was used as a sample. The EPR data shows that the total quantity of paramagnetic admixure (Nd^{3+}, Gd^{3+}, Er^{3+}, Dy^{3+}) in PrF_3 was less than 0.02%. According to mass-spectroscopy measurements mole concentration of ^{4}He in ^{3}He was less than 0.05%. Our investigations of ^{141}Pr and ^{3}He nuclei magnetic properties were made by pulse NMR method at temperature 1.5 K and frequencies 6.63 MHz and 19.7 MHz.

Crystal powder NMR spectrums were measured on frequencies 6.63MHz and 19.7 MHz (fig. 2). NMR spectrums simulation for ^{141}Pr nuclei in PrF_3 crystal powder are in good agreement with measured data. During this experiments PrF_3 sample was in contact with liquid ^{4}He. It is notable that longitudinal relaxation times T_1 of ^{141}Pr nuclei in system “PrF_3 powder” doesn’t change its value at different magnetic fields.

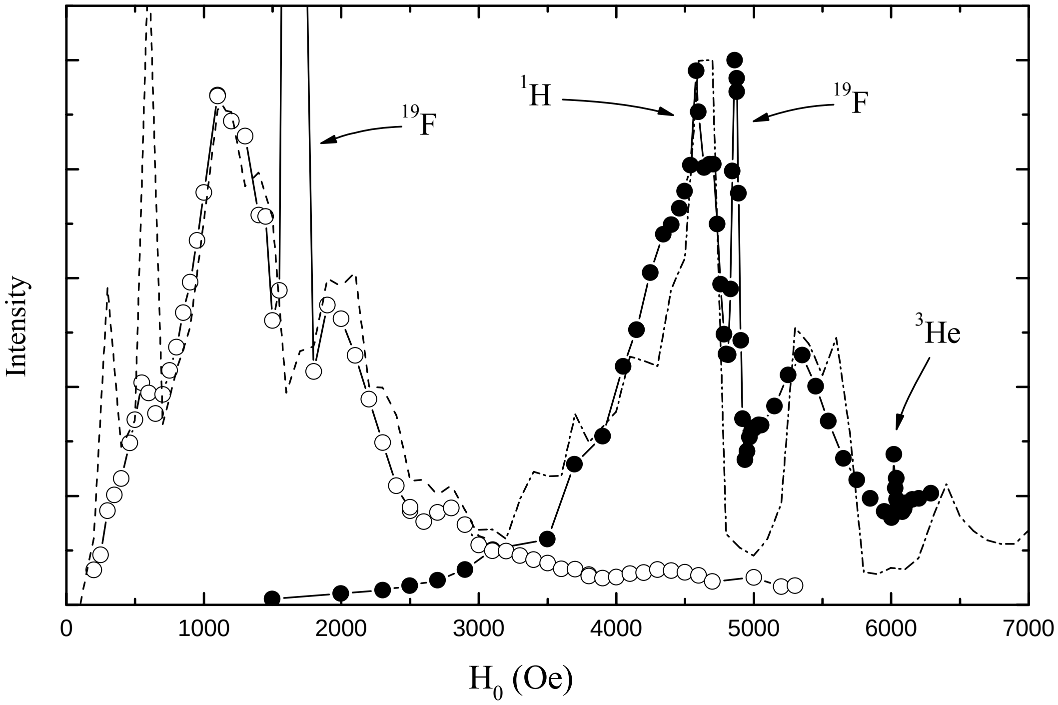

Fig.2 The measured ^{141}Pr NMR spectrum in PrF_3 crystal powder at the 6.63MHz (white circles) and 19.5MHz (black circles) frequencies. The simulated ones are in good agreement with measured data (6.63MHz – dotted line, 19.5MHz – chain line).

The difference between effective gyromagnetic ratios of nuclei ^{141}Pr and ^{3}He leads to differences between durations of spin echo forming. Transversal magnetization relaxation times T_2 of ^{141}Pr and ^{3}He spin systems differ in 4 times: $T_2(^3\mathrm{He})/T_2(^{141}\mathrm{Pr}) \sim 4$ (fig. 3a). As a result there is a possibility to distinguish the signals of spin echo from ^{141}Pr and ^{3}He in conditions of simultaneous observation of NMR signal from both spin systems.

Longitudinal magnetization recovery of system “PrF_3 – liquid ^{3}He” describes with the following function (fig. 3b):

$$A(t) = A(\infty) \cdot \left(1 - A_1 \cdot e^{-\left(t/T_{11}\right)^{0.5}} - A_2 \cdot e^{-t/T_{12}}\right) \tag{2}$$

where A_1, A_2 – nuclei system saturation parameters; T_{11} and T_{12} – longitudinal magnetization relaxation times.

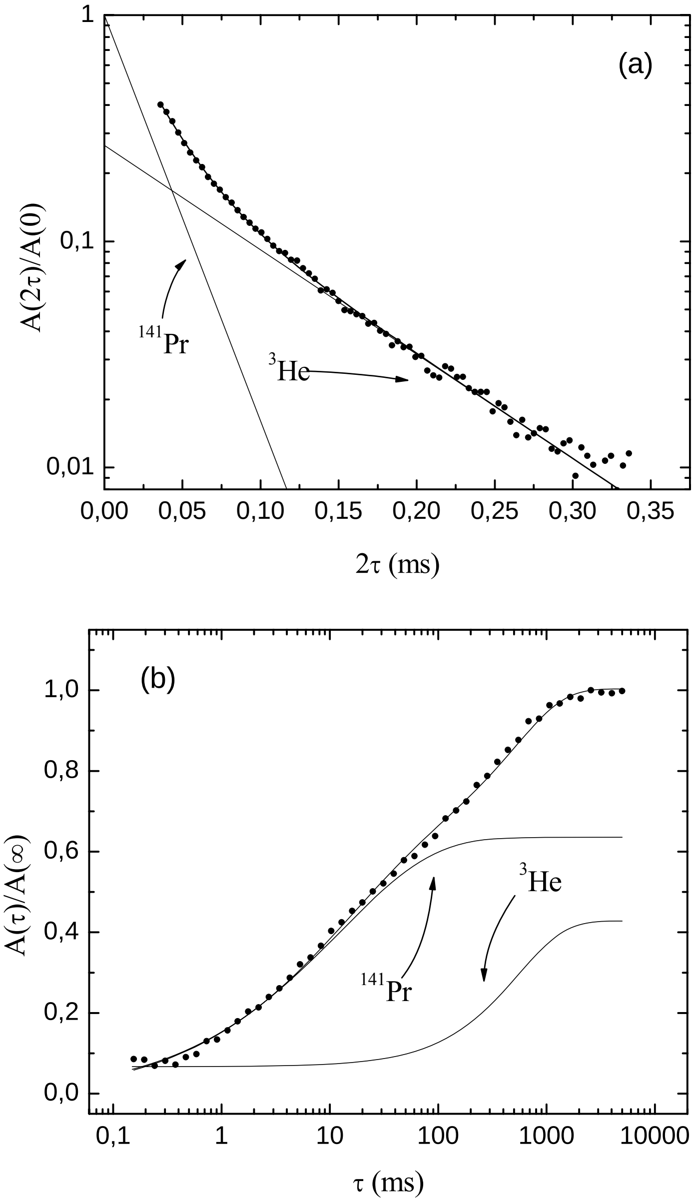

Fig.3. Distinguishable contributions on NMR signal from ^{3}He and ^{141}Pr spin systems at the freqency 6.63MHz at 1.5: a) transversal magnetization decay; b) longitudinal magnetization recovery.

In system “PrF$_3$ – liquid ^{3}He” at frequency 6.63MHz, longitudinal relaxation time T_1 of ^{141}Pr nuclei increases and becomes twice as long. Obtained field dependency of T_1 of ^{141}Pr nuclei is bell-shaped, with the center in 2.05 kOe magnetic field that corresponds to the peak value of ^{3}He nuclei NMR signal (fig. 4). Also at ^{3}He NMR frequency 19.7 MHz longitudinal relaxation time T_1 of ^{141}Pr nuclei doesn’t have resonance behavior.

As stated above this effect on T_1 of ^{141}Pr doesn’t exist in system “PrF$_3$ – liquid ^{4}He”.

Theoretical evaluations show that the ^{3}He nuclei spin system magnetic specific heat 10 times surpasses the resonant ^{141}Pr nuclei spin system one in the case of PrF$_3$ crystal powder.

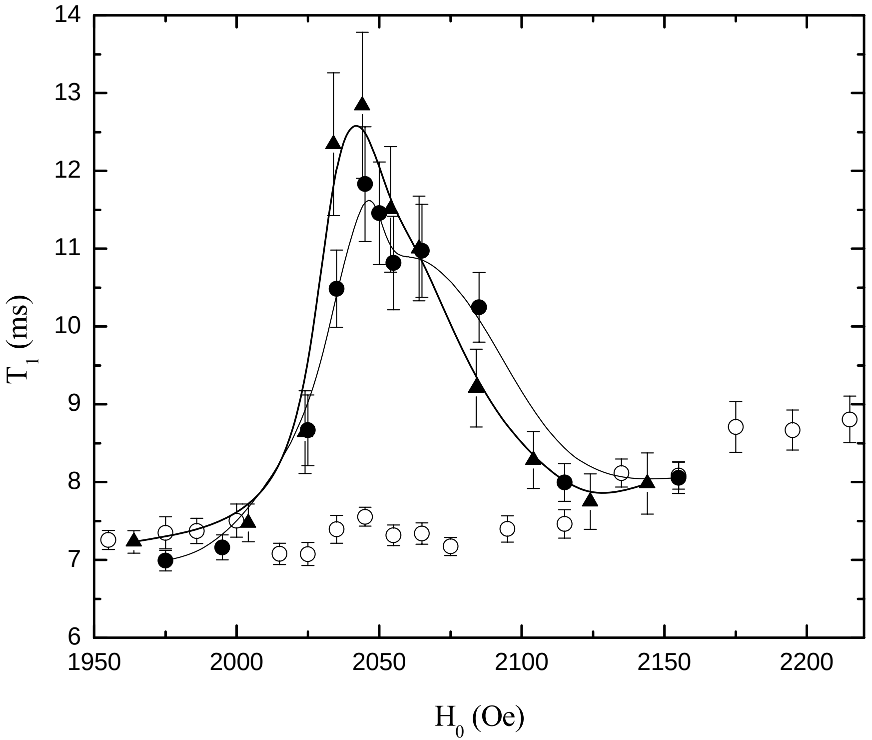

Fig.4 Longitudinal relaxation times T_1 of ^{141}Pr nuclei in systems:
"PrF_3 crystal powder – liquid ^{3}He" (black circles – 6.65MHz, black triangles – 6.63MHz);
"PrF_3 crystal powder – liquid ^{4}He" (white circles – 6.65MHz).

That's why the existence of resonance magnetic coupling leads to deceleration of ^{141}Pr relaxation time T_1. Moreover, according to this evaluations only ^{141}Pr nuclei from 25-30 nm depth surface layer are in magnetic contact with liquid ^{3}He nuclei.

This work is supported by RFBR (grant #06-02-17241) and BRHE (REC-007)

References

[1] A.V. Egorov, F.L. Auhadeev, M.S. Tagirov, M.A. Teplov, JETP Letters. **39**, 584 (1984)

[2] A.V. Savinkov, et al., Journal of Physics: Conference Series. **51**, 79 (2006)

[3] A.V. Egorov, I.R. Mukhamedshin, H.Suzuki, Physica B, **329-333** 1397 (2003)

`1-D Magnetic Photonic Crystals: Dispersion and Optical Properties

S.V. Eliseeva, M.M. Stepanov, D.I. Sementsov

Ulianovsk State University, 432700, Lev Tolstoy 42,Ulianovsk, Russia.

e-mail: yeliseyeva@bk.ru, scaldov@ya.ru

Introduction

Recent years the synthesized periodical structures designed on base of various materials have strong attraction of scientists interest. For the photonic crystal intrinsic effects to be exposed, the length of wave propagated should be compared to the structure period. The Bragg structures formed either by periodical magnetic structure layer growth or by filling cavities in the opals with magnetics are most actual at present. The magnetic substance permeability reveals significant dispersion and resonant frequencies in the microwave band. The use of magnetic materials allows one both to control optical properties of photonic crystals such as width and position of the photonic band gap and to observe magneto-optical effects e.g. Kerr and Faraday ones.

Brief theory

Consider a periodical layer structure composed by homogeneously magnetized magnetic layer of thickness d_1 and non-magnetic insulator of thickness d_2, where $d = d_1 + d_2$ resembles to be the structure period. OZ - axis is aimed normally to the layer interface. Along this direction the bias field is orientated and the circularly polarized microwave band eigenwaves are propagated. The peculiarities of electromagnetic wave interaction with magnetic layers magnetization are described by high-frequency permeability, which being a tensor value in general, for coordinate system and bias direction chosen is written as the following:

$$\mu = \begin{vmatrix} \mu & i\mu_a & 0 \\ -i\mu_a & \mu & 0 \\ 0 & 0 & 1 \end{vmatrix} \tag{1}$$

The isotropic magnetic permeability non-zero components have the following frequency dependence:

$$\mu = 1 + \frac{\omega_M \left(\omega_H^2 + i\omega_r\omega\right)}{\omega_H \left(\omega_H^2 - \omega^2 + 2\mathrm{i}\omega_r\omega\right)}, \; \mu_a = \frac{\omega_M \omega}{\omega_H^2 - \omega^2 + 2\mathrm{i}\omega_r\omega}, \tag{2}$$

where parameters $\omega_M = 4\pi\gamma M$, $\omega_H = \gamma H$, $\omega_r = \xi\omega_H$ are introduced and M, H, γ, ξ denote saturation magnetization, bias field strength, gyromagnetic ratio and magnetic subsystem relaxation factor respectively. In respect to electrical properties magnetic appears to be isotropic medium, therefore permittivity tensor is a diagonal matrix with ε_f components. Insulator permittivity and permeability tensors are also regarded as diagonal ones with corresponding components ε_d, μ_d.

For plane wave $\exp\left(i\omega t + ik_z z\right)$ the lateral wavenumber is

$$\nu_f^{\pm} = k_0\sqrt{\varepsilon_f \mu^{\pm}}\ ,\ \nu_d = k_0\sqrt{\varepsilon \mu_d}\ , \tag{3}$$

where $k_0 = \omega / c$ — is the wavenumber in void and $\mu^{\pm} = \mu \pm \mu_a$ — is effective permeability of the magnetic layer. The resonance and antiresonance for the right-polarized wave are observed at frequencies ω_H and $\omega_a = \omega_H + \omega_M$ respectively, whereas for left-polarized wave the propagation constant frequency dependence has no peculiarities.

In order to periodical layer medium be described, this work involves the method of the transmission matrix, which binds field at the beginning and at the end of the structure period [1]:

$$\begin{pmatrix} h^{\pm}(0) \\ e^{\pm}(0) \end{pmatrix} = \hat{m} \begin{pmatrix} h^{\pm}(d) \\ e^{\pm}(d) \end{pmatrix}. \tag{4}$$

The fields in a periodical structure must fulfill the periodicity condition, so we use the Floquet theorem:

$$h_d^{\pm}(d) = h_f^{\pm}(0)\exp\left(i\nu_{ef}^{\pm} d\right),\ e_d^{\pm}(d) = e_f^{\pm}(0)\exp\left(i\nu_{ef}^{\pm} d\right). \tag{5}$$

The dispersion equation for electromagnetic wave in infinite medium consisted of periodically repeated magnetic and insulator layers is obtained by use of expression for μ matrix diagonal components and is written as:

$$\cos\left(\nu_{ef}^{\pm} d\right) = \frac{m_{11} + m_{22}}{2} = \cos\left(\nu_f^{\pm} d_1\right)\cos\left(\nu_d d_2\right) - \frac{1}{2}\left(\frac{\nu_d \varepsilon_f}{\nu_f^{\pm}\varepsilon_d} + \frac{\nu_f^{\pm}\varepsilon_d}{\nu_d \varepsilon_f}\right)\sin\left(\nu_f^{\pm} d_1\right)\sin\left(\nu_d d_2\right), \tag{6}$$

where $^{\pm}_{ef}$ - is a wave vector longitudinal component of the wave propagating through the structure, that could be considered as Bloch wavenumber [2].

$$e^{i\nu_{ef}^{\pm} d} = \frac{m_{11} + m_{22}}{2} + i\sqrt{1 + \left(\frac{m_{11} + m_{22}}{2}\right)^2} = \cos\left(\nu_{ef}^{\pm} d\right) \pm i\sin\left(\nu_{ef}^{\pm} d\right). \tag{7}$$

The sign of the Bloch wavenumber along with the group velocity one are determined by the sign of the second summand in (7): the negative is for positive direction of the energy flux.

In order to find reflection ratio we make use of expressions for fields in bulk of insulator and magnetic layers, boundary and periodicity conditions between layers as well as boundary conditions at the halfspace-ferrimagnetic interface. Solving this equation system, it is easy to find an expression for amplitude reflection ratio $r^{\pm}$. For further analysis let expression energy reflection ratio be deduced:

$$R^{\pm} = \left(r^{\pm}\right)^2 = \left(\frac{\exp\left(i\nu_{ef}^{\pm} d\right) - m_{11} - ikm_{12} / k_0\varepsilon}{\exp\left(i\nu_{ef}^{\pm} d\right) - m_{11} + ikm_{12} / k_0\varepsilon}\right)^2 . \tag{8}$$

Here $k = k_0\sqrt{\varepsilon\mu}$ is the wavenumber for the uniform semispace.

For the geometry studied polar Kerr effect could be observed. In case of linearly polarized wave impinging on structure the expressions for the rotation angle and ellipticity will be

$$\Theta_{ref} = \frac{\xi^{+} - \xi^{-}}{2}, \quad E_{ref} = \frac{\left(r^{+}\right) - \left(r^{-}\right)}{\left(r^{+}\right) + \left(r^{-}\right)}, \tag{9}$$

Here $\xi^{\pm}$ — are the phases of complex amplitude reflection ratio for left and right circularly polarized wave reflected from layer respectively $r^{\pm} = \left(r^{\pm}\right)\exp\left(i\xi^{\pm}\right)$.

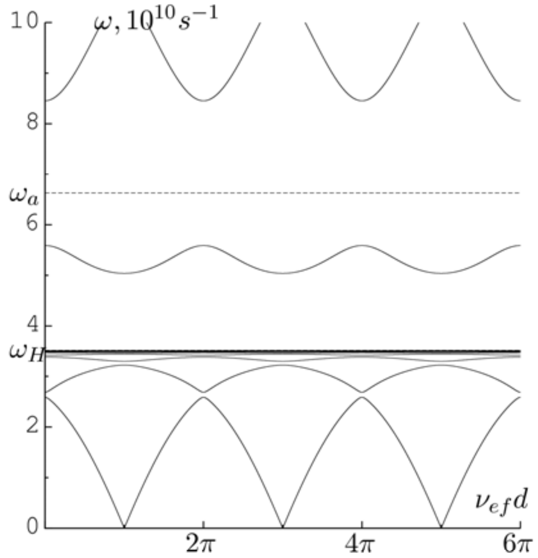

Fig. 1: Bloch wavenumber frequency for right-polarized wave.

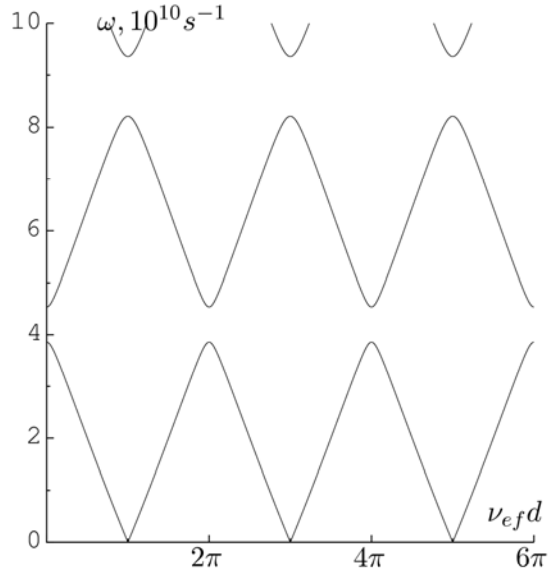

Fig. 2: Bloch wavenumber frequency for left-polarized wave.

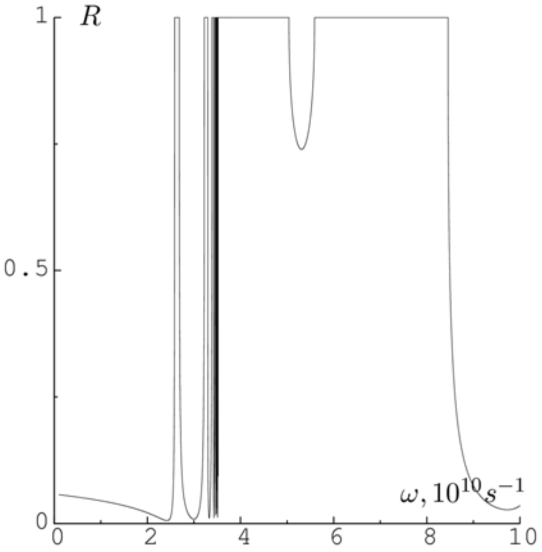

Fig. 3: Reflection ratio for right-polarized wave.

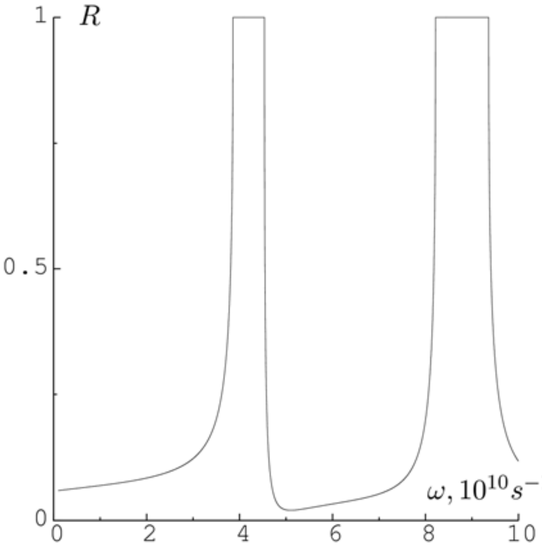

Fig. 4: Reflection ratio for right-polarized wave.

Numeric results

As magnetic material parameters for calculation basis the relevant parameters of the ferro-yttrium garnet were taken [3]. Now let the numeric analysis of dispersion equation (6) be carried out. Fig. (1,2) show the dependence of the frequency on the Bloch wavenumber for left- and right-polarized wave respectively in absence of relaxation in the magnetic subsystem. For the right-polarized wave the effective permeability conditioned peculiarities are revealed. The bandgap width is diminished and as the frequency tends to resonant $\omega_H = 3.52 \cdot 10^{10} s^{-1}$ the bandgaps are condensed. In interval $\omega_H < \omega < \omega_a$ the single surface mode is observed $\omega_a = 6.63 \cdot 10^{10} s^{-1}$. For left-polarized waves the bandgaps are broadened with the frequency growth.

The dependence of the reflection ratio upon frequency for the left- and right-polarized wave in case of normal incidence at periodical structure surface is shown at fig. (3,4) respectively. The figures presented demonstrate that reflection ratio $R = 1$ inside the bandgap and radiation does not penetrate into structure volume, whereas reflection ratio $R \to 0$ inside the allowed band.

Conclusion

Band spectra of left- and right-polarized waves as well as reflection ratios in absence of relaxation have been obtained. Magneto-optical effects have peculiarities connected with periodicity and resonant frequencies. Magneto-photonic crystals can find an application as light polarization transformers and modulators.

References

[1] Bass F.G., Bulgakov A.A., Tetervov A.P. High-Frequency Properties of Semiconductors with Super-Lattices, Moscow: Nauka, 1989.

[2] Yariv A., Yeh P. Optical Waves in Crystals, Wiley, New York, 1984.

[3] Eliseeva S.V., Sementsov D.I. Dispersion des ondes electromagnetiques dans une multicouche periodique dans un champ magnetique exterieur: theorie.// Comptes Rendus Physique, volume 7, issue 2, pp.255-261, 2006.

Conformation of Saturated Five-Membered Heterocecles as Studied by NMR and *ab'initio* Calculations

A.V. Chertkov$^{1)}$, O.I. Pokrovsky$^{1)}$, A.K. Shestakova$^{2)}$, V.A. Chertkov$^{1)}$

$^{1)}$Department of Chemistry, Moscow State University, 1 Leninskie Gory, 119992, Moscow, Russia
$^{2)}$State Research Institute of Chemistry and Technology of Organoelement Compounds, 38 Shosse Entuziastov, 111123 Moscow, Russia

e-mail: alex-chertkov@yandex.ru

Introduction

Nowadays the process of pseudorotation in five-membered saturated heterocycles can be studied by different spectroscopic methods. Inner rotation in these systems can be realized as a fast dynamic process with very low barriers or even none of them. Complete set of possible geometry configuration for the compound contribute to observable parameters. The temperature-averaged spectral data can be defined numerically using additional knowledge of potential energy distribution for every conformer within the processes under study in terms of high-amplitude vibrations. The well-grounded choice of the model of conformation behaviour is highly important for getting proper results. With molecular systems under study, accurate solution of the so-called vibration problem is needed.

Method

We have developed a method of estimation the conformational state of saturated five-membered cycles, based on the complete analysis of high resolution NMR spectra and quantum mechanical estimation of parameters of the pseudorotation process. As a starting point, the undistorted of potential energy surface (PES) of inner rotation for the compounds studied was built by applying the scanning technique to skeletal dihedral angles with GAUSIIAN-98 program [1]. This allows us to get a trial "reaction path" for the pseudorotation process. Conformational dependencies for spin-spin coupling constants (SSCC) for principal points on the reaction path there calculated using FP DFT technique [2] also using GAUSIIAN-98 program (UB3LYP with 6-311G* basis set). ^{1}H NMR spectra were recorded for a series of solvents ($CDCl_3$, CD_3CN and C_6D_6) on "Bruker AV-600" spectrometer at 303K, and were treated using total lineshape analysis technique (program VALISA [3]) which allows us to get very accurate estimates of experimental SSCC values.

Finally, the reverse spectral problem was solved to adjust experimental and calculated data and build up the "true" potential of pseudorotation. We developed REVIBR program, which solves numerically corresponding vibration problem and models the dynamic averaging using the technique of convolution of the spin-spin coupling surfaces using the whole set of vibration energies and eigenvectors (normally, 200 lowest ones). Convolution criterion used in REVIBR program allows to get calculated SSCC for given temperature. Nonlinear optimization (Levenberg-Marquart techniques) of the estimated parameters for the "true" pseudorotation PES (modeling difference of ground states of main conformers and heights for the conformational barriers) used to get best fit of experimental and calculated SSCC values.

Results and discussion

The developed technique was applied to the analysis of conformational state of tetrahydrofuran, tetrahydrothiophene, pyrrolidine, tetrahydrothiophene-1-oxide and proline. In order to calculate the surface of potential energy for pyrrolidine, tetrahydrothiophene-1-oxide and praline, the additional degrees of freedom (they appeared because of inversion movement of substitutes by cyclic heteroatom) have been taken into account. The obtained data shows that pseudorotation in every compound carries out by the mechanism with high-amplitude vibration.

Acknowledgements

This work is supported by the RFBR (grant № 06-03-32800). A.K. Shestakova thanks the fond AVH (Germany).

References

[1] M. J. Frisch, G. W. Trucks, H. B. Schlegel, … , and J. A. Pople, “*Gaussian 98W, Revision A.11*” , *Gaussian, Inc.*, Pittsburgh PA (**2001**).

[2] T. Onak, J. Jaballas, M. Barfield, *J. Am. Chem. Soc*, **121**, 2850-2856 (1999).

[3] S. V. Zubkov, S. S. Golotvin, V. A. Chertkov. - *Russ. Chem. Bull.,* **51**, 1222-1230 (2002).

Engineering and Production of “Fast” Impulse Sequences for Low-Field Magnetic-Resonance Tomographs

A.R. Gabidinova[1)], N.A. Pyrkina[2)]

[1)]Zavoisky Physical-Technical Institute, 420029, 10/7 Sibirsky tract, Kazan, Russia
[2)]Kazan State University, 420008, Kremlevskaya 18, Kazan, Russia

e-mail: aigool@mail.ru

In Zavoisky Physical-Technical Institute an ultra-low-field magnetic resonance tomograph “TMR-0.06-KFTI” with magnetic induction 0.06 Tesla was developed and manufactured.

Tomographs “TMR-KFTI” are intended for diagnostics of various illnesses, planning of surgical operation and radiotherapy, controlling of therapy carried and its effectiveness. The tomographs are used for diagnostics of brain, backbonea and joints.

Magnetic resonance tomograph “TMR-0.06-KFTI” belongs to ultra-low-field tomographs, it allows noticeably decrease equipment power consumption during receiving of images that satisfies medical requirements. Besides the value of the constant magnetic field, radiofrequency field and also switching speed of the gradient magnetic fields many times lower than maximum permissible values that are accepted by World Health Organization.

Outlook of modernization

Tomograph “TMR-0.06-KFTI” has following set of standard methods: Gradient Echo, Spin Echo, Multiple Spin Echo, Saturation – Recovery, Inversion – Recovery.

This methods let to take a diagnostic images. But it taking takes much time, so a survey of patients takes plenty time too.

The time will curtails if we will use fast impulse programs. The purpose of our research is engineering and production of “fast” impulse sequences for low-field magnetic-resonance tomographs.

The first results are presented and discuss.

Impulse sequence of taking T1- suspended images TR=200÷500ms TE=34÷40ms

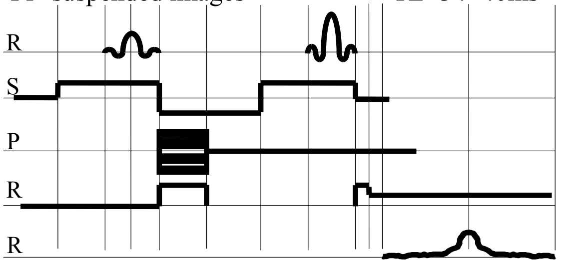

"Gradient Echo" impulse sequence TR=200÷500ms TE=28÷35ms

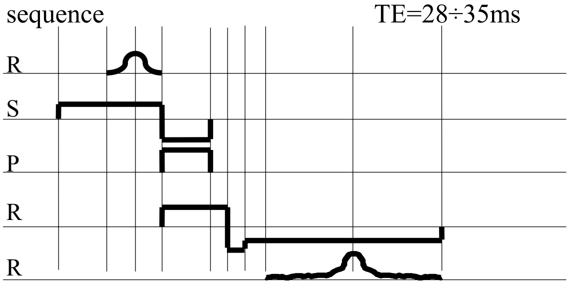

Impulse sequence of taking T2- suspended images TR=1000÷3000ms TE=80÷150ms

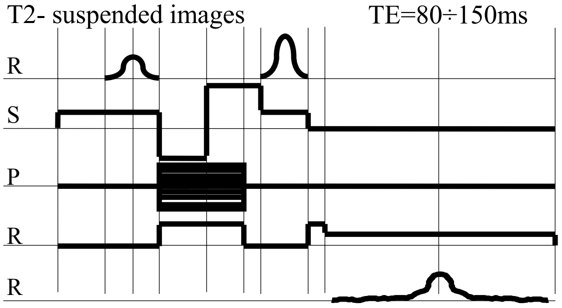

Impulse sequence of inversion-reconstruction TR=200÷500ms TE=34÷40ms TI=50÷150

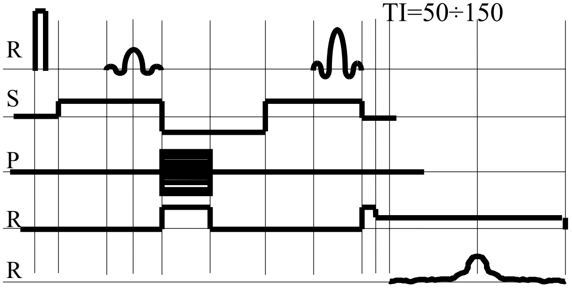

Describing Spin Label Motion: Ordering Potential or Partial Averaging?

V.V. Novikov(1), Ya.V. Tkachev(2), V.P. Timofeev(2)

(1)Nesmeyanov Institute of Organoelement Compounds, Russian Academy of Sciences, 119991, 28 Vavilova str., Moscow, Russia,
(2)Engelhardt Institute of Molecular Biology, Russian Academy of Sciences, 119991, 32 Vavilova str., Moscow, Russia

e-mail: novikov84@gmail.com

Stochastic Liouville equation formalism is commonly used for calculation of the EPR spectra of nitroxide spin labels. Unfortunately, for the description of the complex anisotropic spin label motion, the simulations are extremely time-consuming [1]. Thus, some assumptions should be applied to simplify the calculations. The convenient approach is to use partial averaging of magnetic tensors technique for describing fast motion of spin label with respect to carrier. Nevertheless, this assumption's limitations are still not clearly estimated. In addition, several different methods for magnetic tensors partial averaging exist. In the present work, three possible approaches were used:

1. Direct averaging, which can be accomplished using $B = \langle T^{-1}AT \rangle$ formulae, where A and B are **g** or **A**-tensor values before and after partial averaging, correspondingly, T is the directional cosine matrix, and the angular brackets denote averaging over orientation probability distribution function □□, which characterizes the motion of spin label. This approach was successfully applied for describing the result of fast, low-amplitude oscillation for the sterically restricted spin label, as in the APO-form of spin-labeled myosin [2].
2. Usage of the model, provided by Timofeev et al. [3], where spin label undergoes restricted oscillations around certain axis, which leads to the partial averaging of magnetic tensors. This approach gives additional possibility to consider the existence of different "modes" of oscillation.
3. Application of the approach, described in [4], which uses torsional potentials of spin label tether bonds for estimating components of partially averaged magnetic tensors. This method is quite promising due to the clear physical sense of parameters describing the partial averaging. On the other hand, a wide variety of model parameters results in significant degeneration of the tensor values obtained, so an additional conformational analysis is needed in the case of each spin labeled system.

Firstly, the set of model trajectories for spin label reorientations was generated. Three different approaches were used for calculation of partially averaged magnetic tensors on the basis of these trajectories. The next step was to calculate the slow-motion EPR spectra using the values of partially averaged magnetic tensors in SLE-based program Simult5. The resulting spectra were compared with spectra, obtained by means of SRLS model [1] for the same process, and the discrepancies between them were discussed in terms of validity of each model for different model processes.

References

[1] Polimeno A., Freed J.H.: J. Phys. Chem. **99**, 10995 (1995)

[2] Novikov V.V., Burr A.R., Thomas D.D., Nesmelov Yu.E.: in 51st Ann. Meeting of Biophys. Soc. Abstract Book, Utah, 2815-Pos/B482, (2006)

[3] Timofeev V.P., Samarianov B.A.: J. Chem. Soc., Perkin Trans. **2**, 2175 (1995)

[4] Tombolato F., Ferrarini A., Freed J.H.: J. Phys. Chem. B **110**, 26260 (2006)

Morphometric Analysis MR Imaging of Experimental Ischemic and Hemorrhagic Stroke in Rats

A.A. Uchevatkin[1,2)], N.I. Voblova[2)], E.A. Andreeva[2)]

[1)]Research Center for Magnetic Tomography and Spectroscopy, M.V.Lomonosov Moscow State University, 119991, Leninskie Gori, Moscow, Russia.
[2)]Russian State Medical University, 117997, Ostrovityanova str., Moscow, Russia.

e-mail: uchevatkin@mail.ru

Introduction

The vascular diseases of brain are one of the most urgent neurologic and social problems. According to the data of the World Health Organization the stroke occupies the third place after the diseases of heart and oncologic diseases among the reasons for the mortality of the adult population of planet. Its medium frequency of occurrence in the developed countries is about 2500 cases to 1 mln. populations per year. In the course of the first month after the development of hemorrhagic stroke the mortality from it composes 50%.

Stroke is one of the basic reasons for the invalidization of adult population, with each subsequent year of life the risk of recurrent stroke grows by 5-8%.

Analysis of the mechanisms of the development of this disease, the search for new effective therapeutic means, and also the problem of early diagnostics and treatment of cerebral strokes - some of the most important tasks of contemporary medicine. The large number of studies is devoted to questions of pathogenesis, clinic, diagnostics and treatment of acute stroke [1-5].

One of the main directions in the study of this disease - experimental simulation of disease on laboratory animals.

Purpose

In this work the following purposes were set:

1. To analyze MRT of the image of the brain of rats, subjected to operation on the simulation of focal ischemia of brain via the electrocoagulation of the distal division of average cerebral artery with the trans-cranial access, and to study the influence of mesenchymal stem cells on the data of change.
2. To carry out the morphometric analysis of the pathologically changed zones of the brain (hematoma and perifocal edema) with the experimental hemorrhagic stroke the rats have under treatment conditions by the derivatives of taftsina.

Materials and methods

Experiment was carried out on the males of nonlinear rats by the mass of 180-200 grams (25 rats with the ischemic stroke even of 30 rats with the hemorrhagic stroke).

All NMR measurements were made on a MR-system (BioSpec 70/30, Bruker) operating at 7 T.

For the visualization of ischemia the registration MRI was produced in the regime, which makes it possible to obtain three types of images with different suspension: on the proton density, the T2- weighed images with the moderate suspension and the T2- weighed images with the expressed suspension (TR = 2742ms, TE = 23,2 ms ; TR = 2742 ms, TE = 90,6 ms; TR = 2742 ms, TE = 158ms accordingly) (Fig. 1).

For the visualization of hemorrhagic stroke were used T2- the weighed images, obtained with the aid of pulse sequence RARE (Rapid Acquisition with Relaxation Enhancement) (TR = 2742 ms , TE = 90,6 ms) (Fig. 2).

For obtaining the T1- weighed images was used sequence FLASH (Fast Low Angle Short Imaging) (TR = 700ms, TE = 9,9 ms).

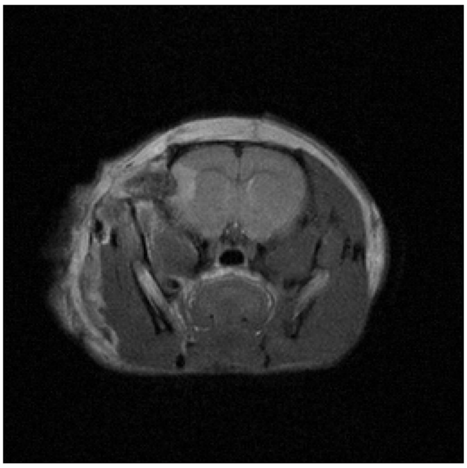

Fig.1 Ischemic stroke in the rats

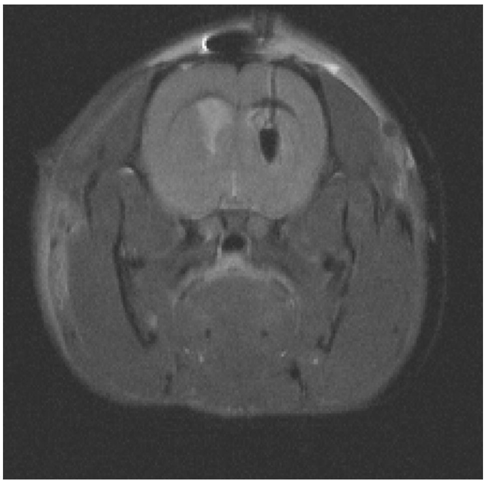

Fig.2 Hemorrhagic stroke in the rats

Images were processed with the aid of the program "ImageJ".

Simulation of the hemorrhagic stroke:

Was used the model of the two-step introduction of the autologous blood employing procedure with the modification [7]. This method makes possible to simulate the spontaneous intra-cerebral hemorrhage, which appears with the break of vessel, with obtaining of hematomas, compared by the volume, for form and localization.

Simulation of the ischemic stroke:

The simulation of focal ischemia of brain was carried out employing the procedure, proposed Chen [6], by the distal occlusion of left middle cerebral artery.

Results:

Ischemic stroke:

In the work the volumetric characteristics of the center of infarction in the dynamics are described; also was investigated the contrast of infarction, what is the novelty of work. It is proposed the diagnostic rule for the differentiation of infarction and cerebritis of the brain with the aid of the indices of volume and contrast, which can simplify the use of a method MRT for the collection of morphometric characteristics.

The side-line pathologic effects for brain and soft tissues of head were described for this experimental model of infarction, such as the depression of soft tissues into the cavity of skull, edema of the brain because of the pressure of soft tissues, edema and hematoma of soft tissues of head, displacement of the middle structures of the brain, cerebritis, inflammatory reaction of meninges, ventriculitis. Considerable attention is given to the description of the dynamics of a volume of ipsilateral hemisphere and volume of entire brain. In the work we made an evaluation of the influence of stem cells on the center of infarction and the remaining pathologic changes in the brain.

The results of this investigation, can be considered in the future with conducting of similar experiments and represent the significant scientific interest. The introduction of mesenchymal stem cells leads to the 7th day to the reliable decrease of the volume of the hemisphere of the brain with the lethal area, which correlates with a reliable improvement in neurologic status of animals.

Hemorrhagic stroke:

The obtained results showed that the volume of hematoma reliably was reduced in both groups of treated rats in comparison with the control group for the elongation of entire study (Fig. 3).

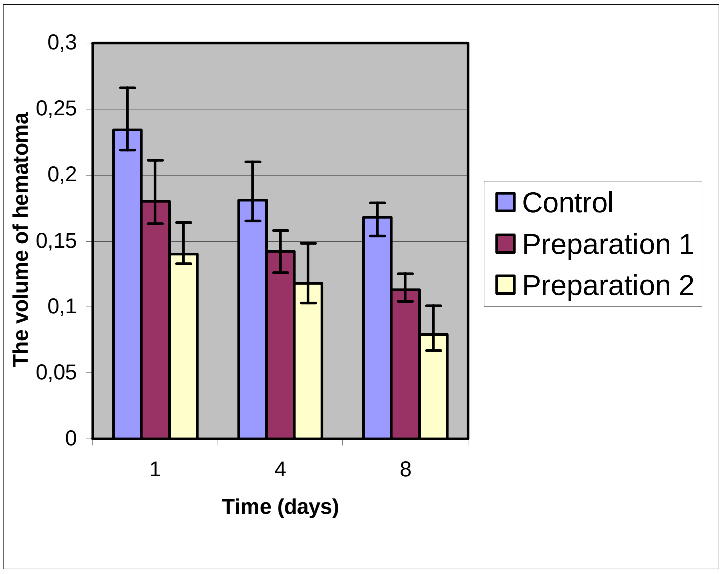

Fig.3 Dynamics of volume of hematoma in the groups of animals.

The volume of perifocal edema of the brain reliably was reduced in both groups of treated rats in comparison with the control group for the elongation of entire study (Fig. 4).

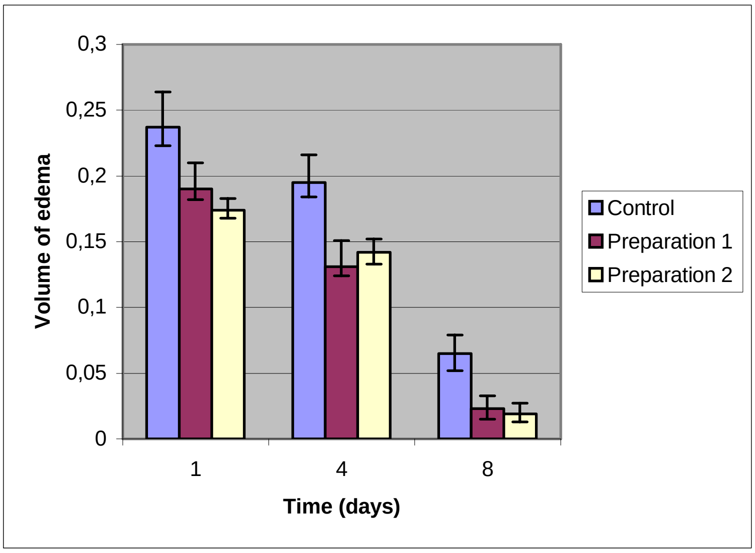

Fig.4 Dynamics of the volume of perifocal edema of the brain the groups of animals

Thus, on the basis of the results given above, it is possible to indicate that the studyes peptide can pretend in the future to the role of neyroprotektions.

References

[1] Dickerson LM, Carek PJ, Quattlebaum RG. Prevention of recurrent ischemic stroke. Am Fam Physician. 2007 Aug 1; 76(3):382-8. Review.

[2] Nor AM, Ford GA. Misdiagnosis of stroke. Expert Rev Neurother. 2007 Aug; 7(8):989-1001. Review.

[3] Ustrell-Roig X, Serena-Leal J. Stroke. Diagnosis and therapeutic management of cerebrovascular disease. Rev Esp Cardiol. 2007 Jul; 60(7):753-69. Review.

[4] Emre U, Rantanen K, Tatlisumak T. Antithrombotic treatment in the prevention of ischemic stroke. Curr Drug Targets. 2007 Jul; 8(7):817-23. Review.

[5] Romero JR. Prevention of ischemic stroke: overview of traditional risk factors. Curr Drug Targets. 2007 Jul; 8(7):794-801. Review.

[6] Chen S.T., Hsu C.Y., Hogan E.L. et al. // Stroke. – 1986. – Vol. 17 – P. 738-745.

[7] Deinsberger W, Vogel J, Kuschinsky W, Auer LM, Boker DK. Experimental intracerebral hemorrhage: description of a double injection model in rats. Neurol Res. 1996 Oct; 18(5):475-7

Table of Contents